MULTI-ACQUISITION AND MULTI-DIMENSIONAL EARTH'S FIELD NUCLEAR MAGNETIC RESONANCE SPECTROSCOPY

By

Meghan Eileen Halse

A thesis
submitted to Victoria University of Wellington
in fulfilment of the requirements for the degree of
Doctor of Philosophy
in Physics

Victoria University of Wellington
2009

Abstract

In this thesis we investigate the ways in which the sensitivity, resolution and overall performance of an Earth's field NMR system can be improved without significantly compromising its simplicity, portability or affordability. We investigate the limits of the information obtainable using this device and present a range of methods for calculating and analyzing NMR spectroscopy experiments detected in the Earth's magnetic field.

We demonstrate significant improvements in the performance of a commercial Earth's field NMR device, the Terranova-MRI, through several apparatus developments. First-order shimming is added to the system in order to counter any local inhomogeneity of the Earth's field. The spectral resolution of the instrument is further improved through the introduction of a field locking system to counter the natural temporal drift in the magnitude of the Earth's magnetic field. External noise interference is reduced through the use of Faraday screening, effectively increasing the signal-to-noise ratio (SNR) performance of the device.

We explore three signal enhancement methodologies for optimizing the SNR performance of the system. Prepolarization, with an electromagnet as well as a permanent magnet array, is considered and compared to dynamic nuclear polarization (DNP) and hyperpolarization via optical pumping. We present a detailed theoretical discussion of DNP in low-fields and demonstrate the application of this technique for signal enhancement in EFNMR. An apparatus for performing DNP in the Earth's field is presented and optimized.

A density matrix approach to simulating one- and two-dimensional Earth's

field NMR experiments is presented. These numerical simulations, along with a perturbation theory approach to calculating one-dimensional EFNMR spectra of tightly coupled heteronuclear systems, are explored and compared to experimental spectra of the tetrahydroborate and ammonium ions. These systems are of particular interest for NMR detected in the Earth's field because they contain strongly coupled nuclei of differing spin, a situation previously unexplored in the literature.

Multi-dimensional Earth's field NMR spectroscopy methods, in particular the correlation spectroscopy (COSY) experiment, are implemented and optimized through the use of shimming, field stabilization and noise screening. The 2D COSY spectrum of monofluorobenzene is analyzed and compared to calculated spectra in order to determine the indirect spin-spin coupling constants of this molecule in the Earth's magnetic field. A 2D COSY spectrum of 1,4-difluorobenzene is also presented and compared to simulation. The SNR performance of COSY in the Earth's field is greatly improved through the use of DNP for signal enhancement. A high-quality, 2D COSY EFNMR spectrum with DNP acquired from 2,2,2-trifluoroethanol is presented and compared to simulation. The particular features of this spectrum, which result from the use of DNP for signal enhancement, are discussed with reference to a density matrix simulation and to a one-dimensional spectrum calculated using perturbation theory.

The strong indirect spin-spin coupling regime in fields weaker than the Earth's magnetic field is explored through exact calculations and density matrix simulations of a ^{13}C-enriched methyl group. A novel multi-dimensional EFNMR method for observing such spectra is discussed. This experiment allows for the resolution of strongly coupled NMR spectra both in the Earth's magnetic field, in the directly detected domain, and in weaker fields, in the indirectly detected domain.

In the final section of this thesis, residual dipolar coupling is observed by EFNMR for the first time in a system of poly-γ-benzyl-L-glutamate (PBLG) in dichloromethane. The form of the EFNMR spectrum of this liquid crystalline system is discussed and compared to equivalent high-field (9.4T) spectra.

Acknowledgments

The completion of this thesis is due, in no small part, to the help and support of a great number of people. Words are truly insufficient to fully express my gratitude but that does not mean that I am not going to give it my best shot!

First and foremost I would like to thank my advisor, Professor Paul Callaghan. Since that first day, back in October 2004, when I found myself, quite unexpectedly, in the middle of a Friday afternoon NMR group meeting, you have demonstrated an unwavering belief in my abilities and an admirable forbearance when it came to my sadly frequent bouts of self-doubt, cynicism and apathy. I am deeply grateful for the opportunity you gave to me, first to work for Magritek and then, later, to embark on a PhD in the NMR lab. Staying in New Zealand was both the easiest and the best decision I have ever made and it has been an honour to work with you. On a more personal note, I am also grateful for your (and Miang's) friendship, in particular during our mutual stay in Berkeley in 2008. I look forward to many enjoyable discussions about science and politics in the future.

The years I have spent in the NMR lab have been productive and scientifically stimulating but most of all just plain good fun. Thank you to all of the students and post docs that have made the NMR lab the welcoming and enjoyable place that it is. To Mark Hunter: thank you for your expert guidance with respect to coil designs, experimental set-ups and other general research trouble-shooting. On a more personal note, thank you for being a great conference travel companion and a reliable fellow coffee connoisseur. To Ben Parkinson: thank you for your endless help with

experimental set-up issues and for continually bringing me back from the brink of ground-loop induced despair. I gladly sacrifice all aspirations to dignity and elegance in return for your friendship. To Simon Rogers: thank you for all of the times you served as a sounding board for my thoughts and frustrations. I hope there are many great coffees to be drunk together in our future. To Kirk Feindel, my fellow Canuck: thank you for your inability to be serious for any extended period of time. I have a great admiration for you, not only as a scientist, but also as someone who possess such unique talents as chest-rubbing to promote communal warmth and pot-stirring for social experimentation. To Lauren Burcaw: thank you for joining me in the league of the quilting physicists and for putting up with my newfound obsession with American politics. To Antoine Lutti: thank you for your overwhelming generosity in all things from endless beers in Japan to welcoming us all to your house in London in 2007. Your restless energy, your endless litany of "I don't wanna work" and charming Friwi accent are very much missed. To Guillaume Madelin: thank you for turning up with a wealth of valuable DNP knowledge just when I needed it and for putting up with my habit of occasionally breaking out into really bad French. Au secours! To Jen Brown: thank you for joining with Lauren and I to create a female presence in the lab, for spectrometer help and for understanding that sometimes having a good cry is really the only solution to experiments that do not work. To Robin Dykstra: thank you for all of your electronics help, for liberating equipment from the Engineering department when I was desperate and for giving me the opportunity to go to Antarctica. To Allan Raudsepp: thank you for those unexpected gestures of kindness which are always much appreciated. To Kate Washburn: thank you for your funny stories and for not being offended by the barricade that I built between our desks to hold back the chaos. To Lichi Buljubasich and Bruno Medronho: neither of you were here for nearly long enough but your absence is certainly felt. Thank you for all of the fun times (Fantastic! Amazing!) and for helping me to forget, for an evening at least, all of my experimental difficulties. To Alan Rennie and Manu Pouajen-Blakiston: thank you for all of your help with building coil formers and copper boxes. I will never understand how you always manage to take what I ask you to build and make something different, but infinitely better. To Margaret Brown: thank you for long chats and for being unfailingly helpful with all administrative things. To Sarah Dadley: thank you for undertaking the often

tedious job of sorting out my quite complicated three-part income situation. To John Ryan and Katherine Allan: thank you for much needed chemistry advice and help with sample preparation. To Evan McCarney, Achim Gadke and the rest of the K131 crew: thank you for making the Antarctic field camp experience both fun and interesting. Thank you, also, to all of the other students, post-docs and visitors (too many to name) who have been part of the lab during my time here and have added to the general atmosphere of fun and friendliness.

An integral part of my New Zealand NMR experience was the year I spent at Magritek. I would like to thank Andrew Coy, my first real boss, for his support, his enthusiasm for my work and for teaching me so many things about science, business and NMR. I hope that Magritek continues its great success in the future and that I always remain, in some way or another, a part of it all. To Craig Eccles: thank you for not once hanging up on me when I called to say, "I broke Prospa!" I continue to be very grateful for your endless help with all of my software problems and for your meticulous editing of my various manuscripts. To Dafnis Vargas: thank you for being a true friend to me even when I felt an overwhelming need to object to your style decisions. Tramping in the rain, fights over tea, "bye, bye, birdie" and ice cream after seven are just a few of the things I will never forget.

In the course of this thesis I have had the opportunity to collaborate with a number of exceptional scientists. I would like to thank these individuals: Professor Rod Wasylishen, Professor Edward Samulski, Professor Thomas Meersman and Dr. Galina Pavlovskya, for their help, support and enthusiasm for my work.

If there is one person, more than any other, who is responsible for my having started this PhD project in the first place it is my cousin, Minna Halse, and her desire to run away for a year and live in New Zealand. Minna, I am forever in your debt for letting me tag along on your adventure, for putting up with me in our damp ridden, one-room bedsit in Mount Cook and for forgiving me when, at the end of our year, I got to stay in New Zealand and you did not. Four years later I still miss you like crazy.

The successful completion of my thesis would not have been possible were it not for my love of living in Wellington, which is due in large part to my adopted Kiwi family. I am extremely grateful to the 42 Hargreaves Street whanau: Nikki Parlane, Nadia and Ryan Watson, Jess Chambers, Mel and Brad Dring and Christy Reed, who

took me in after Minna left. Even now, after we have all moved on to new and exciting things, you continue to hold a very special place in my Wellington memories. To Keith, Theresa and Tandia Vaughan: I cannot begin to sufficiently express my gratitude for your warmth, kindness and generosity. Little did you know when you took me in, the cousin of a girl you barely knew, that you would be stuck with me forever! Having a family and a home to turn to whenever I needed it has helped me get through many a difficult time over the last five years. I love you all very much and sincerely hope that I will continue to see you often in the years to come.

The decision to move half a world away from one's family and friends is never easy and I would like to thank my Mom and my Dad for always being supportive and for simply wanting me to be happy. I love you both very much. I would also like to thank my brothers: Jonathan, Joel and Darryl, my sister, Marika, my Grandma, and my step-mother, Julie, for their love and support over the years. I miss you all and I wish I could see you more often. Thanks are also due to all of my friends and extended family in Canada and England who have made the effort to keep in touch and who welcome me into their homes whenever I can manage to squeeze in a visit. Extra special thanks to Katie Porter and Lisa Gilliss. I am indebted to you for your unfailing support of me in all that I do and I am very glad that you both managed to make it to New Zealand to visit during my years here.

Last but not least, I would like to acknowledge the love and support my Grandma, Betty VanWyngaarden and Grandpa, George Alexander Halse, both of whom passed away during my years in Wellington. While I cannot regret my decision to come to New Zealand, I will always be sad that I did not get the chance to say goodbye.

TABLE OF CONTENTS

CHAPTER 1. Introduction

The nuclear magnetic resonance (NMR) phenomenon was first observed by Felix Bloch at Stanford University and Edward Purcell at Harvard University in 1946. For this discovery they received the Nobel Prize in Physics in 1952. It was in 1954, while NMR was still a very young field of research, that Packard and Varian [1] first demonstrated the detection of nuclear precession in the highly homogeneous Earth's magnetic field. Therefore Earth's field NMR (EFNMR) is almost as old as NMR itself.

Pioneering work in the field of EFNMR was carried out in the 1950s and 1960s [2-8]. In recent years there has been renewed interest in Earth's field NMR due to a combination of factors but perhaps the most significant of these was the development of small, portable, low-cost pulsed Fourier Transform (FT) Earth's field NMR spectrometers ideally suited to teaching the principles of NMR spectroscopy and imaging to students. Indeed it is the potential of EFNMR for pedagogy which served, in a sense, as the starting point for the work contained in this thesis.

In 2004, Paul Callaghan along with co-inventors Mark Hunter, Craig Eccles and Robin Dykstra and in collaboration with Victoria University of Wellington and Massey University formed a spin-out company, Magritek Limited. This company was created to commercialize the portable NMR and MRI technology developed by the inventors as part of an Antarctic research project dating back to the early 1990s [9-13]. This research project centred around the development of a small, portable and

robust Earth's field NMR system capable of carrying out pulsed-gradient-spin-echo (PGSE) NMR diffusion measurements on sea ice *in situ* in Antarctica. The main commercial application of this Earth's field NMR system, which has enjoyed great success over the last 5 years with over 100 units sold, is as a low cost, hands-on apparatus for teaching the basic principles of modern pulsed NMR and MRI to undergraduates. Shortly after the formation of the company, the author of this thesis (Meghan Halse) joined Magritek Limited as an applications engineer whose main role was to expand the range of experiments which could be carried out on this Earth's field apparatus. The capabilities of this simple system were soon discovered to be much more comprehensive than what was first imagined, so much so that what started out as an investigation into the commercial possibilities of a clever little NMR apparatus evolved into a PhD thesis project.

The goal of this thesis can be divided into two main aims. The first aim is to investigate ways in which the sensitivity, resolution and overall performance of the Earth's field NMR system can be improved without significantly compromising its main benefits: simplicity, portability and affordability. The second major aim of this thesis is to investigate and push the limits of the information content available using such a simple, portable and affordable NMR system.

The thesis starts, in Chapter 2, with an overview of the physics of nuclear magnetic resonance (NMR) and an introduction to the quantum mechanical aspects of NMR which are integral to understanding many of the results presented in this thesis.

Chapter 3 provides an introduction to Earth's field NMR including a discussion of the current state-of-the-art in EFNMR and an historical overview of the development of this field of research.

Chapter 4 begins with an introduction to the commercial apparatus at the heart of all of the Earth's field NMR experiment contained herein, the Terranova-MRI by Magritek Limited. Following this introduction, apparatus improvements developed as part of this thesis are presented and the resultant improvement in sensitivity and spectral resolution are discussed. These improvements include: auto-shimming, ultra-low frequency (ULF) noise screening and temporal field stabilization.

Chapter 5 addresses the issue of signal enhancement. Three methods for signal augmentation in Earth's field NMR are considered. First prepolarization, both with an electromagnet and a permanent magnet array, is evaluated. Second, dynamic

nuclear polarization (DNP) is discussed in the context of Earth's field NMR spectroscopy. Experimental DNP enhancement results are presented and compared to theory and to the prepolarization approach. In addition, the design and implementation of the hardware required to achieve optimal DNP enhancements in Earth's field NMR is discussed. The third signal enhancement method explored in this chapter is hyper-polarization of xenon gas via optical pumping. Hyperpolarized xenon gas is considered both for direct detection in the Earth's field and also for polarization transfer to target ^{1}H nuclei using SPINOE (spin polarization-induced nuclear Overhauser effect). The viability and efficacy of this sensitivity enhancement method is evaluated and compared to prepolarization.

Chapter 6 begins our discussion of information content in Earth's field NMR spectroscopy by presenting a description of the density matrix formalism which is used throughout this thesis for numerical simulation of high resolution Earth's field NMR spectroscopy experiments in one and two dimensions. This chapter details how the density matrix simulations are implemented on a standard PC and compares a typical simulated spectrum to an experimental EFNMR spectrum.

Chapter 7 explores a quantitative approach to interpreting 1D Earth's field NMR spectra of systems of hetero-nuclei which are coupled via the indirect spin-spin (J) coupling interaction. Unlike in strong laboratory magnetic fields (> 1 T), the indirect spin-spin coupling constant between hetero-nuclei is often of a similar order of magnitude to the difference in Larmor frequency of nuclei in the Earth's magnetic field. This provides us with the unique opportunity to observe the effect of strong indirect spin-spin coupling between nuclei with differing spin. In this chapter we show how such spectra can be predicted and understood using time-independent perturbation theory.

Chapter 8 extends the discussion of Earth's field NMR spectroscopy to two dimensions. 2D correlation spectroscopy (COSY) experiments, carried out in the Earth's magnetic field, are presented and discussed. The significant improvement in the signal-to-noise ratio (SNR) and resolution of these multi-dimensional spectra as a result of the apparatus improvements presented in Chapters 4 and 5 (ULF noise screening, temporal field stabilization and dynamic nuclear polarization) are demonstrated.

Chapter 9 investigates the strong indirect spin-spin coupling regime which

exists in fields weaker than the Earth's magnetic field. This coupling regime is discussed through the use of exact calculations and density matrix simulations of an illustrative example: a ^{13}C-enriched methyl group. A class of two-dimensional Earth's field NMR spectroscopy experiments, which can be used to simultaneously observe strongly coupled spectra of small molecules in the Earth's magnetic field as well as in weaker fields, is introduced. The implementation of this technique as well as the potential insight it can provide into the sub-Earth's field strong coupling regime is discussed.

Chapter 10 explores the possibility of probing ordering in anisotropic liquids using EFNMR by considering a liquid crystal solution of the polymer poly-γ-benzyl-L-glutamate (PBLG) in dichloromethane. ^{1}H NMR spectra of this sample acquired at high-field (400 MHz) as well as in the Earth's magnetic field are presented and discussed.

The thesis finishes in Chapter 11 with some conclusions and a brief discussion of novel Earth's field NMR spectroscopy experiments which could be carried out in the future.

The density matrix simulation code (introduced in Chapter 6) is included in Appendix A and a list of publications that resulted from this thesis is presented in Appendix B.

CHAPTER 2. Nuclear Magnetic Resonance

2.1. Introduction to Nuclear Magnetic Resonance (NMR)

At the heart of the nuclear magnetic resonance (NMR) phenomenon are atomic nuclei, possessing both magnetism and angular momentum. These nuclei interact with magnetic fields, both static and time-varying, as well as each other and the local environment to give rise to a detectable nuclear precession signal which can contain information about a wide range of properties from the microscopic to the macroscopic. NMR is fundamentally a quantum mechanical phenomenon but there exists a semi-classical picture of NMR which can be used to explain a large range of magnetic resonance and magnetic resonance imaging (MRI) experiments. However, a deep understanding of the underlying quantum mechanics is necessary to successfully design and implement many advanced NMR experiments, particularly in the realm of NMR spectroscopy. In the context of this thesis, an understanding of the true quantum mechanical description of NMR is essential. Therefore, in this Chapter, we present an introduction to the basics of nuclear magnetic resonance using a predominantly quantum mechanical approach. This introduction broadly follows that presented by Slichter [14] as well as that presented by Levitt [15], Abragam [16] and Callaghan [17].

Note that throughout this thesis scalar variables are in italics, such as the spin quantum number I, while boldface is used to denote vector quantities, such as $\mathbf{B}$, as

well as operators which are matrices, be they a vector operator such as total angular momentum, **J**, or a single component operator such as $\mathbf{I}_z$. Hamiltonian operators are denoted using a script "H" which is boldface: $\boldsymbol{\mathcal{H}}$.

2.1.1. Free Spins in a Static Magnetic Field

A free spin is a system with angular momentum $\mathbf{J} = \mathbf{I}\hbar$ and a collinear magnetic moment $\boldsymbol{\mu} = \gamma\hbar\mathbf{I}$, where γ is the gyromagnetic (also called magnetogyric) ratio of the nucleus, $\hbar$ is Plank's constant (6.626×10^{-34} Js) divided by 2π and **I** is a dimensionless angular momentum operator with Cartesian components $\mathbf{I}_x$, $\mathbf{I}_y$ and $\mathbf{I}_z$. In the absence of an external magnetic field, the magnetic moments of an ensemble of free spins are randomly oriented; however, when placed in a uniform magnetic field an average preferential alignment is introduced into the system by means of what is known as the Zeeman interaction. The Hamiltonian which describes the Zeeman interaction is equal to the negative of the dot product between the nuclear magnetic moment, $\boldsymbol{\mu}$, and the external magnetic field, **B**. If we define the laboratory frame of reference such that $\mathbf{B} = B_0\hat{k}$, the Hamiltonian can be written in terms of the z component of the nuclear spin's angular momentum operator, $\mathbf{I}_z$ (Eq. 2-1).

$$\boldsymbol{\mathcal{H}} = -\boldsymbol{\mu} \bullet \mathbf{B} = -\gamma\hbar B_0 \mathbf{I}_z \qquad \text{2-1}$$

The effect of the Zeeman interaction on a free spin can be understood, quantum mechanically, by solving the time-independent Schrödinger equation (Eq. 2-2).

$$\boldsymbol{\mathcal{H}}\left|n\right\rangle = E_n\left|n\right\rangle \qquad \text{2-2}$$

The solution of Eq. 2-2 under the influence of the Zeeman Hamiltonian (Eq. 2-1) can be obtained using a formalism in which the basis states are defined in terms of the spin quantum number I, where $I(I+1)$ is the eigenvalue of the angular

momentum operator $\mathbf{I}^2$, and the azimuthal spin quantum number, m, which is the eigenvalue of the angular momentum operator along z, $\mathbf{I}_z$. In the bra-ket notation these states are written as $|I,m\rangle$. Often the I is omitted and the ket is labeled simply by the azimuthal spin quantum number m. The azimuthal spin quantum number represents a projection of the angular momentum along the longitudinal (z) direction of the quantum system, in this case the direction defined by the static field, **B**. m can take any of $2I+1$ discrete values ranging from $-I$ to I. Each different projection, or orientation, of the spin is associated with a magnetic energy, E_m. These magnetic energies are the eigenvalues of Eq. 2-2 and are defined by Eq. 2-3.

$$E_m = -\gamma B_0 \hbar m \qquad 2\text{-}3$$

For an I =1/2 particle such as the ^{1}H nucleus, there are two possible eigenstate orientations: spin-up ($|\tfrac{1}{2}\rangle$) and spin-down ($|-\tfrac{1}{2}\rangle$), with corresponding energies: $E_{\frac{1}{2}} = -\frac{1}{2}\gamma B_0 \hbar$ and $E_{-\frac{1}{2}} = \frac{1}{2}\gamma B_0 \hbar$. We will call these states $|\alpha\rangle$ and $|\beta\rangle$, respectively. These two possible energy states for the ^{1}H nucleus are illustrated in the energy level diagram in Figure 2.1.

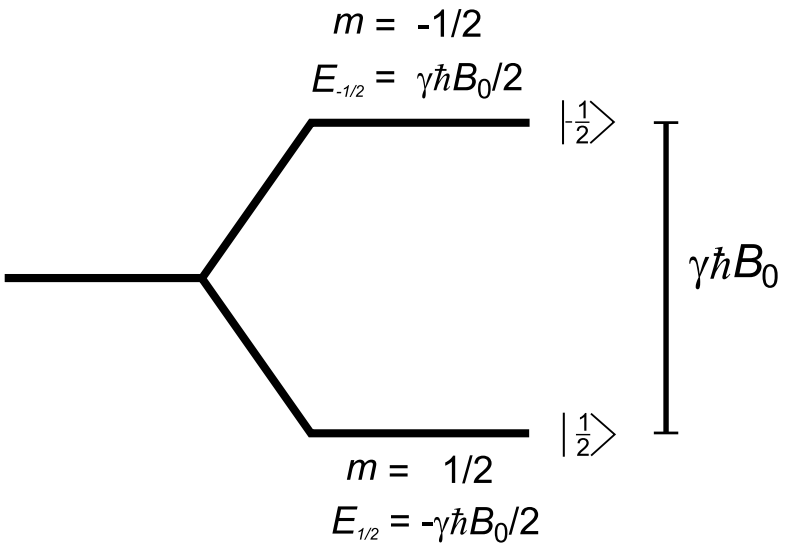

Figure 2.1 Energy level diagram for a ^{1}H nucleus under the influence of a static magnetic field, B_0.

At any given time a nuclear spin can be either in an eigenstate or in a superposition state, $|\psi\rangle$. A superposition state is a linear combination of the available eigenstates weighted by superposition coefficients, c_m.

$$|\psi\rangle = \sum_{m=-I}^{I} c_m |m\rangle$$

2-4

The superposition coefficients, c_m, are complex and are normalized to unity.

$$\sum_{m=-I}^{I} |c_m|^2 = 1$$

It is often convenient to write these superposition states as column vectors. For example a superposition state for an $I = 1/2$ nucleus is written as in Eq. 2-5.

$$|\psi\rangle = \begin{pmatrix} c_{\frac{1}{2}} \\ c_{-\frac{1}{2}} \end{pmatrix}$$

2-5

Similarly, the eigenstates can also be depicted in column vector form.

$$|\alpha\rangle = \begin{pmatrix} 1 \\ 0 \end{pmatrix}$$
$$|\beta\rangle = \begin{pmatrix} 0 \\ 1 \end{pmatrix}$$

2-6

If a spin is in one of the eigenstates, $|m\rangle$, a measurement of angular momentum along the axis of the field ($\mathbf{I}_z$) will result in the value $m\hbar$. However, while the nuclear spin occupies one of these eigenstates, measurements of angular momentum in the transverse plane ($\mathbf{I}_x$ or $\mathbf{I}_y$) will have $2I+1$ equally probable results

given by $m\hbar$ where m = -I, -I+1,…, I. Through the action of measuring $\mathbf{I}_x$ or $\mathbf{I}_y$, the system will be forced into one of the 2I+1 eigenstates of the observed operator but there is no way to say, with certainty, which eigenstate that will be.

If the nuclear spin occupies a superposition state, the measurement of $\mathbf{I}_z$ no longer yields a certain result and we can only define a probability for each of the 2I+1 possible outcomes. Naturally, there exist superposition states which provide certain outcomes for measurements of either $\mathbf{I}_x$ or $\mathbf{I}_y$. These are the eigenstates of $\mathbf{I}_x$ or $\mathbf{I}_y$ in the $|I,m\rangle$ basis. These superposition states are listed below, in column vector notation, for an I = 1/2 particle such as a ^{1}H nucleus. The states are labeled $|x\rangle, |-x\rangle, |y\rangle$ and $|-y\rangle$ according to the component of angular momentum for which it is an eigenstate and the sign of its result. For example $|-x\rangle$ is an eigenstate of $\mathbf{I}_x$ for which a measurement of $\mathbf{I}_x$ yields a result of –½$\hbar$.

$$|x\rangle = \frac{1}{\sqrt{2}}\begin{pmatrix}1\\1\end{pmatrix}$$

$$|-x\rangle = \frac{1}{\sqrt{2}}\begin{pmatrix}-i\\i\end{pmatrix}$$

$$|y\rangle = \frac{1}{2}\begin{pmatrix}1-i\\1+i\end{pmatrix}$$

$$|-y\rangle = \frac{1}{2}\begin{pmatrix}1+i\\1-i\end{pmatrix}$$

2-7

2.1.2. Nuclear Precession

Suppose we know the state of the quantum mechanical spin system at a time t' = 0. What is the state of the system at a later time t' = t if the system is under the sole influence of the Zeeman Hamiltonian in a static field $\mathbf{B} = B_0\hat{k}$ (Eq. 2-1)? To find this out we must solve the time-dependent Schrödinger equation (Eq. 2-8).

$$i\hbar \frac{d}{dt}|\psi\rangle(t') = \mathcal{H}|\psi\rangle(t')$$

2-8

Substituting Eq. 2-1 into Eq. 2-8 we obtain a first-order differential equation.

$$\frac{d}{dt'}|\psi\rangle(t') = i\gamma B_0 \mathbf{I}_z |\psi\rangle(t')$$

2-9

The solution to this equation is well known (Eq. 2-10).

$$|\psi\rangle(t) = \exp(i\gamma B_0 \mathbf{I}_z t)|\psi\rangle(0)$$

2-10

The exponential operator in Eq. 2-10 is simply the rotation operator around the z axis ($\hat{k}$).

$$\mathbf{R}_z(\phi) = \exp(-i\phi \mathbf{I}_z)$$

2-11

Therefore we can rewrite Eq. 2-10 as Eq. 2-12.

$$|\psi\rangle(t) = \mathbf{R}_z(-\gamma B_0 t)|\psi\rangle(0)$$

2-12

This rotation about the z axis by an angle of $-\gamma B_0 t$ is what is known as precession. The characteristic frequency of this precession is called the Larmor frequency and is described by the Larmor equation (Eq. 2-13).

$$\omega_0 = -\gamma B_0$$

2-13

The Larmor equation is the most important equation in NMR. It is interesting to note that Planck's constant does not appear in this expression. This suggests that the quantum mechanical picture is closely associated with a classical description. Indeed this Larmor equation appears repeatedly in both the quantum mechanical and classical descriptions of magnetic resonance.

Consider the case of a ^{1}H nuclear spin. If the initial state of the nuclear spin is an eigenstate ($|\alpha\rangle$ or $|\beta\rangle$), at a later time, t, the spin will remain in an eigenstate but this eigenstate will include a phase term, $\exp(i\gamma B_0 mt)$. We can say that the spin remains in an eigenstate because the complex phase term associated with this new state does not alter the outcome of a measurement of $\mathbf{I}_z$ (or $\mathbf{I}_x$ and $\mathbf{I}_y$) and so satisfies the same Eigen equation as the original eigenstate. This implies that if the spin starts out in an eigenstate of the Zeeman Hamiltonian, the effect of the Larmor precession as a function of time is unobservable. One other interesting thing to note here is that the presence of m in the phase factor means that for an I = ½ nucleus, where $m = \pm$½, the spin precession requires a 720˚ rotation (not 360˚) to return to its initial state.

Now consider the case of a ^{1}H spin which starts out in one of those particular superposition states which are eigenstates of $\mathbf{I}_x$ or $\mathbf{I}_y$: $|x\rangle, |-x\rangle, |y\rangle$ and $|-y\rangle$. The effect of the rotation operator in Eq. 2-12 on these states is elucidated through the use of the matrix representation of $\mathbf{R}_z$ for a spin with I = ½ (Eq. 2-14).

$$\mathbf{R}_z(\phi) = \exp(-i\phi\mathbf{I}_z) = \begin{pmatrix} \exp\left(-i\frac{\phi}{2}\right) & 0 \\ 0 & \exp\left(i\frac{\phi}{2}\right) \end{pmatrix} \qquad \text{2-14}$$

If the ^{1}H spin starts at time t' = 0 in the state $|-x\rangle$ after a time t the state of the spin can be calculated as follows:

$$\mathbf{R}_z(-\gamma B_0 t)|-x\rangle = \frac{1}{\sqrt{2}}\begin{pmatrix} \exp\left(i\frac{\gamma B_0 t}{2}\right) & 0 \\ 0 & \exp\left(-i\frac{\gamma B_0 t}{2}\right) \end{pmatrix}\begin{pmatrix} -i \\ i \end{pmatrix} = \frac{1}{\sqrt{2}}\begin{pmatrix} \exp\left(i\frac{\gamma B_0 t}{2} - i\frac{\pi}{2}\right) \\ \exp\left(-i\frac{\gamma B_0 t}{2} + i\frac{\pi}{2}\right) \end{pmatrix}$$

Now consider the particular case of a fixed period of time, t_1, such that the

phase accumulated is exactly $-\pi/2$ ($\phi = -\gamma B_0 t_1 = -\pi/2$).

$$\mathbf{R}_z\left(-\frac{\pi}{2}\right)\left|-x\right\rangle = \frac{1}{\sqrt{2}}\begin{pmatrix}\exp\left(i\frac{\pi}{4}-i\right) & 0\\ 0 & \exp\left(-i\frac{\pi}{4}\right)\end{pmatrix} = \frac{1}{2}\begin{pmatrix}1-i\\ 1+i\end{pmatrix} = \left|y\right\rangle$$

Therefore we see that the effect of precession on a spin in the $\left|-x\right\rangle$ state is to evolve after a (positive) period of time, $t_1 = \frac{\pi}{2\gamma B_0}$, into the state $\left|y\right\rangle$. If we repeat this calculation we find that after an additional time period, t_1, the spin will evolve from the state $\left|y\right\rangle$ into $\left|x\right\rangle$ and then to $\left|-y\right\rangle$ after yet another time period, t_1. Finally, after a total evolution time of 4 t_1, the spin will return to its initial state $\left|-x\right\rangle$. Therefore if we perform a measurement of either $\mathbf{I}_x$ or $\mathbf{I}_y$ as a function of time we will find that the result will oscillate between maximum and minimum values of $\pm\frac{1}{2}\hbar$ at the Larmor frequency, $\omega_0 = -\gamma B_0$.

We can obtain a more intuitive picture of precession through the use of a semi-classical picture to model the behaviour of a magnetic moment, $\boldsymbol{\mu}$, in a static field $\mathbf{B}$. This magnetic moment will experience a torque, given by Eq. 2-15, which is equal to the time rate of change of the total angular momentum, $\mathbf{J}$.

$$\boldsymbol{\tau} = \boldsymbol{\mu} \times \mathbf{B} = \frac{d\mathbf{J}}{dt} = \hbar\frac{d\mathbf{I}}{dt} \qquad \text{2-15}$$

It is known that $\boldsymbol{\mu} = \gamma\hbar\mathbf{I}$ and so the time rate of change of the magnetic moment can be written as in Eq. 2-16.

$$\frac{d\boldsymbol{\mu}}{dt} = \gamma\boldsymbol{\mu} \times \mathbf{B} \qquad \text{2-16}$$

.

The interpretation of Eq. 2-16 is greatly simplified with the introduction of a rotating frame of reference. Consider the S' frame of reference which rotates with respect to the laboratory frame, S, with an angular velocity of ω about the $\hat{k}$

direction, i.e. about the direction of the static field **B**. The relationship between the time rate of change $\frac{d\mathbf{A}}{dt}$ of any arbitrary vector $\mathbf{A}(t)$ computed in the laboratory frame S and its time rate of change $\frac{\partial \mathbf{A}}{\partial t}$ computed in the rotating frame S' is given by Eq. 2-17.

$$\frac{d\mathbf{A}}{dt} = \frac{\partial \mathbf{A}}{\partial t} + \boldsymbol{\omega} \times \mathbf{A} \qquad \text{2-17}$$

.

Using Eq. 2-17 and Eq. 2-16 the motion of the magnetic moment in the rotating frame, S', can be computed.

$$\frac{\partial \boldsymbol{\mu}}{\partial t} = \gamma \boldsymbol{\mu} \times \mathbf{B} - \boldsymbol{\omega} \times \boldsymbol{\mu} = \gamma \boldsymbol{\mu} \times (\mathbf{B} + \frac{\boldsymbol{\omega}}{\gamma}) \qquad \text{2-18}$$

Eq. 2-18 can be adapted such that it maintains the same form as Eq. 2-16 if the uniform magnetic field **B** is replaced by an effective field: $\mathbf{B}_\mathbf{e} = \mathbf{B} + \frac{\boldsymbol{\omega}}{\gamma}$.

$$\frac{\partial \boldsymbol{\mu}}{\partial t} = \gamma \boldsymbol{\mu} \times \mathbf{B}_\mathbf{e} \qquad \text{2-19}$$

The choice of an angular frequency of $\omega = -\gamma B_o$ about the direction of the field, **B**, results in a vanishing effective field. In this case the magnetic moment is a fixed vector in the rotating frame. In the Laboratory frame, however, the magnetic moment $\boldsymbol{\mu}$ will precess about the static field at the now familiar Larmor frequency, $\omega_0 = -\gamma B_0$. If we relate this back to our quantum picture we see that there is a conceptual correlation between this magnetic moment precessing around the static field at the Larmor frequency (in the Laboratory frame) and the evolution between the

quantum states $|x\rangle, |-y\rangle, |-x\rangle$ and $|y\rangle$ under the influence of the rotation operator, $\mathbf{R}_z$.

Inspection of Eq. 2-19 (or similarly Eq. 2-16) tells us that if the magnetic moment is collinear with the field, **B**, there will be no observed precession. This is equivalent, in the quantum mechanical picture, to a ^{1}H spin which starts out in one of the eigenstates, $|\alpha\rangle$ or $|\beta\rangle$. Recall that in this case the state of the spin will acquire a time dependent phase factor but that this phase factor does not change the outcome of an angular momentum measurement along any of the three Laboratory dimensions, *x*, *y* or *z*, and so the precession is undetected.

2.1.3. Thermal Equilibrium and Spin Ensembles

In a typical nuclear magnetic resonance experiment we are concerned not with a single nuclear spin but rather a very large spin ensemble containing numbers of spins on the order of 10^{25}. In order to understand the behaviour of a large group of non-interacting nuclear spins in a magnetic field we must introduce the idea of thermal energy and thermal equilibrium.

Consider the Zeeman energy diagram for a ^{1}H nucleus in Figure 2.1. It is apparent from this depiction that the low energy state of the ^{1}H nucleus is the spin-up, m = ½, state and therefore this will be the magnetically preferred orientation. In the absence of any thermal energy, i.e. at absolute zero, all spins would populate this lowest energy state. However, under more temperate conditions, interactions between the ensemble spins and the surrounding environment (often called the "lattice") provide the means for spins to exist in the excited, higher energy state or indeed in any super-position state. We cannot know the exact state of each spin at any given point in time without making a measurement, which will drive the system into an eigenstate. What we can define, however, is the probability of a given spin being in either the high energy or low energy state using Boltzmann statistics. Using these probabilities we can compute the ensemble average behaviour of the system as whole.

The probability of a spin populating one of the available states can be thought of as a competition between thermal energy, which excites the spins to the higher energy state(s), and the magnetic energy, which favours the lowest energy state. The

probability, P_m, of a spin occupying a given eigenstate is proportional to the Boltzmann Factor (Eq. 2-20), characterized by an exponential function of the ratio of the magnetic energy, E_m, to the thermal energy, kT, where T is temperature and k is the Boltzmann constant (1.38×10^{-23} J/K)

$$P_m \propto \exp\left(-\frac{E_m}{kT}\right) = \exp\left(\frac{\gamma\hbar m B_0}{kT}\right) \qquad 2\text{-}20$$

The population ratio between two eigenstates $|m\rangle$ and $|m'\rangle$ is given by Eq. 2-21.

$$\frac{P_m}{P_{m'}} = \frac{\exp(-E_m/kT)}{\exp(-E_{m'}/kT)} = \exp\left(\frac{\gamma\hbar(m-m')B_0}{kT}\right) \qquad 2\text{-}21$$

Consider an ensemble of ^{1}H nuclei under the influence of a moderate magnetic field (on the order of 1 T) in thermal equilibrium at room temperature (298 K). The population difference (Eq. 2-21) between the spin-up and spin-down states will be very small ($\sim 10^{-5}$). However, the number of nuclei in the ensemble (on the order of 10^{25}) is so large that this very small excess of spins in the low-energy spin-up state gives rise to a macroscopic bulk magnetization in the "spin-up" orientation, i.e. along the direction of the static field, **B**. It is this bulk magnetization which is manipulated to generate an NMR signal.

$$M = N\gamma\hbar \frac{\sum_{m=I}^{-I} m \exp(\gamma\hbar m B_0/kT)}{\sum_{m=I}^{-I} \exp(\gamma\hbar m B_0/kT)} \qquad 2\text{-}22$$

The magnitude of the bulk magnetization can be computed using Boltzmann statistics. For an ensemble of n nuclear spins in a volume V with spin quantum number I, the magnetic moment per unit volume, M, can be written as the number of

nuclei per unit volume, N, times the average of the magnetic moments, E_m, of the eigenstates weighted by their statistical probability (the Boltzmann Factor), where $N = nV^{-1}$ (Eq. 2-22).

Using the high temperature approximation, $kT >> |\gamma\hbar m B_0|$, which is valid for all temperatures above the mK range, a linear expansion for the Boltzmann exponential term can be substituted into Eq. 2-22 to yield a closed form expression for M (Eq. 2-23).

$$M = \frac{N\gamma^2\hbar^2 B_0}{kT}\frac{\sum_{m=I}^{-I} m^2}{2I+1} = \frac{N\gamma^2\hbar^2 I(I+1)B_0}{3kT}$$

2-23

.

M is very difficult to observe by conventional magnetostatic methods. Nuclear magnetic resonance (NMR) techniques gain a considerable increase in sensitivity over magnetostatic methods by using, as the name suggests, the principle of resonance.

2.1.4. Resonance and the Rotating Frame of Reference

Consider once again the energy level diagram for a ^{1}H nucleus in a static field, B_0 (Figure 2.1). What we wish to detect is some kind of spectral absorption between these Zeeman energy levels and therefore we need to excite transitions. In order to conserve energy, any interaction which achieves this goal must be both time dependent and must fulfill the condition $\hbar\omega = \Delta E$, where ΔE is the energy difference between the initial and final nuclear Zeeman energies.

The most commonly used method for such an excitation in magnetic resonance is a coupling to an alternating magnetic field, B_1, oriented perpendicular to the static field, B_0. The perturbing term to the interaction Hamiltonian (Eq. 2-1) due to an alternating field with amplitude B_1 is given by Eq. 2-24.

$$\mathcal{H}_{\text{pert}} = -\gamma\hbar B_1 \mathbf{I}_x \cos\omega t$$

2-24

The operator $\mathbf{I}_x$ is the component of the spin angular momentum along the $\hat{i}$ direction in the laboratory frame. In order to more intuitively understand the function of this operator we re-write it in terms of the raising, $\mathbf{I}^+$, and lowering, $\mathbf{I}^-$, operators (Eq. 2-25).

$$\mathbf{I}_x = \frac{1}{2}\left(\mathbf{I}^+ + \mathbf{I}^-\right) \qquad 2\text{-}25$$

The raising and lowering operators (also called ladder operators) act on the Zeeman eigenstates according to the rules outlined in Eq. 2-26

.

$$\mathbf{I}^+\left|m\right\rangle = \sqrt{I(I+1)-m(m+1)}\left|m+1\right\rangle$$

.

$$\mathbf{I}^-\left|m\right\rangle = \sqrt{I(I+1)-m(m-1)}\left|m-1\right\rangle \qquad 2\text{-}26$$

By inspection we see that, given the orthogonality of the eigenstates, $\left|m\right\rangle$, the matrix elements $\left\langle m'\left|\mathbf{I}_x\right|m\right\rangle$ vanish unless $m' = m \pm 1$. Thus, only adjacent energy level transitions are permitted. The frequency of the alternating field is therefore given by Eq. 2-27.

$$\hbar\omega = \pm\Delta E = \pm\gamma\hbar B_0 \rightarrow \omega = \pm\gamma B_0 \qquad 2\text{-}27$$

Eq. 2-27 is the familiar Larmor equation. Therefore we find that an alternating magnetic field, $\mathbf{B_1}$, which is perpendicular to $\mathbf{B_0}$ and oscillates in time at the Larmor frequency, will excite transitions between the various Zeeman levels of the system. This simple spectral absorption picture, however, cannot be used to completely explain the NMR experiment. To fully understand how nuclear precession is excited and detected we need to take a closer look at $\mathcal{H}_{\text{pert}}$ (Eq. 2-24) and

its effect on the system.

Under the combined influence of a static magnetic field $\mathbf{B}_0 = B_0\hat{k}$ and an alternating field $\mathbf{B}_1 = 2B_1\cos\omega t\hat{i}$, the total Zeeman interaction Hamiltonian in the laboratory frame is given by Eq. 2-28.

$$\mathcal{H} = -\hbar\gamma B_0\mathbf{I}_z - \hbar\gamma 2B_1\mathbf{I}_x\cos\omega t$$

2-28

Inserting this Hamiltonian into the time-dependent Schrödinger equation (Eq. 2-8) we obtain the differential equation in Eq. 2-29.

$$i\hbar\frac{d}{dt}|\psi\rangle(t) = -\gamma\hbar\left(B_0\mathbf{I}_z + 2B_1\mathbf{I}_x\cos\omega t\right)|\psi\rangle(t)$$

2-29

We can simplify Eq. 2-29 by introducing an exponential operator notation [14] as shown in Eq. 2-30.

$$i\hbar\frac{d}{dt}|\psi\rangle(t) = -\gamma\hbar\begin{pmatrix}B_0\mathbf{I}_z + B_1\exp(i\omega t\mathbf{I}_z)\mathbf{I}_x\exp(-i\omega t\mathbf{I}_z)\\ + B_1\exp(-i\omega t\mathbf{I}_z)\mathbf{I}_x\exp(i\omega t\mathbf{I}_z)\end{pmatrix}|\psi\rangle(t)$$

2-30

In Eq. 2-30 we have a time-dependent Hamiltonian with respect to stationary states, $|\psi\rangle$. What we would like to do is transform this expression in some way to obtain a stationary Hamiltonian. To do this we must transform the stationary states $|\psi\rangle$ into the explicitly time-dependent states $|\psi'\rangle$, as illustrated in Eq. 2-31.

$$|\psi'\rangle = \exp(i\omega t\mathbf{I}_z)|\psi\rangle$$

$$|\psi\rangle = \exp(-i\omega t\mathbf{I}_z)|\psi'\rangle$$

2-31

$|\psi'\rangle(t)$ relates to $|\psi\rangle(t)$ by means of a rotation through an angle of ωt about the z axis, where $|\psi'\rangle(0) = |\psi\rangle(0)$. This is akin to the rotating reference frame, S', introduced in the classical picture which rotates at an angular frequency of ω about the z axis of the stationary laboratory frame, S.

Substituting Eq. 2-31 into Eq. 2-30 and multiplying by $\exp(-i\omega t\mathbf{I}_z)$ from the left, we obtain a new differential equation (Eq. 2-32). The third term in this equation (Eq. 2-32) is time-dependent, rotating at an angular frequency of 2ω. We will see in a moment how this term can be neglected, leaving us with a Hamiltonian which is time-independent relative to the time-dependent states, $|\psi'\rangle$.

$$i\hbar\frac{d}{dt}|\psi'\rangle(t) = -\gamma\hbar\left(\begin{array}{l}\left(B_0 + \frac{\omega}{\gamma}\right)\mathbf{I}_z + B_1\mathbf{I}_x \\ + B_1\exp(-i2\omega t\mathbf{I}_z)\mathbf{I}_x\exp(i2\omega t\mathbf{I}_z)\end{array}\right)|\psi'\rangle(t)$$

2-32

The first two terms in Eq. 2-32 represent a time-independent Hamiltonian, $\mathcal{H}'$, which is simply the interaction of a free spin with an effective field given by Eq. 2-33.

$$\mathbf{B}_{\mathbf{eff}} = \left(B_0 + \frac{\omega}{\gamma}\right)\hat{k} + B_1\hat{i}$$

2-33

If the alternating magnetic field $\mathbf{B_1}$ is applied in resonance with the precession of the nuclear spins, i.e. with $\omega \sim -\gamma B_0$, the static field vanishes and the effective field is reduced to Eq. 2-34. In this case, the frequency of the third term: $2\omega = 2\gamma B_0$ is much larger than its strength, γB_1 and therefore can be neglected.

$$\mathbf{B}_{\mathbf{eff}}(\omega = -\gamma B_0) = B_1\hat{i}$$

2-34

In this new picture, we have replaced the "forward" or active rotation of $\mathbf{I}_x$

relative to stationary wavefunctions, $|\psi\rangle$, with a stationary $\mathbf{I}_x$ relative to "backward" or passively rotating wavefunctions, $|\psi'\rangle$. Furthermore, if the rotation is in resonance with the Larmor frequency, the B_0 field effectively disappears and the spins become quantized along the effective field (Eq. 2-34).

The solution to Eq. 2-32 is presented in Eq. 2-35, using Eq. 2-31 to express the solution in terms of the stationary wavefunctions.

$$|\psi\rangle(t) = \exp(-i\omega t\mathbf{I}_z)|\psi'\rangle(t) = \exp(-i\omega t\mathbf{I}_z)\exp\left(-\frac{i}{\hbar}\mathcal{H}'t\right)|\psi\rangle(0)$$

2-35

Now we can use Eq. 2-35 to compute the expectation value of $\boldsymbol{\mu}_z$ when a rotating field is present. First we assume that the alternating field is in resonance with the Larmor precession of the nucleus such that our time-independent Hamiltonian is defined by Eq. 2-36.

$$\mathcal{H}' = -\gamma\hbar B_1\mathbf{I}_x$$

2-36

Using Eqs. 2-35 and 2-36 and some useful properties of exponential operators [14] we can compute the following expression for the time-dependence of the expectation value of $\boldsymbol{\mu}_z$ under the influence of B_1 in the rotating reference frame (Eq. 2-37) where $\omega_1 = \gamma B_1$.

$$\langle\boldsymbol{\mu}_z(t)\rangle = \langle\boldsymbol{\mu}_z(0)\rangle\cos\omega_1 t - \langle\boldsymbol{\mu}_y(0)\rangle\sin\omega_1 t$$

2-37

If the initial magnetization is purely longitudinal (along z), $\langle\boldsymbol{\mu}_y(0)\rangle = 0$ and so we can further simplify Eq. 2-37, as shown in Eq. 2-38.

$$\langle\boldsymbol{\mu}_z(t)\rangle = \langle\boldsymbol{\mu}_z(0)\rangle\cos\omega_1 t$$

2-38

Therefore, under the influence of the alternating field B_1, the z magnetization oscillates in time at ω_1. This oscillation corresponds to the precession of $\langle \boldsymbol{\mu} \rangle$ about $\mathbf{B_1}$ in the rotating frame at a frequency $\omega_1 = \gamma B_1$. Therefore the effect of an alternating magnetic field, B_1, applied perpendicular to the static field and in resonance with the Larmor frequency for a fixed period of time, τ, is to rotate the magnetization, in the rotating frame, through an angle $\gamma B_1 \tau$ about the direction of the alternating magnetic field, $\mathbf{B}_1$.

2.1.5. Free Induction Decay (FID)

Recall the evolution of the magnetization in the absence of an alternating magnetic field (section 2.1.2). In the laboratory frame, the magnetization precesses about the static field at the Larmor frequency. This precession is most easily observed if the magnetization lies in the transverse plane. That is, if, on average, the spins are in an eigenstate of $\mathbf{I}_x$ (or $\mathbf{I}_y$). At thermal equilibrium the net magnetization is longitudinal, i.e. is aligned with the static magnetic field. In this orientation precession is unobservable. If we apply the alternating magnetic field $\mathbf{B_1}$, perpendicular to $\mathbf{B_0}$ and in resonance with the Larmor frequency of the nuclei for a fixed period of time we can rotate the net thermal equilibrium magnetization away from the longitudinal axis and into the transverse (xy) plane. If we want to leave the magnetization fully in the transverse plane we need to apply the pulse for a time, t_{90}, defined by Eq. 2-39, which corresponds to a rotation of $\pi/2$ radians (90°).

$$t_{90} = \frac{\pi}{2\gamma B_1} \qquad \text{2-39}$$

Immediately following the application of the alternating field, $\mathbf{B_1}$, the magnetization, now in the transverse plane, will begin to precess about $\mathbf{B_0}$ at the Larmor frequency. According to Faraday's law of induction, this precessing magnetization vector will induce an electromotive force (EMF) in a receiver coil which is in an appropriate orientation with respect to the precessing vector and is tuned to the Larmor frequency. This coil detects changes in flux in the transverse

direction. The time dependent signal recorded by the receiver coil is called the free induction decay (FID). It is so-called because the signal is not driven by the presence of the B_1 field at the time of detection.

In most nuclear magnetic resonance applications, oscillating rather than rotating fields are used to excite the NMR signal. A linearly polarized field with amplitude $2B_1\cos\omega t$ can be considered as the sum of two fields rotating at the same angular frequency in opposite directions, i.e. with $\pm\omega$. If ω is in the neighbourhood of the Larmor frequency the effect on the system of the alternating field is significant. As discussed previously, the counter-rotating component of the linearly polarized field, which is rotating at $-\omega$, is off-resonance with respect to the Larmor frequency by 2ω. Therefore the effect of this component is negligible. In most NMR applications the same coil is used to generate the linearly polarized oscillating field for signal excitation as is used to detect the resultant nuclear precession. Therefore it is often called the transceiver (transmitter and receiver) coil. Other common names include B_1 coil and excitation/detection coil.

In laboratory NMR, the Larmor frequencies are generally in the 100 MHz range. In these applications the duration of the alternating magnetic field pulse is typically on the order of μs. In Earth's field NMR, the Larmor frequency is very low (~ 2.3 kHz) and so the length of the Larmor period requires a B_1 pulse with a duration on the order of milliseconds. In laboratory NMR the Larmor frequency is in the radiofrequency range and so this short burst of oscillating magnetic field is commonly referred to as a radiofrequency (RF) pulse. In the case of Earth's field NMR the Larmor frequency is in the ultra-low frequency range of the RF spectrum and so is commonly referred to as an ULF (ultra-low frequency) pulse.

2.2. Relaxation

During the excitation process, an RF (or ULF) pulse at the Larmor frequency induces transitions between energy states. This requires the introduction of energy into the spin system. The process by which the nuclear spin energy is dissipated and thus the excited spins return to their equilibrium energy and orientation is called

relaxation. Spin relaxation is a consequence of coupling within the spin system as well as between the spin system and the surrounding lattice. The molecules of the system are in a state of thermally activated motion, which generates rapidly fluctuating electric and magnetic fields. These oscillating fields provide the mechanisms for absorption of the spin energy. If the frequency of the thermal motions of the lattice matches the Larmor frequency, transitions will be induced in the spin system and hence energy will be removed. The transition energies involved are not large and therefore relaxation can occur as a result of molecular motions such as rotation, translation and reorientation.

2.2.1. Longitudinal (Spin-Lattice) Relaxation

The energy level transitions induced within the spin system due to the excitation pulse causes a change in the populations of the spin energy levels. In this manner, the population difference between the lower energy state and the higher states rapidly decreases and the longitudinal component of the magnetization is reduced.

It is the process of spin-lattice (longitudinal) relaxation which causes a recovery of the equilibrium net longitudinal magnetization, M_z. Spin-lattice relaxation is the coupling of the spin system to the surrounding thermal reservoir, which is termed the lattice. This process can be described by a phenomenological equation, Eq. 2-40, where M_0 is the equilibrium longitudinal magnetization and T_1 is the spin-lattice, or longitudinal, relaxation time. T_1 can range from nanoseconds up to seconds depending on the molecular dynamics of the sample.

$$\frac{dM_z}{dt} = \frac{M_0 - M_z}{T_1} \qquad 2\text{-}40$$

Under the influence of spin-lattice relaxation, the time rate of change of the longitudinal magnetization, M_z, depends on the difference between the current longitudinal magnetization and the equilibrium magnetization, M_0. Therefore the time dependence of M_z can be described by an exponential growth (Eq. 2-41).

$$M_z(t) = M_z(0)\exp\left(-\frac{t}{T_1}\right) + M_0\left(1-\exp\left(-\frac{t}{T_1}\right)\right)$$

2-41

2.2.2. Transverse (Spin-Spin) Relaxation

The net coherent transverse magnetization excited by an RF (or ULF) pulse during the course of an NMR experiment decays with time, i.e. it returns to its equilibrium value, by means of the process of spin-spin relaxation. This relaxation process is characterized by the T_2 time constant. Spin-spin relaxation is due to the interactions between neighbouring spins within the spin system and is a function of the sample as well as the static field strength, B_0.

Macroscopically, the transverse magnetization decay is characterized by the transverse relaxation time, T_2, and a simple rate law, given by Eq. 2-42.

$$\frac{dM_{xy}}{dt} = -\frac{M_{xy}}{T_2}$$

2-42

$$M_{xy}(t) = M_{xy}(0)\exp\left(-\frac{t}{T_2}\right)$$

2-43

The time dependent equation for the transverse magnetization is therefore an exponential decay, given by Eq. 2-43 where $M_{xy}(0)$ is the initial transverse magnetization excited by the RF pulse.

2.2.3. Field Inhomogeneity and Shimming

Homogeneity of the static B_0 field is essential in most applications of nuclear magnetic resonance (NMR) because any inhomogeneities in the field will cause de-phasing of the coherent transverse magnetization. As a consequence of this de-phasing the observed signal, or free induction decay (FID), will decay more rapidly

than is predicted by T_2 relaxation alone. This effect is quantified by the effective spin-spin relaxation time constant: T_2^*. The relationship between the spin-spin relaxation time constant, T_2, and T_2^* is given by Eq. 2-44, where ΔB_0 is a measure of the inhomogeneity of the static field, B_0.

$$\frac{1}{T_2^*} = \frac{1}{T_2} + \frac{\gamma}{2\pi}\Delta B_0 \qquad \text{2-44}$$

In many applications it is desirable to reduce ΔB_0 so that T_2^* is roughly equal to T_2 and Earth's field NMR, the subject of this thesis, is no exception. The Earth's magnetic field in and of itself is highly homogeneous but it is also relatively weak, therefore the local homogeneity of the Earth's field can be significantly disrupted by the presences of ferrous or magnetic objects. It is possible to find locations where these disruptions are minimal; however, it is often not feasible to search out such a spot before performing the desired EFNMR measurements.

In NMR, "shimming" is a method for improving the homogeneity of the static B_0 field. In essence, shimming is accomplished by applying a magnetic field of arbitrary magnitude and geometry such that it cancels out the inhomogeneities in the underlying static magnetic field.

In practice, shim fields of arbitrary geometry and magnitude are generated using a linear combination of spherical harmonics. The simplest spherical harmonics are three orthogonal constant magnetic field gradients corresponding to the x, y and z dimensions in the laboratory frame. These are referred to as first-order shims. In many NMR and MRI systems higher-order shims (higher-order spherical harmonics) are also used to permit the generation of more complex shim fields and so allowing for the correction of more complex field inhomogeneities.

2.3. Information Content in NMR

In theory, all of the information available from NMR signals obtained using a

high-field laboratory instrument is also available from an Earth's field NMR device. However, there are many practical concerns which mean that it is very difficult, and in some cases extremely impractical, to extract the same range and quality of information from an Earth's field device. That being said, there remains a huge potential for obtaining important and useful information using Earth's field NMR if clever acquisition schemes and hardware devices are used. Broadly speaking, the types of information obtained via NMR can be grouped into three categories. The first group of experiments involves spatial encoding. Spatial encoding can be used not only to differentiate between spins in different locations in the sample but also to "tag" spins with their position at one point in time and then observe, at a later time, how the spins have moved. The second group of NMR experiments uses chemical shift and indirect spin-spin coupling for chemical identification and structural analysis. The third group of NMR experiments to be considered in this thesis is those which probe ordering within a sample via the residual dipole-dipole coupling of a probe solvent molecule.

2.3.1. Spatial Encoding

A magnetic resonance imaging (MRI) experiment is essentially a nuclear magnetic resonance (NMR) experiment in which the signal is spatially encoded. That is, the acquired signal contains information about the relative locations of the spins in the sample. This spatial information is acquired through the use of magnetic field gradients. Magnetic field gradients alter the magnitude of the underlying homogeneous field, B_0, as a function of position. Thus different magnetic field strengths will be experienced by groups of spins in different locations in the sample. The consequences of this can be readily illustrated through a consideration of the Larmor equation.

First we will introduce a magnetic field gradient, **G**, which alters the magnitude of the static field, $B_0\hat{k}$, in the $\hat{i}$, $\hat{j}$ and $\hat{k}$ directions. It is important to note that while the *magnitude*, B_0, of the static field is altered in the direction of the gradient the *direction* of the static field remains constant in the $\hat{k}$ direction. The assumption that any concomitant gradients, i.e. magnetic field components generated

by **G** along the $\hat{i}$ and $\hat{j}$ directions, are negligible requires that the magnitude of the static field **B** is much greater than the magnitude of **G***d*, where *d* is the size of the sample.

$$\mathbf{G} = \frac{\partial B_0}{\partial x}\hat{i} + \frac{\partial B_0}{\partial y}\hat{j} + \frac{\partial B_0}{\partial z}k$$

2-45

As a consequence of this alteration in the uniformity of the static field by **G**, the Larmor frequency becomes dependent on position (Eq. 2-46).

$$\omega(\mathbf{r}) = \gamma(B_0 + \mathbf{G} \bullet \mathbf{r})$$

2-46

This means that the spins at a point $\mathbf{r}_1$ within the sample will precess at a different frequency than the spins at a point $\mathbf{r}_2$. Thus we have encoded spatial information into the frequency.

Consider an isochromat within the sample at point $\mathbf{r}_1$, i.e. a localized collection of spins which precess at the same frequency. The phase of these spins can be written as in Eq. 2-47.

$$\exp\left(i\omega(\mathbf{r_1})t\right) = \exp\left(i\gamma(B_0 + \mathbf{G} \bullet \mathbf{r}_1)t\right)$$

2-47

If we represent the spatial distribution of spins in the sample with $\rho(\mathbf{r})$ then we can write the total signal acquired, in an idealized experiment, as the sum of the density of spins at each location weighted by the spatially dependent phase term.

$$S(\mathbf{G}, t) = \iiint \rho(\mathbf{r}) \exp\left(i\gamma(B_0 + \mathbf{G} \bullet \mathbf{r})t\right) d\mathbf{r}$$

2-48

The interpretation of Eq. 2-48 can be greatly simplified through the

introduction of the concept of k-space. First we assume that we detect only the deviations from the Larmor frequency, ΔB_0, and therefore can reduce the exponential term to $\exp(i\gamma \mathbf{G} \bullet \mathbf{r}t)$. Second we introduce a k-space encoding vector (Eq. 2-49). In many experimental situations the magnetic field gradient is time varying. In this case **k** is more properly defined as in Eq. 2-50.

$$\mathbf{k} = \frac{1}{2\pi}\gamma \mathbf{G}t \qquad 2\text{-}49$$

$$\mathbf{k} = \frac{\gamma}{2\pi}\int \mathbf{G}(t)t \qquad 2\text{-}50$$

Eq. 2-49 defines what is known as k-space. Substituting the k-space vector into Eq. 2-48 we obtain an expression for the signal, *S*, as a function of **k**.

$$S(\mathbf{k}) = \iiint \rho(\mathbf{r}) \exp(i2\pi \mathbf{k} \bullet \mathbf{r}) d\mathbf{r} \qquad 2\text{-}51$$

By inspection we find that there is a Fourier relationship between the MRI signal in k-space, $S(\mathbf{k})$, and the spin density, $\rho(\mathbf{r})$. Therefore we may write the spin density as the inverse Fourier transform of $S(\mathbf{k})$.

$$\rho(\mathbf{r}) = \iiint S(\mathbf{k}) \exp(-i2\pi \mathbf{k} \bullet \mathbf{r}) d\mathbf{k} \qquad 2\text{-}52$$

.

Eq. 2-52 demonstrates that the spin density function, and hence an image of the sample, can be obtained by the application of a Fourier transform to the k-space signal. Therefore, the complexity of the basic MRI experiment is focused almost entirely on how you chose to sample k-space.

2.3.2. Indirect spin-spin coupling

Indirect spin-spin coupling is an interaction between nuclei through the mediation of non-localized electrons. This interaction occurs through a covalent bond and so is only present between nuclei on the same molecule, i.e. it is entirely intra-molecular. The full indirect spin-spin coupling interaction is characterized by a second rank tensor, **J**. However, in liquids we need only be concerned with the isotropic coupling part, *J*, which is a scalar quantity given by one-third of the trace of the tensor **J** [18].

The Hamiltonian for the isotropic component of the indirect spin-spin coupling interaction between two spins with angular momentum operators, $\mathbf{I}_1$ and $\mathbf{I}_2$, is given by Eq. 2-53.

$$\mathcal{H} = 2\pi J \mathbf{I}_1 \bullet \mathbf{I}_2 \qquad \text{2-53}$$

Note that this coupling term is independent of field strength and so the magnitude of this interaction will be the same in a high-field spectrometer as it is in the Earth's magnetic field. Despite this lack of field dependence, in many cases there is an important difference between the case of indirect spin-spin coupling at high-fields and at ultra-low fields. In the case of B_0 field strengths on the order of a Tesla, the indirect spin-spin coupling will typically be much weaker than the Zeeman interaction; therefore it is appropriate to use the secular approximation, i.e. to keep only the $\mathbf{I}_{z1}\mathbf{I}_{z2}$ from the scalar product of $\mathbf{I}_1$ and $\mathbf{I}_2$, where *z* is the direction of the static field. In the case of ultra-low fields, on the order of μT, the contribution of indirect spin-spin coupling terms are often of a similar magnitude to the Zeeman interaction terms and so all parts of the scalar product must be included. This results in a much more complicated calculation for the ultra-low field case, which can significantly lengthen computation times when simulating multi-dimensional NMR experiments with systems of four or more spins and greatly complicates the interpretation of the spectra. These details will be discussed in much more detail in Chapters 6, 7, 8 and 9.

2.3.3. Chemical Shift

In the solid or liquid state a given nucleus is surrounded by atomic or molecular electron clouds which can interact with the nuclear spin angular momentum in a way which is characteristic of the local electronic environment. The most significant effect of the surrounding electron clouds is magnetic shielding, which results when the electronic orbitals are perturbed by the applied field, B_0. This shielding causes the Larmor frequency to be shifted slightly. This is the so-called chemical shift and can be used to identify the chemical environment of the nucleus. The Hamiltonian term due to chemical shift is simply a Zeeman operator with a slight reduction in the apparent static magnetic field (see Eq. 2-54 and Eq. 2-55).

Chemical shifts are highly dependent on atomic number and so while the observed chemical shifts for ^{1}H (protons) are on the order of only a few ppm (parts per million) the chemical shifts for heavier nuclei such as ^{13}C and ^{31}P can be hundreds of ppm [17].

In ordered environments, molecular orbitals can exhibit rotational anisotropy and therefore the shielding effect of the electron cloud has a tensorial character. The full Hamiltonian term for the chemical shift is given by Eq. 2-54, where **S** is the chemical shift tensor.

$$\mathcal{H}_{CS} = -\mathbf{I} \bullet \mathbf{S} \bullet \mathbf{B}_0 \qquad \text{2-54}$$

Under rapid isotropic rotation, as in most rapidly tumbling liquid samples, the chemical shift Hamiltonian can be simplified to contain only an isotropic chemical shift term, σ_i [17].

$$\mathcal{H}_{CS} = -\sigma_i \omega_0 \mathbf{I}_z$$
$$\sigma_i = \tfrac{1}{3}(\sigma_{xx} + \sigma_{yy} + \sigma_{zz}) \qquad \text{2-55}$$

In ultra-low fields, the chemical shifts of most nuclei are vanishingly small

and so cannot be observed except in a few special cases [19].

2.3.4. Direct Dipolar (DD) Coupling

In liquid systems, the magnetic moments of individual nuclei interact with the magnetic moments of surrounding nuclei even though the separation between them is much greater than their physical dimensions. The interaction between these magnetic dipoles is mutual and arises from the magnetic field of one dipole acting on the magnetic moment of other remote dipoles [17]. This is called the magnetic dipole-dipole interaction or direct dipolar (DD) coupling.

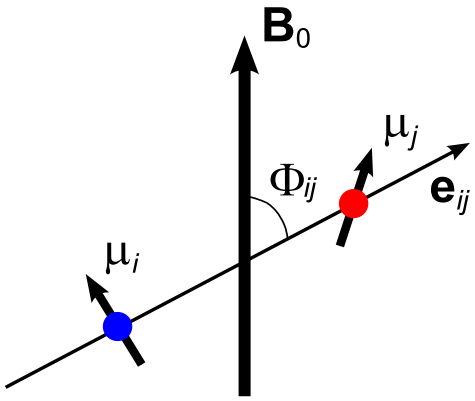

Figure 2.2 A schematic of direct dipolar coupling between two dipoles, $\boldsymbol{\mu}_i$ and $\boldsymbol{\mu}_j$. $\mathbf{e}_{ij}$ is a unit vector connecting the dipoles and Φ_{ij} is the angle between this unit vector and the static field, $\mathbf{B}_0$.

Figure 2.2 presents a schematic of direct dipolar coupling between two dipoles i and j with dipole moments $\boldsymbol{\mu}_i$ and $\boldsymbol{\mu}_j$, respectively. $\mathbf{e}_{ij}$ is a unit vector connecting the two dipoles, Φ_{ij} is the angle between this unit vector and the static field, $\mathbf{B}_0$ and r_{ij} is the distance between the dipoles.

The Hamiltonian which describes the direct dipolar interaction between two spins is given by Eq. 2-56 where b_{ij}, the dipolar coupling constant, is given by Eq. 2-57 [15].

$$\mathcal{H}_{ij}^{DD,full} = b_{ij}\left(3\left(\mathbf{I}_i \cdot \mathbf{e}_{ij}\right)\left(\mathbf{I}_j \cdot \mathbf{e}_{ij}\right) - \mathbf{I}_i \cdot \mathbf{I}_j\right)$$

2-56

$$b_{ij} = -\frac{\mu_0}{4\pi}\frac{\gamma_i \gamma_j \hbar}{r_{ij}^3}$$

2-57

$$\begin{aligned}
\mathcal{H}_{ij}^{DD,full} &= b_{ij}\left(A + B + C + D + E + F\right) \\
A &= \mathbf{I}_{iz}\mathbf{I}_{jz}\left(3\cos^2\Theta_{ij} - 1\right) \\
B &= -\frac{1}{4}\left(\mathbf{I}_i^+\mathbf{I}_j^- + \mathbf{I}_j^+\mathbf{I}_i^-\right)\left(3\cos^2\Theta_{ij} - 1\right) \\
C &= \frac{3}{2}\left(\mathbf{I}_i^+\mathbf{I}_{jz} + \mathbf{I}_{iz}\mathbf{I}_j^+\right)\sin\Theta_{ij}\cos\Theta_{ij}e^{-i\phi_{ij}} \\
D &= \frac{3}{2}\left(\mathbf{I}_i^-\mathbf{I}_{jz} + \mathbf{I}_{iz}\mathbf{I}_j^-\right)\sin\Theta_{ij}\cos\Theta_{ij}e^{i\phi_{ij}} \\
E &= \frac{3}{4}\left(\mathbf{I}_i^+\mathbf{I}_j^+\right)\sin^2\Theta_{ij}e^{-2i\phi_{ij}} \\
F &= \frac{3}{4}\left(\mathbf{I}_i^-\mathbf{I}_j^-\right)\sin^2\Theta_{ij}e^{2i\phi_{ij}}
\end{aligned}$$

2-58

The full expansion of the Hamiltonian in Eq. 2-57 is presented in Eq. 2-58 where ϕ_{ij} is the azimuthal component of Φ_{ij} and Θ_{ij} is the polar angle.

If the static field, B_0, is large the dipolar interaction will be much weaker than the Zeeman interaction and so we need to maintain only the secular (*A* and *B*) terms of the full expansion in Eq. 2-56. The secular dipolar coupling Hamiltonian is given in Eq. 2-59.

$$H_{ij}^{DD} = b_{ij}\,\tfrac{1}{2}\left(3\cos^2\Theta_{ij} - 1\right)\left(3\mathbf{I}_{zi}\mathbf{I}_{zj} - \mathbf{I}_i\cdot\mathbf{I}_j\right)$$

2-59

In a liquid system, Θ_{ij} is time dependent due to the tumbling of the molecule containing the coupled nuclei. In all but the most viscous isotropic liquids, these molecular motions will average the overall effect of dipolar coupling to zero on the timescale of the NMR experiment. In an anisotropic liquid, that is a liquid which is weakly oriented either locally or globally, the freely tumbling molecules feel a slight preference for a particular orientation or set of orientations. In this case, the intra-

molecular dipolar interactions do not average to zero. This is called residual dipolar coupling (RDC). The secular residual dipolar coupling Hamiltonian is defined by Eq. 2-60 where the residual dipolar coupling constant is defined by Eq. 2-61. The overbar in Eq. 2-61 denotes an average over all possible values of Θ_{ij} weighted by their corresponding statistical probabilities [15].

$$H_{ij}^{RDC} = d_{ij}\left(3\mathbf{I}_{zi}\mathbf{I}_{zj} - \mathbf{I}_i \cdot \mathbf{I}_j\right)$$

2-60

$$d_{ij} = b_{ij}\,\tfrac{1}{2}\overline{\left(3\cos^2\Theta_{ij} - 1\right)}$$

2-61

Consider the case of intra-molecular dipolar coupling between nuclei on a molecule whose motion is partially restricted because of local anisotropy in the system. In this case the angle Θ_{ij} can be broken up into two parts: (a) a fixed angle θ between the anisotropy director, a unit vector in the direction of the anisotropy, and the magnetic field and the time dependent angle $\alpha_{ij}(t)$ between $\mathbf{e}_{ij}$, the unit vector connecting the coupled dipoles, and the anisotropy director. The time averaged value of $\alpha_{ij}(t)$ is a function of the degree of orientation in the system and provides us with a measure of the anisotropy, while the absolute value of θ quantifies the direction of the anisotropy relative to the static magnetic field. Using the spherical harmonic addition theorem, we can re-write the residual dipolar coupling constant as shown in Eq. 2-62, where *S*, the so-called structure factor, is described by Eq. 2-63.

$$d_{ij} = b_{ij} S\,\tfrac{1}{2}\overline{\left(3\cos^2\theta - 1\right)}$$

2-62

$$S = \tfrac{1}{2}\overline{\left(3\cos^2\alpha_{ij}(t) - 1\right)}$$

2-63

The observation of residual dipolar coupling of a probe solvent molecule in a weakly aligned liquid crystal system in the Earth's magnetic field is explored in Chapter 10.

CHAPTER 3. Earth's Field NMR

3.1. Introduction

Earth's field NMR (EFNMR) refers to a class of nuclear magnetic resonance experiments where the nuclear spin precession is detected in the Earth's magnetic field [20; 21]. The use of the Earth's magnetic field for NMR experimentation is attractive because this field is highly spatially homogeneous, globally available and free. In EFNMR the signal is typically detected in the Earth's field, to take advantage of this high degree of homogeneity, but polarization is often achieved using additional fields to augment sensitivity. In this chapter we will present a historical overview of EFNMR, discuss some of the applications of this technology and outline the challenges associated with performing modern, sophisticated NMR experiments in the Earth's field.

3.2. Sensitivity and Resolution in EFNMR

The sensitivity of a basic NMR experiment is typically governed by the available equilibrium magnetization of the sample which is in turn given by the thermal polarization of the spin system. This thermal polarization is described by Eq. 3-1.

$$M = \frac{N\gamma^2\hbar^2 I(I+1)B_0}{3kT}$$

3-1

NMR signal is traditionally detected by an induction coil and therefore the strength of the signal will be proportional to the frequency of the oscillating magnetization, which is in turn determined by the field strength through the Larmor equation (Eq. 3-2).

$$\omega = -\gamma B_0$$

3-2

Inspection of Eq. 3-1 and 3-2 indicates that the signal strength, and hence the NMR sensitivity, is approximately proportional to B_0^2. In the case of Earth's field NMR, B_0 is on the order of 50 μT (0.5 G) and so sensitivity is a significant problem when compared to laboratory NMR instruments with fields on the order of a few Tesla. The many strategies available for augmenting the sensitivity of EFNMR by increasing the available NMR signal are discussed in Chapter 5. Other strategies to improve sensitivity include minimizing the noise pickup of the detection coil through screening (see Chapter 4) and changing the detection scheme to reduce the field strength dependence from B_0^2 to B_0. This thesis deals exclusively with EFNMR strategies and experiments within the realm of Faraday induction detection. However, a couple of the alternate detection schemes will be briefly mentioned later in this chapter.

In addition to sensitivity, another feature of any NMR instrument which governs its overall performance is spectral resolution. The final frequency resolution of a given NMR experiment is the result of a combination of instrument dependent, sample dependent and methodology dependent factors. Inspection of the Larmor equation (Eq. 3-2) reveals the relationship between the NMR frequency resolution and the spatial homogeneity of the static field, B_0. If the strength of the B_0 field varies with position, so too will the precession frequency of the spins. This frequency variance across the sample will cause a de-phasing of the signal in the transverse plane and consequently a rapid decay of the transverse magnetization in the time

domain. In the frequency domain this spread of frequencies will cause a broadening of spectral lines and therefore a coarsening of the actual spectral resolution.

It is the relationship between field homogeneity and frequency resolution which provides some of the impetus for working in the Earth's magnetic field, which is highly homogeneous over very large volumes. This homogeneity is harnessed not only for frequency resolution in spectroscopic applications but also for improving sensitivity because it means that very large samples can be used, i.e. 100s of mL instead of a few mL, a typical sample size in laboratory NMR spectroscopy instruments.

Due to the weak nature of the Earth's magnetic field there are a few sources of degradation of its natural homogeneity which must be considered and, if possible, eliminated. First the homogeneity of a 50 μT field is easily disrupted by magnetic or ferrous objects in close proximity to the detection coil. Second, time varying field components, either due to the local environment or the diurnal variations of the Earth's field itself, can cause a degradation of frequency resolution over the course of long experiments. These issues are addressed in detail in Chapter 4.

One of the central themes of this thesis is the optimization of sensitivity and resolution of Earth's field NMR. In some cases, improving the resolution of an instrument will concurrently result in improved sensitivity. However, as will be seen with dynamic nuclear polarization (Chapter 5), some improvements to sensitivity can only be made at the expense of the spectral resolution and so a good compromise between resolution and sensitivity must be achieved. This compromise is typically dictated by the requirements of a particular application.

3.3. Information Content in Earth's Field NMR

In addition to a discussion of resolution and sensitivity, no evaluation of an NMR device would be complete without a consideration of the information available using that instrument. In theory, all of the information available on a high field NMR device is available in the Earths' magnetic field; however, in practice there are certain limitations typically governed by either sensitivity, resolution or a combination of

both.

As at high-field, NMR parameters such as the T_1 and T_2 relaxation times can be measured; however, the long dead-times between signal excitation and detection, experienced by the B_1 excitation coil due to the long Larmor period of the spins in the Earth's magnetic field, prevent the accurate determination of T_2 times much less than 100 ms.

Spatial encoding of the NMR signal in order to measure diffusion and/or flow as well as for imaging applications have been shown to be possible in the Earth's field using specially designed gradient coils and pulse sequences analogous to those used for MRI in high fields [9; 10; 12; 22-25].

A range of spectroscopic information is available using EFNMR and it is the exploration of this application which is the major focus of the latter part of this thesis. For most nuclei chemical shift is vanishingly small in the Earth's magnetic field but J coupling interactions, both hetero-nuclear and homo-nuclear, can be observed in a range of small molecules. In addition, the intra-molecular residual dipolar coupling of ^{1}H nuclei on a solvent molecule in an aligned medium, such as a liquid crystal, can be observed in the Earth's magnetic field. These spectroscopic applications of EFNMR are explored in Chapters 7 through 10 of this thesis.

3.4. Historical Overview of Earth's Field NMR

3.4.1. First Observation of EFNMR

Eight years following the first observations of Nuclear Magnetic Resonance (NMR) by Purcell and Bloch in 1946, Packard and Varian demonstrated the free precession of water molecule protons in the terrestrial magnetic field [1]. Therefore, Earth's field NMR (EFNMR) can be said to be almost as old as NMR itself.

In the Packard and Varian approach to the observation of proton free-precession in the Earth's magnetic field, a relatively strong but not necessarily homogeneous prepolarizing magnetic field, oriented perpendicular to the Earth's magnetic field, is applied to the sample allowing the spin ensemble to come to an a priori thermal equilibrium polarization at this field strength. This prepolarizing field

is then switched-off non-adiabatically, i.e. quickly on the timescale of the precessing magnetization, such that the net magnetization remains in a plane perpendicular to the Earth's magnetic field and the subsequent free precession of the magnetization can be observed.

3.4.2. EFNMR of Monofluorobenzene

Along with this first demonstration of EFNMR using water, Packard and Varian also observed the beat pattern of the free precession of fluorine and proton nuclei coupled via the indirect spin-spin interaction in monofluorobenzene [1]. At this time the mechanism and form of the indirect spin-spin coupling interaction were not yet well understood. The subsequent observation of this coupled spin system in the Earth's magnetic field by Elliott and Schumaker in 1957 [26] was explained as a doublet with an observed splitting of 5.8 ± 0.2 Hz, an "average" of the range of H-F couplings within the monofluorobenzene molecule. However, high resolution observations of monofluorobenzene by Bak, Schoolery and Williams [27] demonstrated that the indirect spin-spin coupling constants for the ortho, meta and para protons in the monofluorobenzene molecule were approximately 10 Hz, 6 Hz and 0.5 Hz, respectively. This suggested that, unless there was a significant field dependence of indirect spin-spin coupling constants, the "average" coupling interpretation of Elliott and Schumaker was incorrect. In 1962, Thompson and Brown presented a letter to the editor of the Journal of Chemical Physics [5] indicating that a detailed study of the beat patterns of the free precession of monofluorobenzene in the Earth's field does indeed show a range of frequency components, as was consistent with the high-resolution observations at high-field. This particular issue is of interest to this thesis because it can be resolved unequivocally through the combined use of 2D NMR spectroscopy techniques employed in the Earth's magnetic field and numerical simulations. This issue is addressed in Chapter 8.

3.4.3. Geophysical Applications of EFNMR

In the early years of Earth's field NMR, the method was used primarily for gaining low frequency data for relaxation dispersion and for the measurement of

scalar spin-spin coupling effects between hetero-nuclei [20]. These experiments were typically confined to remote outdoor environments for practical reasons addressed in the apparatus overview in Chapter 4. Taking advantage of this ability to perform NMR outside of the laboratory with a small portable instrument, a number of predominantly geophysical applications of Earth's field NMR were developed.

The first, somewhat obvious, geophysical application of Earth's field NMR is for the measurement of the terrestrial magnetic field, i.e. for Earth's field magnetometry. Recent developments in sensitivity enhancements schemes, which will be discussed in Chapter 5, have greatly improved the sensitivity and versatility of these devices [28; 29].

Another historic application of EFNMR is well-logging [30]. The idea of performing Earth's field NMR inside a borehole in order to investigate the properties of oil reservoirs was first put forward by Brown and Gamson in 1960 [2] and has laid the foundation for modern NMR well-logging techniques using permanent magnet NMR devices.

An application of Earth's field NMR, which has become more prevalent in recent times, is NMR pedagogy. In 1982, Callaghan and Legros presented a paper detailing a simple Earth's field NMR apparatus that could be used in a teaching laboratory environment to demonstrate the basic principles of NMR to students [31]. With the increasing importance of NMR and MRI in a wide range of scientific disciplines from Chemistry to Medicine, it has become more and more important to expose students to the principles of magnetic resonance at an undergraduate level.

This contribution of Callaghan and Legros not only demonstrated the use of EFNMR for teaching but also presented an important improvement to the traditional scheme of Packard and Varian which uses the non-adiabatic switch off of the polarization field for signal excitation. In practice, the rapid switch-off condition is not easy to achieve and so an adiabatic switching protocol was adopted in [31] whereby the net magnetization follows the slowly changing net field, the vector sum of the decreasing prepolarization field and the static Earth's field, such that at the end of the switching process the enhanced net magnetization vector is aligned with the Earth's magnetic field. Using the receiver coil as a transmitter, the NMR signal is excited in the Earth's field by a radiofrequency pulse at the Larmor frequency of the sample, in the manner of high-field NMR. It should be noted that the Larmor

frequency of nuclei in the Earth's field falls in the ultra-low frequency range of the electromagnetic spectrum and so this excitation pulse is referred to as a "ULF pulse" as opposed to the common high-field NMR nomenclature of an "RF pulse". In 2009 there are two commercially available Earth's field NMR teaching systems, the Teach-spin system (www.teachspin.com) and the Magritek Terranova-MRI (www.magritek.com). The latter, described in detail in Chapter 4, was used as the basis for the apparatus used throughout this thesis.

Building on the use of ULF pulses to excite an NMR signal in the Earth's field, a surface NMR method for groundwater prospecting was proposed by Semenov et al. in 1989 [32]. This method is capable of detecting ground water reserves at depths of up to 100 m through the use of a 100 m diameter wire loop arranged on the surface for both excitation and the detection of the NMR signal in the Earth's magnetic field [33-37]. No prepolarization is required because of the huge volumes of water which are detected and the extremely high spatial homogeneity of the Earth's magnetic field which permits the detection of a coherent free precession over large physical volumes. Using both the amplitude and the phase of the NMR signal as a function of excitation pulse strength, an inversion method yields a depth profile of groundwater beneath the surface coil.

In the early 1990s, Callaghan et al. developed an Earth's field apparatus for in situ measurements of brine diffusivity of Antarctic sea ice using pulsed gradient spin echo (PGSE) NMR techniques [9-13; 38]. This application required the development of a specialized magnetic field gradient coil for use in the relatively weak Earth's magnetic field (~ 0.6 G in Antarctica). The gradient requirements of a PGSE measurement of brine diffusivity are such that, in the Earth's field, the concomitant gradients generated by the magnetic field gradient coil, i.e. the components of the gradient field orthogonal to the main static field, cannot be neglected. Therefore in the design process it is the net gradient in the magnitude of **B** that needs to be considered rather than simply the gradient in the component of the field parallel to a strong, dominant B_0 field, as is the case in high-field PGSE NMR. A combined Maxwell–Helmholtz configuration can be employed to produce a gradient in $|\mathbf{B}|$ along the axis of the gradient coil. The superposition of the Maxwell pairs (opposed currents) and Helmholtz pairs (parallel currents) produces a nearly uniform $\mathrm{d}|\mathbf{B}|/\mathrm{d}x$ gradient in which the null point of the field is shifted out of the sample volume [12].

3.4.4. Earth's Field NMR Imaging

In the 1990's, Stepisnik and coworkers [22; 24; 25; 39; 40] developed a system for performing MRI using the Earth's magnetic field. In addition to the traditional components of the system such as a transmit/detect coil tuned to the Larmor frequency of the sample, a pre-polarization coil and a magnetic field gradient coil set, their Earth's field imaging system also required a secondary detection coil, which was located a small distance from the main apparatus. This second detection system, containing a standard sample such as water, was used as a frequency probe to track any fluctuations in the Earth's magnetic field. The NMR signal acquired with the reference sample was mixed with the NMR signal from the target sample in such a way that the resultant signal contained only deviations from the reference signal. This heterodyne detection approach was important in order to correct for fluctuations in the magnitude of the Earth's magnetic field due either to changes in the underlying field itself or changes in the immediate environment of the apparatus. Although highly effective, this approach is slightly cumbersome in that it requires a second device and a feedback channel for the combining of the reference and sample signals.

In addition to basic 2D imaging in the Earth's magnetic field, Mohoric et al. [24] also demonstrated self-diffusion imaging and reported the implementation of other MRI techniques such as velocity imaging and slice selection. 3D MRI in the Earth's magnetic field was demonstrated by Halse et al. in 2006 [41].

In recent years, noteworthy advancements have been made in imaging in fields on the order of the Earth's magnetic field using either Superconducting Quantum Interference Devices (SQUIDs) [42-50] or atomic magnetometers [51; 52] for non-Faraday detection of the MRI signals. One exciting application of this technology is for the concurrent acquisition of magnetoencephalography (MEG) and MRI data using SQUIDs [49; 50; 53]. Using SQUIDs to perform MRI detection in microtesla fields, the Earth's field range, allows these two methodologies to be naturally combined in the same system and so provides an anatomical map for MEG-localized neural sources. Another biomedical application is the simultaneous detection of MRI and biological signals, such as neuronal currents, with SQUIDs [46; 54; 55].

3.4.5. High-resolution Earth's Field NMR Spectroscopy

Another area in which significant advancements in Earth's field NMR have occurred in recent years is NMR spectroscopy. In early Earth's field NMR experiments, the conventional wisdom was that the only spectroscopic information available was indirect spin-spin coupling between hetero-nuclei because chemical shifts in such a weak field are vanishingly small. Recent experiments highlight, however, that this is not always the case.

In 2005, Appelt et al. [56] demonstrated that the chemical shifts of ^{129}Xe can be observed in the Earth's magnetic field using ^{129}Xe gas which has both exceptionally long T_2's, 10 – 1000 s in liquid solvents, and a very large chemical shift difference of about 200 ppm between the free flowing gas and gas dissolved in a liquid solvent, such as toluene [56]. Key to the observation of ^{129}Xe chemical shifts in the Earth's magnetic field is the use of hyperpolarized ^{129}Xe gas, thus overcoming the very low thermal polarization of ^{129}Xe in the Earth's magnetic field, which has a Larmor frequency of approximately 570 Hz. The method for generating hyperpolarized ^{129}Xe gas is discussed in Chapter 5.

More recently, Appelt et al. [57-59] demonstrated that in cases where the magnetic equivalence between two groups of homonuclear spins is broken by the presence of unique indirect spin-spin couplings to a heteronucleus, homonuclear indirect spin-spin couplings can be observed in the Earth's magnetic field. In these experiments, the samples were pre-polarized by a 1 T Halbach permanent magnet array and then manually transported to the Earth's field NMR probe for excitation by a ULF pulse and subsequent detection of the free precession. The use of the Halbach array for prepolarization provides a polarization advantage that is orders of magnitude greater than the more traditional electromagnet approach because the latter is limited to much weaker magnetic fields for the practical reasons of field switching and resistive heating. The use of the Halbach permanent magnet for prepolarization is especially advantageous because this type of array is largely self-screening and therefore can be located relatively close to the Earth's field NMR probe without perturbing the homogeneity of the Earth's field.

In addition to these advancements in 1D spectroscopy, multi-dimensional spectroscopy has also been demonstrated to be possible in the Earth's field. In 2006,

Robinson et al. [60] presented the first 2D COSY acquired in the Earth's magnetic field. The multi-dimensional spectroscopy developments presented in this thesis (see Chapter 8) are a continuation of this 2D COSY work.

CHAPTER 4. EFNMR Apparatus

4.1. Introduction

All experiments presented in this thesis were performed using a Terranova-MRI Earth's field system (Magritek Ltd., Wellington, NZ), an example of which is pictured in Figure 4.1.

Figure 4.1 Terranova-MRI probe and spectrometer (Photo courtesy of Magritek Limited. © Magritek Limited 2006)

This system consists of three main parts: a three-component probe, an ultra-

low frequency spectrometer and the Prospa software package running on a PC. The components of the standard Terranova-MRI system are detailed in sections 4.2, 4.3 and 4.4. Several hardware and software improvements were made to this commercial apparatus as part of this thesis project. These include: ultra-low-frequency noise shielding (4.5), auto-shimming (4.6.1) and temporal field stabilization (4.7). Note that, where appropriate, some experiment specific hardware additions/improvements are detailed in later chapters.

4.2. Terranova-MRI Three-coil Probe

At the centre of the Terranova-MRI apparatus is a three-component probe which is responsible for pre-polarization, signal excitation and detection, shimming and spatial encoding. The probe can be divided into three parts: the polarizing coil, the excitation/detection coil and the gradient coil set. A schematic of the probe is presented in Figure 4.2.

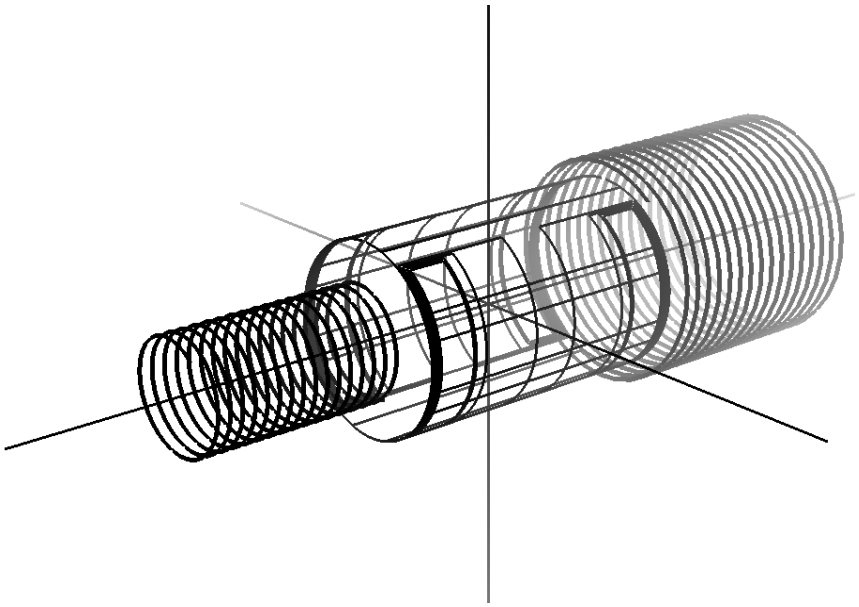

Figure 4.2 A schematic of the three coil probe: an outer solenoid for pre-polarization, an inner solenoid for signal excitation and detection and a set of gradient coils for imaging and/or shimming. (This schematic is courtesy of Mark Hunter, Victoria University of Wellington.)

4.2.1. Polarizing Coil

The polarizing coil is a large solenoidal coil which is capable of providing a static magnetic field along the axis of the probe with a magnitude of 3.13 mT/A at its peak. At the standard current of 6 A, this coil provides maximum prepolarization field of 18.7 mT. The simple solenoidal design means that over a standard 75 mm diameter, 100 mm long sample the field has an inhomogeneity on the order of 10-15 %. This renders the field unsuitable for NMR detection but is perfectly viable for prepolarization. This coil is used to enhance the sensitivity of Earth's field NMR by allowing the sample to come to an a priori thermal equilibrium at the moderate field strength provided by the prepolarization coil before excitation and detection in the very weak, but highly homogeneous Earth's magnetic field. The theory of prepolarization is discussed in detail in Chapter 5.

In addition to enhancing sensitivity thorough polarization enhancement, the pre-polarization coil increases the signal-to-noise ratio (SNR) of the NMR signal by acting as a shield from external ULF noise sources. This is achieved by shorting the polarizing coil to ground during the detection stage of the pulse sequence [9; 61]. The polarizing coil has multiple layers of copper windings. On average, the thickness of the copper is 10 mm. Thus it is a very good shield for ULF noise. If the external noise is directional, as is often the case, the shielding will be most effective at a very specific orientation. Any deviation from this orientation results in a dramatic increase in the observed noise on the NMR signal. Therefore the orientation of the long axis of the probe must be chosen according to noise shielding considerations in order to obtain good SNR.

4.2.2. B_1 (Transmit and Receive) Coil

Signal excitation and detection is achieved using the innermost component of the Terranova-MRI probe, which is a solenoid with several thousand turns. This coil is connected to a series of capacitors under software control within the ultra-low frequency spectrometer. By changing the capacitance, the B_1 coil is tuned to the Larmor frequency of the sample. The coil has a DC resistance of approximately 330 Ω, an inductance of approximately 0.5 H and requires a tuning capacitance in the nF

range to tune to the Larmor frequency of protons in the Earth's field (~ 2.3 kHz). The quality factor, Q, of the coil is about 20. The ring-down of the coil, i.e. the characteristic time of the dissipation of the energy in the coil following an excitation pulse, can be approximated by Q times the Larmor period. Therefore, for a Larmor frequency of 2.3 kHz, the ring-down time constant is 9 ms. A delay of 20 ms is typically introduced between the end of an excitation pulse and the beginning of signal acquisition in order to avoid any corruption of the detected signal by the ring-down of the coil.

4.2.3. Gradient Coils

In order to encode spatial information into the NMR signal, it is necessary to perturb the homogeneity of the Earth's magnetic field in a very controlled way, such that the magnitude of the field varies in the direction of the desired spatial encoding. This is achieved through the use of a three-axis gradient coil set. For the most part, designing a gradient coil set for spatial encoding in the Earth's magnetic field is analogous to gradient coil design in the high-field case. However, there is one point of difference which is significant for imaging applications. This difference is the orientation of the Earth's field, $\mathbf{B}_E$, relative to the vertical.

The orientation of $\mathbf{B}_E$ for most locations on the planet is neither vertical nor horizontal but rather at a declination angle, d, to the vertical, z. This magnetic field orientation affects the magnitude and direction of the magnetic field gradients generated by the gradient coil set. In applications such as imaging, it is very important to be aware of the actual gradient fields produced by the gradient coil set. Therefore, as part of this thesis the effect of the relative orientation of the gradient coil set and the Earth's magnetic field, $\mathbf{B}_E$, on the strength and orthogonality of the gradients was considered and characterized.

In order to understand this problem we define two frames of reference: the laboratory frame, xyz, and the gradient coil set frame, $x'y'z'$. For simplicity, we define the x axis of the laboratory frame such that it is aligned with x', which represents the long axis of the gradient coil set; however it is important to note that the relative alignment of the coil frame and the laboratory frame is arbitrary.

The gradient coil set consists of a saddle coil and two quadrupolar coils 45°

apart as in the standard electromagnet geometry [17]. This arrangement generates three linear magnetic field gradients that operate in the weak gradient field approximation: $|\mathbf{B}_g| << \mathbf{B}_E$. Ideally the *z*' axis of the gradient coil set is aligned with the field, $\mathbf{B}_E$, and so the magnetic field gradients generated by the gradient coil set are orthogonal and are directed along *x*', *y*' and *z*' respectively. However, if the Earth's magnetic field vector does not point along *z*' in the gradient coil reference frame, non-orthogonal gradients will result.

As explained in section 4.2.1, when using the standard Terranova-MRI apparatus, the amount of external noise detected by the B_1 coil is highly dependent of the orientation of *x*' axis of the probe. If we fix the absolute orientation of the *x*' axis to minimize noise pickup (and so maximize SNR) we will typically not be able to align the *z*' axis of the gradient coil set with $\mathbf{B}_E$. This will lead to non-ideal gradient orientations and strengths. In early work associated with this thesis, a compromise was determined whereby the single degree of freedom of the probe, a rotation about *x*', is used to minimize the problems associated with the non-orthogonality of the gradients.

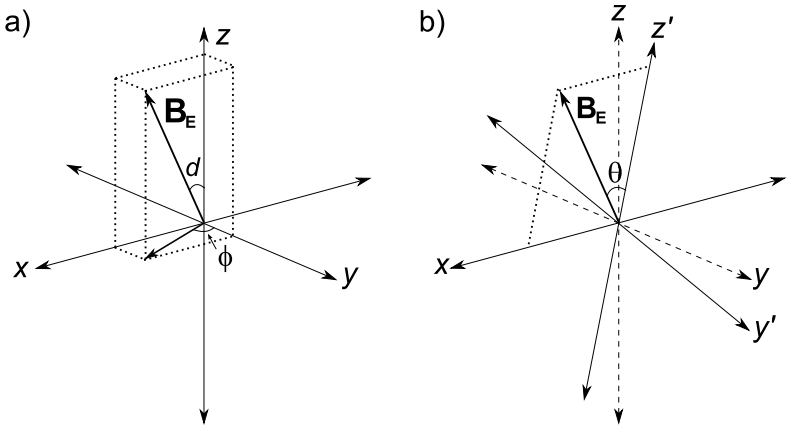

Figure 4.3 (a) Gradient coil orientation such that *z*' and *y*' are coincident with *z* and *y*. The gradients which result from this orientation are all non-orthogonal. (b) Gradient coil orientation where *z*' and *y*' are rotated about the *x* axis such that $\mathbf{B}_E$ lies in the *xz*' plane. $\mathbf{B}_E$ is now at an angle θ with respect to *z*' and is perpendicular to *y*'. G_y is orthogonal to both G_z and G_x but G_x and G_z are non-orthogonal relative to each other. The magnitude of G_y and G_z are reduced by a factor of cos θ. (Figure courtesy of Mark Hunter, VUW)

Consider the situation presented in Figure 4.3a where *y*' and *z*' are aligned with *y* and *z* in the laboratory frame. The magnetic field vector, $\mathbf{B}_E$, points at a declination angle, *d*, to the vertical and is at an angle ϕ to the *y* axis in the horizontal plane. The magnetic field gradients G_x, G_y and G_z generated by the gradient coil set in this orientation are non-orthogonal and their exact orientation is a complicated function of the angles *d* and ϕ.

Now consider the situation presented in Figure 4.3b. The gradient coil has been rotated about the *x* axis such that $\mathbf{B}_E$ lies in the *xz*' plane. $\mathbf{B}_E$ is now at an angle θ to the *z*' axis but is perpendicular to the *y*' axis. In this orientation, G_y and G_z will be directed along *y*' and *z*', respectively; however, G_x will be generated in the *xz*' plane, rotated away from the *x* axis by an angle θ about the *y*' axis. Therefore G_y is orthogonal with respect to both G_z and G_x but G_x and G_z will be non-orthogonal with respect to each other. In addition to this non-orthogonality of the gradients, the magnitude of G_y and G_z will be reduced by a factor of cos θ. As a result, a 3D MRI acquired with this gradient orientation will be geometrically correct in the *xy'* and *z'y'* planes but will be skewed by an angle θ in the *xz* plane and the field of view (FOV) of the image along *y'* and *z'* will be incorrect by a factor of cos θ. This non-ideal character of the gradients can be countered if θ is well known because linear combinations of G_x and G_z can be used to generate two orthogonal gradients in the *xz*' plane and compensate for the reduced strength of G_y and G_z.

It should be noted that, as well as creating artifacts in images, any non-orthogonality will also reduce the effectiveness of the gradients as first-order shims, particularly when the auto-shimming routine is used because this algorithm assumes that the optimal shim values for the three dimensions, *x*, *y* and *z* are independent. This is only true if the three gradients are orthogonal. (Auto-shimming is discussed in detail in section 4.6.1.)

In the final apparatus used to obtain the results presented in this thesis, additional noise screening was achieved using a Faraday cage (see section 4.5). The effectiveness of this additional screening is independent of the orientation of the *x'* axis of the gradient coil and therefore the optimal gradient coil orientation, where z' of the gradient coil set is aligned with $\mathbf{B}_E$, can be achieved without any decrease in signal-to-noise (SNR). Therefore the above compromise between SNR and gradient

orthogonality becomes unnecessary.

4.3. Terranova-MRI Ultra-low Frequency Spectrometer

In some sense, the core of the Terranova-MRI apparatus is the ultra-low field spectrometer which executes and controls the pulse sequence, from turning on and off the polarizing coil to recording and processing the FID signal. The Terranova-MRI ULF spectrometer described herein is very similar to a conventional high field laboratory system except that it operates in the kHz range. Therefore relatively simple transceiver circuitry can be used and the signal can be sampled directly, eliminating the need for intermediate frequency (IF) stages.

The control and signal processing part of the Earth's field apparatus consists of a Digital Signal Processor (DSP) based pulse programmer and data acquisition unit that uses a Universal Serial Bus (USB) interface to communicate with a host computer. By using a DSP a lot of the functional blocks can be implemented in software instead of hardware, and therefore greater flexibility can be achieved.

The transmit (Tx) signal is generated using a digital oscillator algorithm running on the DSP. Multiple oscillators are implemented for multiple phases. The power required for the B_1 excitation is minimal therefore a low noise preamp can be connected permanently to the probe and ordinary operational amplifiers can be used to drive the probe. A series of capacitors, under software control, are switched in for probe tuning. Probe impedance matching is not required due to the very long wavelength; the probe operates with a resonant impedance of several tens of kilo-ohms.

In addition to controlling the transmitting and receiving portions of the NMR experiment, the ULF spectrometer also contains five current controlled amplifiers which are used to drive the pre-polarizing coil, the three imaging/shimming gradient coils and either the PGSE gradient coil or the B_0 lock coil depending on the requirements of the given experiment.

The entire ULF spectrometer is housed within a box with physical dimensions of 340 x 240 x 160 mm and a mass of less than 5 kg. This spectrometer can be run off of a 24 V, 10 A power supply or two series connected 12 V car batteries and so is

useful for both outdoor operation and laboratory use.

4.4. Terranova-MRI Software Package: Prospa

All of the Terranova-MRI pulse sequences are controlled by the Prospa software package (Magritek Ltd., Wellington, NZ) running on a PC. Typically a laptop is used for portability and also because CRT monitors often produce noise in the 2 kHz range, which can be picked up by the B_1 coil and degrade its SNR performance. Experiments are executed by running macros within Prospa. The software interfaces with the spectrometer via a USB connection, initiating the experiment and subsequently performing all of the post-processing and display of the detected signals.

Within this thesis the Prospa software package is not only used for controlling the Terranova-MRI experiments but is also employed for data manipulation and display and for calculations and simulations.

4.5. Ultra-low Frequency Noise Shielding

Historically, one of the most significant practical limitations of NMR experiments carried out using the Earth's magnetic field was the need to set-up the instrument in a remote, non-urban environment. One of the reasons for this is that the Larmor frequency of protons in the Earth's magnetic field is approximately 2.3 kHz, a frequency at which external noise pick-up in urban environments exceeds the Johnson noise of the receive coil by several orders of magnitude.

In this thesis a two-fold strategy for noise reduction is used. As described in section 4.2.1, the standard Terranova-MRI polarizing coil is shorted to ground during signal acquisition. This shorted coil acts as a screen to ultra-low frequency noise. While this approach reduces the noise picked up by the detection coil sometimes by as much as two orders of magnitude, it is often insufficient to reduce noise to the level of either the Johnson noise of the coil (~ 0.6 μV) or the noise floor of the spectrometer

(1-2 μV). Therefore a grounded Faraday cage is used to provide additional screening.

Skin depths in common conductors such as copper and aluminium are quite significant at 2 kHz (approximately 1.5 mm for copper and 2 mm for aluminium). Therefore the wall thickness of the Faraday cage needs to be very large. A copper box with a wall thickness of 10 mm and a mass of approximately 50 kg was found to reduce the amplitude of the external pick-up noise in the time domain by a factor of about 25, e.g. from 400 μV to 17 μV. The shorting of the polarization coil further reduces this noise amplitude to 2.5 μV. Note that when designing such a Faraday cage, care must be taken that the box is sufficiently large that any eddy currents induced by the switching of the polarizing or gradient fields do not disrupt the homogeneity of the field during signal detection.

In addition to the significant reduction in noise compared to using the shorted polarization coil alone, the use of the grounded Faraday cage also typically removes the angular dependence of the observed noise. This means that the coil orientation can be determined by the relative orientation of the gradient coils and $\mathbf{B}_E$, thus ensuring the orthogonality of the gradient fields.

It was found that the effectiveness of the Faraday cage was only slightly reduced when the end plates of the copper box were removed (as shown in Figure 4.4) such that the resultant open-ended box was oriented collinear with the sinusoidal receiver coil. The substantial weight reduction of the Faraday cage achieved by removing the end caps is a very significant advantage and therefore the open-ended design is a good compromise between weight and effectiveness. It was also found that an open-ended box of 12 mm thick aluminium achieved similar screening results as the 10 mm thick copper box. The aluminium box is a much more attractive solution to the screening problem because, despite the increased wall thickness, the overall weight and cost of the aluminium Faraday cage will be greatly reduced when compared to the equivalent in copper.

Note that in all of the experiments reported in this thesis, the copper box pictured in Figure 4.4 was used. Following construction, it was found that the physical dimensions of this Faraday cage (260 mm x 220 mm x 300 mm) were not large enough to avoid eddy current problems associated with the switch-off of the polarizing coil and so a delay (typically 300 ms) is introduced between the switching

of the prepolarization field and the excitation of the signal to ensure that these eddy currents do not disrupt the homogeneity of the Earth's field during signal detection.

Figure 4.4 A photo of the Terranova-MRI probe within an open-ended copper box used as a Faraday cage. This copper box is connected to the ground end of the B_1 connector to ensure a common ground for the system.

4.6. Field Homogeneity

The second reason that EFNMR has traditionally been performed outdoors is because of the degradation in the natural homogeneity of the Earth's magnetic field which occurs due to the proximity of ferrous or magnetic materials in an indoor environment. This can be overcome by a combination of a judicious placement of the apparatus and the use of first-order shimming.

In order to ensure a high degree of field homogeneity, it is important to place the probe portion of the apparatus on a table or stand that is free of ferrous materials and to remove to a distance of 1 – 2 m any objects likely to disturb the field homogeneity. It is often advisable to place the probe roughly in the centre of a room,

at a significant distance from all walls including the ceiling and the floor.

As described in Chapter 2, shimming is the process by which a set of specially designed coils are used to generate weak, spatially varying magnetic fields that oppose any inhomogeneities in the underlying static magnetic field. The simplest set of shims, so-called first-order shims, vary the magnitude of the magnetic field linearly in space. In the case of Earth's field NMR, it has been found that once the above described isolation of the apparatus is achieved, the dominant inhomogeneities in the field are linear and so can be effectively countered by first-order shimming. The three orthogonal gradients designed for imaging and described above were found to be well suited for the purpose of first-order shimming.

4.6.1. Auto-shimming

As most experienced NMR spectroscopists know, shimming can often be a very tedious and time consuming process. In order to obtain an efficient and consistent set-up procedure for the Terranova-MRI, an auto-shimming routine was developed. This method employs a simple pre-polarize, pulse and collect experiment during which small currents, on the order of a few mA, are output to the three orthogonal gradient coils, which act as first-order shims. The resultant FID and spectrum can be used to assess the quality or effectiveness of the given shim current values. As the overall homogeneity of the field increases the time domain decay constant, T_2*, will lengthen. This results in a decrease in the linewidth of the peak in the frequency domain as it tends toward the so-called "homogeneous" or "T_2-limited" linewidth. As the linewidth decreases the peak height will increase, such that the totally peak integral remains roughly constant. Therefore the height of the peak in the frequency domain provides a convenient measure of the quality of the shim.

The optimal shim current values are obtained by repeating the pre-polarize, pulse and collect experiment with different shim current values until the peak height is maximized. In order to arrive at the optimal shim values in an efficient and timely manner, a modified bisection approach is used. At the beginning of the experiment, the user defines a search range, ΔI_{max}, a final precision value, ΔI_{min}, and initial shim values, I_x, I_y and I_z. As a first point of reference an experiment is performed with the initial shim values and the peak height, h_{max}, is recorded. An initial current step is

defined as $\Delta I = 0.25*\Delta I_{max}$. Starting first with I_x the shim current is updated to $I_x' = I_x + \Delta I$. An experiment is performed and the peak height, h_{new}, is compared to the reference, h_{max}. If $h_{new} > h_{max}$, I_x is replaced with I_x', h_{max} is replaced with h_{new} and the process is repeated with I_y. If $h_{new} < h_{max}$ the shim current is updated to $I_x' = I_x - \Delta I$ and another experiment is performed. Again, if $h_{new} > h_{max}$ for this new shim current value, I_x is replaced with I_x' and h_{max} is replaced with h_{new}. If $h_{new} < h_{max,}$ I_x and h_{max} remain unchanged and the process is repeated with I_y and then I_z. Following the I_z step, the search window is reduced by 25%: $\Delta I \rightarrow 0.75*\Delta I$. The search window is reduced by three quarters instead of a half to allow for the possibility of misidentifying the quality of a certain set of shim current values due to noise or other sources of external interference. The autoshim experiment completes when the search window is less than the target precision stipulated by the user, $\Delta I < \Delta I_{min}$. Visual progress of the autoshim experiment is provided by a plot of peak height, h_{new}, as a function of iteration number.

If a good initial guess of the optimal shim values is unavailable this macro typically takes 10 to 15 minutes to complete. However, in day to day use when the apparatus is not moved significantly and so a good initial guess is available, a quick autoshim can be used to optimize the linewidth in just a few minutes. For a large sample of tap water with a T_2 of 2 s, a linewidth of better than 0.5 Hz is routinely obtained. The T_2 limited linewidth for water with a T_2 of 2 s is 0.16 Hz.

$$\Delta f = \frac{1}{\pi T_2} = 0.16 Hz$$

A linewidth of better than 0.5 Hz for water in a field of 54 μT, therefore, corresponds to a residual inhomogeneity of less than 25 nT (467 ppm).

Presented in Figure 4.5 are sample ^{1}H FIDs (and corresponding spectra) acquired in the Earth's field before (Figure 4.5a) and after (Figure 4.5b) auto-shimming. Note the concurrent increase in resolution and sensitivity achieved through the act of shimming; i.e. the 10-fold decrease in linewidth from 2 Hz to 0.2 Hz results in a concurrent 10-fold increase in peak height from 0.4 to 4 (x 10^5 a.u.). In this way a good shim is essential to optimizing both sensitivity and resolution.

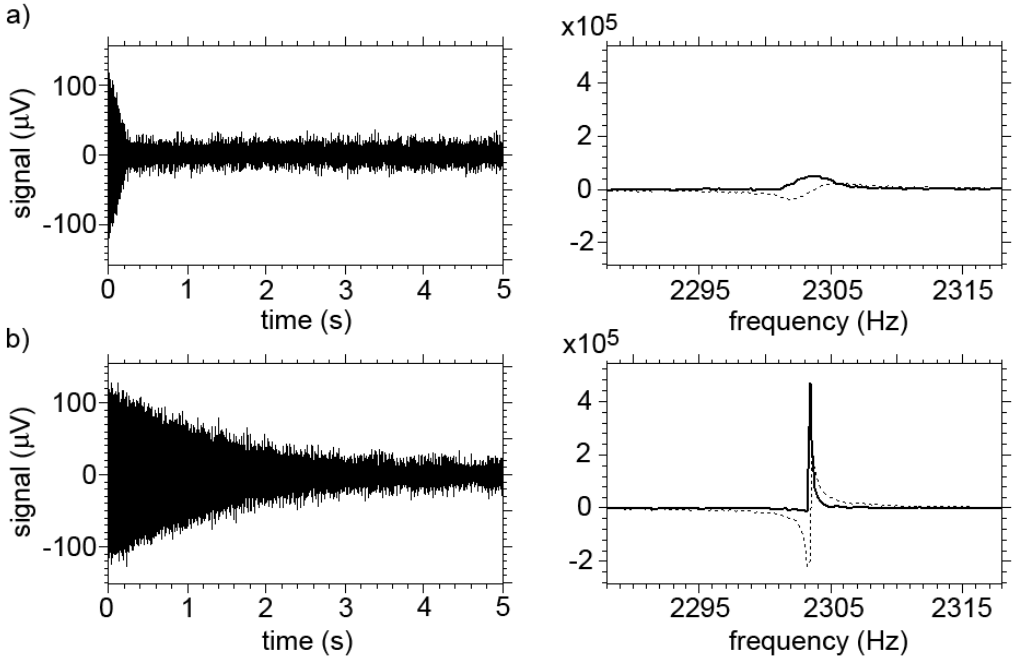

Figure 4.5 (a) A sample ^{1}H EFNMR FID and corresponding spectrum acquired prior to running the auto-shim routine. The linewidth is approximately 2 Hz. (b) A ^{1}H EFNMR FID and corresponding spectrum acquired after optimization of the shim currents using the auto-shimming routine. The linewidth is approximately 0.2 Hz.

4.7. Temporal Field Stabilization

4.7.1. Temporal Drift of Earth's Field

Another feature of the Earth's magnetic field that presents a challenge to NMR and MRI alike is that there exist temporal changes in the magnitude of B_E on the order of tens of nanotesla, changes which can occur on a time scale of hours or even minutes. These daily, or diurnal, variations are caused by electric currents induced in the Earth by currents in the ionosphere [62]. In imaging, this temporal instability of the detection field can introduce a frequency shift and phase drift between successive lines in k-space resulting in artifacts in the reconstructed image. In spectroscopy this temporal instability significantly degrades the resolution of the resultant spectra, can cause significant phase artifacts in multi-dimensional experiments and reduces the effectiveness of signal averaging.

4.7.2. Frequency Tracking

High resolution NMR is naturally well suited to detecting small changes in frequency. Therefore it is possible to track any changes in the Earth's magnetic field with a high degree of precision through the use of a reference scan interleaved into any multi-step pulse sequence.

There are several ways to process this reference scan in order to obtain a measure of the observed frequency drift. The simplest approach is to record the frequency position of the maximum of the sample peak in the spectrum. In order to improve the resolution of this approach without resorting to excessively long acquisition times, the FID can be zero-filled, i.e. padded with trailing zeros to artificially increase the spectral resolution upon Fourier transformation. There are a few drawbacks to this simple approach. First, a very high SNR is required to obtain a good measure of the frequency and second, if the line-shape is not symmetrical it is difficult to use this method to obtain the true central frequency of the peak. Third, if the sample has a spectrum composed of several different peaks this is not a very efficient use of the available signal.

A slightly more complicated, but computationally straight forward, approach is to use a cross-correlation. The cross-correlation function can be thought of as a measure of the similarity of two functions with a time lag, or in our case a frequency shift, between them. Mathematically the cross-correlation, $C(\omega)$, between two functions $f(\omega)$ and $g(\omega)$ can be written as in Eq. 4-1, where $\circ$ denotes a cross-correlation and f^* denotes the complex conjugate of f.

$$C(\omega) = f(\omega) \circ g(\omega) = \int_{-\infty}^{\infty} f^*(\omega') g(\omega' + \omega) d\omega' \qquad 4\text{-}1$$

The maximum of this cross-correlation between f and g will occur at the frequency shift, ω, for which the spectra are the most similar. Therefore the frequency offset obtained from the maximum of the cross-correlation function provides a measure of the frequency drift measured not from the single datum point at the top of a single spectral peak but rather from every point in the spectrum. In this

way, the SNR performance of the cross-correlation method is superior to that of the peak height approach in cases of spectra with either (a) more than one peak or (b) a single broad and asymmetrical peak.

The calculation of a cross-correlation between two spectra is greatly facilitated by the use of the Fourier Transform (FT) cross-correlation theorem. This theorem states that the cross-correlation of two functions (in frequency space) is equal to the FT of the product of the complex conjugate of the inverse FT of the first function and the inverse FT of the second function. This is written mathematically in Eq. 4-2, where the functions F(t) and G(t) are defined by Eq. 4-3, $FT\{\}$ denotes a Fourier transform, $FT^{-1}\{\}$ denotes an inverse Fourier transform, $\circ$ denotes a cross-correlation, and $F^*(t)$ is the complex conjugate of $F(t)$.

$$C(\omega) = f(\omega) \circ g(\omega) = FT\{F^*(t)G(t)\} \qquad 4\text{-}2$$

$$F(t) = FT^{-1}\{f(\omega)\}$$
$$G(t) = FT^{-1}\{g(\omega)\} \qquad 4\text{-}3$$

.

In this cross-correlation method for frequency tracking, a target spectrum obtained at the beginning of the measurement is stored and cross-correlated with all subsequent reference spectra to track any frequency drift. Using the FT cross-correlation theorem, $C(\omega)$ is easily calculated from the complex conjugate of the FID of the target spectrum and the FID of the reference spectrum. As this method takes into account every point in the spectra, it is advantageous from an SNR standpoint to compare only a relevant frequency window, which can be easily extracted from the full spectrum prior to data analysis.

On the left in Figure 4.6 two narrow, high SNR (~270) ^{1}H EFNMR spectra of a 300 mL water sample are presented. These spectra are shifted in frequency relative to one another by 1 Hz. This frequency shift was achieved by changing the current in the B_0 lock coil between measurements (see section 4.7.4 for details on the B_0 lock coil). On the right is the cross-correlation function of these two spectra, calculated

using the Fourier theorem in Eq. 4-2. The peak of the cross-correlation function occurs at a frequency offset of 1 Hz, which reflects the shift observed between the two spectra on the left. In this example, where the spectra have good SNR, are well resolved and contain a single intense peak, it would be expected that a simple peak maximum algorithm would determine the frequency drift as reliably as the cross-correlation method.

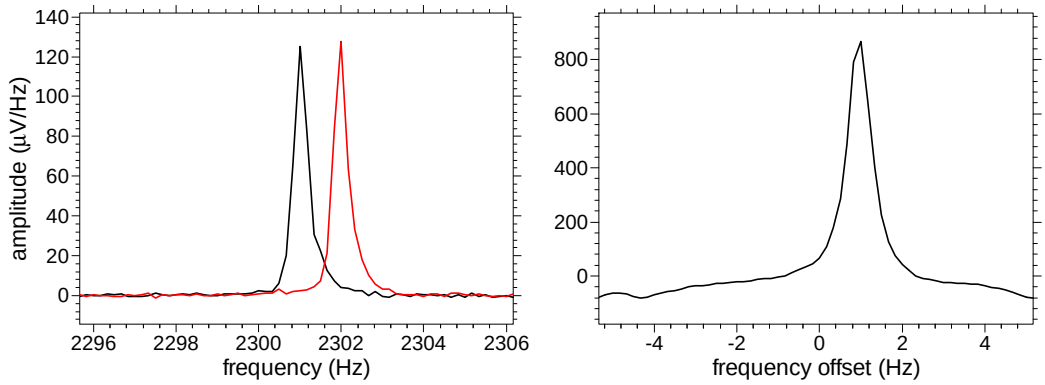

Figure 4.6 Two example ^{1}H EFNMR spectra of water shifted relative to each other in frequency by 1 Hz (left) and the cross-correlation function of these spectra (right) calculated using the Fourier theorem in Eq. 4-2.

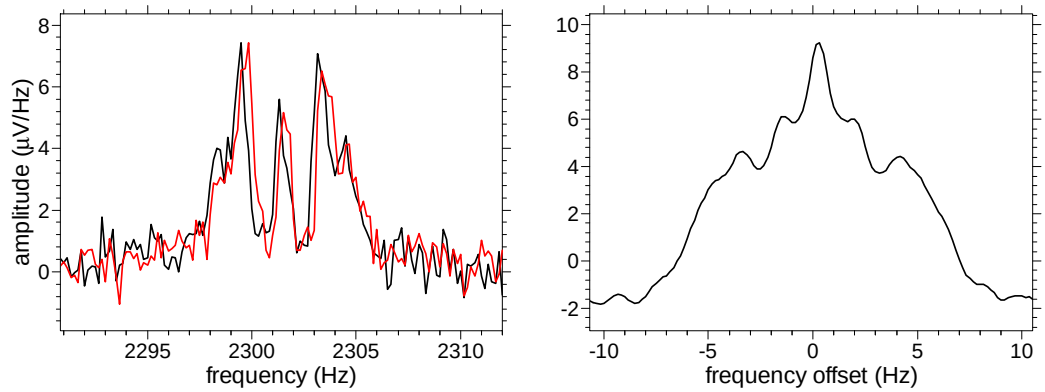

Figure 4.7 Two example ^{1}H EFNMR spectra of pure diethylphosphite, shifted relative to each other in frequency (left) and the cross-correlation function of these spectra (right) calculated using the Fourier theorem in Eq. 4-2.

Now consider the case depicted in Figure 4.7. The ^{1}H EFNMR spectra on the left were acquired of 300 mL of pure diethylphosphite which has a very complicated spectrum and consequently much lower SNR than the water example in Figure 4.6.

Looking at these spectra, it is readily apparent that simply monitoring the change in the frequency at which the maximum peak height occurs will not accurately track the drift of the Earth's field because there is a high probability of the algorithm sometimes choosing the peak around 2299 Hz as the maximum and sometime choosing the peak around 2304.5 Hz as the maximum. However if we use the cross-correlation method we see that the cross-correlation function (on the right in Figure 4.7) has a single well defined maximum at the frequency offset of the two spectra. Therefore using a cross-correlation we obtain a robust measure of the frequency drift.

4.7.3. Frequency Drift in Imaging

In imaging applications we found that a measure of Earth's field drifts can be used to set experimental time limits such that no field drift correction is required.

In order to determine these experimental time constraints it is important to first understand the effect of the temporal changes in B_E on an image. To this end, we consider the effect of small changes in Larmor frequency, $\Delta\omega_n$, on a typical two dimensional imaging experiment, where n is an integer denoting the phase encode gradient step.

First we consider fluctuations in B_E on a time scale of milliseconds. Such fluctuations, occurring during the acquisition of a single transient, will cause a broadening of the line in the frequency domain and therefore limit the minimum achievable frequency resolution in the read or directly detected dimension of an image. The extent of this broadening, and hence the frequency limitation, can be assessed using the acquisition of a single transient and observing the resultant frequency spectrum.

Next we consider the longer time fluctuations, occurring over minutes and hours. For the purpose of a discussion of these longer characteristic time fluctuations we define a phase evolution time, t_0. This is the time during which the spins acquire a phase offset due to the frequency shift, $\Delta\omega_n$. This phase evolution time is dependent on the imaging pulse sequence employed.

Let t be the time as measured from the centre of the echo signal, τ_E be the time between the 90˚ and 180˚ pulses, G_x be the read gradient amplitude and k_y be the k-

space encoding vector in the primary phase encode direction. The signal, as a function of t and k_y, is shown in Eq. 4-4.

$$S_n(t,k_y) = \iint \rho(x,y)\exp(i\gamma G_x xt)\exp(i\Delta\omega_n(t+t_0))\exp(i2\pi k_y y)dxdy$$

4-4

In the read direction the k-space encoding vector is defined as follows.

$$k_x = \frac{1}{2\pi}\gamma G_x t$$

Therefore the signal can be re-written as shown in Eq. 4-5.

$$S_n(k_x,k_y) = \iint \rho(x,y)\exp\left(i2\pi k_x\left(x+\frac{\Delta\omega_n}{\gamma G_x}\right)\right)\exp(i\Delta\omega_n t_0)\exp(i2\pi k_y y)dxdy$$

4-5

.

Taking the inverse Fourier transform with respect to k_x yields the expression given by Eq. 4-6.

$$FT_{k_x}^{-1}\{S_n(k_x,k_y)\} = \int \rho(x-\frac{\Delta\omega_n}{\gamma G_x},y)\exp(i\Delta\omega_n t_0)\exp(i2\pi k_y y)dy$$

4-6

.

Therefore the consequence of a shift in the Larmor frequency of $\Delta\omega_n$ between successive lines in k-space is a shift of $\frac{\Delta\omega_n}{\gamma G_x}$ in the image space read dimension and a phase shift of $\Delta\omega_n t_0$.

Consider first the effect on the read dimension. The pixel size, Δx, is given by the field of view (FOV_x) divided by the number of points in the read dimension (N_{read}). If the shift in the image due to drift in the Earth's magnetic field is less than the pixel size then no image artifacts will results from this shift. Therefore we require

Eq. 4-7 to be fulfilled.

$$\frac{\Delta\omega_n}{\gamma G_x} < \frac{FOV_x}{N_{read}} \qquad 4\text{-}7$$

If we consider the magnitude of the Earth's field to have a maximum rate of change with respect to time, dB_E/dt, then we can define the following maximum rate of change, with respect to time, of the Larmor frequency: $\frac{df}{dt} = \frac{\gamma}{2\pi}\left|\frac{dB_E}{dt}\right|$. This quantity can be used to define a condition for the maximum total experiment time, as shown in Eq. 4-8.

$$T_{\max} < \frac{\gamma G_x FOV_x}{2\pi \dot{f} N_{read}} = \frac{1}{t_{acq}\frac{df}{dt}} \qquad 4\text{-}8$$

The simplified form on the right hand side of Eq. 4-8 uses Eq. 4-9 as the definition of the read gradient strength.

$$G_x = \frac{2\pi N_{read}}{\gamma t_{acq} FOV_x} \qquad 4\text{-}9$$

Now consider the phase encode dimensions. The phase shift $\Delta\omega_n t_0$ is proportional to the time t_0 and therefore is dependent on the choice of pulse sequence. Consider the two pulse sequences in Figure 4.8. In the case of the spin-echo pulse sequence (Figure 4.8a) the phase offset acquired during the first τ_E time period is unwound for all frequencies during the second τ_E time period, following the 180° pulse. Therefore the phase evolution time, t_0, is zero. Consequently, for spin-echo imaging we need only be concerned with the read dimension shift (Eq. 4-8).

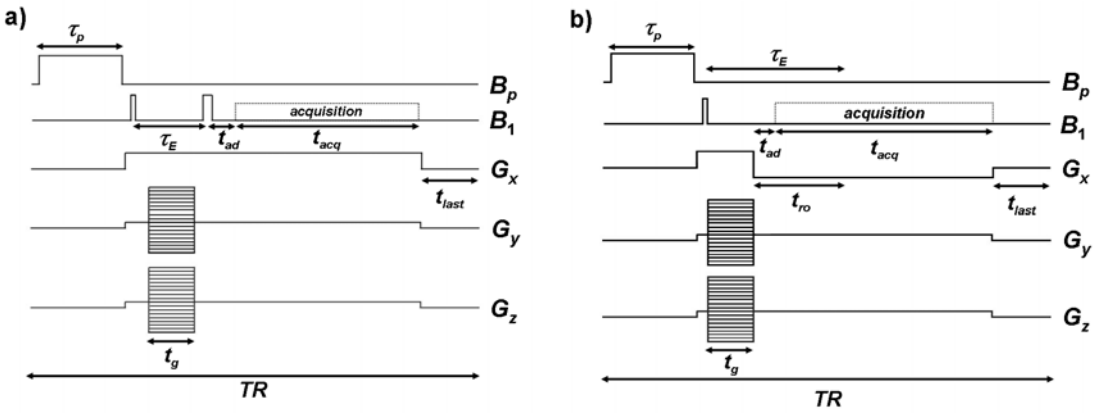

Figure 4.8 (a) Spin-echo imaging pulse sequence. (b) Gradient-echo imaging pulse sequence.

In the case of the gradient-echo pulse sequence (Figure 4.8b) a phase offset due to a change in the Larmor frequency is acquired throughout the τ_E time period between excitation and the centre of the echo. Thus $t_0 = \tau_E$ and the phase offset term is non-zero. We require that the phase drift over the whole experiment be much less than 2π. Therefore we define a factor α, which takes values less than one, to quantify the extent to which the total phase drift must be less than 2π. The required value of α will be set by the available signal-to-noise ratio and the need to keep image artifacts below the noise level.

Accordingly, the total phase drift over the experiment must satisfy Eq. 4-10.

$$\Delta\omega_n \tau_E < 2\pi\alpha$$

4-10

In terms of the maximum rate of change of the Larmor frequency with respect to time, $\frac{df}{dt} = \frac{\gamma}{2\pi}\left|\frac{dB_E}{dt}\right|$, the maximum total experiment time for a gradient echo imaging sequence, T_{max}, is given by Eq. 4-11.

$$T_{\max} < \frac{\alpha}{\left(\tau_E \frac{df}{dt}\right)}$$

4-11

Notice that Eq. 4-11 has the same form as the read dimension constraint, Eq. 4-8, scaled by a factor β, where $\beta = \frac{t_{acq}}{\tau_E}\alpha$. In the simplest implementation of gradient echo $t_{acq} = \tau_E$ and so $\beta = \alpha$. However, it is common to reduce τ_E by employing a large amplitude, short duration initial gradient pulse followed by longer duration, low amplitude gradient pulse during echo acquisition. This is done to improve SNR and can also slightly improve the total experiment time constraint because in this case, $\tau_E < t_{acq}$ and so β will be greater than α.

The choice of the α factor is experiment specific. If there is a random distribution of phase shifts between lines in k-space, the image will suffer from ghosting artifacts in the phase dimension. If the phase shifts correspond to a linear change in Larmor frequency, the image will be translated in the phase dimension. In the former case, if the smearing of image intensity is less than the baseline noise in the image then no artifacts will be observed. The SNR of the image will simply appear reduced. In the second case, if the extent of the translation in the phase dimension is small compared to the pixel size then no artifacts will be observed.

4.7.4. Frequency Stabilization using a B_0 Lock

While we can, in some cases, limit our total experiment time to avoid the observable manifestation of the effects of temporal field drift in imaging, there are many other NMR experiments, such as multi-dimensional spectroscopy pulse-sequences, which are far more sensitive to temporal drifts in the Earth's field. In these cases we must actively correct for this drift in some way in order to optimize resolution and information content.

In work on Earth's Field NMR imaging by Stepisnik et al. [22] and Mohoric et al. [22; 24; 25], a reference coil, coupled with heterodyne detection, was used to compensate for any drift in the Larmor frequency during an imaging experiment. This method provides a good way of tracking the changes in frequency concurrently with the EFNMR experiment but the post-processing mixing stage does not correct for phase artifacts accrued during evolution times in multi-dimensional spectroscopy experiments. Therefore a different approach is required to solve this problem.

As a result of the phase artifact problem in multi-dimensional experiments, which include evolution periods as well as signal detection periods, it is essential that the nuclear spins experience a constant background magnetic field. Therefore any temporal changes in the Earth's magnetic field need not only to be tracked but also need to be removed. This can be achieved by an appropriately designed B_0 lock coil, which produces a small offset field which can be used to oppose any drift in the Earth's field.

The design requirements for a B_0 lock coil for the Earth's field are three-fold: (1) it must be tunable by means of a current value under software control, (2) it must be able to generate a B_0 field offset equal to the largest observed fluctuation in the Earth's field (100 nT) and (3) the homogeneity of the B_0 offset field must be such that target linewidths of better than 0.1 Hz (2 nT) can be achieved. These conditions require only a 2% field homogeneity, which is easily realized using modern coil design techniques.

One such coil, designed by Mark Hunter from the NMR group at Victoria University of Wellington, a multi-turn saddle coil, is pictured in Figure 4.9. This coil is designed to generate a field homogeneous to better than 2 nT (0.1 Hz) for fields of ± 117 nT (± 5 Hz) over a 100 mm sample diameter.

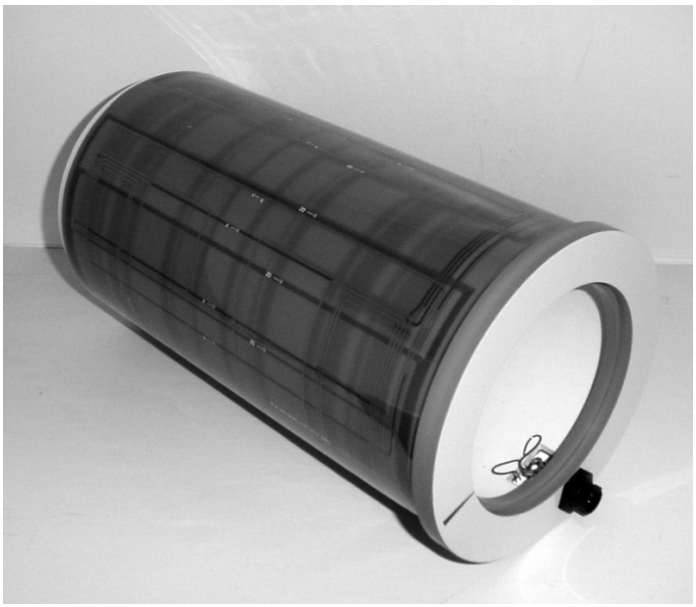

Figure 4.9 Photo of a B_0 lock coil used to counter temporal drift in the Earth's magnetic field.

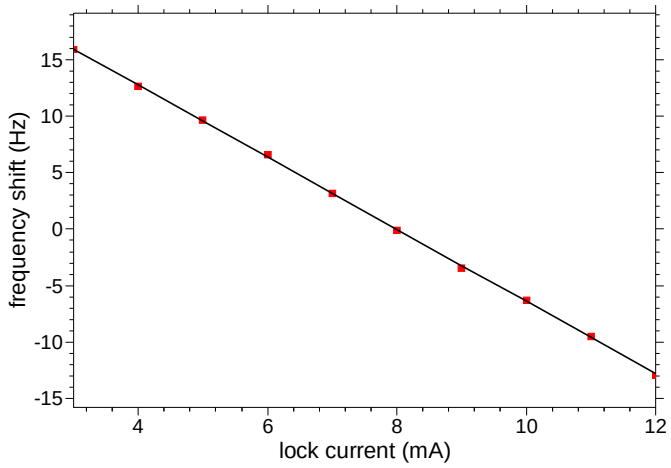

Figure 4.10 A calibration curve for the B_0 lock coil (red squares) overlaid with a linear fit to determine the calibration constant (black line). The calibration constant is -0.313 ± 0.003 mA/Hz.

For a well designed coil, the linearity of the relationship between the current and the B_0 lock field produced over the range of offset fields required is such that no iteration is necessary in order to compensate for the observed field drift. The field shift is simply quantified using a single reference scan and the current through the B_0 lock coil is adjusted according to a linear calibration curve. A sample calibration curve for the coil pictured in Figure 4.9 is shown in Figure 4.10.

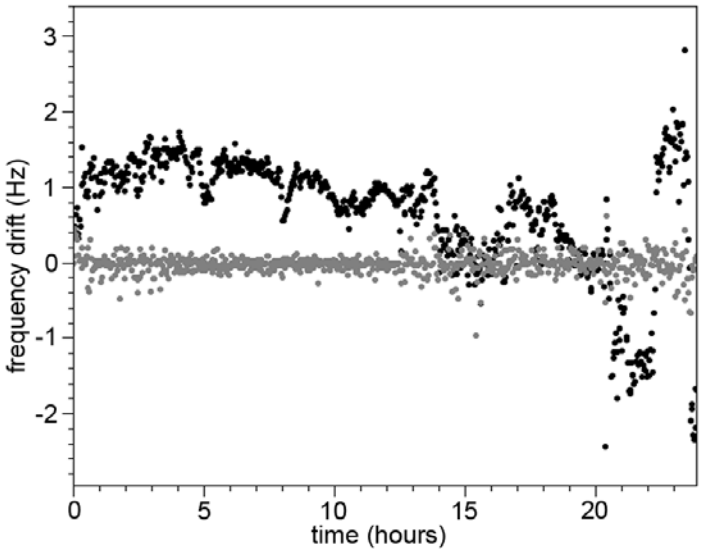

Figure 4.11 A comparison of the observed frequency drift of NMR signals acquired over a period of 24 hours both with (gray) and without (black) the use of field stabilization.

Figure 4.11 presents a the Larmor frequencies of a series of spectra acquired every minute over a period of 24 hours, both with and without the use of the B_0 lock. The sample used was a 500 mL bottle of tap water. The Larmor frequencies of the spectra acquired with frequency locking (shown in gray) is stable to within approximately ±0.3 Hz, which was the linewidth of the water peak in a single spectrum. Meanwhile, the frequency of the series of spectra acquired without frequency locking (shown in black) experiences variations on the order of ±2 Hz.

CHAPTER 5. Sensitivity Enhancement

5.1. Introduction

As noted in previous chapters, EFNMR enjoys the advantage of sub-hertz spectral resolution over large (> 100mL) sample volumes due to the natural homogeneity of the Earth's field but it suffers from low sensitivity, a consequence of the approximate B_0^2 dependence of signal-to-noise ratio (SNR) on field strength, which for the Earth's field is on the order of 50 μT (0.5 G). Therefore the viability of most applications of EFNMR depends on devising clever schemes for sensitivity enhancement.

Sensitivity enhancement has two parts: decreasing the detected noise per unit signal and increasing the available signal. The former is achieved in Earth's field NMR through screening of external interference (pick-up noise reduction), as discussed in Chapter 4, or through the use of non-faraday detection as mentioned in Chapter 3. The latter component of sensitivity enhancement, which we will call signal enhancement, is achieved in NMR through increasing the available magnetization or polarization. Three approaches to signal enhancement were investigated as part of this thesis: prepolarization, dynamic nuclear polarization and hyperpolarization via optical pumping.

5.2. Prepolarization

5.2.1. Theory

Conceptually, one of the simplest approaches to signal enhancement is to pre-polarize the sample using a strong but not necessarily homogeneous magnetic field prior to excitation and detection in a weaker but highly homogeneous magnetic field. In the pulse sequence presented in Figure 5.1, the sample is exposed to the polarizing field, B_{polz}, for a period, t_{polz}, during which it comes to either full or partial thermal equilibrium with this field. This prepolarization field is then removed from the sample and following a delay, t_d, the enhanced polarization is excited and detected in the highly homogeneous Earth's magnetic field, B_E,.

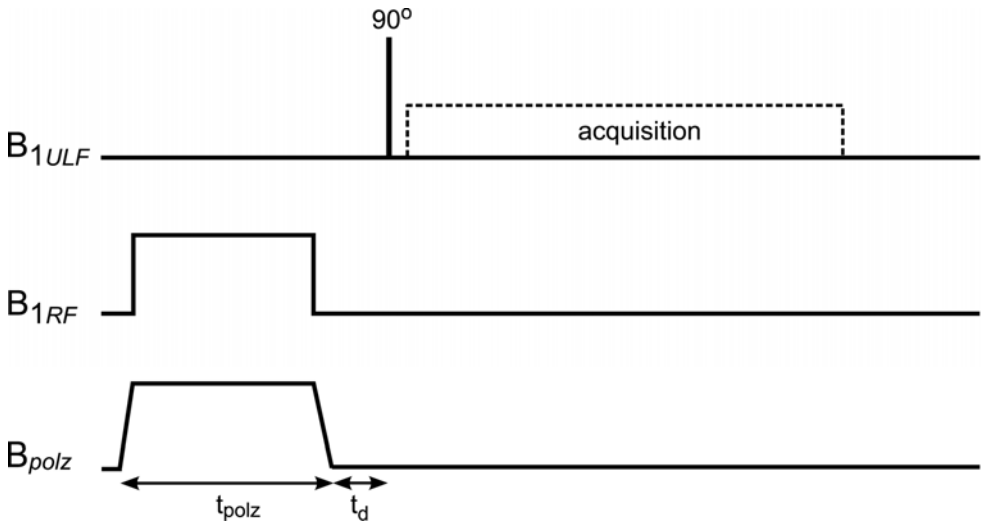

Figure 5.1 Basic pre-polarize, pulse and collect pulse sequence. The prepolarization pulse, B_{polz} and/or the DNP irradiation, B_{1RF}, are applied for a fixed period t_{polz}. Following an adiabatic switch-off of the pre-polarization pulse and a delay t_d, a 90° ULF excitation pulse, B_{1ULF}, is applied and the subsequent precessing transverse magnetization is detected.

The maximum achievable enhancement factor (*EF*) relative to thermal polarization in the Earth's field is given by Eq. 5-1. Note that this expression assumes that the sample is allowed to come to full thermal equilibrium in the prepolarization field, i.e. $t_{polz} \geq 5T_1$.

$$EF = \frac{B_{polz}}{B_E} e^{-\frac{t_d}{T_1}}$$

5-1

Eq. 5-1 indicates that in order to achieve significant enhancements the polarization field must be large relative to the Earth's field and the delay time, t_d, between the polarization phase and the detection phase of the pulse sequence must be very short compared to T_1. In the context of multi-dimensional spectroscopy it is very important that the enhancement factor is constant between successive transients. Therefore, it is imperative that the polarizing field strength, B_{polz}, the polarizing time, t_{polz}, and the prepolarization to detection delay, t_d, are constant.

In any prepolarization scheme, the prepolarization field can be generated by either an electromagnet or a permanent magnet array. We start by considering the case of an electromagnet, which is very advantageous for a variety of reasons. First, it is relatively easy and cost effective to construct an electromagnet which is not particularly homogeneous, that is with a homogeneity on the order of a few percent rather than a few parts per million (ppm). Second, the field of the electromagnet can be switched on and off as required, providing the user with sufficient control over B_{polz}, t_{polz} and t_d to ensure a constant enhancement factor between transients. Third, the field is under software/spectrometer control and therefore is easily used in multi-dimensional experiments. There are, however, several practical limitations. The first concern is field strength. In order to achieve large magnetic fields with an electromagnet, large currents must be used and this can result in significant resistive heating in the coil. Coil heating can be dealt with through the use of water cooling but this greatly complicates the overall system and limits its size, cost and portability. The second concern, which is also a matter of resistive heating, is the polarization time. Long T_1 samples will require long polarization times which will enhance the problem of coil heating. The final practical concern is associated with the rapid switching of a strong polarizing field. If Faraday screening is employed to reduce pick-up of external ULF noise, rapid switching of a strong polarizing field will give rise to strong eddy currents in the screen and so the delay time, t_d, will need to be sufficiently long so that there are no time dependent disruptions to the homogeneity of

the Earth's field during detection.

As shown by Appelt *et al.* [57], an attractive solution for single-shot experiments is the use of a permanent magnet Halbach array for prepolarization. If high homogeneity is not a concern, Halbach arrays with field strengths of up to 2 T can be constructed without much difficulty. A 300 mT Halbach array, built by Ben Parkinson at Victoria University of Wellington for use in this thesis, is pictured in Figure 5.2.

One of the significant advantages of the Halbach design is that these arrays are largely self screening and so can be located within a few meters of the Earth's field NMR probe without significantly disrupting the homogeneity of the detection field. If shimming is available, the Halbach array can be located as close as 1-1.5 m from the EFNMR probe without disrupting the sub-hertz spectral resolution. A photo showing the position of the 300 mT Halbach array relative to the EFNMR probe is presented in Figure 5.3.

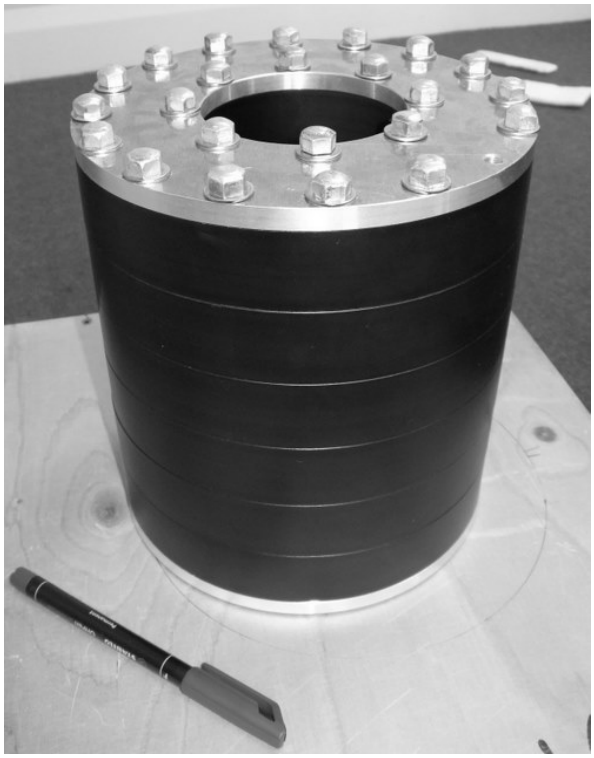

Figure 5.2 A photo of a 300 mT Halbach array with a 80 mm inner diameter. This permanent magnet array was designed and built by Ben Parkinson of VUW. The weight of the magnet is about 5 kg.

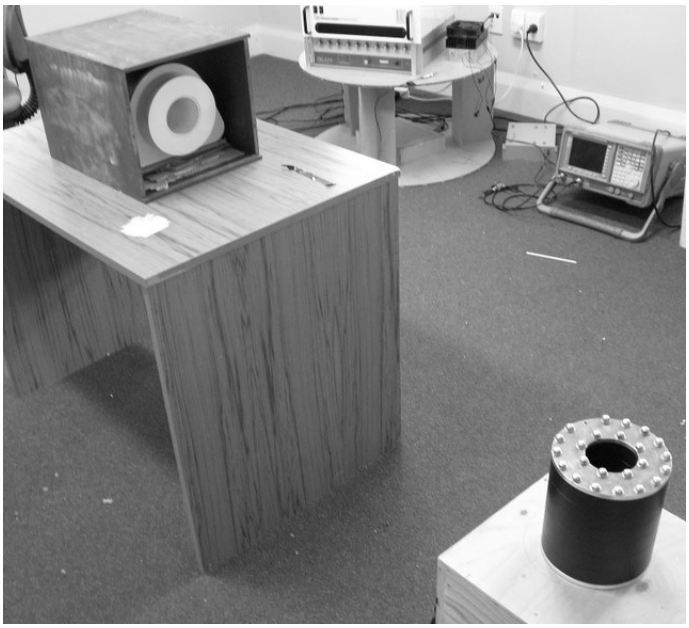

Figure 5.3 A photo of the position of the Halbach array relatvie to the Earth's field NMR probe.

Another attractive feature of the permanent magnet approach is that all of the electromagnet concerns of resistive heating and field switching are removed with the use of a Halbach array.

The most significant disadvantage of the Halbach prepolarization approach lies in the transfer of the sample from the Halbach array to the EFNMR probe. In reference [57] this transfer was done manually and transfer times were on the order of seconds. In a multi-dimensional experiment, sample transport from Halbach to EFNMR probe would be very challenging to automate, especially in terms of maintaining a constant polarization time and transfer time. Therefore this is not an attractive solution for the purposes of multi-dimensional experiments, such as the spectroscopy experiments discussed in Chapter 8.

5.2.2. Comparison: Halbach and Electromagnet Prepolarization

Figure 5.4 presents a comparison of two ^{1}H EFNMR spectra acquired of 500 mL of tap water, with $T_1 \approx T_2 \approx 2$ s, using 18.7 mT electromagnetic prepolarization (black) and 300 mT Halbach prepolarization (red). The transfer time, t_d, for the Halbach spectrum was approximately 1 s. In the electromagnet spectrum, the delay

time, t_d, between the switch-off of the prepolarization coil and the signal excitation was 350 ms. The observed SNR advantage of the Halbach prepolarization over the electromagnet prepolarization in this example is 10.3. The theoretical relative enhancement, as predicted by Eq. 5-1, is 10.5.

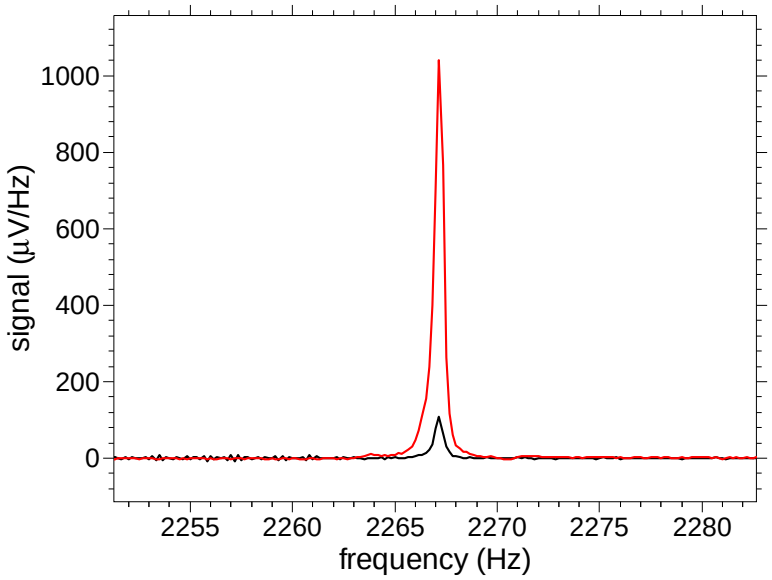

Figure 5.4 Comparison of two ^{1}H EFNMR spectra of 500 mL of water. The spectrum in red was obtained using a 300 mT Halbach for pre-polarization. The spectrum in black was obtained using an 18.7 mT electromagnet for pre-polarization. The signal enhancement advantage of prepolarization with the Halbach relative to the electromagnet is 10.3.

5.3. Dynamic Nuclear Polarization (DNP)

5.3.1. Introduction

Dynamic Nuclear Polarization (DNP) can be defined as a technique for enhancing the polarization of a target nuclear spin, a ^{1}H nucleus for example, above its equilibrium thermal polarization by means of a net polarization transfer from an excited free electron spin. This polarization transfer is typically mediated by the Overhauser effect [63]. In most applications where DNP is used for signal enhancement, the free electron must be introduced into the sample via the addition of

a free radical. The most commonly used DNP free radicals are nitroxide radicals [64], such as 4-oxo-TEMPO.

The complete process of DNP can be broken down into three phases: (1) the excitation of the electron spins, (2) the polarization transfer between the excited electron spin and the target nuclear spin and (3) the detection of the enhanced nuclear polarization. The detection of the nuclear polarization, phase 3, is analogous to a typical NMR experiment and so requires no new investigation in this context.

The excitation of the electron spins, phase 1, can only be achieved and optimized through a thorough theoretical understanding of the energy levels and transition probabilities of the free electron spin system. The transfer of polarization between the electron spins and the target nuclear spins, phase 2, can be understood and quantified through a consideration of the so-called Solomon Equations [65].

5.3.2. Nitroxide Free Radicals in Ultra-low Magnetic Fields

For the purposes of this discussion of DNP in the Earth's magnetic field, the free radical 4-oxo-TEMPO containing ^{14}N at natural abundance (99.6%) will be considered, exclusively. Therefore, the intra-molecular free radical spin system under consideration contains a single free-electron spin, with a spin quantum number $S = ½$, and a single ^{14}N nuclear spin, with a spin quantum number $K = 1$. There exist a plurality of ^{1}H spins within the free radical molecule; however, these nuclear spins are far removed from the site of the free-electron. For the purposes of this discussion, any intra-molecular hyperfine coupling between the free electron and these ^{1}H nuclear spins present in the 4-oxo-TEMPO molecule will be considered to be negligible. The following theoretical treatment follows that of Guiberteau and Grucker [66].

For a given solvent-dependent hyperfine coupling constant, A, between the electron spin with angular momentum operator, **S**, and the nuclear spin with angular momentum operator, **K**, and in the presence of an external magnetic field $\mathbf{B}_0 = B_0\hat{z}$ the spin Hamiltonian can be written, in angular frequency units, as in Eq. 5-2.

$$\mathcal{H} = -\gamma_S B_o \mathbf{S}_z - \gamma_K B_o \mathbf{K}_z + A\mathbf{S} \bullet \mathbf{K}$$

5-2

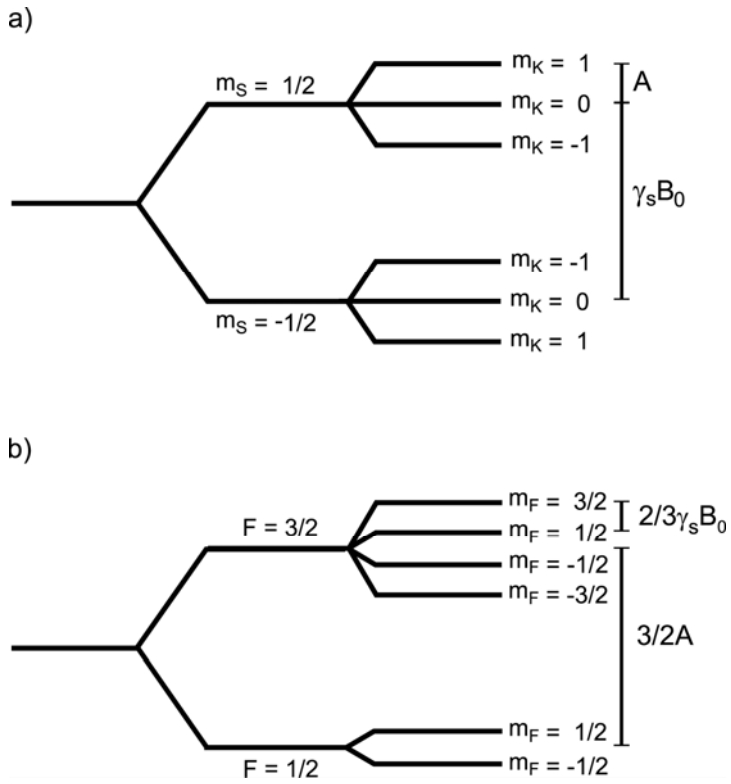

Figure 5.5 Energy level diagram for an unpaired electron spin, *S*, coupled to a ^{14}N nucleus, *K*, in (a) the high-field case where $\gamma_S B_0 >> A$ and (b) the ultra-low field case where $\gamma_S B_0 << A$.

The Hamiltonian in Eq. 5-2 is not diagonal in either of the product operator or the total angular momentum representations. In the high-field case (Figure 5.5a), where $\gamma_S B_0 >> A$, the product operator formalism, characterized by the spin quantum numbers m_S and m_K, is typically used and the hyperfine coupling term is treated as a perturbation to the dominant Zeeman terms. However, in ultra-low fields, such as the Earth's magnetic field (~50 μT) the hyperfine coupling term is strongly dominant (Figure 5.5b). Therefore, the diagonal representation is very closely related to the total angular momentum picture, characterized by the total angular momentum quantum number, *F*, and the total azimuthal spin quantum number, m_F, where $\mathbf{F} = \mathbf{S} + \mathbf{K}$. Due to this close association between the true diagonal representation of the Hamiltonian at very low fields and the total angular momentum picture, some aspects of this problem, the transition selection rules for example, can be best understood in terms of the total angular momentum basis. However, as most of the operations on the system will be applied exclusively to the electron spin, *S*, it is also useful to

maintain the connection between the more commonly used and more intuitive product operator formalism and the exact diagonal representation.

Accordingly, we can write down the six eigenfunctions of the spin Hamiltonian (Eq. 5-2) in terms of the product operator basis set (Eq. 5-3), where the constants α and β are defined by Eq. 5-4.

$$
\begin{aligned}
\left|1\right\rangle_{Diag} &= \left|\tfrac{1}{2},1\right\rangle_{SK} = \left|\tfrac{3}{2},\tfrac{3}{2}\right\rangle_{F} \\
\left|2\right\rangle_{Diag} &= \cos\alpha\left|\tfrac{1}{2},0\right\rangle_{SK} + \sin\alpha\left|-\tfrac{1}{2},1\right\rangle_{SK} \approx \left|\tfrac{3}{2},\tfrac{1}{2}\right\rangle_{F} \\
\left|3\right\rangle_{Diag} &= \cos\beta\left|\tfrac{1}{2},-1\right\rangle_{SK} + \sin\beta\left|-\tfrac{1}{2},0\right\rangle_{SK} \approx \left|\tfrac{3}{2},-\tfrac{1}{2}\right\rangle_{F} \\
\left|4\right\rangle_{Diag} &= \left|-\tfrac{1}{2},-1\right\rangle_{SK} = \left|-\tfrac{3}{2},-\tfrac{3}{2}\right\rangle_{F} \\
\left|5\right\rangle_{Diag} &= -\sin\beta\left|\tfrac{1}{2},-1\right\rangle_{SK} + \cos\beta\left|-\tfrac{1}{2},0\right\rangle_{SK} \approx \left|\tfrac{1}{2},-\tfrac{1}{2}\right\rangle_{F} \\
\left|6\right\rangle_{Diag} &= -\sin\alpha\left|\tfrac{1}{2},0\right\rangle_{SK} + \cos\alpha\left|-\tfrac{1}{2},1\right\rangle_{SK} \approx \left|\tfrac{1}{2},\tfrac{1}{2}\right\rangle_{F}
\end{aligned}
$$

5-3

$$
\begin{aligned}
\tan\alpha &= \frac{(\gamma_S-\gamma_K)B_0 - \tfrac{1}{2}A + \sqrt{\tfrac{9}{4}A^2 - A(\gamma_S-\gamma_K)B_0 + (\gamma_S-\gamma_K)^2 {B_0}^2}}{\sqrt{2}A} \\
\tan\beta &= \frac{(\gamma_S-\gamma_K)B_0 + \tfrac{1}{2}A + \sqrt{\tfrac{9}{4}A^2 + A(\gamma_S-\gamma_K)B_0 + (\gamma_S-\gamma_K)^2 {B_0}^2}}{\sqrt{2}A}
\end{aligned}
$$

5-4

It is important to note that while the above system of equations defines the eigenfunctions of the spin Hamiltonian, $\left|i\right\rangle_{Diag}$, exactly in terms of the product operator kets, $\left|m_S,m_K\right\rangle_{SK}$, for all values of A and B_0, they are only approximately related to the total angular momentum kets, $\left|F,m_F\right\rangle_{F}$. This approximate relationship is only appropriate for the ultra-low field case, where the hyperfine coupling term dominates the Hamiltonian, and is included in this treatment because it promotes an intuitive understanding of how a transition between the diagonal eigenstates relates to changes in the total angular momentum and azimuthal total angular momentum quantum numbers, F and m_F. In the case of $B_0 = 0$, the relationship between the diagonal and product operator kets and the total angular momentum kets becomes absolute and the coefficients $\sin\alpha$, $\cos\alpha$, $\sin\beta$ and $\cos\beta$ reduce to the expected values

given by the Clebsch-Gordan coefficients. In the opposite case, where $\gamma_S B_0$ becomes large compared to A, the coefficients $\cos\alpha$ and $\cos\beta$ tend to 1, while the coefficients $\sin\alpha$ and $\sin\beta$ tend to 0. The diagonal kets are, in this case, close to the product operator kets.

The eigenvalues, or energy levels, of the spin system, which correspond to the eigenfunctions listed above, are the diagonal elements of the Hamiltonian in the diagonal representation. Therefore the energy levels can be determined by applying the unitary transformation, $\mathbf{U}_{SK\to diag}$, between the diagonal and product operator representations to the Hamiltonian written in the product operator formalism. For transparency the product operator Hamiltonian matrix and the unitary transformation matrix are written explicitly below.

$$\mathcal{H}_{\mathrm{SK}} =$$

$$\begin{bmatrix}
\frac{A}{2}-\frac{\gamma_S B_0}{2}-\gamma_K B_0 & 0 & 0 & 0 & 0 & 0 \\
0 & -\frac{1}{2}\gamma_S B_0 & 0 & \frac{A}{\sqrt{2}} & 0 & 0 \\
0 & 0 & \frac{A}{2}-\frac{\gamma_S B_0}{2}+\gamma_K B_0 & 0 & \frac{A}{\sqrt{2}} & 0 \\
0 & \frac{A}{\sqrt{2}} & 0 & -\frac{A}{2}+\frac{\gamma_S B_0}{2}-\gamma_K B_0 & 0 & 0 \\
0 & 0 & \frac{A}{\sqrt{2}} & 0 & \frac{1}{2}\gamma_S B_0 & 0 \\
0 & 0 & 0 & 0 & 0 & \frac{A}{2}+\frac{\gamma_S B_0}{2}+\gamma_K B_0
\end{bmatrix}$$

$$\mathbf{U}_{\mathrm{SK}\to\mathrm{Diag}} = \begin{bmatrix}
1 & 0 & 0 & 0 & 0 & 0 \\
0 & \cos\alpha & 0 & 0 & 0 & -\sin\alpha \\
0 & 0 & \cos\beta & 0 & -\sin\beta & 0 \\
0 & \sin\alpha & 0 & 0 & 0 & \cos\alpha \\
0 & 0 & \sin\beta & 0 & \cos\beta & 0 \\
0 & 0 & 0 & 1 & 0 & 0
\end{bmatrix}$$

$$\mathcal{H}_{Diag} = \mathbf{U}_{SK\to Diag}\mathcal{H}_{SK}\mathbf{U}^{*}_{SK\to Diag} = \begin{bmatrix}
E_1 & 0 & 0 & 0 & 0 & 0 \\
0 & E_2 & 0 & 0 & 0 & 0 \\
0 & 0 & E_3 & 0 & 0 & 0 \\
0 & 0 & 0 & E_4 & 0 & 0 \\
0 & 0 & 0 & 0 & E_5 & 0 \\
0 & 0 & 0 & 0 & 0 & E_6
\end{bmatrix}$$

The expressions for the exact energy levels, which are valid for all values of A and B_0, are given by Eq. 5-5. (Note that these energy levels are written in angular frequency units.)

$$
\begin{aligned}
E_1 &= \tfrac{1}{2}A - \tfrac{1}{2}\gamma_S B_0 - \gamma_K B_0 \\
E_2 &= -\tfrac{1}{4}A - \tfrac{1}{2}\gamma_K B_0 + \tfrac{1}{2}\sqrt{\tfrac{9}{4}A^2 - A(\gamma_S - \gamma_K)B_0 + (\gamma_S - \gamma_K)^2 B_0^{\,2}} \\
E_3 &= -\tfrac{1}{4}A + \tfrac{1}{2}\gamma_K B_0 + \tfrac{1}{2}\sqrt{\tfrac{9}{4}A^2 + A(\gamma_S - \gamma_K)B_0 + (\gamma_S - \gamma_K)^2 B_0^{\,2}} \\
E_4 &= \tfrac{1}{2}A + \tfrac{1}{2}\gamma_S B_0 + \gamma_K B_0 \\
E_5 &= -\tfrac{1}{4}A + \tfrac{1}{2}\gamma_K B_0 - \tfrac{1}{2}\sqrt{\tfrac{9}{4}A^2 + A(\gamma_S - \gamma_K)B_0 + (\gamma_S - \gamma_K)^2 B_0^{\,2}} \\
E_6 &= -\tfrac{1}{4}A - \tfrac{1}{2}\gamma_K B_0 - \tfrac{1}{2}\sqrt{\tfrac{9}{4}A^2 - A(\gamma_S - \gamma_K)B_0 + (\gamma_S - \gamma_K)^2 B_0^{\,2}}
\end{aligned}
$$

5-5

In the total angular momentum regime, the dominant (zeroth order) transition energy term corresponds to a transition between F = 3/2 and F = 1/2, which is characterized by the hyperfine coupling constant multiplied by a factor of 3/2, as calculated below.

$$
\begin{aligned}
E_{F=\frac{3}{2}} &= \tfrac{A}{2}\big(F(F+1) - s(s+1) - k(k+1)\big) = \tfrac{A}{2}\big(\tfrac{15}{4} - \tfrac{3}{4} - 2\big) = \tfrac{1}{2}A \\
E_{F=\frac{1}{2}} &= \tfrac{A}{2}\big(F(F+1) - s(s+1) - k(k+1)\big) = \tfrac{A}{2}\big(\tfrac{3}{4} - \tfrac{3}{4} - 2\big) = -A \\
\Delta E &= E_{F=\frac{3}{2}} - E_{F=\frac{1}{2}} = \tfrac{3}{2}A
\end{aligned}
$$

In the product operator regime, the dominant (zeroth order) transition energy is given by a transition from m_S = -1/2 to m_S = +1/2. Naturally, this transition is characterized by the Larmor frequency for the electron, as demonstrated below.

$$
\begin{aligned}
E_{m_S=-\frac{1}{2}} &= -m_S\gamma_S B_0 = \tfrac{1}{2}\gamma_S B_0 \\
E_{m_S=\frac{1}{2}} &= -m_S\gamma_S B_0 = -\tfrac{1}{2}\gamma_S B_0 \\
\Delta E &= E_{m_S=-\frac{1}{2}} - E_{m_S=\frac{1}{2}} = \gamma_S B_0
\end{aligned}
$$

Figure 5.6 presents a plot of the exact energy levels of Eq. 5-5 over a range of values of B_0. This plot demonstrates the shift from the total angular momentum

regime at low B_0, where the zeroth order energy difference is (3/2)A (A = 2π*42 MHz in this and all subsequent calculations) to a product operator regime at larger values of B_0, where the zeroth order energy difference is $\gamma_S B_0$ (2π x 280 MHz at 10 mT). The Earth's magnetic field is typically on the order of 50 μT and therefore falls into the total angular momentum regime. However, the prepolarization field used with the Earth's field apparatus, at 18.7 mT, is well into the product operator regime. Therefore it is important to continue to work with the exact expressions of the diagonal representation in order to maintain the ability to compare the potential of the DNP effect in both the Earth's field and the prepolarizing field.

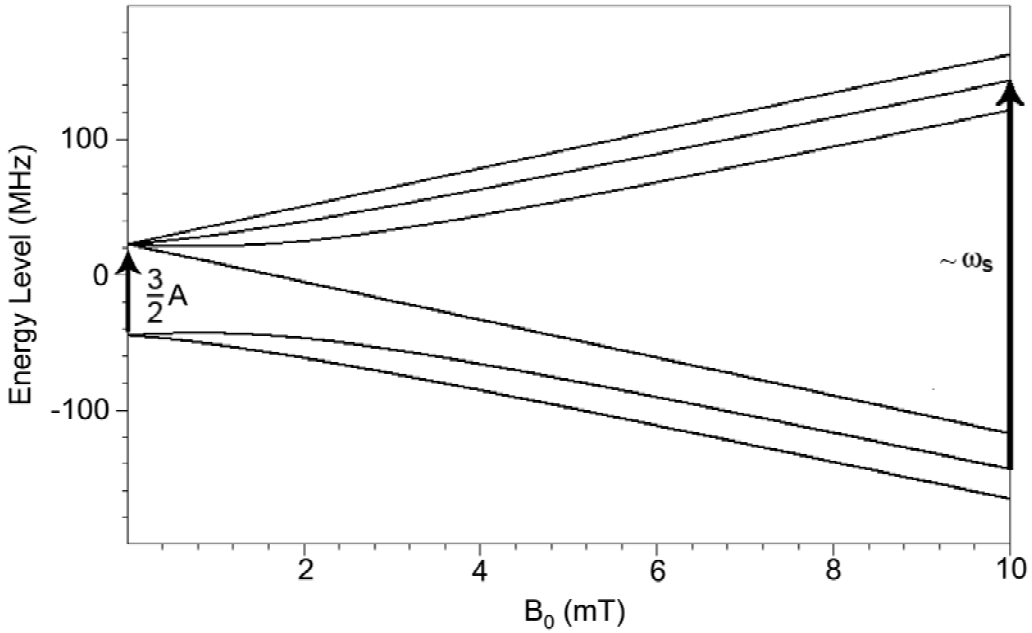

Figure 5.6 Energy levels (in frequency units) of a coupled electron-^{14}N system over a range of field values, B_0, for a fixed hyperfine coupling constant A = 2π*42 MHz. At ultra-low fields, such as the Earth's magnetic field (50 μT), the dominant energy splitting is (3/2)A (2π*63 MHz). In the higher field case, B_0 = 10 mT, the dominant energy splitting is given by the Larmor frequency of the electron (2π*280 MHz at 10 mT).

Knowing the eigenfunctions and eigenvalues of the spin Hamiltonian, it is possible to determine which transitions are allowed and which are forbidden. In NMR, the traditional means of inducing transitions within a spin system is through the

application of an RF field. In a slight deviation from the traditional protocol of NMR, an RF field oriented parallel to B_0 as well as an RF field oriented perpendicular to B_0, will be considered. The operator corresponding to the parallel orientation is $\mathbf{S}_z$, and the operator corresponding to the perpendicular orientation is $\mathbf{S}_x$. [Note that only the electron spin operator, **S**, is used. The nitrogen nucleus is left relatively undisturbed. Any disturbance felt by the ^{14}N nucleus is a result of the hyperfine interaction with the electron.] In order to obtain a more intuitive look at how the operator interacts with the product operator kets, the $\mathbf{S}_x$ operator is rewritten in terms of the raising and lowering operators, $\mathbf{S}_x = ½(\mathbf{S}^+ + \mathbf{S}^-)$.

Consider the system of equations in Eq. 5-3. The allowed transitions excited by an RF field perpendicular to $\mathbf{B}_0$ are those having a non-zero transition probability under the influence of this field. The transition probability is calculated according to Eq. 5-6.

$$W_{ij} = C\left|\left\langle i\left|\tfrac{1}{2}(\mathbf{S}^+ + \mathbf{S}^-)\right|j\right\rangle\right|^2 \qquad 5\text{-}6$$

.

The resultant eight allowed transitions are: T_{12}, T_{16}, T_{23}, T_{25}, T_{34}, T_{36}, T_{45}, and T_{56}. These are called π transitions. The selection rules for π transitions can be obtained from inspection of the total angular momentum states associated with each of the diagonal states. The allowed transitions correspond to $\Delta F = 0$ or ±1 and $\Delta m_F = \pm 1$.

Similarly, the allowed transitions under the influence of an RF field oriented parallel to B_0 can be determined from the transition probabilities, which are calculated according to Eq. 5-7. The resultant two allowed transitions, called σ transitions, are T_{26} and T_{35}. The selection rules for these transitions are $\Delta F = \pm 1$ and $\Delta m_F = 0$.

$$W_{ij} = C\left|\left\langle i\left|\mathbf{S}_z\right|j\right\rangle\right|^2 \qquad 5\text{-}7$$

Figure 5.7 presents a plot of the transition energies (in frequency units) as a

function of B_0 for all of the allowed transitions. This plot suggests that at ultra-low fields the most promising transitions, those with the largest transition energies, are T_{16}, T_{25} and T_{45} (π transitions) as well as T_{26} and T_{35} (σ transitions). As B_0 increases, the energy of the T_{45} transition decreases dramatically, while the T_{34} transition energy rapidly increases.

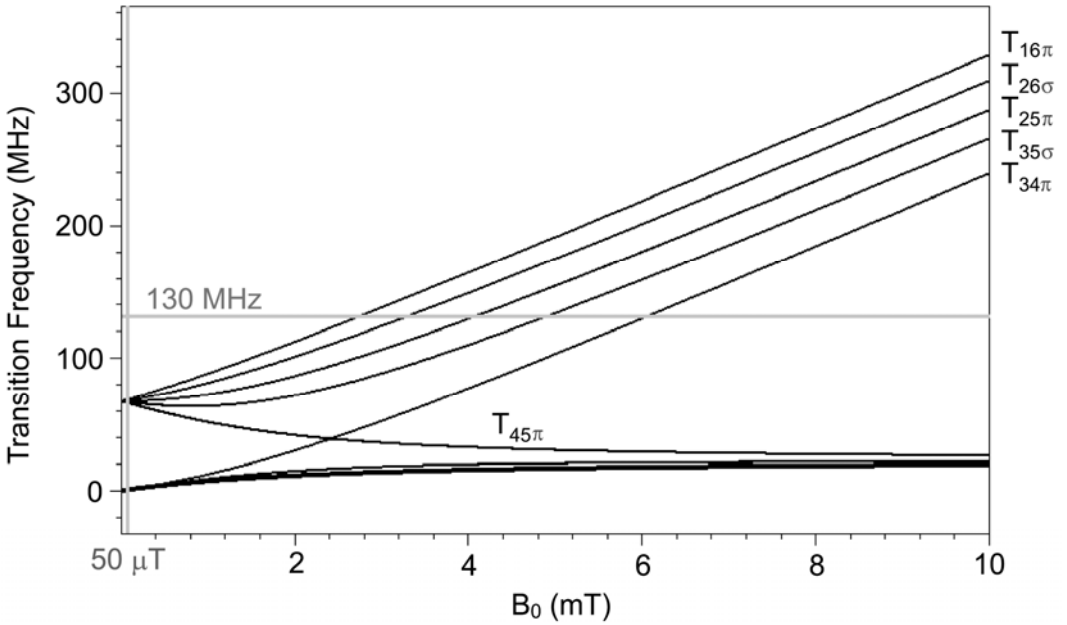

Figure 5.7 Transition frequencies for all of the ten allowed transitions of the coupled electron-^{14}N system as a function of B_0 where $A = 2\pi*42$ MHz. The vertical gray line indicates the Earth's magnetic field at approximately 50 μT. The horizontal line corresponds to a fixed irradiation frequency of 130 MHz. This fixed frequency is in resonance with a single electron transition at five specific values of B_0, corresponding to the intersection of the horizontal gray line with the lines indicating the transition frequencies as a function of field.

Expressions for the transition probabilities of each of the ten allowed transitions are given in Eq. 5-8. Note: these transition probability calculations assume the optimal orientation of the RF field, i.e. for the π transitions the RF is perpendicular to B_0 and for the σ transitions the RF is parallel to B_0. The constant C is a normalization factor which is calculated such that, for a given orientation of the RF field, $\sum W_{ij} = 1$.

$$
\begin{aligned}
W_{12} &= \tfrac{1}{4} C \sin^2 \alpha \\
W_{23} &= \tfrac{1}{4} C \cos^2 \alpha \sin^2 \beta \\
W_{34} &= \tfrac{1}{4} C \cos^2 \beta \\
W_{56} &= \tfrac{1}{4} C \cos^2 \beta \sin^2 \alpha \\
W_{16} &= \tfrac{1}{4} C \cos^2 \alpha \\
W_{25} &= \tfrac{1}{4} C \cos^2 \alpha \cos^2 \beta \\
W_{36} &= \tfrac{1}{4} C \sin^2 \alpha \sin^2 \beta \\
W_{45} &= \tfrac{1}{4} C \sin^2 \beta \\
W_{26} &= C \sin^2 \alpha \cos^2 \alpha \\
W_{35} &= C \sin^2 \beta \cos^2 \beta
\end{aligned}
\qquad 5\text{-}8
$$

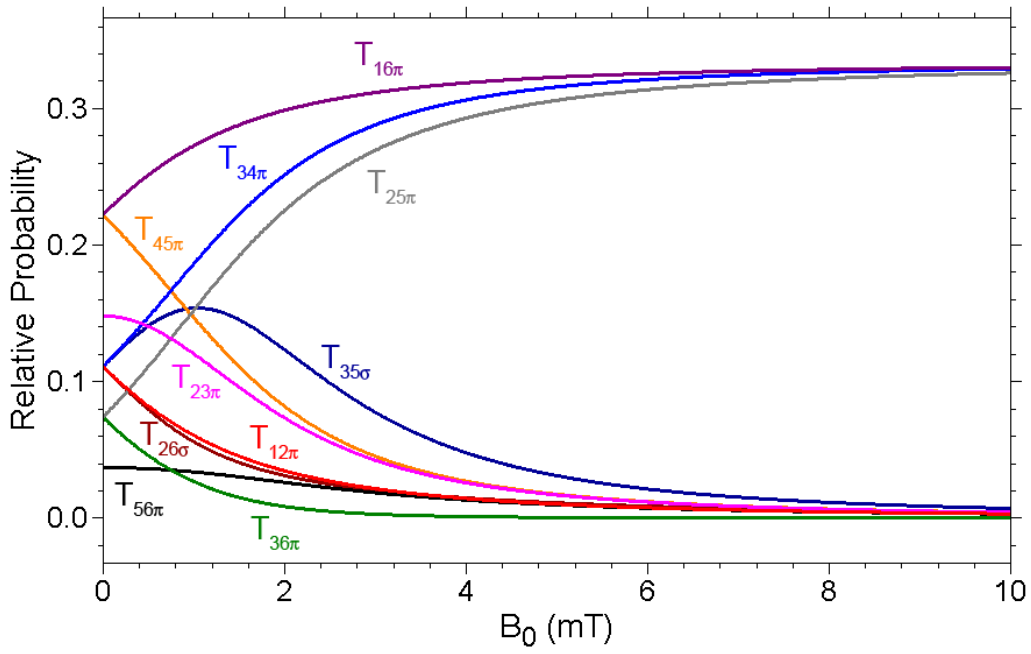

Figure 5.8 Transition probabilities for the ten allowed transitions of the coupled electron-^{14}N system as a function of B_0 for A = 2π*42 MHz.

Plots of the transition probabilities for the allowed π and σ transitions as a function of B_0 are shown in Figure 5.8. At very low fields, the π transitions T_{45} (orange) and T_{16} (dark purple) have the greatest transition probability and therefore these will be the easiest π transitions to saturate. However, as B_0 increases, the transition probability for T_{45} tends toward zero and the transition probabilities of T_{34}

(blue) and T_{25} (gray) increase dramatically. Therefore at higher fields T_{16}, T_{34} and T_{25} are the easiest π transitions to saturate. Both of the σ transitions (T_{35} in dark blue and T_{26} in dark red) have relatively large transition probabilities at low values of B_0; however, their relative probabilities drop off significantly as B_0 increases. Therefore the σ transitions are more easily induced in ultra-low magnetic fields.

In order to achieve a polarization transfer between the unpaired electron spins and the target nuclear spins of the solvent, one or more of these transitions needs to be excited. This is achieved through the application of a continuous wave (CW) radiofrequency (RF) field, B_{1RF}, at a particular transition frequency. There are two approaches to selecting the transition and field strength at which this is achieved.

The first and most straightforward approach is to apply the RF excitation in the presence of only the Earth's magnetic field, B_E. This approach has been previously reported for sensitivity enhancement of Earth's field magnetometers [6, 7] and for Earth's field NMR imaging [67-69]. As indicated by the vertical line in Figure 5.7, this corresponds to a transition frequency (for T_{16}) of approximately 68 MHz. Since the field value is fixed as $B_0 = B_E$, determining the exact transition frequency in practice requires successive re-tuning and re-matching of the B_{1RF} coil over a range of frequencies. The exact resonant frequency of the transition is then deduced as that corresponding to the largest observed signal enhancement. This process can be time consuming and is not easily automated; however it does have the advantage of requiring no other external magnetic field than the Earth's field itself.

In the second approach, following the field-cycled DNP experiment previously reported for indirect observation of electron paramagnetic resonance (EPR) spectra via DNP [66; 70-72], a higher frequency is chosen, for example 130 MHz, at which the B_{1RF} coil tunes and matches very well. A CW RF field at this frequency is applied in the presence of a weak prepolarizing field generated by an electromagnet (as in the pulse sequence in Figure 5.1). Note that this prepolarizing field will necessarily be stronger than the Earth's magnetic field, but it can be far below the value where some of the heating and eddy current problems of large electromagnetic prepolarization fields are experienced. In order to determine the field at which a maximum enhancement is achieved, the strength of the prepolarizing field is iteratively varied, in the manner of field-cycled NMR, and the resultant signal is observed. The DNP enhancement will increase and decrease as the chosen irradiation frequency moves in

and out of resonance with the various electron transitions. This is illustrated by the horizontal line in Figure 5.7. The benefit of this "field-cycled" approach for optimizing the DNP signal enhancement is not only larger signal enhancements compared to DNP performed directly in the Earth's magnetic field due to the higher irradiation frequency but also a simplification and potential automation of the signal enhancement optimization.

5.3.3. Polarization Transfer via the Overhauser Effect

Given the excitation of one of the specific electron transitions discussed in the previous section, the resultant polarization transfer from the excited electron spins, **S**, to the target nuclear spins of the solvent, **I**, can be described and quantified using the Solomon equation [65], which defines the maximum DNP factor, *DNPF*, in terms of the ratio of the polarization of the excited electron spins to the thermal equilibrium polarization of the nuclear spins, I_0, scaled by *f*, the leakage factor, *s*, the saturation factor and ρ, the coupling factor. S_0 is the thermal polarization of the electron spins and $\langle S_z \rangle$ is the ensemble average expectation value of the electron polarization under the influence of the CW DNP irradiation.

$$DNPF = \frac{\langle I_z \rangle - I_0}{I_o} = -\rho f s \left(\frac{\langle S_z \rangle - S_0}{I_0} \right) \qquad 5\text{-}9$$

The coupling factor, ρ, is a measure of the efficiency of the coupling between the electron spin and the nuclear spin and is a function of the dominant coupling mechanism. Theoretically, ρ has a value of -1 for pure indirect spin-spin interactions and has a value of 0.5 for pure direct dipolar coupling [64]. In this thesis, liquid systems with relatively low free radical concentrations are used and therefore it is assumed that the dominant coupling mechanism between the target nuclear spins and the unpaired electron spins is the direct dipolar interaction.

The leakage factor is a measure of how much of the spin-lattice relaxation of the target nuclei is driven by interactions with the electron spins. The leakage factor,

f, can be calculated using Eq. 5-10, where $T_{1,0}$ is the spin-lattice relaxation time of the nuclear spin ensemble in the absence of the free radical and T_1 is the spin-lattice relaxation time in the presence of the free radical.

$$f = 1 - \frac{T_1}{T_{1,0}} \qquad 5\text{-}10$$

Clearly Eq. 5-10 presents us with the need for a compromise. A value of f close to the maximum of unity implies a significantly faster free-radical induced relaxation and hence a broadening of the proton homogeneous linewidth.

The saturation factor is a measure of the saturation of the chosen transition and is a function of RF power and the properties of the RF resonator. A more comprehensive discussion of the saturation factor, the coupling factor and the leakage factor in the context of DNP at high magnetic fields can be found in [64].

In order to determine the maximum DNP factor for the various transitions as a function of B_0, the expectation value of the electron spin system is evaluated assuming total saturation of the transition, i.e. assuming the equalization of the populations of the two energy levels involved in the chosen transition. For the calculation of the maximum DNP factors, the saturation and leakage factors are assumed to be 1 and the coupling factor is assumed to be 0.5, the theoretical maximum for a liquid system where cross-relaxation is dominated by dipole coupling. Enhancement factors are calculated relative to the thermal equilibrium polarization of protons in the Earth's magnetic field (54 μT).

Figure 5.9 presents the relative enhancement factors of four π transitions, T_{16}, T_{45}, T_{25} and T_{34}, and two σ transitions, T_{26} and T_{35}, over a range of prepolarization fields from 54 μT (no prepolarization) to 10 mT (moderate prepolarization). For comparison, the maximum enhancement factor achievable by a prepolarizing field of 1 T (without DNP) is indicated by the dotted line.

This plot illustrates the dramatic sensitivity enhancements which are possible using DNP. This enhancement is much larger than the high field maximum DNP enhancement given by the ratio of gyromagnetic ratios (~658 for protons) because of

the presence of the strong hyperfine coupling between the electron spin and the nitrogen nucleus. In effect, the electron "sees" the field of the nitrogen nucleus perturbed by the Earth's magnetic field rather than the Earth's magnetic field perturbed by the nitrogen nucleus and so the thermal polarization of the electron spins, and in turn the maximum possible DNP enhancements, are much greater than is predicted by the electron Zeeman interaction in the external magnetic field alone.

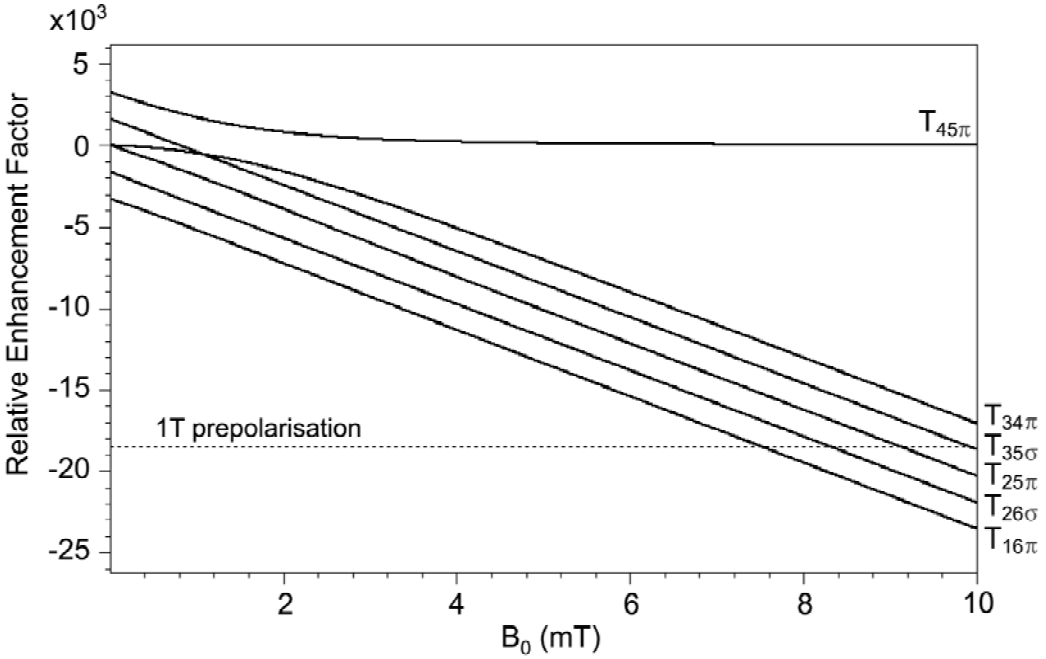

Figure 5.9 DNP Enhancement Factors calculated relative to thermal polarization of ^{1}H nuclei in the Earth's field (54 μT). In this calculation $A = 2\pi*42$ MHz, $s = 1$, $\rho = 0.5$ and $f = 1$. The enhancement factor of prepolarization at 1 T is indicated by the horizontal dotted line.

5.3.4. DNP Apparatus

In order to perform DNP in the Earth's magnetic field a few extra pieces of equipment are required. These additions to the apparatus can be easily retro-fitted to the existing Terranova-MRI system described in Chapter 4. The upgrade required for DNP includes: a function generator and high powered amplifier which operate in the 100 MHz range, a B_{1RF} coil tuned to the excitation frequency of the unpaired electrons and a means of controlling the high frequency RF with the existing Terranova

spectrometer. The full DNP system is pictured in Figure 5.10.

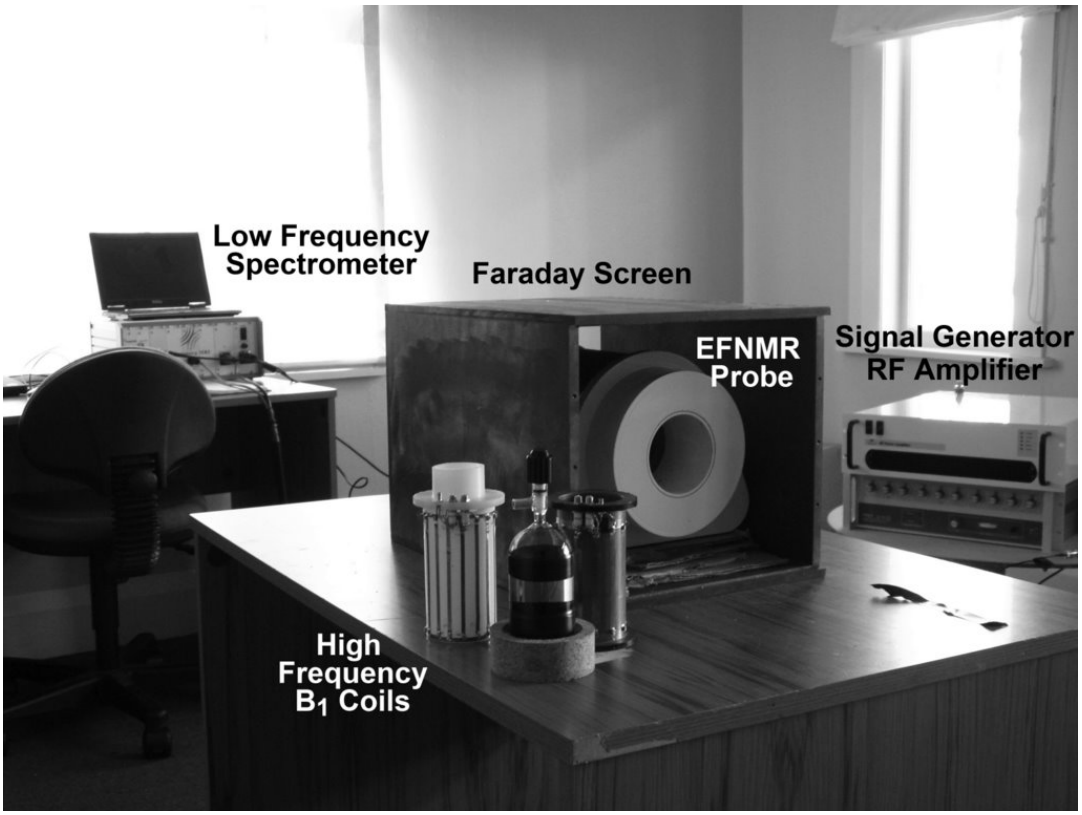

Figure 5.10 Full EFNMR DNP System

The RF irradiation was generated by a PTS synthesizer (Programmed Test Sources, Littleton, MA, USA) which operates up to 250 MHz and was amplified by a Tomco AlphaS high powered amplifier (Tomco, Norwood, SA, Australia) which operates up to 150 MHz with a maximum power of 50 W. The DNP irradiation pulses were triggered using a TTL pulse from the spectrometer and so were easily incorporated into all existing pulse sequences.

The B_1 coil used for the DNP irradiation, B_{1RF}, was built to fit inside the existing ULF B_1 coil, B_{1ULF} , which has an i.d. of 75 mm. In order to excite the π transitions, described above, it is necessary to design a coil such that B_{1RF} is perpendicular to both the polarization field, B_p and the Earth's field, B_E. It is not possible to use a simple solenoid because the self-resonance of a 75 mm diameter solenoid with a single turn is less than the target RF frequencies.

The first DNP experiments were carried out with the simple, single turn saddle coil pictured in Figure 5.11.

Figure 5.11 A photo of the single turn saddle coil used for DNP irradiation at 64.4 MHz.

The self-resonance of this single-turn saddle coil, with a diameter of 75 mm, was found to be very low and so it was difficult to tune the coil to the range of frequencies required (64 MHz to 150 MHz). A DNP signal in the Earth's magnetic field was observed at 64.4 MHz with this coil; however, it was very weak because of the inefficiency of the coil design.

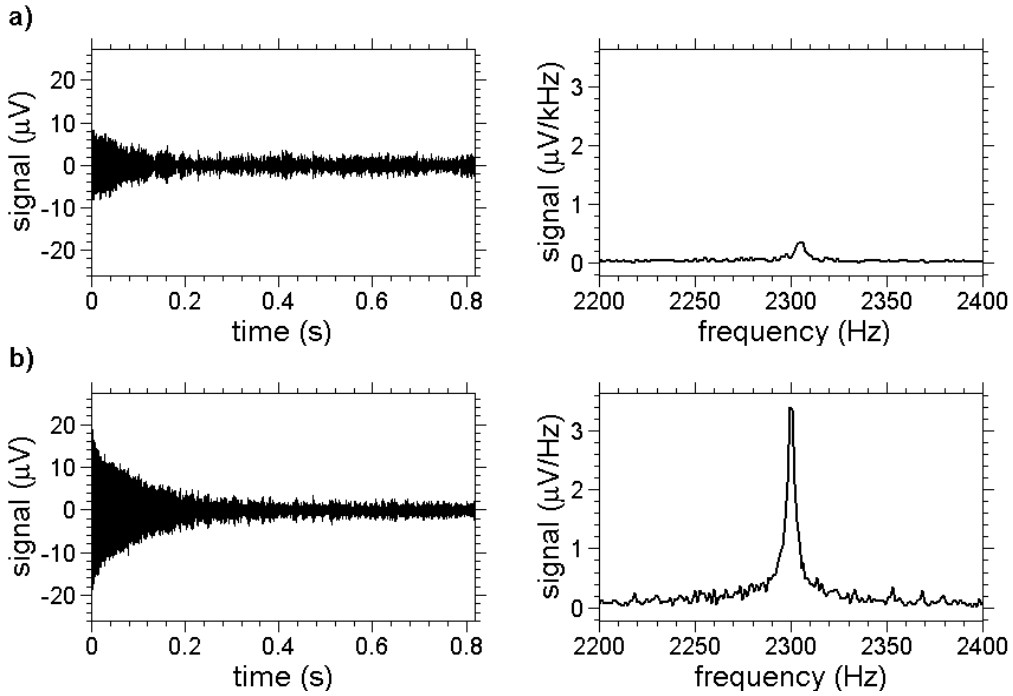

Figure 5.12 A comparison between ^{1}H EFNMR FIDs and spectra of 100 mL of water doped with 1.5 mM of TEMPO acquired with (a) DNP irradiation in the Earth's field at 64.4 MHz and (b) prepolarization at 18.7 mT.

A comparison of the DNP enhanced signal observed in the Earth's magnetic field using the saddle coil resonating at 64.4 MHz with a 50 W input signal and a spectrum acquired using 18.7 mT prepolarization is presented in Figure 5.12. The DNP signal is approximately an order of magnitude weaker than the prepolarization signal.

Figure 5.13 A photo of the three birdcage coils used for DNP irradiation which resonate at 68 MHz, 124 MHz and 131.5 MHz, respectively. Design parameters for these coils are presented in Table 5.1.

In order to improve the DNP performance, new coils were built in a low-pass birdcage configuration. We wish to perform DNP in a range of fields, from the Earth's magnetic field up to a few mT, and so a number of low-pass birdcage coils were designed and constructed with the aid of BirdcageBuilder version 1.0 (Penn State, PA, USA). These coils, pictured in Figure 5.13, were designed to tune to frequencies ranging from 68 MHz to 150 MHz. A list of the design parameters of the various coils along with their resonant frequencies are listed in Table 5.1.

The variable capacitors used to tune the B_{1RF} coils were high power, non-magnetic capacitors (Voltronics Corporation, Denville, NJ, USA) with a dynamic range of 2 – 20 pF. The chip capacitors used on the rungs of the birdcage coils were

obtained from ATC Ceramics (Huntington Station, NY, USA). It was found that the line of capacitors used for the original set of birdcage coils (ATC Ceramics, 100 series) were slightly magnetic. This compromised the field homogeneity and so the final B_{1RF} coil was constructed from a line of non-magnetic chip capacitors (ATC Ceramics, 700 series). A schematic of the tuning circuit is shown in Figure 5.14.

Table 5.1 Design parameters for DNP low-pass birdcage coils

Frequency (MHz)	Diameter (mm)	Length (mm)	Number of Rungs	Rung Width (mm)	Capacitance (pF)
68	59.1	105	16	3.0	47
131.5	56.1	98	12	6.3	15
124	65.0	113	8	7.0	27

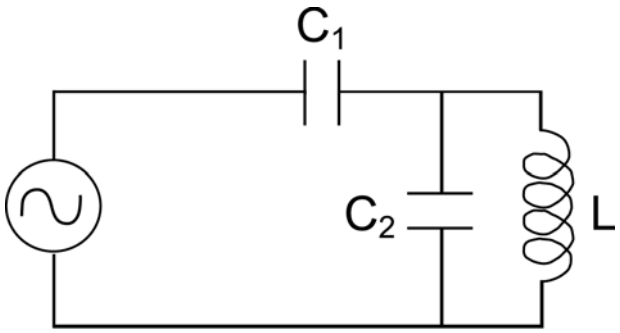

Figure 5.14 Resonant circuit used to tune and match the radiofrequency (RF) DNP irradiation coils. This circuit is constructed such that C_1 and C_2 are variable and L is the B_{1RF} coil.

5.3.5. Preliminary DNP Results

Figure 5.15 presents a comparison of Earth's field NMR spectra acquired of 100 mL of water doped with 1.5 mM of TEMPO. The spectrum in gray was acquired with an 18.7 mT prepolarizing field generated by an electromagnet. The spectrum in black was acquired with a DNP irradiation at 68 MHz and no prepolarization. By integrating the peaks we find that the DNP signal enhancement is greater than the prepolarization signal enhancement by a factor of -6.5. Extrapolating this back to the Earth's field strength of 54 μT, this is an enhancement over thermal equilibrium polarization of -2250.

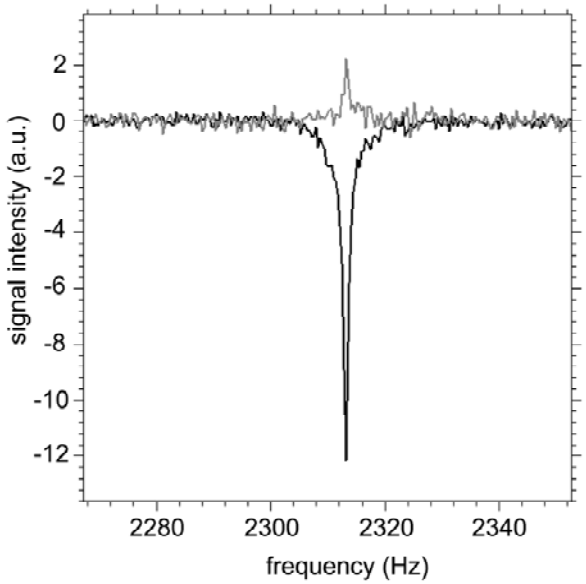

Figure 5.15 A comparison between two ^{1}H EFNMR spectra of 100 mL of water doped with 1.5 mM of TEMPO acquired with 18.7 mT prepolarization (gray) and with DNP irradiation at 68 MHz (black). The ratio of the integrals of the two peaks is -6.5. *DNPF* = -2250 (@ 54 μT)

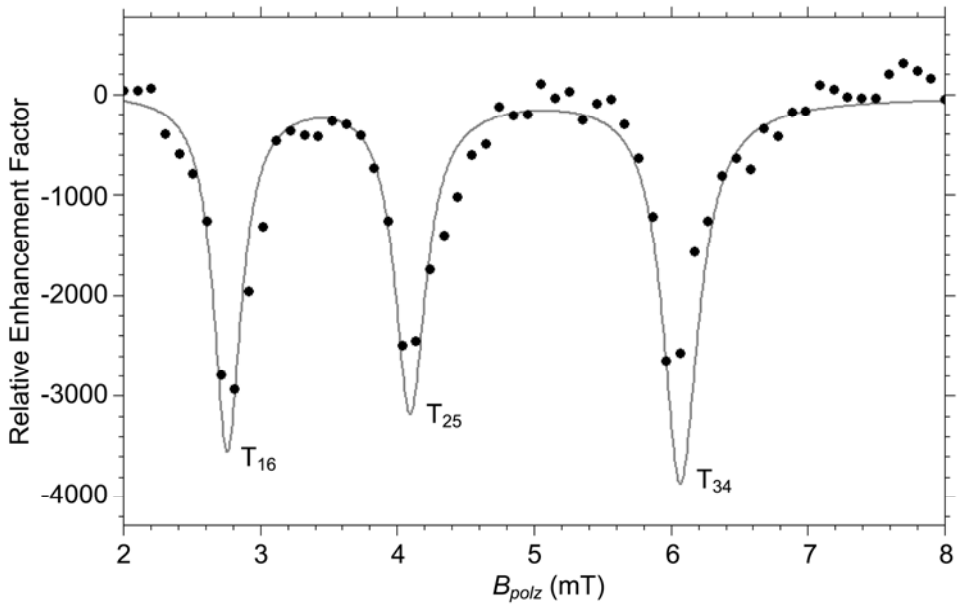

Figure 5.16 The observed relative enhancement factor of a ^{1}H EFNMR spectrum acquired with DNP irradiation at 131.5 MHz in the presence of prepolarization fields ranging from 2 mT to 8 mT. The enhancement factor is calculated relative to thermal polarization at B_E = 54 μT. The black circles are the experimental data and the solid line is a fit to Eq. 5-11. Only π transitions are excited because of the relative orientation of B_{1RF} and B_{polz}.

Using a DNP irradiation of 131.5 MHz and the field cycling approach, a larger signal enhancement of approximately -3100 over thermal equilibrium at B_E = 54 μT can be achieved in the presence of a 2.7 mT prepolarizing field. This is illustrated by Figure 5.16, a field cycled DNP experiment which shows the DNP enhancement relative to thermal polarization in the Earth's field as a function of prepolarization field strength. The experimental spectrum (black dots) is compared to a simulated DNP spectrum (solid gray line) which was generated using the expression for the DNP factor as a function of prepolarization field, B_{polz}, presented in Eq. 5-11 [66].

$$DNPF(B_{polz}) = \sum_{ij} DNPF_{ij}\, g(E_i - E_j - \omega_{RF}, T_2^*) \qquad 5\text{-}11$$

In Eq. 5-11 $g(E_i\text{-}E_j\text{-}\omega_{RF},T_2^*)$ is a Lorentzian shape function and $DNPF_{ij}$ is the calculated DNP enhancement factor at the polarization field B_{polz} relative to thermal polarization in the Earth's field (B_E = 54 μT) for the transition T_{ij}.

Due to the perpendicular orientation of B_{1RF} relative to B_p, DNP enhancements are only observed when irradiating the three π transitions: T_{16}, T_{25} and T_{34}. Under these experimental conditions it is clear that the maximum enhancement arises from irradiating T_{16}.

5.3.6. B_p Field Inhomogeneity

The results presented in the previous section are not optimized because full saturation of the electron transitions has not been achieved. This is due in large part to the inhomogeneity of the polarizing coil relative to the size of the sample. This inhomogeneity has two adverse effects on the field-cycled DNP experiment. First, it creates an ambiguity regarding the true field, B_p, experienced by the free electrons at a given polarizing current, I_p. This means that it is difficult to properly calibrate the measurement and compare to the theoretical prediction. Second, the inhomogeneity broadens the EPR spectral lines to such an extent that only partial saturation is possible.

Figure 5.17 presents a plot of the field of the standard polarizing coil measured

along the axis of the probe and with I_p = 1 A. Over a 100 mm sample, the field has an inhomogeneity of about 15%. This corresponds to ΔB_p (at 1 A) of 0.5 mT. For an electron this will result in a broadening of the transition frequency by almost 15 MHz. The spin-spin relaxation time of the unpaired electrons in TEMPO is on the order of 400 ns. This means that the electron transitions are homogeneously broadened by 0.8 MHz. Compared to this, the 15 MHz broadening by the inhomogeneity of the polarizing coil is very significant and so we would expect full saturation of a given transition to require very high power irradiation.

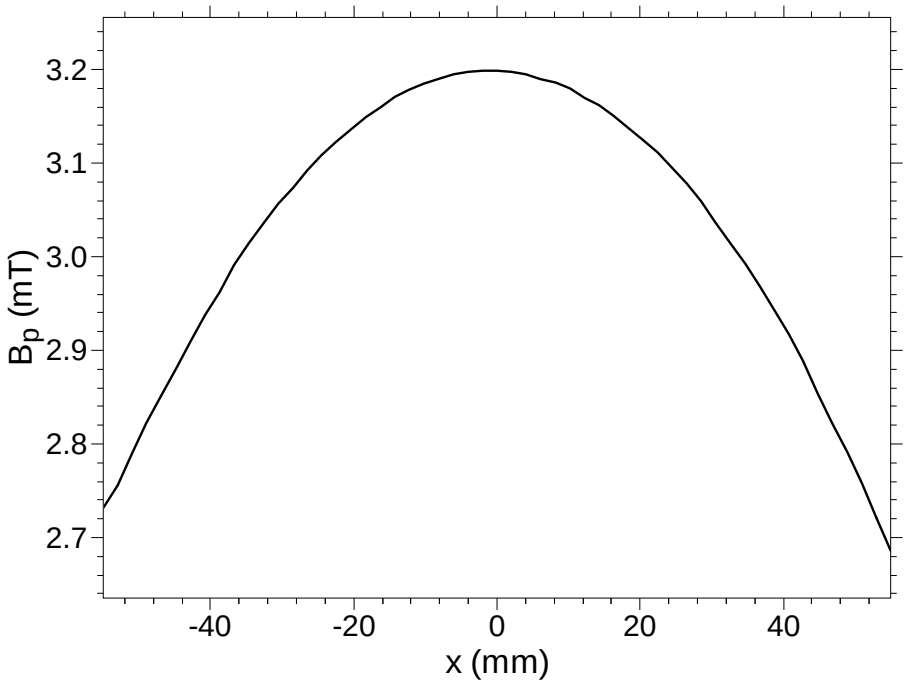

Figure 5.17 The field of the standard prepolarizing coil along the axis of the solenoid with I_p = 1 A.

The saturation of a given electron transition can be measured by plotting the observed DNP enhancement factor, *DNPF*, as a function of the output power of the high-power amplifier, *P*. We expect the rate of change of the DNP enhancement, with respect to irradiation power, to be proportional to the difference between the enhancement factor at full saturation, $DNPF_0$, and $DNPF(P)$. This dependence of a rate of change on a difference gives rise to an exponential growth of enhancement factor, as shown in Eq. 5-12, where P_1 is the characteristic power which describes the exponential growth of DNP enhancement as a function of irradiation power.

$$DNPF(P) = DNPF_0\left(1 - \exp\left(-\frac{P}{P_1}\right)\right)$$

5-12

Figure 5.18 presents a saturation measurement for the $T_{16\pi}$ transition at 124 MHz in the field from a standard Terranova-MRI polarizing coil at 0.88 A. This plot indicates that at 50 W we are not yet close to saturation and no exponential growth to a saturated enhancement value is evident. Greatly increasing the irradiation power above the P = 50 W maximum shown here will cause significant heating in the sample and so should be avoided. In addition increased RF input power may cause arcing in the tuning circuit and so degrade the performance of the resonator.

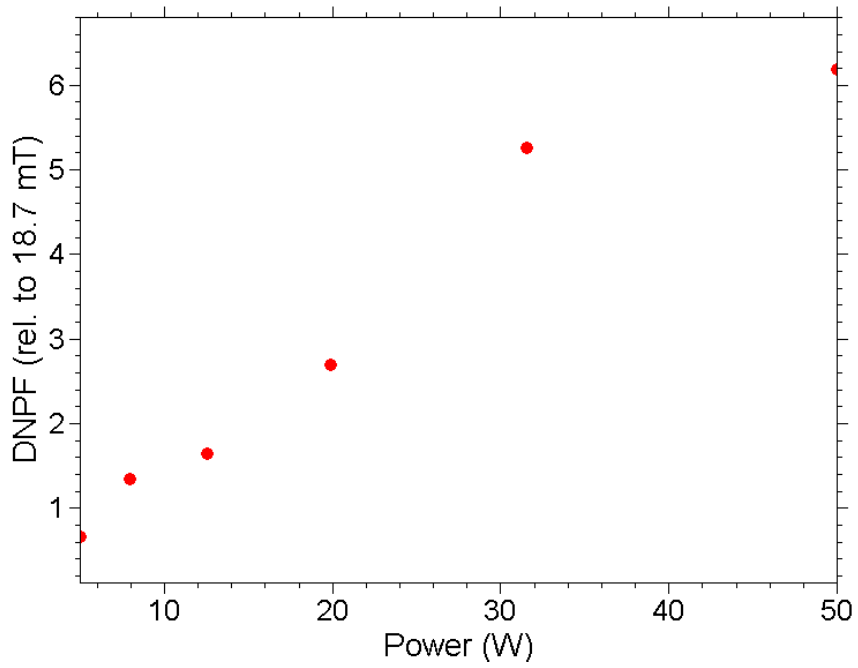

Figure 5.18 A plot of DNPF, relative to thermal polarization at 18.7 mT, as a function of irradiation power. This measurement was performed in the field from a standard prepolarizing coil with I_p = 0.88 A and irradiation at 124 MHz. This corresponds to the $T_{16\pi}$ transition.

Our inability to saturate the electron transitions with 50 W of irradiation power suggests that we are only obtaining signal from a small region of the sample in which the unpaired electrons experience a similar prepolarizing field.

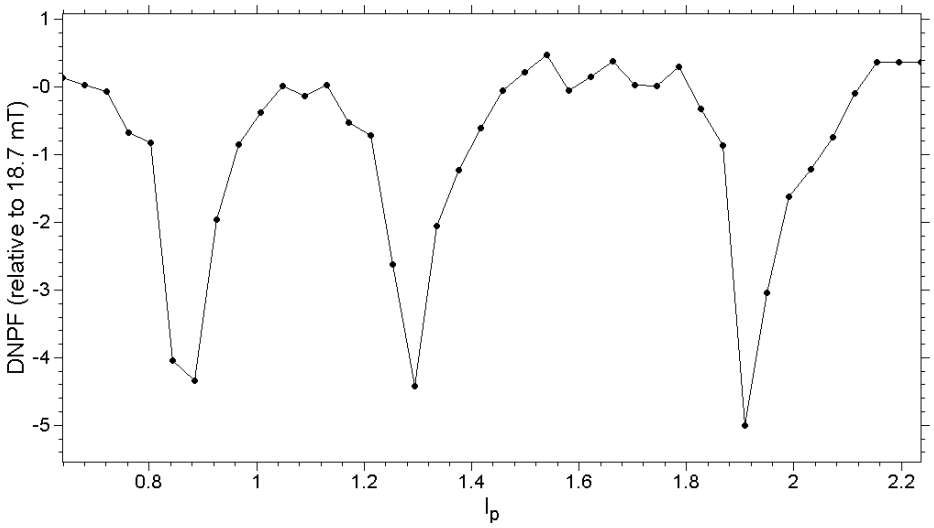

Figure 5.19 Field-cycled DNP experiment at 124 MHz using the standard polarizing coil.

Consider Figure 5.19, which presents the result from a field-cycled DNP measurement plotted as DNPF (relative to 18.7 mT thermal polarization) as a function of prepolarization current. There are a number of things to notice about this measurement. First, the transition peaks are very broad, spanning as much as 0.3 A (~ 0.9 mT). Second the peaks are highly asymmetrical, which suggests that this is not a result of homogeneous broadening of the electron transitions.

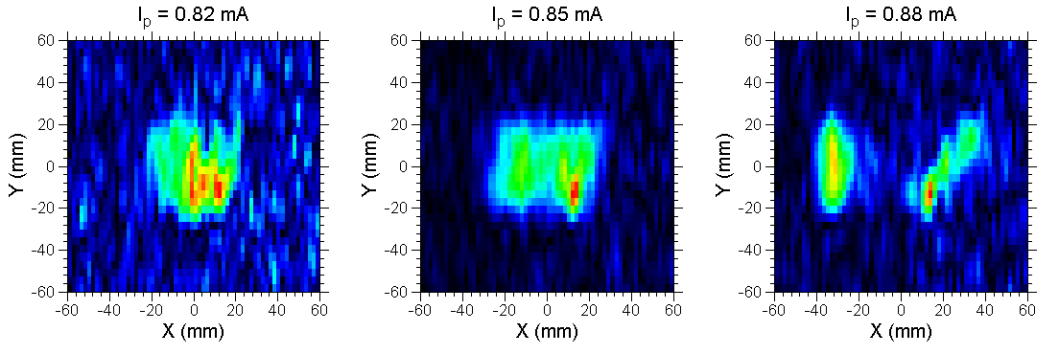

Figure 5.20 2D ^{1}H NMR spin-echo images acquired with DNP irradiation at 124 MHz with I_p = 0.82 mA (left), I_p = 0.85 mA (centre) and I_p = 0.88 mA (right). Images were acquired in a single scan with 64x16 points. Images were zero-filled to a matrix of 64x64 points and were processed with a sine-bell-squared filter.

In order to determine which region of the sample is excited at a given value of I_p, we acquire 2D YX ^{1}H NMR images of a 50 mm o.d. and 90 mm long round bottom glass vessel containing 100 mL of an aqueous solution of 1.5 mM 4-oxo-

TEMPO. The three images shown in Figure 5.20 were acquired with DNP irradiation at 124 MHz and with three different prepolarization current values: 0.82 mA, 0.85 mA and 0.88 mA, respectively. Referring to the field-cycled DNP measurement in Figure 5.19, these values of I_p span the peak which, at 124 MHz, corresponds to $T_{16\pi}$.

Based on the field profile in Figure 5.17, we expect the central region of the sample to be in resonance with $T_{16\pi}$ at lower I_p values while we expect the extremities of the sample to be in resonance at higher values of I_p. This is clearly demonstrated by the images in Figure 5.20. We find that the maximum enhancement in Figure 5.19 actually corresponds to the excitation of signal from a very small region at the edges of the sample. In order to maximize the DNP enhancement by saturating the electron transition over the entire sample, a much more homogeneous polarization field is required.

5.3.7. Homogeneous Prepolarization Coil

A prepolarization coil homogeneous to approximately 1% over a 100 mm long, 75 mm diameter sample size was designed by Mark Hunter to replace the standard coil on the Terranova-MRI. The B_p/I_p for this coil, estimated to be 0.93 mT/A, is approximately one-third that of the original prepolarizing coil (3.13 mT/A). Consequently, the homogeneous coil has a maximum field of 5.58 mT at 6 A, in contrast to the standard coil which has a maximum field of 18.7 mT at 6 A. The new prepolarization coil was built on the same former as the original coil so that it could be easily incorporated into the original apparatus. The finished coil is pictured in Figure 5.21.

Figure 5.21 A photo of the homogeneous prepolarization coil

In order to compare the fields of the standard Terranova-MRI prepolarization coil and the new coil, 1D magnetic field maps were obtained along the long axis of the probe (x) at a current of 1 A. The results of these field maps are presented in Figure 5.22.

The plot in Figure 5.22a presents the absolute value of the field while Figure 5.22b shows the deviation of the field from the mean, as a percentage of the mean field. It is clear that the new coil is much more homogeneous than the previous coil. It is homogeneous to 0.5% and 1% over sample lengths of 90 mm and 105 mm, respectively. The original coil is homogeneous to 0.5% and 1% over lengths of only 12 mm and 39 mm, respectively.

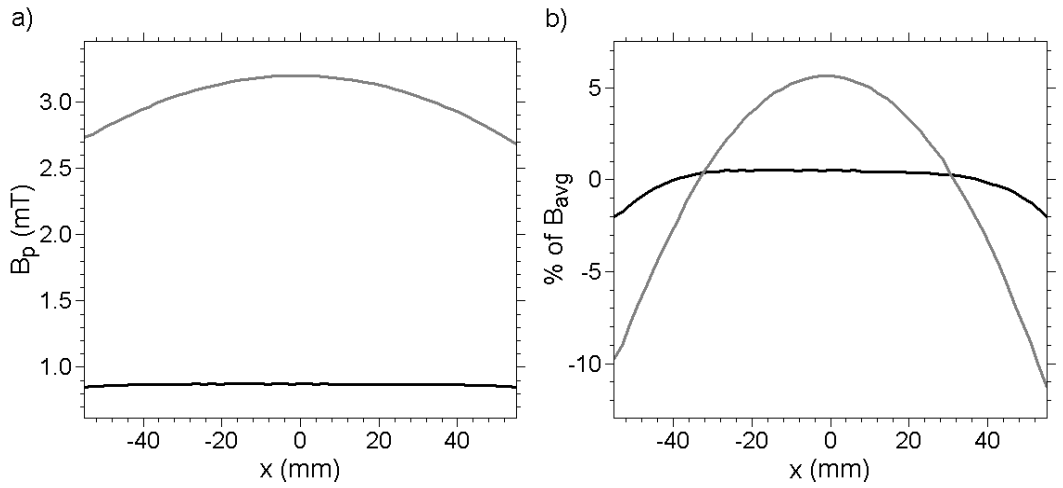

Figure 5.22 A comparison of field plots (along the long axis of the probe, x, at a current of 1 A) of the standard Terranova-MRI polarizing coil (gray) and the new homogeneous polarizing coil (black). (a) A comparison of the raw magnetic field data shows that the new polarizing coil is 3 times weaker than the standard coil. (b) A comparison of the % deviation of the field from the mean as a function of x. This plot clearly illustrates the homogeneity advantage of the new coil.

A comparison of the thermally polarized NMR signal at 5 mT, obtained using the two different prepolarization coils and a large water sample, is presented in Figure 5.23. The SNR of the signal acquired using the new prepolarization coil is 83, which is an improvement over that of the original coil, which has an SNR of 50. This result is not entirely unexpected because of the two-fold effect of shorting the polarization

coil during signal detection. First and foremost, the shorted prepolarization coil acts as a Faraday cage and so greatly reduces the pick-up of external ULF interference. This effect would be expected to be much greater using the original prepolarization coil because this coil has a much thicker layer of copper than the new coil. Second, the shorting of the prepolarization coil reduces the quality factor of the detection coil. It is expected that the new coil will reduce the Q of the B_1 coil much less than the old coil. As a result, it was expected that both the signal level and the noise level would increase, in absolute terms, using the new prepolarization coil. Prior to testing the coils it was difficult to predict what the relative SNR performance of the two prepolarization coils would be.

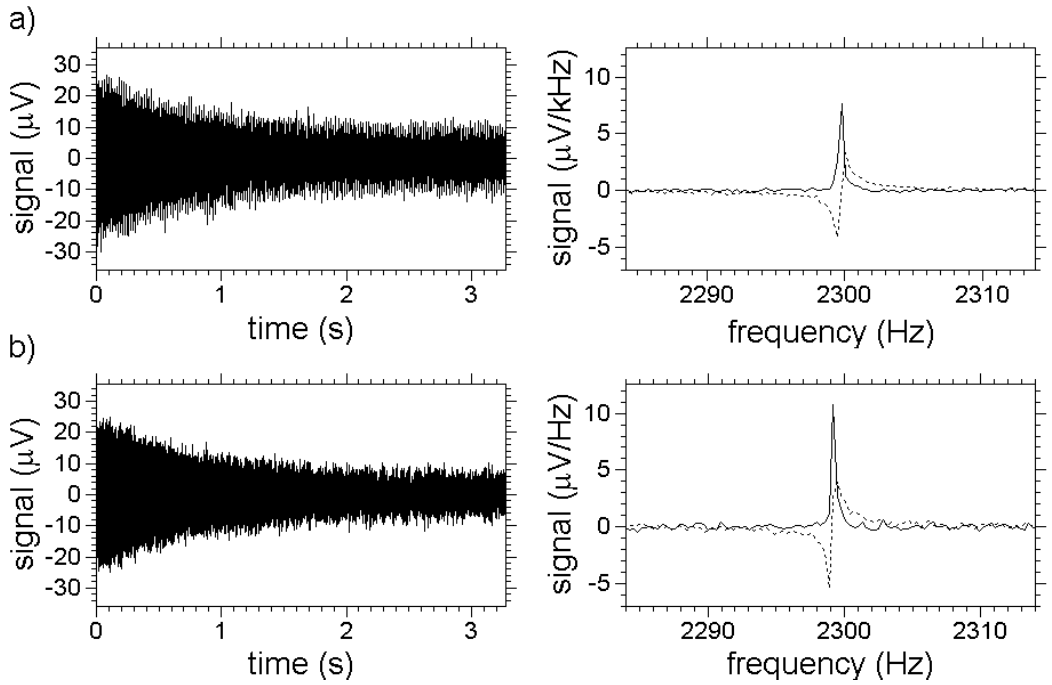

Figure 5.23 A comparison between ^{1}H EFNMR spectra of 500 mL of water prepolarized at 5 mT using (a) the homogeneous polarizing coil and (b) the standard polarizing coil. Notice that both the absolute signal and absolute noise detected by the homogeneous polarizing coil in (a) are less than that of the standard coil in (b); however, the SNR of the spectrum in (a) is 83 whereas the SNR of the spectrum in (b) is 50. There is a net SNR advantage when using the homogeneous polarization coil when compared to the standard polarizing coil at the same prepolarization field strength.

Figure 5.23 demonstrates something unexpected. Not only does the result from the new prepolarization coil have a higher SNR it also has, contrary to our expectation, a lower absolute level of detected signal and noise. This indicates that the Q is reduced much more by the shorting of the new prepolarization coil than by the original coil.

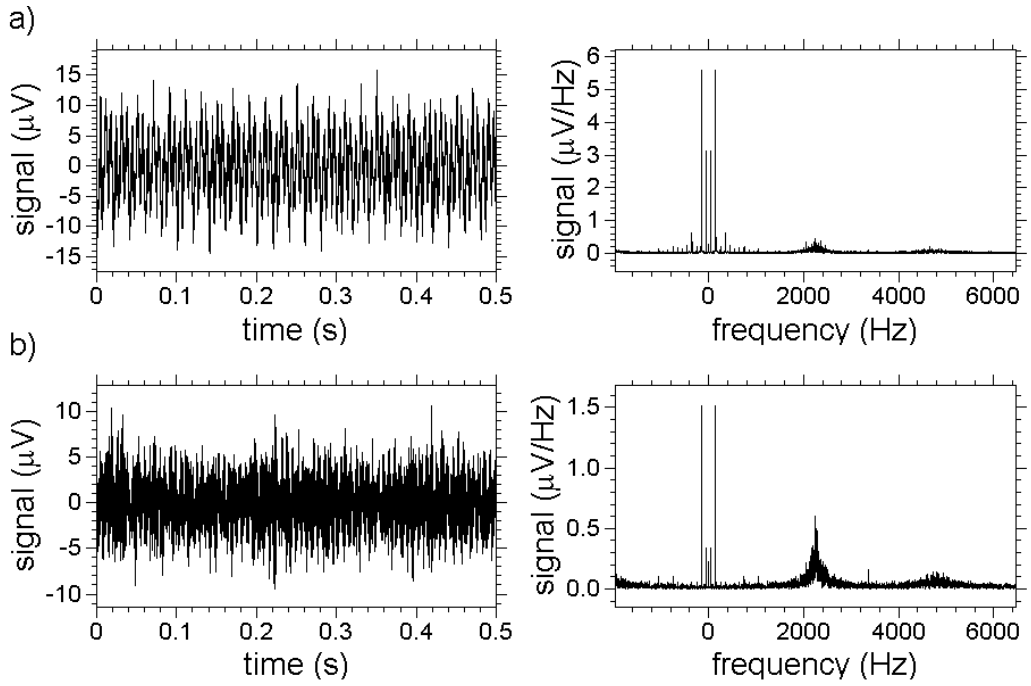

Figure 5.24 A comparison of the time domain (left) and frequency domain (right) pick-up noise of the EFNMR B_1 coil (a) inside the homogeneous pre-polarization coil, shorted to ground, and (b) inside the standard pre-polarization coil, shorted to ground.

An observation of the full noise spectrum (Figure 5.24), acquired without exciting any NMR signal, shows that in terms of efficacy of noise screening, the original coil performs much better at lower frequencies, as expected; however in the tuned region of the coil it appears as if the pickup noise in the case of the shorted homogeneous prepolarizing coil is less than in the case of the shorted standard coil. Therefore it seems that, in addition to the anticipated DNP advantages of the homogeneous coil, we also obtain an SNR advantage through reduced noise pick-up per unit detected signal.

Figure 5.25 presents a field-cycled DNP experiments with 124 MHz irradiation using the homogeneous prepolarizing coil (blue dots) along with a

theoretical spectrum (black solid line) calculated from Equation 5-11 with A = 2π*44.8 MHz, T_2 = 200 ns, f = 0.7, s = 1, ρ = 0.3 and ΔB_p = 0.3 %. The field of the homogeneous coil was calculated from the prepolarization current using B_p/I_p = 0.932 mT/A. This value deviates slightly from the field calibration measured using a three-axis hall probe (0.939 mT/A). The average field experienced by the unpaired electrons in the sample is highly dependent on the sample size and shape. Therefore a 0.7% discrepancy between the field calibration at which we can obtain a reasonable fit to Equation 5-11 and that predicted by hall-probe measurements taken along the axis of the probe is to be expected.

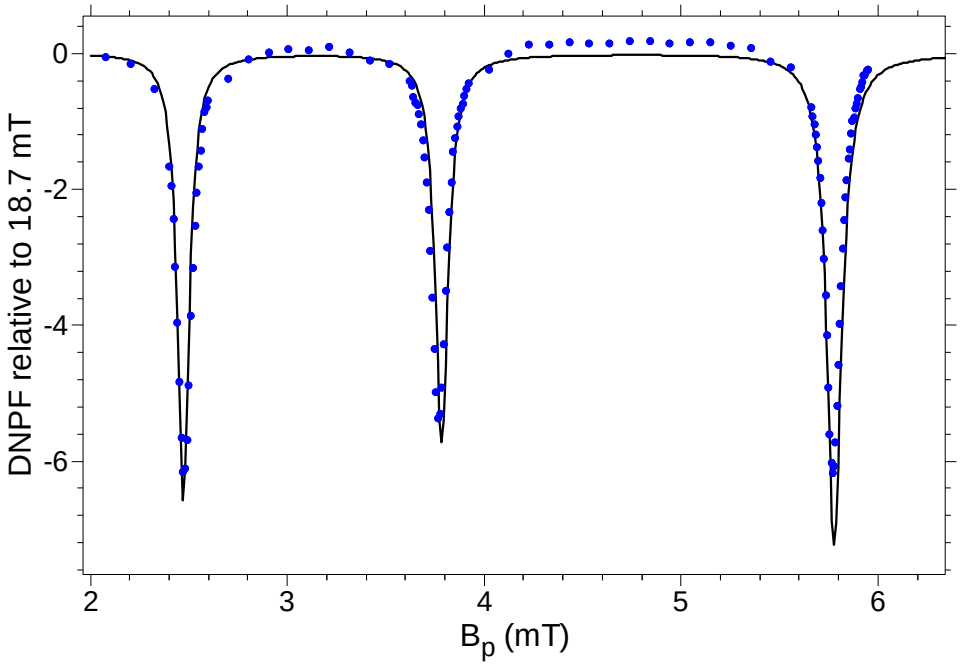

Figure 5.25 Field-cycled DNP result with irradiation at 124 MHz using the standard the homogeneous prepolarizing coil and B_p/I_p = 0.932 mT/A (blue). The black line corresponds to a theoretical DNP spectrum calculated with A = 2π*44.8 MHz, T_2 = 200 ns, ΔB = 0.3%, s = 1, ρ = 0.3 and f = 0.7.

Inspection of the plot in Figure 5.25 illustrates a number of advantages of the homogeneous coil over the standard prepolarization coil. First, in comparison to the results presented in Figure 5.19, the maximum DNP enhancement factor is greater with the homogeneous coil than the standard coil. Second, the three electron transitions are much sharper and more symmetrical in the homogeneous coil case

compared to the standard coil case. Third, the calculated DNP spectrum is in very good agreement with the homogeneous coil spectrum with reasonable parameters such as an unpaired electron T_2 of 200 ns.

The advantage of the homogeneous coil is further illustrated by the saturation experiment shown in Figure 5.26. Full saturation of the $T_{16\pi}$ transition is achieved with an RF power of only 50 W. The increase in relative DNPF as a function of RF power obeys an exponential increase to a final saturated value, as expected.

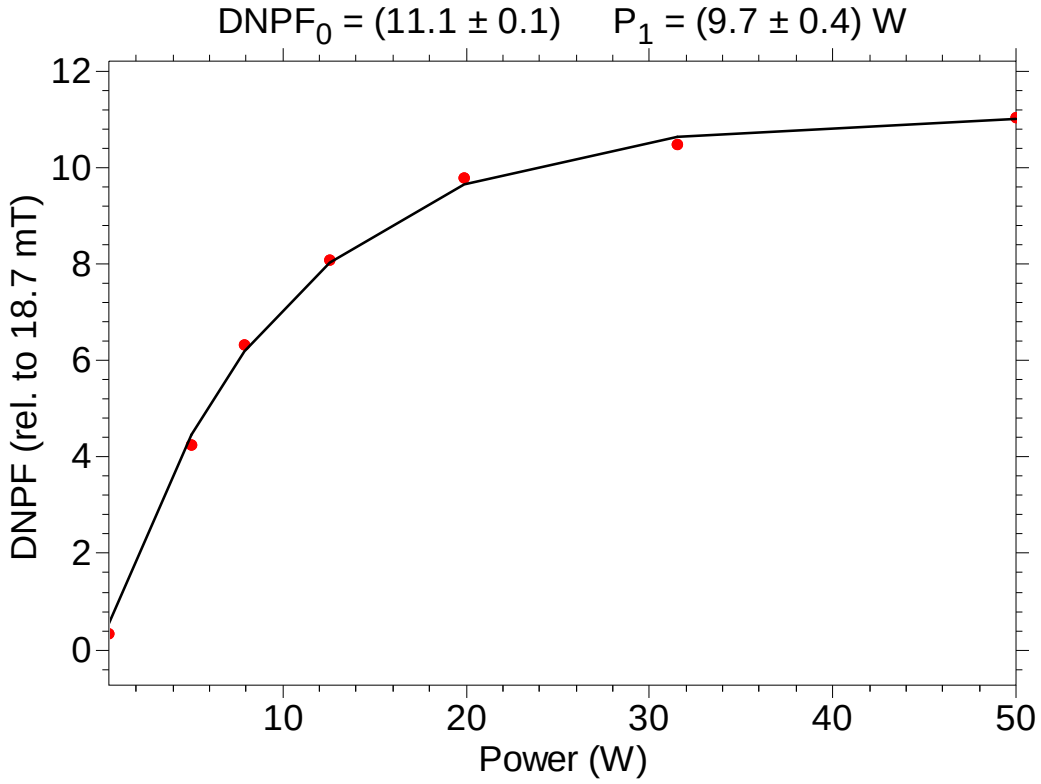

Figure 5.26 *DNPF* relative to standard prepolarization (18.7 mT) as a function of irradiation power of the $T_{16\pi}$ transition in the homogeneous polarizing coil with 124 MHz irradiation and I_p = 2.65 A. A fit to the exponential growth function in Eq. 5-12 (black line) indicates that full saturation is reached with 50 W.

2D ^{1}H EFNMR images of a 50 mm diameter, 90 mm long round bottom vessel containing 100 mL of a 1.5 mM aqueous solution of 4-oxo-TEMPO are presented in Figure 5.27. These image, acquired with DNP irradiation at 124 MHz in the field from the homogeneous prepolarization coil (B_p = 2.5 mT at I_p = 2.65 A), clearly demonstrate that the DNP signal excitation achieved in the field from this new prepolarization coil is homogeneous throughout the sample.

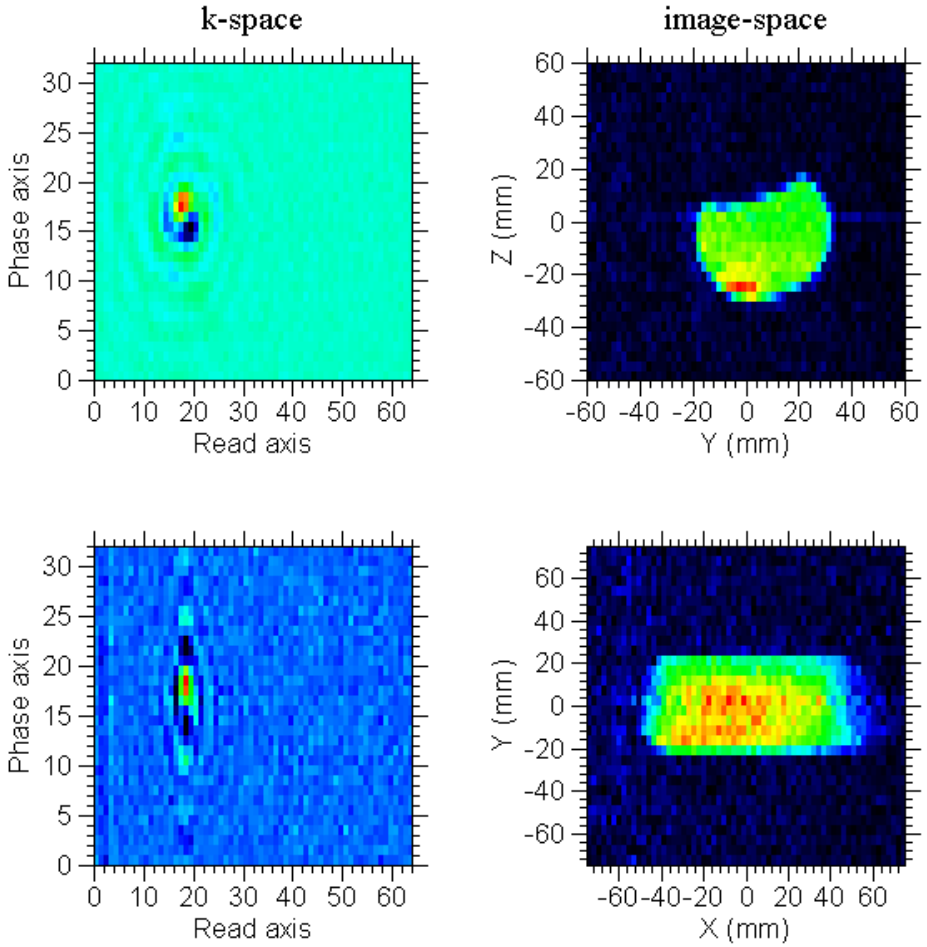

Figure 5.27 2D 64x32 ^{1}H NMR images of a 1.5 mM aqueous solution of 4-oxo-TEMPO in a 50 mm o.d., 90 mm long round bottom glass vessel. The images were acquired with DNP irradiation at 124 MHz in the homogeneous prepolarization coil with I_p = 2.65 mA (B_p = 2.5 mT). Each image was acquired in 5 minutes with two scans.

While the maximum DNP enhancement, relative to prepolarization at 18.7 mT, indicated by Figure 5.25 is only 6.2 the actual SNR advantage is greater because a number of pulse sequence parameters, such as the delay between the switch-off of the prepolarization coil and the excitation pulse, can be optimized for the DNP case to further increase SNR. Figure 5.28 presents a comparison of ^{1}H EFNMR FIDs and spectra acquired of 100 mL of 1.5 mM aqueous solution of 4-oxo-TEMPO acquired with DNP in the homogeneous coil (Figure 5.28a) and with prepolarization at 18.7 mT using the standard coil (Figure 5.28b). The SNR of the DNP enhanced spectrum is 943, a factor of 14 greater than the SNR of the prepolarized spectrum, 68.

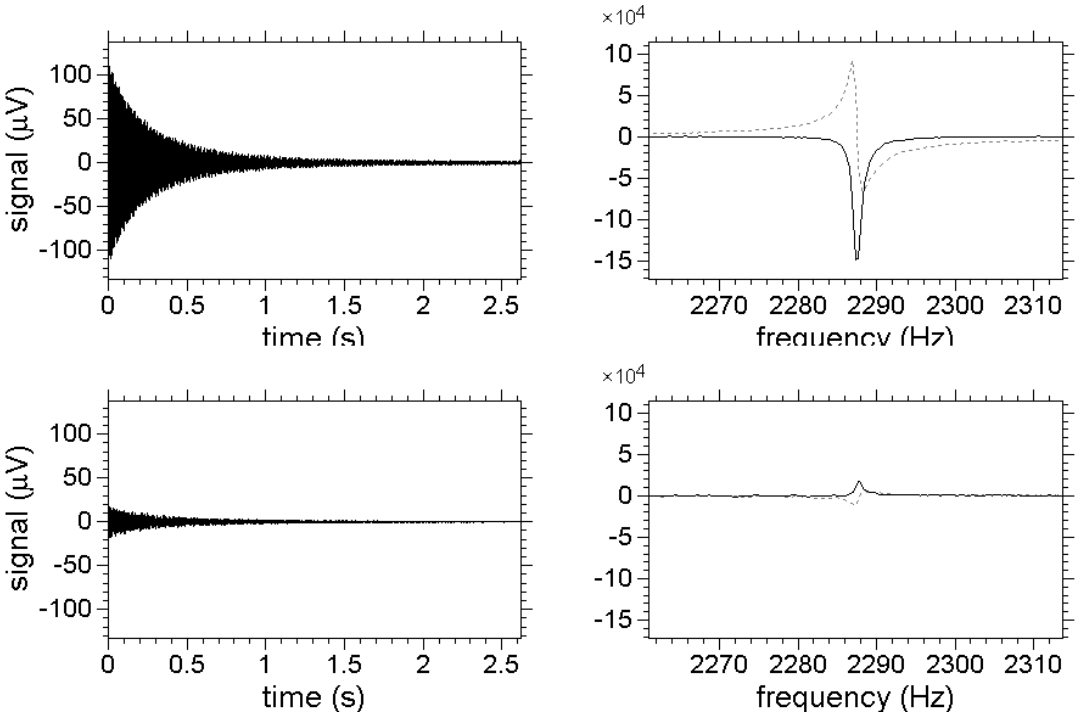

Figure 5.28 A comparison of ^{1}H EFNMR FIDs and spectra of 100 mL of 1.5 mM 4-oxo-TEMPO in water acquried with (a) DNP in the homogeneous prepolarization coil (SNR = 943) and (b) pre-polarization at 18.7 mT with the standard prepolarization coil (SNR = 68). The observed SNR improvement is 14.

5.4. Hyper-polarization via Optical Pumping

5.4.1. Theory

Hyper-polarization of noble gas nuclei via optical pumping was first introduced by William Happer in 1972 [73]. In this method, circularly polarized resonance light is directed into a glass cell containing a saturated alkali metal vapor, typically rubidium, which has a high vapor pressure at moderate temperatures. This incident circularly polarized light is absorbed by the alkali metal atoms and so the valence electrons of these atoms become spin polarized. In properly designed systems almost half of the spin polarization of the incident photons is absorbed by the alkali metal atoms [74].

In addition to the alkali metal vapor, the glass cell contains an abundance of

noble gas nuclei. Collisions between the alkali metal and noble gas atoms result in a net transfer of spin polarization from the alkali metal valence electrons to the noble gas nuclei. This polarization transfer is mediated by the hyperfine interaction. An efficient optical pumping system can generate noble gas nuclear polarizations of tens of percent, five orders of magnitude greater than the thermal nuclear polarization available in even the strongest laboratory NMR magnets [74].

In order to prevent depolarization of the target noble gas nuclei, nitrogen gas is also present in the glass cell. The N_2 atoms act as a quench, relaxing the excited rubidium atoms before they can depolarize the target noble gas nuclei. Hyper-polarization via optical pumping is possible in a glass cell containing only the alkali metal vapor and the target noble gas atoms but the hyper-polarization process is much less efficient in this case and so the maximum achievable hyper-polarization levels of the noble gas nuclei are reduced in the pure gas case compared to optical pumping in the presence of nitrogen. For ^{129}Xe hyper-polarization a typical optical-pumping pumping mixture contains on the order of 2% N_2 and 3-5% xenon pressurized to 60 atm with ^{4}He.

The level of nuclear polarization achieved in an optical-pumping apparatus is dependent on the number of collisions between atoms and consequently on the amount of time the noble gas nuclei are in contact with the alkali metal atoms. Therefore, if the goal is to create a constantly flowing stream of hyperpolarized gas in real time, there will be a limit on the polarization level achieved which is dependent on the flow rate. However, if the goal is to produce as high a level of gas polarization as possible, a so-called “stop-flow” approach is used. In this case the noble gas is kept in the glass cell for a fixed period of time, during which it experiences multiple collisions with the excited alkali metal atoms and so acquires a large nuclear polarization. Subsequently, the hyperpolarized gas is released from the optical pumping cell, either for immediate use in an NMR or MRI experiment or into some sort of storage container for later use.

Once hyper-polarized, the T_1 of noble nuclei is very long, anywhere from 100s of seconds to days depending on the nucleus and the storage conditions. Therefore it is possible to hyperpolarize the noble gas nuclei in a mixture with a stop-flow protocol, collect the noble gas nuclei into a pure mixture for storage and then use this pure, maximally polarized gas in an NMR or MRI experiment at a later time.

In MRI, hyper-polarization of ^{3}He and ^{129}Xe nuclei via optical pumping is widely used as a means of producing large numbers of spin polarized nuclei for applications such as medical lung imaging [75; 76]. The viability of hyper-polarized ^{83}Kr lung MRI has also recently been demonstrated [77]. Another promising application of hyperpolarized gas is for NMR and MRI performed in weak magnetic fields because the gas polarization is independent of field strength.

From August 2007 to January 2008, Associate Professor Thomas Meersman and Dr. Galina Pavlovskaya from the Department of Chemistry, Colorado State University visited the NMR group at Victoria University of Wellington to implement an optical pumping apparatus for producing hyperpolarized xenon gas. Additional help with this project was provided by Dr. Mike Barlow from the University of Nottingham. As a part of this thesis, and in collaboration with Prof. Meersman and Dr. Pavlovskaya, the potential for using hyperpolarized xenon gas for both direct ^{129}Xe detection in the Earth's field and for polarization enhancement of solvent nuclei via the Spin Polarization-Induced Nuclear Overhauser Effect (SPINOE) was explored.

5.4.2. Hyperpolarized ^{129}Xe in the Earth's Magnetic Field

NMR spectroscopy of optically pumped ^{129}Xe was first performed in the Earth's magnetic field by Appelt et al. in 2005 [56]. In this paper, it was shown that because of the exceptionally long T_2 of ^{129}Xe in the gas phase, the large ^{129}Xe chemical shifts (100s of ppm between ^{129}Xe gas dissolved in a solvent, such as toluene, and ^{129}Xe as a free gas) can be resolved in the Earth's magnetic field. In addition to providing spectroscopic information about the ^{129}Xe gas, EFNMR also provides a way of evaluating the polarization level of the optically pumped ^{129}Xe.

Figure 5.29 presents a comparison of a ^{1}H EFNMR spectrum of toluene pre-polarized at 18.7 mT and a ^{129}Xe EFNMR spectrum of hyperpolarized ^{129}Xe gas at STP. The ^{129}Xe has much higher SNR, due to a very narrow linewidth of 0.1 Hz, but the integral of the peaks, 20.3 for toluene and 18.4 for the ^{129}Xe gas, is comparable. The toluene linewidth is 0.4 Hz. Note that the ^{129}Xe was hyperpolarized using a stop-flow protocol in which the gas is optically pumped in the rubidium cell for several seconds and then released into the sample vessel in the EFNMR probe for excitation and detection.

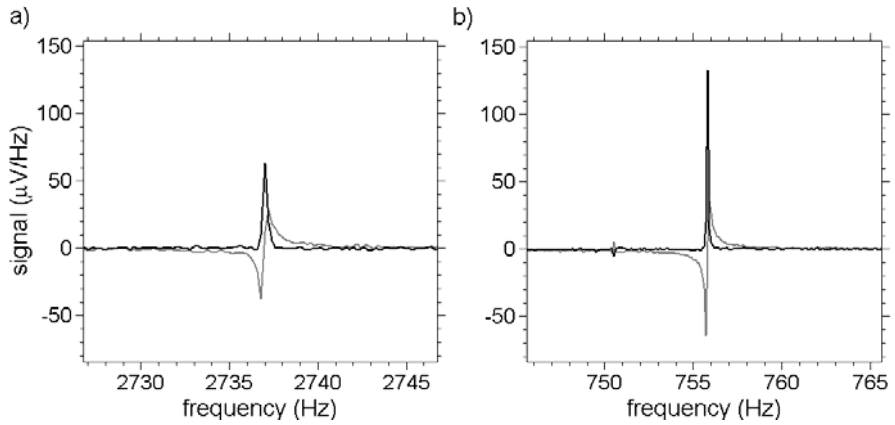

Figure 5.29 A comparison of (a) A ^{1}H EFNMR spectrum of toluene thermally polarized at 18.7 mT and (b) a ^{129}Xe EFNMR spectrum of hyperpolarized ^{129}Xe gas (3% Xe gas mixture at STP).

In order to calculate the polarization of the ^{129}Xe we must first deduce the polarization of the toluene at 18.7 mT. This can be estimated as the population excess between spin-up and spin-down states of the ^{1}H nuclei. In the high temperature limit, this spin-up excess is proportional to the Boltzmann factor, Eq. 5-13, where k is Boltzmann's constant ($1.38\text{x}10^{-23}$ J/K), T is the temperature in K, B_p is the polarization field, $\hbar$ is Planck's constant ($6.626\text{x}10^{-34}$ Js) divided by 2π and γ is the gyromagnetic ratio of ^{1}H ($2.675\text{x}10^{8}$ T s^{-1}).

$$P_{^1H} \cong \frac{\gamma \hbar B_p}{kT}$$

5-13

The Boltzmann factor is equal to $1.27\text{x}10^{-7}$ for protons at 18.7 mT and 298 K. The number of protons per unit volume of a given solvent is given by Eq. 5-14, where N_{av} is Avogadro's number ($6.022\text{x}10^{23}$), $N_{1H/solvent}$ is the number of ^{1}H nuclei in each solvent molecule, $M_{solvent}$ is the molecular mass of the solvent and $\rho_{solvent}$ is the density of the solvent.

$$\frac{N_{^1H}}{V_{solvent}} = N_{av} \frac{\rho_{solvent}}{M_{solvent}} N_{^1H/solvent}$$

5-14

The number of ^{129}Xe nuclei per unit volume of a given ideal gas mixture at standard temperature and pressure (STP) is given by Eq. 5-15 where f_{Xe} is the fraction of the gas mixture which is xenon and f_{129Xe} is the natural abundance of ^{129}Xe (26.4%).

$$\frac{N_{^{129}Xe}}{V_{gas}} = N_{av}\frac{f_{^{129}Xe}f_{Xe}}{22.4L/mol}$$

5-15

The ratio, R, of the ^{1}H signal from a volume of solvent to the ^{129}Xe signal from a similar volume of gas at STP is given by Eq. 5-16.

$$R = \frac{\gamma_{^{129}Xe}N_{^{129}Xe}P_{Xe}}{\gamma_{^{1}H}N_{^{1}H}P_{^{1}H}} = \frac{\gamma_{^{129}Xe}}{\gamma_{^{1}H}}\frac{M_{solvent}}{\rho_{solvent}N_{^{1}H/solvent}}\frac{f_{^{129}Xe}f_{Xe}}{22.4L/mol}\frac{kT}{\hbar\gamma_{^{1}H}B_p}P_{Xe}$$

5-16

For a comparison with toluene pre-polarized at 18.7 mT and a 3% Xe gas mixture, the polarization of the ^{129}Xe nuclei can be estimated using Eq. 5-16 to be $P_{^{129}Xe} = 0.1R$.

In the example in Figure 5.29, the integral of the toluene peak is 20.4 and the integral of the xenon peak is 18.3. Therefore the ^{129}Xe polarization is approximately 9.2%. This value is comparable to the ^{129}Xe polarization levels measured at high-field using the same apparatus and a stop-flow optical-pumping protocol.

5.4.3. Spin Polarization-Induced Nuclear Overhauser Effect (SPINOE)

Spin polarization-induced nuclear Overhauser effect (SPINOE), first presented by Navon et al. in 1996 [78], is a method whereby the hyperpolarization of optically pumped noble gas nuclei is transferred to target nuclei, typically in a liquid solvent or on a surface, via the nuclear Overhauser effect. This polarization transfer between hyperpolarized noble gas nuclei and surface or solvent nuclei is analogous to the polarization transfer between excited free electron spins and target solvent nuclei in DNP and can be described by the Solomon Equations [65]. Hyperpolarized gas nuclei

are naturally in an excited state and so, unlike DNP, no irradiation of these spins is necessary.

In order to observe the SPINOE effect, the hyperpolarized nuclei need to come into contact with the target nuclei in such a way that the preferred relaxation pathway for these excited nuclei is via cross-relaxation to the target nuclei in the solvent or on the surface. The polarization transfer is mediated by the dipole interaction and so its efficiency is related to the distance of closest approach between the hyperpolarized nuclei and the target nuclei. If the application involves the transfer of polarization to surface nuclei, the hyperpolarized gas is typically blown across the surface and the polarization transfer occurs at the boundary between the gas and the surface. In the case of the polarization of a significant volume of liquid, contact between the hyperpolarized nuclei and the target nuclei is achieved by dissolving the gas in the solvent, often by means of bubbling the gas through the liquid.

In 2001, Appelt et al. [79] used SPINOE to obtain significant NMR sensitivity enhancements in detection fields as low as 1 mT for 0.2 mL volumes of a range of solvents. In order to obtain dissolution of the hyperpolarized gas in these solvents, the liquid solvent is frozen in a liquid nitrogen bath and a layer of xenon ice is allowed to form on the surface for a fixed period of time, on the order of minutes. The nitrogen bath is then removed and a hot air stream is applied to the solvent and xenon ice. As the ice melts it dissolves in the solvent and so the contact between the hyperpolarized xenon nuclei and the solvent nuclei is achieved. At 1 mT, for an ice accumulation time of 12 minutes a signal enhancement of almost 1000 was obtained for 0.2 mL of toluene.

At first glance these experiments seem to imply that SPINOE would be a very useful tool for signal enhancement of NMR experiments carried out in the Earth's magnetic field. However, attempts made in the course of this thesis to observe a SPINOE signal in the Earth's magnetic field using hyperpolarized ^{129}Xe gas bubbled through a large volume of toluene were ultimately unsuccessful. Herein we will present a calculation of the maximum possible SPINOE enhancement compared to the prepolarization enhancement observed at 18.7 mT, which demonstrates that in the case of Earth's field NMR where large sample volumes (100s of mL) can be used without a loss of spectral resolution, the scope for signal enhancement using SPINOE is very limited.

Consider a large 500 mL volume of toluene in a 75 mm diameter vessel within the Terranova-MRI probe. Contained within this volume are approximately 2.3×10^{25} ^{1}H nuclei (from Eq. 5-14) with a spin polarization of 1.3×10^{-7} in a prepolarization field of 18.7 mT (from Eq. 5-13). In order to polarize this sample in the Earth's field with hyperpolarized ^{129}Xe we bubble a gas mixture, containing a volume fraction, f_{Xe}, of xenon through the bulk solvent.

Consider a bubble with a radius, r, containing a gas with diffusion coefficient, D_g, within a solvent with viscosity, η, and density, ρ_s.

From Stoke's Law we know that the drag force, F, on the bubble is given by Eq. 5-17 where v is the velocity of the bubble.

$$F = 6\pi\eta r v \tag{5-17}$$

This force is balanced by the buoyancy force, Eq. 5-18, where $\Delta\rho$ is the difference in density between the liquid and the gas and g is the acceleration due to gravity (9.8 ms^{-2}).

$$F = \Delta\rho g\left(\frac{4}{3}\pi r^3\right) \tag{5-18}$$

Solving Eq. 5-17 and Eq. 5-18 for the ascension velocity of a bubble as a function of its radius we obtain the "terminal velocity" given by Eq. 5-19.

$$v(r) = \frac{2}{9}\frac{\Delta\rho g}{\eta} r^2 \tag{5-19}$$

The rise time, t, of the bubble in a vessel of height, z, is given by Eq. 5-20. [Note that this calculation neglects the initial velocity and so will overestimate the rise time for bubbles with an initial velocity, v_0.]

$$t = \frac{z}{v(r)} = \frac{9}{2}\frac{\eta z}{\Delta\rho g r^2}$$

5-20

The average contact rate for the gas within the bubble hitting the surface is proportional to the diffusion constant divided by the radius of the bubble squared. The approximate number of collisions between a single xenon nucleus and the surface of the bubble which will occur during a given residence time, *t*, is described by Eq. 5-21.

$$N_{col} = \frac{4D_g}{r^2}t$$

5-21

A number of collisions greater than or equal to one indicates that every xenon nucleus within the bubble will come into contact with solvent nuclei at least once during the residence time and so, assuming an 100% efficiency of polarization transfer between hyperpolarized xenon and target nuclei, the limiting factor on the maximum polarization enhancement of the solvent nuclei is the number of xenon nuclei in the bubble, not the contact rate. Assuming more realistic polarization transfer efficiencies, more collisions are required to maximize polarization transfer, i.e. for a 20% efficiency five collisions are required to ensure a complete transfer of polarization to the target nuclei in the solvent. If the number of collisions is less than the critical number stipulated by the transfer efficiency, only a fraction of the xenon nuclei within the bubble will interact with the solvent nuclei.

Substituting Eq. 5-20 into Eq. 5-21 we find that the number of collisions, N_{col}, between an individual xenon nucleus and the surface during the rise time of the bubble is on the order of:

$$N_{col} = \frac{18\eta z D_g}{\Delta\rho g r^4}.$$

5-22

Solving for *r* we find that, assuming a polarization transfer efficiency of C_{eff}

equal to N_{col}^{-1}, the maximum bubble radius, r_{max}, for total polarization transfer between hyperpolarized xenon and the target solvent nuclei is given by Eq. 5-23.

$$r_{\max} = \sqrt[4]{\frac{18\eta z D_g}{\Delta\rho g} C_{eff}}$$

5-23

For the case of pure xenon gas in toluene (η = 5.9x10^{-4} Pa s; $\Delta\rho$ = 0.8669 g ml^{-1}; D_g = 1x10^{-5} m^{2}s^{-1}; $f_{X\ e}$= 1) where z = 7.5 cm and C_{eff} = 0.2, we find that the maximum radius is 0.7 mm. This corresponds to a residence time of 0.1 s.

Now that we have determined the critical bubble size we can determine the number of bubbles required to hyperpolarize the solvent nuclei to a higher level than prepolarization at 18.7 mT. The number of ^{129}Xe atoms (at 26.4% natural abundance) in a bubble of radius, r, is:

$$N_{^{129}Xe/bubble} = \frac{4}{3}\pi r^3 \frac{N_{av}}{22.4L/mol} f_{Xe} * 26.4\% .$$

5-24

Recall that the polarization of protons in a prepolarization field of 18.7 mT is 1.3x10^{-7} and 2.3x10^{25} protons are present in a 500 mL volume of toluene. Therefore the product of the hyper-polarization of the xenon nuclei, P_{129Xe}, and the number of ^{129}Xe nuclei bubbled through 500 mL of toluene must exceed the product of the 18.7 mT prepolarization level and the number of target toluene protons.

$$N_{^{129}Xe} P_{^{129}Xe} > 3x10^{18}$$

The number of bubbles, with a radius smaller than the critical radius, required to hyperpolarize the toluene protons to a level greater than prepolarization at 18.7 mT is therefore:

$$N_{bubbles} > \frac{N_{^{129}Xe}}{N_{^{129}Xe/bubble}} = \frac{3}{4}\frac{22.4L/mol}{\pi r^3 N_{av}}\frac{1}{f_{Xe} * 26.4\%}\frac{3x10^{18}}{P_{^{129}Xe}}.$$

5-25

Using our critical bubble radius, 0.7 mm, and a pure xenon mixture with a polarization of 10%, $3.5x10^6$ bubbles are required. This corresponds to a volume of 4.2 mL of the pure xenon gas mixture. The polarization transfer must occur within the T_1 time of the protons (on the order of 5 s) so that detection of the enhanced polarization can occur. Therefore a flow rate of around 1 mL/s or $7x10^5$ bubbles/s is required.

1 mL/s is an feasible flow rate and so it is expected that if pure xenon gas, hyperpolarized to 10% were passed through 500 mL of toluene with bubbles smaller than 0.7 mm in radius, a polarization on par with prepolarization at 18.7 mT would be observed. The situation is somewhat different, however, if we cannot generate bubbles with dimensions smaller than the critical radius. In this case, we must define a critical length, $l_{critical}$, such that only xenon nuclei within one critical length of the surface will collide with the surface a sufficient number of times during the residence time of the bubble to transfer polarization to the solvent nuclei.

$$l_{critical} = \sqrt{4D_g C_{eff} t} = \sqrt{\frac{18\eta z D_g C_{eff}}{\Delta\rho g r^2}}$$

5-26

The number of interacting xenon nuclei within a bubble, where $r > r_{max}$, is given by Eq. 5-27.

$$N_{^{129}Xe/bubble} = \frac{4}{3}\pi\left(r^3 - \left(r - l_{critical}\right)^3\right)\frac{N_{av}}{22.4L/mol} f_{Xe} * 26.4\%$$

5-27

Inserting this into Eq. 5-25 we obtain the following expression for the number of bubbles required to reach our required polarization level for $r > r_{max.}$

$$N_{bubbles} > \frac{N_{^{129}Xe}}{N_{^{129}Xe/bubble}} = \frac{3}{4}\frac{22.4L/mol}{\pi\left(r^3-\left(r-l_{critical}\right)^3\right)N_{av}}\frac{1}{f_{Xe}*26.4\%}\frac{3x10^{18}}{P_{^{129}Xe}}$$

For a large bubble of 5 mm, approximately an order of magnitude larger than the critical bubble size, the critical length is 0.2 mm and $7.2x10^4$ bubbles are required. This corresponds to a volume of 38 L of hyperpolarized xenon gas! This catastrophic increase in required gas volume is due to a combination of the inverse square dependence of residence time and inverse square dependence of collision rate, on bubble radii above the critical r_{max}. Therefore it is absolutely essential to the success of the SPINOE experiment to have bubbles below the critical size (0.7 mm under the conditions indicated above).

In the experiments undergone for this thesis we were unable to produce bubbles of less than a few mm and therefore it is not surprising that any SPINOE effect was too small to be observed. However, there are several practical reasons why, even had we managed to generate small enough bubbles, the experiment would provide *at best* a polarization equal to 18.7 mT prepolarization. Recall that the goal of these experiments is to greatly increase the polarization of the target nuclei to at least an order of magnitude above that achieved using 18.7 mT prepolarization.

The first limitation, not considered in the discussion above, is the difficulty associated with producing pure xenon gas hyperpolarized to 10% in a continuous flow regime. This can only be achieved if the xenon were first hyperpolarized in a different gas mixture (3% Xe, 2% N, 95% He, for example) and then separated out and stored for later use in a continuous flow SPINOE experiment. Depending on the storage conditions some T_1 relaxation will occur and so 10% polarization is an optimistic polarization level. (It should be noted, however, that this is not an impossible condition as the experiments presented by Appelt et al. [79] used pure xenon gas hyperpolarized to 20%.) Using a 3% Xe mixture, instead of pure xenon increases the required gas volume to 140 mL, corresponding to a flow rate of 28 mL/s. Reducing the polarization level from 10% to 2% (a more realistic projection in a continuous flow regime) the required flow rate increases to more than 100 mL/s and therefore the experiment rapidly becomes unfeasible.

The second assumption made above, which is unlikely to hold up in practice, is the idea of a total transfer of the xenon hyper-polarization to the target protons.

The polarization transfer, like that encountered in DNP, is governed by the Solomon Equations (Eq. 5-9) and so the maximum enhancement depends on many things including a coupling factor. In the system for SPINOE described above the coupling mechanism is dipolar in nature and so the theoretical maximum coupling factor would be 0.5.

The third issue is that during the discussion above we neglected the T_1 relaxation of the hyperpolarized gas which will result in irreversible depolarization of the xenon nuclei during the storage, flow and residence time periods and so decrease the polarization available for transfer.

The final issue which will decrease the observed signal is T_1 relaxation of the hyperpolarized protons during the period in which the xenon gas interacts with the solvent protons.

Therefore based both on the theoretical projections and experimental results presented in this chapter we can conclude that (a) SPINOE is not effective for hyperpolarizing large volumes of sample for NMR or MRI in the Earth's magnetic field, (b) DNP is the most promising method for signal enhancement of multi-dimensional/multi-acquisition experiments and (c) for simple pulse and collect experiments, prepolarization by a strong permanent magnet, such as a Halbach array, is a very attractive and simple signal enhancement solution.

CHAPTER 6. Simulating EFNMR Spectra

6.1. Introduction

The interpretation of NMR spectra in an ultra-low field, such as the Earth's magnetic field, is very difficult using a traditional high-field NMR approach. The non-intuitive form of Earth's field NMR spectra arises from (a) the lack of chemical shift information in all but a few very specialized cases, (b) the relative strength of indirect spin-spin coupling between hetero-nuclei compared to their difference in Larmor frequency and (c) the observation of homo-nuclear indirect spin-spin coupling due to a magnetic non-equivalence between homonuclei, which are otherwise chemically equivalent. Given the complexity of EFNMR spectra, numerical simulations provide a powerful tool for proper interpretation of the various spectral features and for determining coupling constants. In this chapter, a density matrix and product operator formalism [14; 80-82] will be presented as a useful way to numerically simulate EFNMR spectra.

6.2. The Hamiltonian in Ultra-Low Fields

In an ultra-low magnetic field, such as the Earth's magnetic field, the Hamiltonian which describes a system of N interacting spins, including both

heteronuclear and homonuclear indirect spin-spin coupling but neglecting the vanishingly small effects of chemical shift is described, in angular frequency units, by Eq. 6-1.

$$\mathcal{H} = -B_0 \sum_{i=1}^{N} \gamma_i \mathbf{I}_{zi} + 2\pi \sum_{i=1}^{N} \sum_{j>i} J_{ij} \mathbf{I}_i \bullet \mathbf{I}_j \qquad 6\text{-}1$$

In the high-field case, any heteronuclear indirect spin-spin couplings between spin *i* and spin *j* always satisfy the weak coupling condition, given by Eq. 6-2, where ω_i and ω_j are the Larmor frequencies of spin *i* and spin *j*, respectively.

$$\left| \omega_i - \omega_j \right| >> 2\pi J_{ij} \qquad 6\text{-}2$$

In addition, many observable homonuclear indirect spin-spin couplings also fulfill the weak coupling limit in high-fields because their Larmor frequencies are separated by significant chemical shifts. Under these weak coupling conditions, it is permissible to apply what is known as the secular approximation to the Hamiltonian, which states that the indirect spin-spin coupling terms are small compared to the Zeeman terms and so only the $\mathbf{I}_{zi}\mathbf{I}_{zj}$ components of the indirect spin-spin coupling interaction need to be considered. Using this approximation, the Hamiltonian is reduced to the expression in Eq. 6-3.

$$\mathcal{H}_{secular} = -B_0 \sum_{i=1}^{N} \gamma_i \mathbf{I}_{zi} + 2\pi \sum_{i=1}^{N} \sum_{j>i} J_{ij} \mathbf{I}_{zi} \mathbf{I}_{zj} \qquad 6\text{-}3$$

The modified Hamiltonian in Eq. 6-3 is diagonal in the product operator formalism and so is relatively easy to manipulate, which greatly simplifies any numerical simulations. However, in the ultra-low field case it is the exception rather than the rule that the observed indirect spin-spin couplings satisfy the weak coupling

condition (Eq. 6-2). Therefore, for simulations in the Earth's magnetic field, the secular approximation cannot be applied to the Hamiltonian and so the full Hamiltonian in Eq. 6-1 must be used.

6.3. The Density Matrix

A density matrix is a mathematical tool for representing the statistical state of a quantum system and is typically denoted by the Greek letter ρ. The density matrix is particularly useful for describing the state of an ensemble of spins and has a number of very convenient properties which can be exploited to track the evolution of a complex quantum system as a function of time and under the influence of various interactions.

A density matrix is described, in general, by an ensemble average over the various eigenstates of the system. Numerical simulations of EFNMR spectra start with an initial density matrix, $\rho(0)$, which corresponds to the statistical state of the spin ensemble at thermal equilibrium. The ensemble average of a group of spins at thermal equilibrium in the Earth's magnetic field is given by Eq. 6-4, where α denotes the various eigenstates of the system, $\mathcal{H}$ is the full interaction Hamiltonian (Eq. 6-1), k is Boltzmann's constant ($1.38\text{x}10^{-23}$ m^2 kg s^{-2} T^{-1}), T is the temperature in Kelvin and the overbar denotes an ensemble average.

$$\boldsymbol{\rho}(0) = \overline{|\alpha\rangle\langle\alpha|} = \frac{\exp\left(-\mathcal{H}/kT\right)}{Tr\left(\exp\left(-\mathcal{H}/kT\right)\right)} \qquad 6\text{-}4$$

Eq. 6-4 can be simplified by using the high temperature approximation, $|\mathcal{H}| \ll kT$, which holds true for all temperatures above a few mK. This approximation allows us to simplify the above relation with a first order Taylor expansion. The result of this expansion is shown in Eq. 6-5, where I is the spin quantum number of the nuclei in the system and **1** is the identity matrix.

$$\boldsymbol{\rho}(0)=\frac{\mathbf{1}-\mathcal{H}/kT}{Tr\left(\mathbf{1}-\mathcal{H}/kT\right)}=\frac{1}{2I+1}\left(\mathbf{1}-\frac{\mathcal{H}}{kT}\right)$$

6-5

There are two major terms in this first-order expansion. The first is the identity matrix which corresponds to the unobservable portion of the spin system that has a net magnetization of zero. No matter how we perturb the system, this term will never give rise to observable magnetization and so can be neglected. The second term: $\mathcal{H}/kT$, representing the spin excess in thermal equilibrium at a temperature T, is the observable portion of the density matrix. The goal of these numerical simulations is to correctly represent the form of the NMR spectra and the relative peak heights. Therefore any constant scaling factor can be neglected. In this way we can further simplify Eq. 6-5 as shown in Eq. 6-6.

$$\boldsymbol{\rho}(0)=\frac{1}{2I+1}\left(\mathbf{1}-\frac{\mathcal{H}}{kT}\right)\approx\mathcal{H}$$

6-6

Eq. 6-6 provides us with a starting point for our numerical simulation. In addition to this density matrix, we require a few mathematical tools. These tools provide a means of perturbing the spin ensemble from equilibrium, evolving the system with time and determining the observable magnetization at various points throughout the experiment.

It is well known that the excitation phase of a basic NMR experiment is equivalent to a rotation. A derivation of this well known principle can be found in Chapter 2. Therefore the action of RF pulses (ULF pulses in the case of EFNMR) can be included in a density matrix calculation through the use of rotation operators. Operators for rotations of a spin-1/2 particle by an angle θ about the transverse axes x and y, are listed in Eq. 6-7.

$$\mathbf{R}_x=\exp\left(-i\theta\mathbf{I}_x\right)=\begin{bmatrix}\cos\left(\frac{\theta}{2}\right) & -i\sin\left(\frac{\theta}{2}\right)\\ -i\sin\left(\frac{\theta}{2}\right) & \cos\left(\frac{\theta}{2}\right)\end{bmatrix}$$

$$\mathbf{R}_y = \exp\left(-i\theta\mathbf{I}_y\right) = \begin{bmatrix} \cos\left(\frac{\theta}{2}\right) & -\sin\left(\frac{\theta}{2}\right) \\ \sin\left(\frac{\theta}{2}\right) & \cos\left(\frac{\theta}{2}\right) \end{bmatrix}$$

6-7

All NMR experiments include time periods during which the spin system evolves with time under the influence of the time-independent spin Hamiltonian (Eq. 6-1). These evolutions are included in a density matrix calculation through the use of the evolution operator, defined in Eq. 6-8.

$$\mathbf{U}(t) = \exp\left(-i\mathcal{H}t\right)$$

6-8

If the secular approximation is used, the Hamiltonian is diagonal in this representation and so the evaluation of Eq. 6-8 is relatively straight forward. However we have already noted that the secular approximation cannot be used in the context of ultra-low field NMR and so $\mathbf{U}(t)$ must be approximated by a discrete Taylor expansion up to an arbitrary order O with a carefully chosen time step, Δt (Eq. 6-9).

$$\mathbf{U}(\Delta t) \approx \sum_{n=0}^{O} \frac{(-1)^n i^n}{n!} \mathcal{H}^n \Delta t^n = \mathbf{1} - i\mathcal{H}\Delta t - \frac{1}{2}\mathcal{H}\mathcal{H}\Delta t^2 + \ldots$$

6-9

The evolution time step, Δt, and the order of the Taylor expansion, O, in Eq. 6-9 must be chosen such that the error associated with the truncation of the Taylor Series is much less than 1. The dimensionless error for a single application of the evolution operator is on the order of $\frac{(\Delta\omega\Delta t)^O}{O!}$, where $\Delta\omega$ is the bandwidth, in angular frequency, of the calculated spectrum. This error is additive with each application of the evolution operator and so over the course of the simulation the cumulative error becomes $Err \approx 2\pi N_{pts} \frac{(\Delta\omega\Delta t)^{O-1}}{O!}$, where N_{pts} is the total number of spectral points

spanning $\Delta\omega$. For the numerically simulated NMR spectra presented in this thesis an order of $O = 28$ and evolution time steps on the order of a hundred μs were used to simulate spectra with $N_{pts} = 32768$. This gives rise to an error of 10^{-11}. The evolution operator is calculated only once at the start of the numerical simulation and so using a large value of O does not carry a significant computational time penalty.

The final tool required to use the density matrix formalism for simulating NMR spectra is the observation operator. One of the most powerful aspects of the density matrix representation is the ability to calculate the expectation value of any Hermitian operator, i.e. perform a measurement using that operator, at any point in time by simply applying the operator to the density matrix and taking the trace of the result. This is shown mathematically for an observation operator, $\mathbf{I}_{obs}$, in Eq. 6-10.

$$\left\langle \mathbf{I}_{obs} \right\rangle = Tr(\mathbf{I}_{obs}\boldsymbol{\rho}(t)) \qquad \text{6-10}$$

A measurement of the NMR signal is a combination of the projection of the density matrix onto the x axis using the spin operator, $\mathbf{I}_x$, (the real signal) and the projection along the y axis using the spin operator, $\mathbf{I}_y$ (the imaginary signal). The form of the total observation operator is therefore given by Eq. 6-11, where the sum is performed over only those groups of spins within the ensemble which we wish to observe and N^* is the number of observed spin groups.

$$\mathbf{I}_{obs} = \sum_{n=1}^{N^*} (\mathbf{I}_{xn} + i\mathbf{I}_{yn}) \qquad \text{6-11}$$

An example, in which we would not wish to observe all of the groups of spins represented in the density matrix, is if we had a system of protons coupled to a ^{13}C. The ^{13}C would be included in the density matrix because it is coupled to the protons but it would neither be excited (rotated) by the ULF pulses nor observed in the final stage of the experiment.

6.4. Simulating EFNMR Experiments

Implementing a simulation of any given EFNMR experiment is relatively straight forward using the density matrix formalism outlined above. For example, consider a basic pulse and collect experiment, where a 90˚ excitation is applied to a system of spins in thermal equilibrium and the subsequent evolution as a function of time is observed with a dwell time, Δt_2.

The first step is to define the spin system. This includes the following information:

- Number and type of nuclei
- Indirect spin-spin coupling constants
- Field strength, B_E
- Relaxation time, T_2

The next step is to define the parameters of the experiment. This includes:

- Sampling time, Δt_2
- Number of sample points, n_2
- Evolution time step, Δt
- Order of evolution operator expansion, O

[Note: the sampling time must be an integer multiple of the evolution time step in order to properly evolve and sample the system.]

Next, we must generate the product spin operators, $\mathbf{I}_{xn}$, $\mathbf{I}_{yn}$ and $\mathbf{I}_{zn}$, for each spin in the system. A product operator for a system of N spin-1/2 nuclei is represented by a matrix with dimensions: 2^N x 2^N and is defined using the inner product of operators acting on each of the individual spins. For example, the product operator $\mathbf{I}_{zn}$, for a system of N spin-1/2 nuclei, is equal to the inner product between a series of (n-1) 2 x 2 identity operators, $\mathbf{1}$, the spin operator $\mathbf{I}_z$ and a second series of (N-n) 2 x 2 identity operators. If $n = 2$ and $N = 2$, this would be:

$$\mathbf{I}_{z2} = \mathbf{1} \otimes \mathbf{I}_z = \begin{bmatrix} 1 & 0 \\ 0 & 1 \end{bmatrix} \otimes \begin{bmatrix} \frac{1}{2} & 0 \\ 0 & -\frac{1}{2} \end{bmatrix}$$

$$\mathbf{I}_{z2} = \begin{bmatrix} 1 \otimes \begin{bmatrix} \frac{1}{2} & 0 \\ 0 & -\frac{1}{2} \end{bmatrix} & 0 \otimes \begin{bmatrix} \frac{1}{2} & 0 \\ 0 & -\frac{1}{2} \end{bmatrix} \\ 0 \otimes \begin{bmatrix} \frac{1}{2} & 0 \\ 0 & -\frac{1}{2} \end{bmatrix} & 1 \otimes \begin{bmatrix} \frac{1}{2} & 0 \\ 0 & -\frac{1}{2} \end{bmatrix} \end{bmatrix} = \begin{bmatrix} \frac{1}{2} & 0 & 0 & 0 \\ 0 & -\frac{1}{2} & 0 & 0 \\ 0 & 0 & \frac{1}{2} & 0 \\ 0 & 0 & 0 & -\frac{1}{2} \end{bmatrix}$$

In this two spin example the final product operator is a 4 x 4 matrix. Similarly, we can use inner products to calculate product operator matrices for the rotation operator which will represent our 90_x pulse. This product operator is the inner product of $\mathbf{R}_x(90^\circ)$ (Eq. 6-7) operators for the spins which are excited by the pulse and identity operators, **1**, for the spins which are not excited by the pulse.

The observation matrix is calculated next using the $\mathbf{I}_x$ and $\mathbf{I}_y$ product operators for the groups of spins to be observed and Eq. 6-11.

The full Hamiltonian (Eq. 6-1) is calculated using the spin product operators and indirect spin-spin coupling constants as defined at the start of the simulation. The initial density matrix can then be calculated as $\boldsymbol{\rho}(0) = \mathcal{H}$. The final operator to be calculated is the evolution operator (Eq. 6-9). It is advisable at this point to confirm that the error term is much less than 1.

To start the experiment we apply the rotation operator to the density matrix by "sandwiching" the density matrix, $\boldsymbol{\rho}(0)$ between the operator, **R**, and its Hermitian conjugate, $\mathbf{R}^\dagger$.

$$\boldsymbol{\rho}\left(0^+\right) = \mathbf{R}_x \boldsymbol{\rho}(0) \mathbf{R}_x{}^\dagger$$

6-12

Note the designation of "$^+$" on argument of the density matrix indicates that this is the density matrix immediately following the rotation. This notation is used because in this context, the rotation is considered to be instantaneous and so involves no increase in time.

Following the rotation we must evolve the system for the sample time period Δt_2. In almost all cases the evolution time, Δt, will be less than the sample time and

therefore several applications of the evolution operator will be required to evolve for the time period Δt_2. To evolve the system by a time Δt_2 we perform the operation in Eq. 6-13, where the evolution operator $\mathbf{U}(\Delta t)$ and it's conjugate $\mathbf{U}^{\dagger}(\Delta t)$ are applied m times.

$$\boldsymbol{\rho}(\Delta t_2) = \mathbf{U}(\Delta t)...\mathbf{U}(\Delta t)\boldsymbol{\rho}(0^+)\mathbf{U}^{\dagger}(\Delta t)...\mathbf{U}^{\dagger}(\Delta t), \qquad 6\text{-}13$$

$$m = \frac{\Delta t_2}{\Delta t}$$

Next we take a measurement of the observable magnetization. This is done by multiplying the current density matrix by the observation operator matrix and taking the trace. An exponential decay, with time constant T_2, is added to the observation step to take into account spectral broadening due to transverse relaxation.

$$S(\Delta t_2) = \langle \mathbf{I}_{obs} \rangle = Tr(\mathbf{I}_{obs}\boldsymbol{\rho}(\Delta t_2)) \exp\left(-\frac{\Delta t_2}{T_2}\right) \qquad 6\text{-}14$$

To complete the experiment, we repeat the evolution (Eq. 6-13) and observation (Eq. 6-14) steps n_2 times. The result of this sampling step is a complex vector with n_2 points that corresponds to our FID signal. It can be Fourier transformed to obtain the full spectrum.

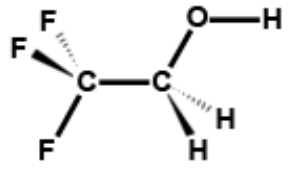

Figure 6.1 A diagram of the 2,2,2-trifluoroethanol molecule

An example of a simulated 1D spectrum of 2,2,2-trifluoroethanol (pictured in

Figure 6.1) acquired in an Earth's field of 53.9 μT with a coupling constant of 8.5 Hz between the C^1H_2 and $C^{19}F_3$ nuclei is shown in Figure 6.2. All protons and the fluorine nuclei were rotated and observed in this example. An experimental spectrum is presented in Figure 6.3 for comparison with the simulation.

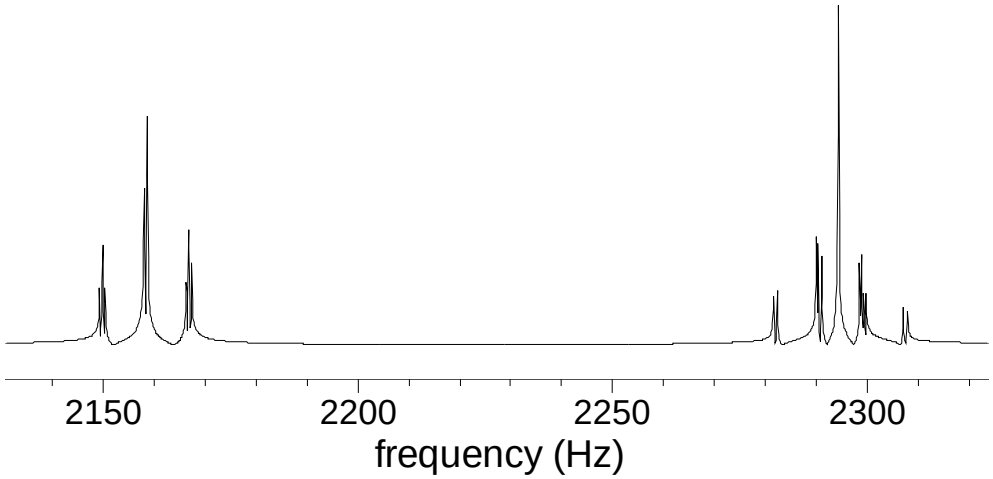

Figure 6.2 A simulated spectrum of 2,2,2-trifluoroethanol at 53.9 μT with a hetero-nuclear spin-spin coupling constant: $^3J(^1H,^{19}F) = 8.5$ Hz.

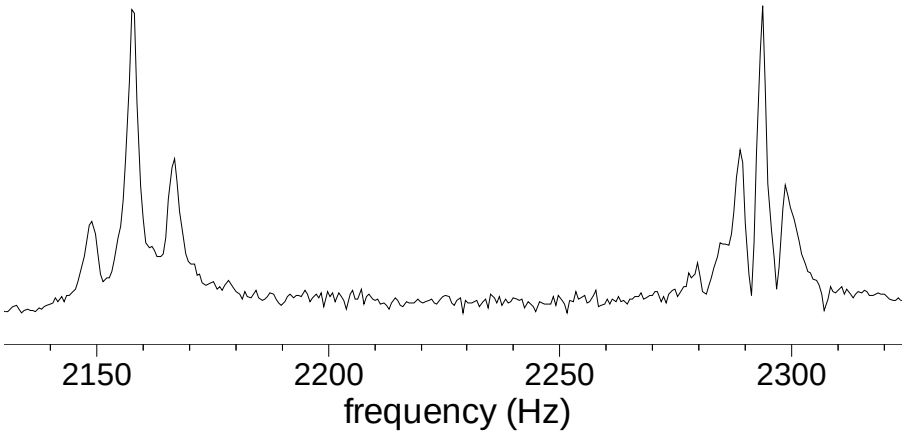

Figure 6.3 An example experimental spectrum of 2,2,2-trifluoroethanol for comparison with the simulation in Figure 6.2.

The density matrix simulation macro was programmed in Prospa v2.1 (Magritek Limited, New Zealand). A copy of the simulation code can be found in Appendix A. Simulation times were prohibitively long on a basic laptop computer for any more than six spins in 2D and seven in 1D. However, if in 1D the Hamiltonian is

simplified to only calculate the deviation in frequency from a central frequency, thereby reducing the bandwidth of the calculation and so the number of evolution points required, systems with up to 8 or 9 spins are viable. It is important to note that (a) the full Hamiltonian must be used to define the initial density matrix and (b) this same trick cannot be used in 2D because of the aliasing which occurs in the second under-sampled frequency dimension. 2D experiments and simulations will be discussed in more detail in Chapter 8.

CHAPTER 7. Analysis of EFNMR Spectra in 1D

7.1. Introduction

One of the distinguishing features of ^{1}H NMR spectroscopy carried out in the relatively weak Earth's magnetic field is the observation of strong indirect spin-spin (J) coupling between heteronuclei. While the NMR spectra of tightly coupled nuclei of the same species, so-called AB spectra, are commonly observed using high field laboratory NMR spectrometers, the difference in Larmor frequency between heteronuclei in super-conducting magnets is such that the weak coupling condition is always satisfied for heteronuclear indirect spin-spin coupling. Therefore working in the Earth's magnetic field provides a unique opportunity to observe and analyze the spectra of tightly coupled nuclei of differing spin.

As described in Chapter 6, density matrix simulations can be used to calculate the form of spectra acquired in the Earth's magnetic field. This is a very useful tool but in some cases a more intuitive understanding of strongly-coupled Earth's field NMR spectra can be obtained using a different approach. For strongly coupled systems of heteronuclei, perturbation theory can be used to predict the form of 1D EFNMR spectra and to promote an understanding of the connection between the various spectral features and the underlying quantum states of the system.

The work presented in this chapter was carried out with the invaluable assistance of Professor Roderick Wasylishen from the University of Alberta,

Edmonton, AB, Canada. The research was part of a collaboration which included a one week research visit to the University of Alberta by Meghan Halse in August 2008 followed by a visit to Victoria University of Wellington by Prof. Wasylishen in February 2009. Additional assistance with experiments carried out at the University of Alberta was provided by Brett Feland and Dr. Guy Bernard.

7.2. Time-Independent Perturbation Theory

Consider a time-independent Hamiltonian, $\mathcal{H}_0$, for which the solution of the Schrödinger equation is known exactly.

$$\mathcal{H}_0 \left| n^0 \right\rangle = E_n^0 \left| n^0 \right\rangle$$

7-1

Now consider a time-independent perturbation to this Hamiltonian, $\mathcal{H}_1$. Under these conditions we write the full Hamiltonian, $\mathcal{H}$, as in Equation 7-2, where λ is a dimensionless quantity which ranges in value from 0 (no perturbation) to 1 (full perturbation).

$$\mathcal{H} = \mathcal{H}_0 + \lambda \mathcal{H}_1$$

7-2

The time-independent Schrödinger equation for the full Hamiltonian (Eq. 7-2) is therefore given by Eq. 7-3.

$$\left(\mathcal{H}_0 + \lambda \mathcal{H}_1 \right) \left| n \right\rangle = E_n \left| n \right\rangle$$

7-3

The eigenvalues and eigenvectors of the full Hamiltonian can be written as linear combinations of the unperturbed eigenfunctions of $\mathcal{H}_0$.

$$|n\rangle = N(\lambda)\left(|n^0\rangle + \sum_{k\neq n} C_{n,k}(\lambda)|k^0\rangle\right)$$

7-4

In Eq. 7-4 $N(\lambda)$ is a normalization factor. $N(0)$ is set to zero to fulfill the condition: $|n\rangle \rightarrow |n^0\rangle$ as $\lambda \rightarrow 0$. The constants, $C_{n,k}(\lambda)$, can be represented as a power series in λ as shown in Eq. 7-5. Note that $C_{n,k}(0)$ is set to zero to fulfill the condition: $|n\rangle \rightarrow |n^0\rangle$ as $\lambda \rightarrow 0$.

$$C_{n,k}(\lambda) = \lambda C^{(1)}_{n,k} + \lambda^2 C^{(2)}_{n,k} + \lambda^3 C^{(3)}_{n,k} + \lambda^4 C^{(4)}_{n,k} + \ldots$$

7-5

The eigenvalues of Eq. 7-3, E_n, can also be written as a power series in λ.

$$E_n = E^0_n + \lambda E^{(1)}_n + \lambda^2 E^{(2)}_n + \lambda^3 E^{(3)}_n + \lambda^4 E^{(4)}_n + \ldots$$

7-6

Using Eq. 7-4 and Eq. 7-6, we can expand the Schrödinger equation (Eq. 7-3) and write it explicitly in powers of λ.

$$(\mathcal{H}_0 + \lambda\mathcal{H}_1)\left(|n^0\rangle + \sum_{k\neq n}\lambda C^{(1)}_{n,k}|k^0\rangle + \sum_{k\neq n}\lambda^2 C^{(2)}_{n,k}|k^0\rangle + \ldots\right)$$

$$= \left(E^0_n + \lambda E^{(1)}_n + \lambda^2 E^{(2)}_n + \ldots\right)\left(|n^0\rangle + \sum_{k\neq n}\lambda C^{(1)}_{n,k}|k^0\rangle + \sum_{k\neq n}\lambda^2 C^{(2)}_{n,k}|k^0\rangle + \ldots\right)$$

7-7

Identifying powers of λ in Eq. 7-7 provides a set of equations from which we can determine the energies, $E_n^{(i)}$, and the constants, $C_{n,k}^{(i)}$. The zeroth-order in λ corresponds to the unperturbed solution of the Schrödinger Equation (Eq. 7-1). The first-order in λ yields Eq. 7-8.

$$\mathcal{H}_0 \sum_{k \neq n} C_{n,k}^{(1)} \left| k^0 \right\rangle + \mathcal{H}_1 \left| n^0 \right\rangle = E_n^0 \sum_{k \neq n} C_{n,k}^{(1)} \left| k^0 \right\rangle + E_n^{(1)} \left| n^0 \right\rangle .$$

7-8

In order to determine the first-order energy, $E_n^{(1)}$, we take the scalar product of Eq. 7-8 with the eigenfunctions, $\left| n^0 \right\rangle$, of the unperturbed Hamiltonian. Following simplification we find that the first order energy is simply the diagonal elements of the perturbation Hamiltonian, $\mathcal{H}_1$, written in the basis of the unperturbed eigenfunctions, $\left| n^0 \right\rangle$.

$$E_n^{(1)} = \left\langle n^0 \left| \mathcal{H}_1 \right| n^0 \right\rangle$$

7-9

To determine the coefficient, $C_{n,k}^{(1)}$, we take the scalar product of Eq. 7-8 with the eigenfunction, $\left| k^0 \right\rangle$, of the unperturbed Hamiltonian, where $k \neq n$.

$$C_{n,k}^{(1)} = \frac{\left\langle k^0 \left| \mathcal{H}_1 \right| n^0 \right\rangle}{E_n^0 - E_k^0}$$

7-10

Repeating this procedure for the second, third and fourth powers of λ we obtain Eqs. 7-11 and 7-12.

$$E_n^{(2)} = \sum_{k \neq n} \frac{\left\langle n^0 \left| \mathcal{H}_1 \right| k^0 \right\rangle \left\langle k^0 \left| \mathcal{H}_1 \right| n^0 \right\rangle}{E_n^0 - E_k^0}$$

$$E_n^{(3)} = \sum_{j \neq n} \sum_{k \neq n} \frac{\left\langle k^0 \left| \mathcal{H}_1 \right| n^0 \right\rangle \left(\left\langle j^0 \left| \mathcal{H}_1 \right| k^0 \right\rangle - E_n^{(1)} \delta_{jk} \right)}{E_n^0 - E_k^0} \frac{\left\langle n^0 \left| \mathcal{H}_1 \right| j^0 \right\rangle}{E_n^0 - E_j^0}$$

$$E_n^{(4)} = \sum_{j\neq n}\sum_{k\neq n}\left[\frac{\left\langle n^0\left|\mathcal{H}_1\right|k^0\right\rangle\left\langle j^0\left|\mathcal{H}_1\right|n^0\right\rangle\left|\left\langle k^0\left|\mathcal{H}_1\right|n^0\right\rangle\right|^2}{\left(E_n^0-E_k^0\right)^2}\times \frac{\left|\left\langle n^0\left|\mathcal{H}_1\right|n^0\right\rangle\delta_{jk}-\left\langle k^0\left|\mathcal{H}_1\right|j^0\right\rangle\right|^2-\left|\left\langle j^0\left|\mathcal{H}_1\right|n^0\right\rangle\right|^2}{\left(E_n^0-E_j^0\right)}\right]$$

7-11

$$C_{n,k}^{(2)} = \sum_{j\neq n}\frac{\left\langle j^0\left|\mathcal{H}_1\right|n^0\right\rangle\left(\left\langle k^0\left|\mathcal{H}_1\right|j^0\right\rangle-E_n^{(1)}\delta_{jk}\right)}{\left(E_n^0-E_k^0\right)\left(E_n^0-E_j^0\right)}$$

$$C_{n,k}^{(3)} = \sum_{j\neq n}\sum_{k\neq n}\frac{\left\langle j^0\left|\mathcal{H}_1\right|n^0\right\rangle\left|\left\langle n^0\left|\mathcal{H}_1\right|n^0\right\rangle\delta_{jk}-\left\langle k^0\left|\mathcal{H}_1\right|j^0\right\rangle\right|^2-\left\langle k^0\left|\mathcal{H}_1\right|n^0\right\rangle\left|\left\langle j^0\left|\mathcal{H}_1\right|n^0\right\rangle\right|^2}{\left(E_n^0-E_j^0\right)^2\left(E_n^0-E_k^0\right)}$$

7-12

7.3. Strong Heteronuclear Indirect Spin-Spin Coupling

7.3.1. Indirect Spin-Spin Coupling Analysis using Perturbation Theory

In 1956, W. A. Anderson [83] used perturbation theory to derive expressions which could be used to predict the form of tightly coupled NMR spectra for systems of chemically non-equivalent spins in laboratory magnetic fields. Using a similar approach, time-independent perturbation theory can be used to estimate the NMR spectra of groups of nuclei in the Earth's magnetic field which are coupled via hetero-nuclear indirect spin-spin coupling. In this case the unperturbed Hamiltonian (in angular frequency units) is simply the sum of the Zeeman terms for each of the spins in the system.

$$\mathcal{H}_0 = -\sum_R \gamma_R B_E \mathbf{I}_{zR}$$

7-13

The eigenvalues of this Hamiltonian are given by Eq. 7-14 where *R* refers to

each group (A, B, C…) of magnetically equivalent spins in the system and m_{Rn} denotes all of the values of the quantum numbers, m_A, m_B, m_C… of the system.

$$E_n^0 = -\sum_R \gamma_R B_E m_{Rn}$$

7-14

No chemical shift term is included in Eq. 7-13 because, except in a few unusual cases such as hyperpolarized ^{129}Xe gas [56], chemical shifts are vanishingly small in the Earth's field. Also it is important to note that this approach does not take into account the possibility of chemically equivalent but magnetically non-equivalent nuclei. Hence, in Earth's field NMR, this approach only applies to heteronuclear indirect spin-spin coupling. To include the effects of chemically equivalent but magnetically non-equivalent nuclei, the secular terms of the indirect spin-spin coupling Hamiltonian must be included in the unperturbed Hamiltonian as demonstrated by Hecht [84].

The unperturbed eigenfunctions, which correspond to the eigenvalues in Eq. 7-14, are the product operator kets $\left|m_A, m_B, m_C ...\right\rangle$, where the individual terms in the product operator kets represent groups of magnetically equivalent spins. Each of these groups of magnetically equivalent spins are characterized by: (a) a total spin angular momentum quantum number I_R, which represents the vector sum of the individual spin angular momenta of the constituent spins and so can have a plurality of values and (b) the corresponding quantum number m_R, which the takes values $m_R = -I_R, -I_R+1 \ldots +I_R$. For example, a group of two magnetically equivalent $I = 1/2$ nuclei would be represented by total angular momentum values $I_R = 1$ and $I_R = 0$ with corresponding sets of azimuthal angular momentum values: $m_R = -1, 0, 1$ and $m_R = 0$. This grouping of magnetically equivalent nuclei is possible because, by definition, magnetically equivalent nuclei have identical Larmor frequencies as well as identical indirect spin-spin coupling constants with respect to all of the other nuclei in the system. Therefore any indirect spin-spin coupling between these magnetically equivalent spins is unobservable.

In the case of heteronuclear indirect spin-spin coupling, the perturbation Hamiltonian is given by Eq. 7-15, where J_{RS} is the indirect spin-spin coupling

constant (in frequency units) between the *R* and *S* groups of magnetically equivalent spins. Note that this perturbation Hamiltonian deviates from that used by Anderson [83] by the inclusion of the $\mathbf{I}_R^-\mathbf{I}_S^+$ term and the ½ factor.

$$\mathcal{H}_1 = \sum_R \sum_{S>R} 2\pi J_{RS} \left\{ \mathbf{I}_{zR}\mathbf{I}_{zS} + \tfrac{1}{2}\left(\mathbf{I}_R^+\mathbf{I}_S^- + \mathbf{I}_R^-\mathbf{I}_S^+ \right) \right\}$$

7-15

Inserting Eq. 7-15 into Eq. 7-9 we find that the first-order energy difference is given by Eq. 7-16.

$$E_n^{(1)} = \sum_R \sum_{S>R} 2\pi J_{RS} m_{Rn} m_{Sn}$$

7-16

The first-order perturbation theory result (Equation 7-16) is the solution to the weak indirect spin-spin coupling problem, in which the secular approximation is applied to the full Hamiltonian. Heteronuclear indirect spin-spin coupling in the relatively weak Earth's magnetic field rarely fulfills the weak coupling condition and so higher-order terms in the perturbation theory expansion must be included to effectively model the system. The second-, third- and fourth-order energy terms are given below (Eq. 7-17) for the case of heteronuclear indirect spin-spin coupling in the Earth's magnetic field. As mentioned above, these results were derived following the method used by Anderson [83]. Upon re-deriving the expressions for the second- and third-order energies (and the corresponding transition frequencies) some differences were found between our expressions and the results presented by Anderson. Our expressions for the perturbation energies (Eq. 7-17) and transition frequencies (Eq. 7-19) were found to be in much closer agreement with density matrix simulations than the previous expressions of Anderson.

$$E^{(2)}(I_A, m_A, I_B, m_B \ldots)$$
$$= -4\pi^2 \sum_R \sum_{S>R} \frac{J_{RS}^2}{2(\omega_R - \omega_S)} \left[m_R \left(I_S^2 + I_S - m_S^2 \right) - m_S \left(I_R^2 + I_R - m_R^2 \right) \right]$$

$$E^{(3)}(I_A, m_A, I_B, m_B \ldots)$$
$$= -8\pi^3 \sum_R \sum_{S>R} \frac{J_{RS}^3}{2(\omega_R - \omega_S)^2} \left[F(R)F(S) + F(R) m_S (1 - m_S + m_R) + F(S) m_R (1 - m_R + m_S) \right]$$
$$+ 8\pi^3 \sum_R \sum_{S>R} \sum_{T>S} \frac{J_{RS} J_{RT} J_{ST}}{(\omega_R - \omega_S)(\omega_R - \omega_T)(\omega_S - \omega_T)} \begin{bmatrix} m_S m_T F(R)(\omega_S - \omega_T) \\ - m_R m_T F(S)(\omega_R - \omega_T) \\ + m_R m_S F(T)(\omega_R - \omega_S) \end{bmatrix}$$

$$E_n^{(4)} * = \frac{J_{RS}^4}{4(\omega_R - \omega_S)^3} \begin{bmatrix} F(S)F(R)\left(F(S)m_R - F(R)m_S + 4(m_R - m_S)\right) \\ + F^2(S) {m_R}^2 - F^2(R) {m_S}^2 - 2F(S) m_R (1 - m_R + m_S)^2 \\ + 2F(R) m_S (1 + m_R - m_S)^2 \end{bmatrix}$$

7-17

$$\omega_R = \gamma_R B_E$$
$$F(R) = I_R (I_R + 1) - m_R (m_R + 1)$$

All of the energy terms presented in Eq. 7-17 are summed over an arbitrary number of groups of magnetically equivalent spins with the exception of the fourth-order energy term, highlighted by a "*". This fourth-order term has been calculated for a system of <u>two</u> groups of magnetically equivalent spins only.

The energy terms in Eq. 7-17 can be used, along with the selection rules listed in Eq. 7-18, to determine the transition frequencies of a system containing two groups of magnetically equivalent spins.

$$\Delta I_R = 0; \Delta I_S = 0; \Delta m_R = 0; \Delta m_S = \pm 1$$

7-18

The selection rules in Eq. 7-18 represent a single quantum coherence of the *S* (^{1}H) spins. This single quantum coherence corresponds to no change in the total angular momentum quantum number of the detected *S* spins, I_S, but a change of ±1 in

the azimuthal angular momentum quantum number, m_S. The R spins are not detected and so the selection rules do not allow for changes in I_R or m_R. Remember that if there is more than one magnetically equivalent S nucleus, the total angular momentum quantum number is the vector sum of the spin quantum numbers of the individual spins and so a plurality of values will result. All of the permutations of I_S and m_S must be included when calculating the transition frequencies for a given spin system.

$$\omega_n^0 = \gamma_S B_E$$
$$\omega_n^{(1)} = -J_{RS} m_R$$
$$\omega_n^{(2)} = -\frac{J_{RS}^2}{2(\omega_R - \omega_S)}\left[I_R^2 + I_R - m_{Rn}(m_{Rn} - 1) + 2m_R m_S\right]$$
$$\omega_n^{(3)}$$
$$= \frac{J_{RS}^3}{2(\omega_R - \omega_S)^2}\left[F(R)(m_{Rn} - 4m_{Sn} - 2) + F(S)m_{Rn} - 2m_{Rn}(m_{Sn} + 1)(2 - m_{Rn} + m_{Sn})\right]$$

7-19

The probabilities of a ^{1}H transition between an initial state $|n\rangle$ and final state $|n'\rangle$ can be calculated according Eq. 7-20, where $\mathbf{I}_x$ is a product operator which acts on the observed nuclei only, i.e. the protons. The initial and final states can be calculated using the expansion in Eq. 7-4 of the perturbed states in terms of the unperturbed (product operator) states.

$$P_{nn'} = \left|\langle n|\mathbf{I}_x|n'\rangle\right|^2$$

7-20

For the spectra calculated using perturbation theory in this thesis, the transition probabilities for the various ^{1}H transitions were not explicitly calculated and it is assumed that all transitions are equally probable. In the simulations and calculations presented herein, we compare only peak positions not peak integrals or heights.

7.3.2. Strongly Coupled Two Spin System

In this chapter we wish to explore the situation of a group of $I = ½$ nuclei (e.g. ^{1}H's) coupled to a quadrupolar nucleus such as ^{14}N ($I = 1$), ^{10}B ($I = 3$) or ^{11}B ($I = 3/2$). In order to determine the validity of the perturbation theory approach to modeling this problem we first take a simple two spin case, which can be solved exactly through digitalization of the full Hamiltonian, and compare the resultant exact transition frequencies with those given by first-, second- and third-order perturbation theory.

$$
\begin{aligned}
E_1 &= \frac{3}{2}\nu_{^{11}B} + \frac{1}{2}\nu_{^{1}H} + \frac{3}{4}J \\
E_2 &= -\nu_{^{11}B} - \frac{1}{4}J + \frac{1}{2}\sqrt{\left(\nu_{^{1}H} - \nu_{^{11}B}\right)^2 - 2J\left(\nu_{^{1}H} - \nu_{^{11}B}\right) + 4J^2} \\
E_3 &= -\nu_{^{11}B} - \frac{1}{4}J - \frac{1}{2}\sqrt{\left(\nu_{^{1}H} - \nu_{^{11}B}\right)^2 - 2J\left(\nu_{^{1}H} - \nu_{^{11}B}\right) + 4J^2} \\
E_4 &= -\frac{1}{4}J + \frac{1}{2}\sqrt{\left(\nu_{^{1}H} - \nu_{^{11}B}\right)^2 + 4J^2} \\
E_5 &= -\frac{1}{4}J - \frac{1}{2}\sqrt{\left(\nu_{^{1}H} - \nu_{^{11}B}\right)^2 + 4J^2} \\
E_6 &= \nu_{^{11}B} - \frac{1}{4}J + \frac{1}{2}\sqrt{\left(\nu_{^{1}H} - \nu_{^{11}B}\right)^2 + 2J\left(\nu_{^{1}H} - \nu_{^{11}B}\right) + 4J^2} \\
E_7 &= \nu_{^{11}B} - \frac{1}{4}J - \frac{1}{2}\sqrt{\left(\nu_{^{1}H} - \nu_{^{11}B}\right)^2 + 2J\left(\nu_{^{1}H} - \nu_{^{11}B}\right) + 4J^2} \\
E_8 &= -\frac{3}{2}\nu_{^{11}B} - \frac{1}{2}\nu_{^{1}H} + \frac{3}{4}J
\end{aligned}
$$

7-21

$$
\begin{aligned}
\nu_{^{11}B} &= \frac{1}{2\pi}\gamma_{^{11}B}B_E \\
\nu_{^{1}H} &= \frac{1}{2\pi}\gamma_{^{1}H}B_E
\end{aligned}
$$

7-22

Expressions for the exact energy levels for the coupled ^{11}B – ^{1}H system are presented in Eq. 7-21, where ν_H and ν_B are the Larmor frequencies in Hertz, as defined by Eq. 7-22.

While this is a strongly coupled system, the Zeeman terms are dominant and so each of the eigenstates of this system are closely associated with, but not exactly

equal to, a product operator state of the form $\left|m_{^1H}, m_{^{11}B}\right\rangle$, as defined by Equations 7-23. By inspection of these product operator states, we find that there are four allowed transitions for the observation of the proton ($\Delta m_H = \pm 1$). These transitions are $T_{16} = E_1 - E_6$, $T_{38} = E_3 - E_8$, $T_{52} = E_5 - E_3$ and $T_{74} = E_7 - E_4$.

$$
\begin{aligned}
|1\rangle &\approx \left|\tfrac{1}{2}, \tfrac{3}{2}\right\rangle \\
|2\rangle &\approx \left|-\tfrac{1}{2}, -\tfrac{1}{2}\right\rangle \\
|3\rangle &\approx \left|\tfrac{1}{2}, -\tfrac{3}{2}\right\rangle \\
|4\rangle &\approx \left|-\tfrac{1}{2}, \tfrac{1}{2}\right\rangle \\
|5\rangle &\approx \left|\tfrac{1}{2}, -\tfrac{1}{2}\right\rangle \\
|6\rangle &\approx \left|-\tfrac{1}{2}, \tfrac{3}{2}\right\rangle \\
|7\rangle &\approx \left|\tfrac{1}{2}, \tfrac{1}{2}\right\rangle \\
|8\rangle &\approx \left|-\tfrac{1}{2}, -\tfrac{3}{2}\right\rangle
\end{aligned}
$$

7-23

Using Equations 7-21 we can compare the exact transition frequencies with those predicted by first-, second- and third-order perturbation theory for this two spin system as a function of the relative strength of the indirect spin-spin coupling between the spins.

In Figure 7.1 the difference between the exact ^{1}H transition frequencies and the transition frequencies calculated from first-order (short dashed line), second-order (long dashed line) and third-order (solid line) perturbation theory is shown as a function of the indirect spin-spin coupling constant between the ^{1}H and the ^{11}B nuclei. J is expressed as a fraction of the difference between the Larmor frequency of the protons and that of the ^{11}B nucleus (1561 Hz at 54 μT). The shaded area in Figure 7.1 indicates the range of frequency differences which are unobservable in an experimental spectrum, assuming a resolution of 0.1 Hz. Using this region as a guide, we can define values of J for which (A) first-order, (B) second-order and (C) third-order perturbation theory accurately models the observed spectrum.

A similar comparison can be done for the system of an I = 1/2 nucleus (^{1}H) coupled to an I = 1 nucleus (^{14}N) using the exact energy levels and transition frequencies calculated for the coupled free electron and ^{14}N nucleus system discussed

in Chapter 5, where the hyperfine coupling constant, A, is replaced by the indirect spin-spin coupling constant, J. The results of this calculation are comparable to those presented in Figure 7.1.

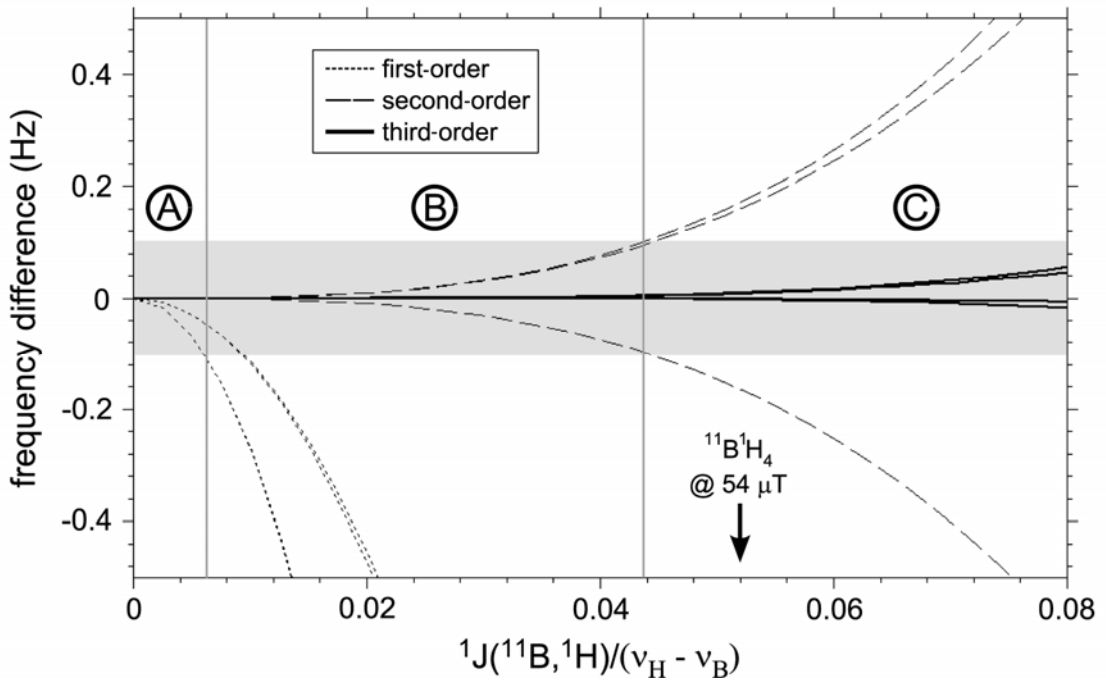

Figure 7.1 The difference between the exact ^{1}H transition frequencies and those predicted by first-order (short dashed line) second-order (long dashed line) and third-order (solid line) perturbation theory as a function of the relative strength of the indirect spin-spin coupling constant for a single ^{1}H nucleus coupled to a single ^{11}B nucleus in a field of 54 μT. The shaded area highlights the range of unobservable frequency differences which are less than the target resolution of the experiment (0.1Hz). Using this target resolution as a guide, the plot can be divided into the regions A, B and C in which first-, second- and third- order perturbation theory (respectively) can be used to accurately model the spin system.

For the $NaBH_4$ sample examined in section 7.3.6, $^1J(^1H,^{11}B)$ = 80.9 Hz is 5.2% of the difference in Larmor frequency between ^{11}B and ^{1}H in a field of 54 μT. Therefore it is expected that this spectrum can be described using third-order perturbation theory. For the NH_4NO_3 sample examined in section 7.3.5, $^1J(^1H,^{14}N)$ = 52.75 Hz is approximately 2.5% of the difference in Larmor frequency between ^{14}N

and ^{1}H in a field of 54 μT. Therefore it is expected that this spectrum can be described using second-order perturbation theory.

7.3.3. Multiple ^{1}H Spin Systems: $^{14}N^{1}H_4$ and $^{11}B^{1}H_4$

While the two spin example in section 7.3.2 is informative, it does not fully illustrate the effect of the second- and third-order energy contributions for an AB_n spectrum where $n > 1$ and A is a quadrupolar ($I > ½$) nucleus. Due to the complexity involved in obtaining closed form analytical solutions to the Schrödinger equation for large spin systems under the influence of strong indirect spin-spin coupling, we use density matrix simulations to generate the exact spectra for the case of more than two spins and compare these results with perturbation theory.

Consider the case of $^{11}B^{1}H_4^-$, where we have an $I = 3/2$ nucleus coupled to four $I = 1/2$ nuclei with a coupling constant of $^{1}J(^{11}B,^{1}H) = 80.3$ Hz. In Figure 7.2 we present calculated and simulated ^{1}H NMR spectra of this anion acquired in a field of 54 μT. The spectrum calculated using first-order perturbation theory (Figure 7.2a) contains four lines, separated by $^{1}J(^{11}B,^{1}H)$, which correspond to the four spin states of the ^{11}B nucleus (m = +3/2, +1/2, -1/2 and -3/2). This is the form of the $^{11}B^{1}H_4^-$ spectrum in the high-field case, where the spins are weakly coupled and so the presence of a plurality of magnetically equivalent protons has no observed effect on the spectrum.

In the second-order perturbation theory case (Figure 7.2b) the complexity of the spectrum is dramatically increased, with each of the four first-order lines further split into quartets. It is also interesting to note that in the spectrum calculated from second-order perturbation theory the four multiplets are shifted to a higher frequency, relative to the first-order peaks, and are no longer equally spaced.

The additional peak multiplicity in the second-order perturbation theory case is due to the presence of the four magnetically equivalent protons coupled to the ^{11}B nucleus. This multiplicity in tightly coupled heteronuclear systems has previously been observed in the Earth's magnetic field in strongly coupled ^{13}C-^{1}H systems [58]. The spectrum calculated from second-order perturbation theory does not capture the full 6-fold multiplicity predicted for this system by the vector model of Appelt et al. [59]. According to this model, if we consider one of the four protons as the observed

proton, the expected multiplicity is explained by the total angular momentum states of the remaining three protons. The total angular momentum quantum number of these spins can have a value of 3/2 or 1/2 with corresponding azimuthal quantum numbers of m = 3/2, 1/2, -1/2, -3/2 and m = 1/2, -1/2, respectively. To second-order, the states I = 3/2, m = 1/2 and I = 1/2, m = 1/2 are degenerate. So too are the states I = 3/2, m = -1/2 and I = 1/2, m = -1/2. As a result, only four lines are observed in the calculated spectrum instead of the full six.

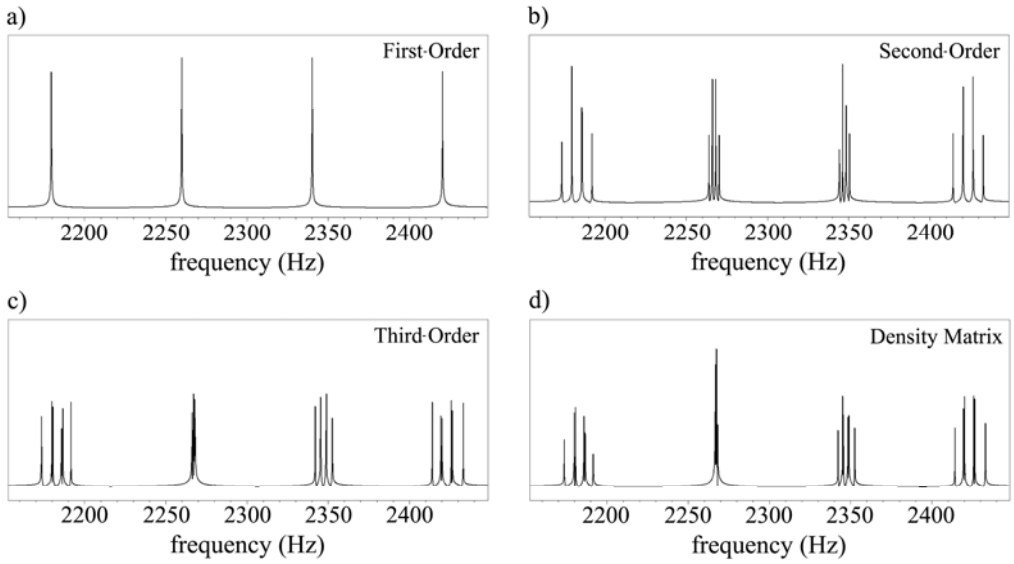

Figure 7.2 Calculated and simulated ^{1}H NMR spectra of $^{11}B^{1}H_4^-$ in a field of 54 μT with $^{1}J(^{11}B,^{1}H)$ = 80.3 Hz using: (a) first-order perturbation theory, (b) second-order perturbation theory, (c) third-order perturbation theory and (d) a density matrix simulation.

In the spectrum calculated from third-order perturbation theory (Figure 7.2c) the full 6-fold multiplicity of the set of four peaks is observed. The most striking feature of this spectrum is the strong asymmetry associated with this splitting of these multiplets. In this tightly coupled regime, the second multiplet collapses to what would, at a resolution of 0.5 Hz, appear to be a singlet. In the perturbation theory calculation there are six distinct transition frequencies associates with this multiplet but the splitting is very small and difficult to observe at the resolution (0.16 Hz) of the calculated spectrum.

Comparison of the calculated perturbation theory spectra (Figure 7.2a-c) with the spectrum calculated using a density matrix simulation (Figure 7.2d) illustrates, definitively, that a third-order calculation is necessary to accurately model this system. A fourth-order energy term was calculated and compared with the density matrix simulation. While the transition frequencies calculated from fourth-order perturbation theory provide better agreement with those of the density matrix simulation, the fourth-order contribution is very small and no significant difference in the overall characteristics of the spectrum is observed between third- and fourth-order. Therefore we conclude that, for this specific case, the addition of the fourth-order term is not particularly informative.

Now consider the case of $^{14}N^{1}H_4^+$, where we have an $I = 1$ nucleus coupled to four $I = 1/2$ nuclei with a coupling constant of $^{1}J(^{14}N,^{1}H) = 52.75$ Hz. In Figure 7.3 we present calculated and simulated ^{1}H NMR spectra of this ion acquired in a field of 54 μT.

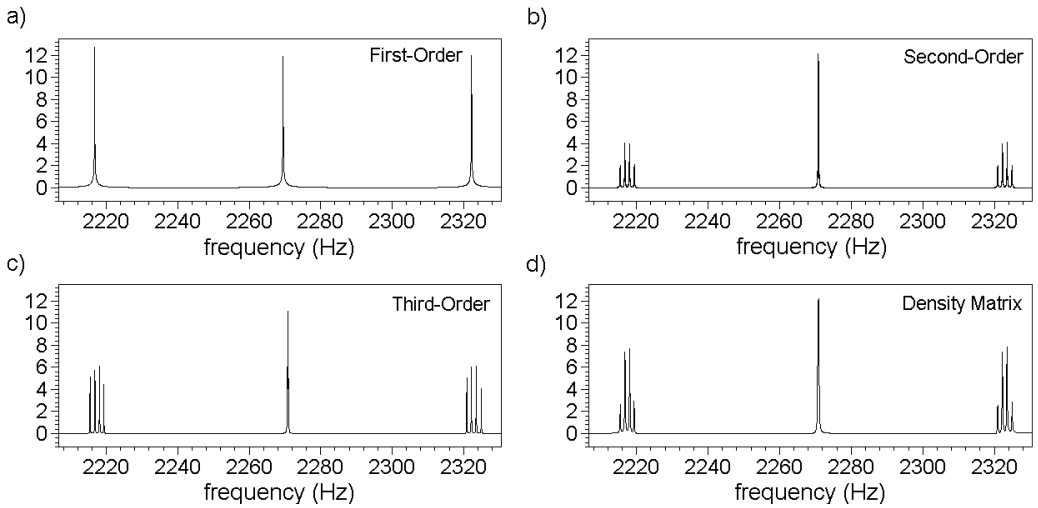

Figure 7.3 Calculated and simulated ^{1}H NMR spectra of $^{14}N^{1}H_4^+$ in a field of 54 μT with $^{1}J(^{14}N,^{1}H) = 52.75$ Hz using: (a) first-order perturbation theory, (b) second-order perturbation theory, (c) third-order perturbation theory and (d) a density matrix simulation.

As with the borohydride anion, a dramatic increase in spectral complexity is observed as we shift from the first-order perturbation theory calculation, shown in Figure 7.3a, to the second-order calculation, shown in Figure 7.3b. In the second-

order calculation, the peaks corresponding to the $m = \pm 1$ spin states of the ^{14}N nucleus are quartets with a uniform splitting, while the $m = 0$ spin state is a singlet. $^{14}N^{1}H_4^{+}$ in a field of 54 μT and with $^{1}J(^{1}H,^{14}N) = 52.75$ Hz, is not as strongly coupled as the $^{11}B^{1}H^{-}$ case presented in Figure 7.2 and so we observe very little difference between the spectra calculated using second-order perturbation theory (Figure 7.3b) and third-order perturbation theory (Figure 7.3c). Indeed the form of the density matrix simulation in Figure 7.3d indicates that this system is well described by second-order perturbation theory.

7.3.4. Determining the Sign of Indirect Spin-Spin Coupling Constants

At the Colloque Ampère XIV in 1967, Georges-J. Béné showed a portion of a frequency domain ^{1}H NMR spectrum of NH_4NO_3 acquired in the Earth's magnetic field and suggested that with improved resolution one could deduce the sign of $^{1}J(^{14}N,^{1}H)$ based on corrections to frequencies calculated using third-order perturbation theory [85]. However, density matrix simulations of the ^{1}H NMR spectrum of a strongly coupled $^{14}N^{1}H_4^{+}$ spin system in the Earth's magnetic field show that the form of this spectrum is independent of the absolute sign of $^{1}J(^{14}N,^{1}H)$.

We believe that this misconception came about because of an error in W.A. Anderson's original expression for the third order perturbation energy (appendix II in reference [83]). NMR spectra calculated from this third order energy term exhibit spectral features which are dependent on the absolute sign of $^{1}J(A,B)$ for strongly coupled AB_n systems, where $n > 1$, A is a quadrupolar ($I > ½$) nucleus and B is the observed spin ½ nucleus. For example, in the case of $^{11}B^{1}H_4^{-}$, discussed in section 7.3.3, the asymmetry of the splitting of the multiplets which correspond to the $m = \pm ½$ spin states of the ^{11}B nucleus depends on the sign of J if the spectra are calculated using Anderson's expression for the third-order perturbation energy. However, density matrix simulations show that the form of this spectrum is independent of the sign of J and ^{1}H NMR spectra of this system calculated using the third-order energy term presented in Equation 7-17, are also independent of the sign of J. Indeed we find that third-order perturbation theory, or for that matter exact analysis, will not yield the sign any indirect spin-spin coupling constant in an AB spin system regardless of the spin of nucleus "A" and nucleus "B". This is further illustrated by considering the

exact expressions for the transition frequencies (Equations 7-24) for the coupled ^{11}B – ^{1}H system discussed in section 7.3.2

$$T_{16} = -\frac{1}{2}\nu_{^{11}B} - \frac{1}{2}\nu_{^{1}H} - J + \frac{1}{2}\sqrt{\left(\nu_{^{1}H} - \nu_{^{11}B}\right)^2 + 2J\left(\nu_{^{1}H} - \nu_{^{11}B}\right) + 4J^2}$$

$$T_{38} = -\frac{1}{2}\nu_{^{11}B} - \frac{1}{2}\nu_{^{1}H} + J + \frac{1}{2}\sqrt{\left(\nu_{^{1}H} - \nu_{^{11}B}\right)^2 - 2J\left(\nu_{^{1}H} - \nu_{^{11}B}\right) + 4J^2}$$

$$T_{52} = -\nu_{^{11}B} + \frac{1}{2}\sqrt{\left(\nu_{^{1}H} - \nu_{^{11}B}\right)^2 + 4J^2} + \frac{1}{2}\sqrt{\left(\nu_{^{1}H} - \nu_{^{11}B}\right)^2 - 2J\left(\nu_{^{1}H} - \nu_{^{11}B}\right) + 4J^2}$$

$$T_{74} = -\nu_{^{11}B} + \frac{1}{2}\sqrt{\left(\nu_{^{1}H} - \nu_{^{11}B}\right)^2 + 2J\left(\nu_{^{1}H} - \nu_{^{11}B}\right) + 4J^2} + \frac{1}{2}\sqrt{\left(\nu_{^{1}H} - \nu_{^{11}B}\right)^2 + 4J^2}$$

7-24

Equations 7-24 show that $T_{16}(-J) = T_{38}(J)$ and $T_{52}(-J) = T_{74}(J)$. Therefore a change in the sign of J will have no observable effect on the spectrum regardless of the relative strength of J and $(\nu_H - \nu_B)$.

A theorem which states that the sign of any indirect spin-spin coupling constant cannot be determined by NMR in systems of only two groups of spins with no additional coupling present is presented and proved by Corio in his classic text on high-resolution NMR [86]. The absolute sign of J can only be determined by NMR if there is another interaction present such as residual dipolar coupling in an aligned medium [87].

It is possible, however, to use EFNMR to determine the relative sign of J in systems of more than two groups of magnetically equivalent spins. This application was discussed by Béné in his review of EFNMR in 1980 [20].

7.3.5. Analysis of an Experimental Spectrum of NH_4NO_3

Consider the ^{1}H NMR spectrum of an aqueous solution of ammonium nitrate. In the Earth's magnetic field, this spin system is an AB_4 spin-system where A = ^{14}N has a nuclear spin, I = 1 and the B spins are the four magnetically equivalent ^{1}H nuclei. In this case the natural abundance of ^{14}N and ^{1}H (99.6% and 99.9%, respectively) is such that no other isotopes of N and H need to be considered. This particular spin system was first investigated in the Earth's field by Brown and

Thompson [3] who analyzed the free-induction decay and compared the observed frequency components with a spectrum calculated using second-order perturbation theory. The ammonium ion was studied at high-field by Wasylishen and Friedrich in 1984 [88].

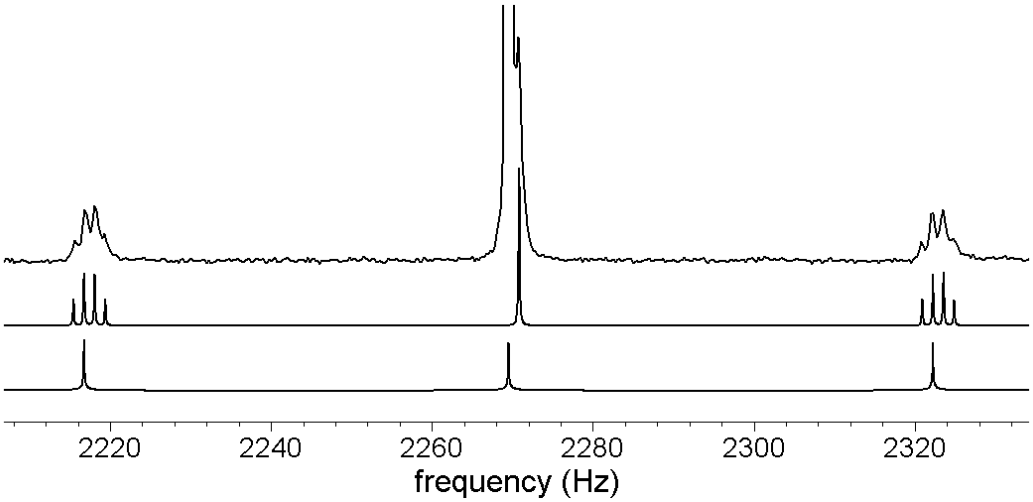

Figure 7.4 ^{1}H NMR spectrum of 500 ml 8 M NH_4NO_3 in 2 M HCl. Directly below the experimental spectrum is a spectrum calculated from second-order perturbation theory using $^{1}J(^{14}N,^{1}H)$ = 52.75 Hz and B_E = 53.3 μT. Very good agreement between the observed and calculated spectra is observed. For comparison, a spectrum calculated using first-order perturbation theory is shown below the second-order perturbation theory result.

Figure 7.4 presents a ^{1}H EFNMR spectrum acquired of a 500 ml solution of 8 M NH_4NO_3 in 2 M HCl. This spectrum was acquired using 49 scans in a total experiment time of 12 minutes. Directly below the experimental spectrum is a ^{1}H NMR spectrum calculated using second-order perturbation theory with $^{1}J(^{14}N,^{1}H)$ = 52.75 Hz, B_E = 53.3 μT and a line broadening of 0.16 Hz. Below the second-order result is a spectrum calculated using first-order perturbation theory and the same coupling and field strength parameters. In this case $^{1}J(^{14}N,^{1}H)$ is 2.5 % of the difference in Larmor frequency between ^{14}N and ^{1}H (2105.5 Hz). Note that a portion of a ^{1}H NMR spectrum of NH_4NO_3 acquired in the Earth's magnetic field was previously presented, in 1967, by Georges-J. Béné [7]. The spectrum presented in Figure 7.4 is of comparable quality to this previously reported result.

By inspection, we see that the features of this $^{14}N^{1}H_4$ spectrum are well

characterized by second-order perturbation theory. The central peak in the observed spectrum is split into a dominant solvent proton peak and a weaker peak, shifted to a slightly higher frequency, which corresponds to the spin state $m = 0$ of the ^{14}N nucleus. The two multiplets, corresponding to the $m = \pm 1$ spin states of the ^{14}N nucleus, consist of four peaks and are not symmetric about the central peak but rather are shifted to higher frequency relative to the first-order peak positions of $\nu_H \pm J$, where ν_H is the proton Larmor frequency.

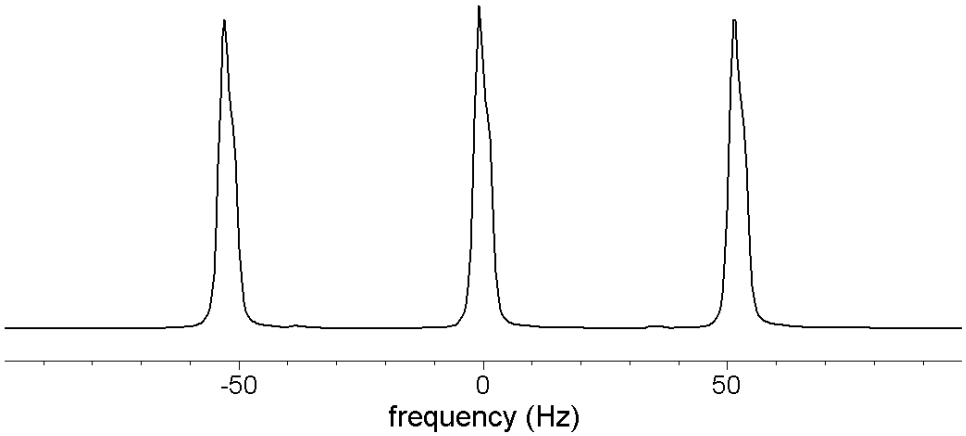

Figure 7.5 A ^1H NMR spectrum of the solution of 8M NH_4NO_3 in 2 M HCl acquired at 600 MHz on a standard high resolution Varian spectrometer. As expected, this is a first-order spectrum with a uniform splitting of 52.5 Hz.

For comparison with Figure 7.4, a high resolution ^1H NMR spectrum of the ammonium ion was acquired at 600 MHz by Dr. John Ryan of Victoria University of Wellington on a laboratory Varian spectrometer. This spectrum, presented in Figure 7.5, is a classic first-order spectrum with $^1J(^1H,^{14}N) = 52.5$ Hz.

7.3.6. Analysis of an Experimental Spectrum of $NaBH_4$

An experimental ^1H EFNMR spectrum of the borohydride anion in an aqueous solution of sodium borohydride and sodium hydroxide is presented in Figure 7.6.

This system was first studied at high-field by Smith et al. in 1977 [89]. In this case we will be focusing our attention on two different species, $^{11}BH_4^-$ where ^{11}B has a nuclear spin of $I = 3/2$ and a natural abundance of approximately 80% as well as $^{10}BH_4^-$ where ^{10}B has a nuclear spin of $I = 3$ and a natural abundance of approximately

20%. Prior to taking the magnitude of the spectrum in Figure 7.6, a complex Lorentzian line, centred about 2269.4 Hz and with a 1.1 Hz linewidth, was subtracted from the complex experimental spectrum to suppress the dominant central peak which corresponds to the solvent protons. This was done so that all of the BH_4 multiplets could be easily indentified in the magnitude spectrum. The central peak in the resultant spectrum is the unsuppressed portion of this solvent proton peak. Due to imperfections in the B_1 transceiver coil, the spectrum could not be correctly phased over the full bandwidth. Portions of the real spectrum, which have been phased locally, are shown in the insets to Figure 7.6 to illustrate the spectral resolution available in the complex spectrum.

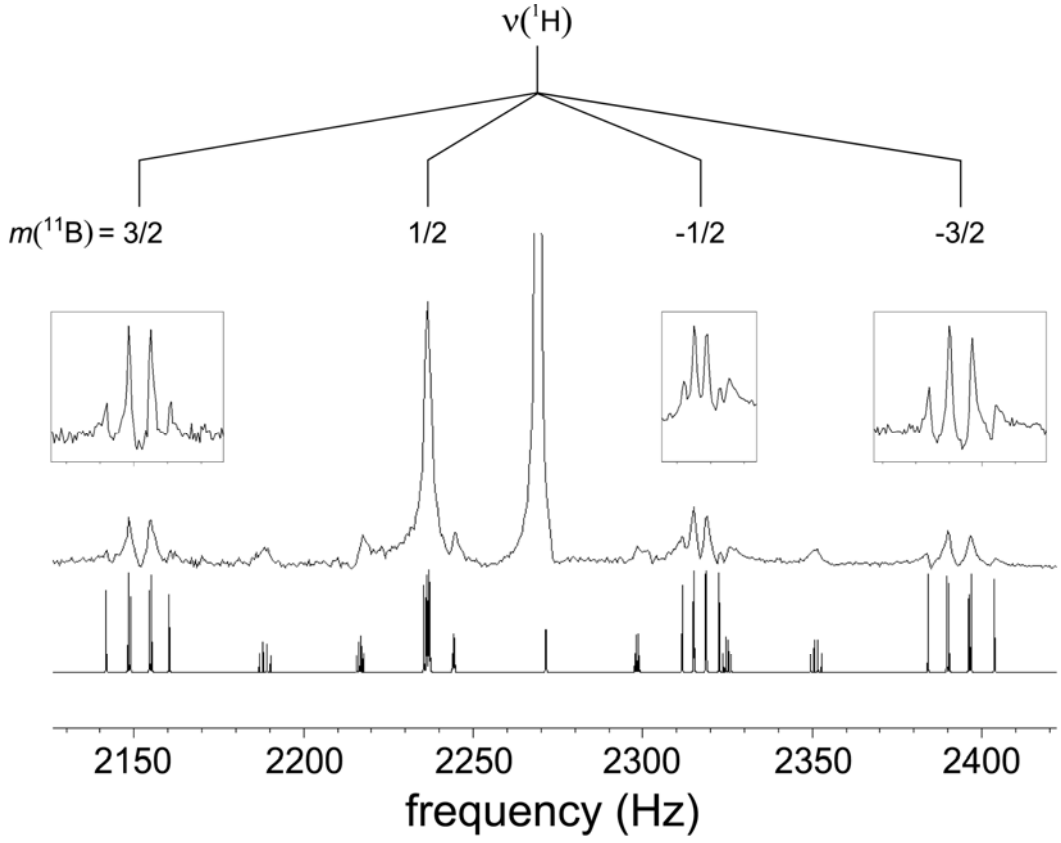

Figure 7.6 ^{1}H NMR spectrum of 500 ml 4.5 M $NaBH_4$ in 8 M NaOH. Below the experimental spectrum is a spectrum calculated using third-order perturbation theory with $^1J(^{11}B,^1H)$ = 80.9 Hz $^1J(^{10}B,^1H)$ = 27. 1 Hz and B_E = 53.3 μT, where the contributions from $^{11}BH_4$ and $^{10}BH_4$ are weighted by 80% and 20%, respectively. Inset into the figure are three regions of the real spectrum which have been phased locally.

Below the experimental spectrum is a spectrum calculated using third-order perturbation theory with $^1J(^{11}B,^1H)$ = 80.9 Hz $^1J(^{10}B,^1H)$ = 27. 1 Hz, B_E = 53.3 mT and a linewidth of 0.16 Hz, where the contributions from $^{11}BH_4$ and $^{10}BH_4$ are weighted by 80% and 20%, respectively. As explored in section 7.3.2, the $^{11}B^1H_4$ portion of the spectrum, whose indirect spin-spin coupling constant is 5.2% of the difference in Larmor frequency between ^1H and ^{11}B, can be described by third-order perturbation theory, where the splitting of the four multiplets is strongly dependent on the spin state of the ^{11}B nucleus. T_2 broadening gives the multiplet at 2235 Hz the appearance of a singlet; however the linewidth of this peak is consistent with the splitting of the multiplet predicted by third-order perturbation theory.

The contribution from $^{10}BH_4^-$ is a set of seven multiplets, where the central multiplet is largely obscured by the solvent peak. Under the conditions of this experimental spectrum, $^1J(^{10}B,^1H)$ is only 1.3% of the difference in Larmor frequency between ^{10}B (243.8 Hz) and ^1H (2269.4 Hz) and so it is anticipated that second-order perturbation theory would be sufficient to describe this portion of the spectrum. While the resolution of the experimental spectrum is insufficient to resolve individual peaks within the seven multiplets, the width of these peaks corresponds well with the spectrum calculated using third-order perturbation theory.

For comparison, a high resolution spectrum of the sodium borohydride solution was acquired at 600 MHz by Dr. John Ryan on a laboratory Varian spectrometer. This spectrum, presented in Figure 7.7, is a first-order spectrum with $^1J(^1H,^{11}B)$ = 80.7 Hz and $^1J(^1H,^{10}B)$ = 27.1 Hz.

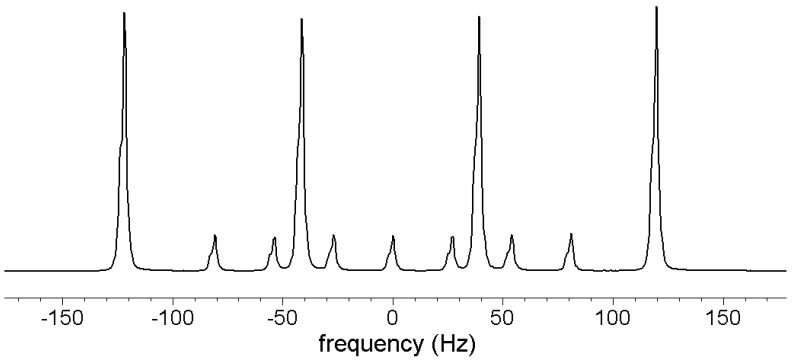

Figure 7.7 A ^1H NMR spectrum of the BH_4 anion acquired at 600 MHz on a Varian spectrometer. This is a classic first-order spectrum with $^1J(^1H,^{11}B)$ = 80.7 Hz and $^1J(^1H,^{10}B)$ = 27.1 Hz.

CHAPTER 8. Multi-dimensional EFNMR Spectroscopy

8.1. Introduction

The suggestion that conventional 1D NMR spectroscopy could be expanded to incorporate multiple dimensions, i.e. one or more indirect evolution dimensions as well as a directly detected dimension, was first put forward by Jean Jeener at the Ampere international summer school in 1971 [90]. Although Jeener never published this idea, it was picked up by Ernst and co-workers who analyzed this experiment in greater detail and immediately recognized its potential for a wide range of applications [91]. The subsequent development of high-resolution, multi-dimensional NMR spectroscopy by Ernst earned him the Nobel Prize in Chemistry in 1991.

Modern multi-dimensional NMR spectroscopy is an essential tool used for a wide range of applications in Chemistry, Physics, Biology and Medicine [82; 92]. In addition, many of the ideas and methods of multi-dimensional NMR spectroscopy were instrumental to the development of multi-dimensional magnetic resonance imaging (MRI).

High-resolution 2D NMR spectroscopy was first performed in the Earth's magnetic field by Jeremy Robinson, Dr. Andrew Coy and co-workers at Victoria University of Wellington and Magritek Ltd. in 2006 [60]. The development of multi-dimensional Earth's field NMR spectroscopy presented in this thesis is a continuation of this work and we gratefully acknowledge the helpful advice and guidance provided by both Jeremy and Andrew at the outset of this project.

8.1.1. 2D Correlation Spectroscopy (COSY)

Modern multi-dimensional NMR spectroscopy includes a wide range of correlation and exchange pulse sequences. In this chapter we will focus on the original experiment proposed by Jeener [90] and later explored in greater detail by Ad Bax and coworkers [92; 93]. This is the so-called correlation spectroscopy, or COSY, experiment.

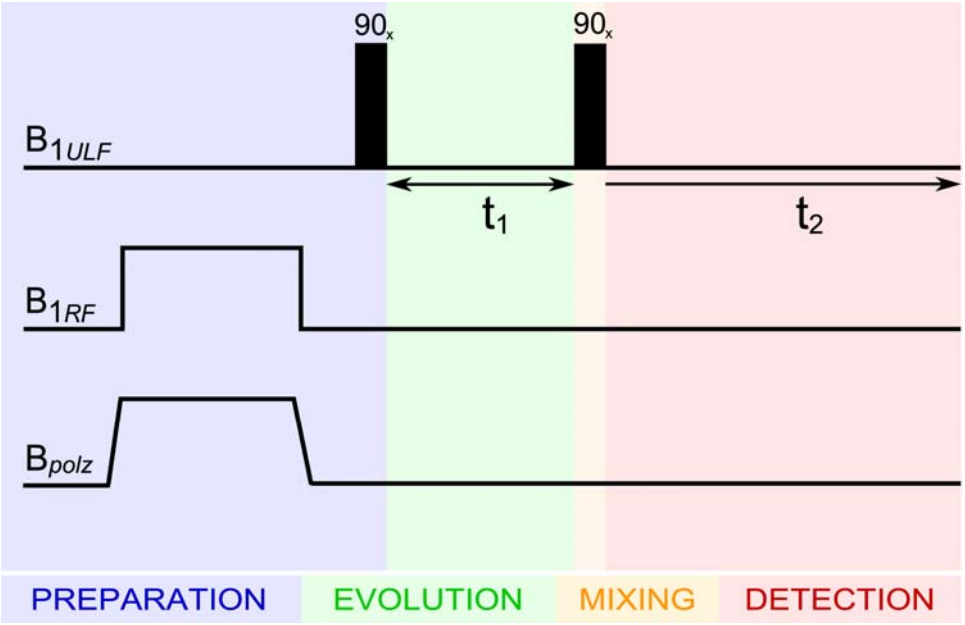

Figure 8.1 Earth's field NMR COSY pulse sequence with prepolarization (B_{polz}) and/or DNP irradiation (B_{1RF}).

The COSY experiment consists of two 90_x pulses, separated by an evolution time, t_1, as illustrated in the pulse sequence in Figure 8.1. In order to understand this experiment we divide it into four regions: preparation, evolution, mixing and detection. In the Earth's field NMR version of this pulse sequence, the preparation period includes the prepolarization and/or DNP irradiation, which enhances our available longitudinal magnetization, followed by the first 90_x pulse, which tips the longitudinal magnetization into the transverse plane. Evolution occurs during the delay period, t_1, between the two 90_x pulses. Mixing is achieved by the second 90_x pulse. Finally, detection occurs as a function of the time t_2 following the mixing pulse. The experiment is repeated as a function of the evolution delay and so we

obtain a two dimensional matrix, $S(t_2,t_1)$, which spans both the direct (t_2) and the indirect (t_1) dimensions. A two-dimensional Fourier transform of this dataset yields a 2D spectrum, $s(f_2,f_1)$, with a direct (f_2) and an indirect (f_1) frequency dimension.

To further explore the COSY pulse sequence we consider the simplest case of two heteronuclei with Larmor frequencies $\omega_1 = \gamma_1 B_E$ and $\omega_2 = \gamma_2 B_E$, respectively. The two nuclei are coupled via an indirect spin-spin coupling constant $2\pi J$. This coupling constant satisfies the weak coupling condition, i.e. $2\pi J << |\omega_1 - \omega_2|$, and so the secular approximation can be applied to the interaction Hamiltonian (Eq. 8-1).

$$\mathcal{H} = -\omega_1 \mathbf{I}_{z1} - \omega_2 \mathbf{I}_{z2} + 2\pi J \mathbf{I}_1 \cdot \mathbf{I}_2 \rightarrow -\omega_1 \mathbf{I}_{z1} - \omega_2 \mathbf{I}_{z2} + 2\pi J \mathbf{I}_{z1} \mathbf{I}_{z2} \qquad 8\text{-}1$$

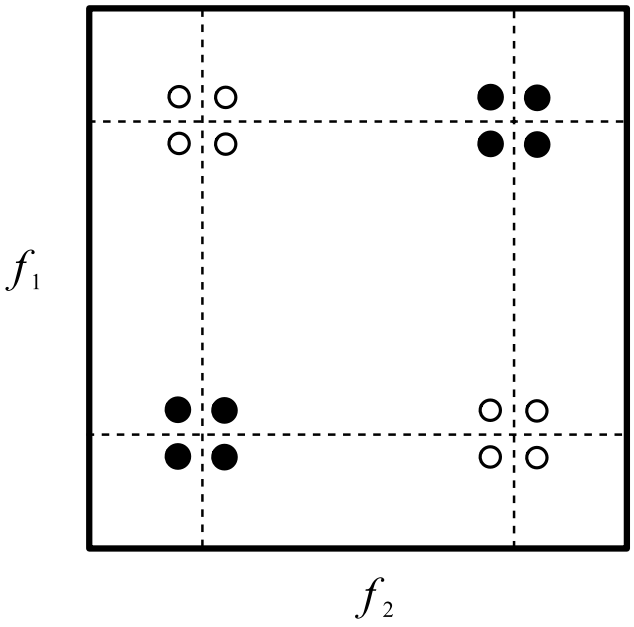

Figure 8.2 A schematic of a 2D COSY spectrum of two *J*-coupled spin-1/2 nuclei.

Figure 8.2 presents a schematic of a 2D COSY spectrum of two *J*-coupled spin-1/2 nuclei. The diagonal peaks (solid circles) correspond to magnetization which was associated with the same spin during both evolution (t_1) and detection (t_2) and so experienced the same Larmor frequency in both time periods. The off-diagonal peaks (open circles) arise from magnetization which originated on one spin during the evolution period (t_1) and then was transferred to the other spin by the mixing pulse and so experienced a different Larmor frequency during the detection period (t_2).

This transfer of magnetization occurs only if there is a coupling between the two spins and so off-diagonal peaks in a COSY spectrum can be used to determine connectivity in a molecule.

In order to better understand the form of the COSY spectrum we present an analytical calculation for the simple case of two weakly coupled spins. For convenience and tractability, we use the density matrix formalism to explore the evolution of the spin system throughout the pulse sequence in Figure 8.1 and under the influence of the interaction Hamiltonian in Eq. 8-1 [17; 94]. Recall that at thermal equilibrium (or in the case of Earth's field NMR, directly following prepolarization or DNP signal enhancement) the magnetization is aligned with the static field. Therefore the density matrix prior to the first 90_x pulse, $\rho(0)$, is proportional to $\mathbf{I}_{z1} + \mathbf{I}_{z2}$. The application of a broadband 90_x pulse tips this magnetization into the transverse plane, as indicated by Eq. 8-2. This pulse acts on both of the spins.

$$\mathbf{I}_{z1} + \mathbf{I}_{z2} \xrightarrow{-\frac{\pi}{2}(\mathbf{I}_{x1}+\mathbf{I}_{x2})} \mathbf{I}_{y1} + \mathbf{I}_{y2} \qquad 8\text{-}2$$

Following the first 90_x pulse, the system evolves under the influence of Eq. 8-1 for a period of time, t_1. Having applied the secular approximation to the interaction Hamiltonian, the Zeeman and the indirect spin-spin coupling terms commute. Therefore we can apply these terms sequentially.

First consider the indirect spin-spin coupling interaction, $2\pi J\mathbf{I}_{z1}\mathbf{I}_{z2}$. The evolution of the $\mathbf{I}_{y1}$ and $\mathbf{I}_{x1}$ operators under the influence of this interaction is illustrated in the precession diagrams presented in Figure 8.3(a) and Figure 8.3(b). With a characteristic frequency of πJ, $\mathbf{I}_{y1}$ evolves into $2\mathbf{I}_{x1}\mathbf{I}_{z2}$ and $\mathbf{I}_{x1}$ evolves into $2\mathbf{I}_{y1}\mathbf{I}_{z2}$.

$$\mathbf{I}_{y1} + \mathbf{I}_{y2} \xrightarrow{2\pi J\mathbf{I}_{z1}\mathbf{I}_{z2}} (\mathbf{I}_{y1} + \mathbf{I}_{y2})\cos(\pi J t_1) - 2(\mathbf{I}_{x1}\mathbf{I}_{z2} + \mathbf{I}_{z1}\mathbf{I}_{x2})\sin(\pi J t_1) \qquad 8\text{-}3$$

Next we apply the Zeeman terms of the interaction Hamiltonian: $-\omega_1\mathbf{I}_{z1}$ $-\omega_2\mathbf{I}_{z2}$

for the time period, t_1.

$$\xrightarrow{-\omega_1 \mathbf{I}_{z1} - \omega_2 \mathbf{I}_{z2}}$$

$$\left[\mathbf{I}_{y1}\cos(\omega_1 t_1) + \mathbf{I}_{x1}\sin(\omega_1 t_1) + \mathbf{I}_{y2}\cos(\omega_2 t_1) + \mathbf{I}_{x2}\sin(\omega_2 t_1)\right]\cos(\pi J t_1)$$

$$-\left[2\left(\mathbf{I}_{1x}\cos(\omega_1 t_1) - \mathbf{I}_{y1}\sin(\omega_1 t_1)\right)\mathbf{I}_{z2} + 2\mathbf{I}_{z1}\left(\mathbf{I}_{x2}\cos(\omega_2 t_1) - \mathbf{I}_{y2}\sin(\omega_2 t_1)\right)\right]\sin(\pi J t_1) \qquad 8\text{-}4$$

During the evolution (t_1) portion of the pulse sequence (Eq. 8-4) we see that the bilinear J-coupling interaction ($2\pi J\mathbf{I}_{z1}\mathbf{I}_{z2}$) creates a series of one- and two-spin coherences which are tagged with an evolution under the influence of either ω_1 or ω_2 by means of the Zeeman interaction.

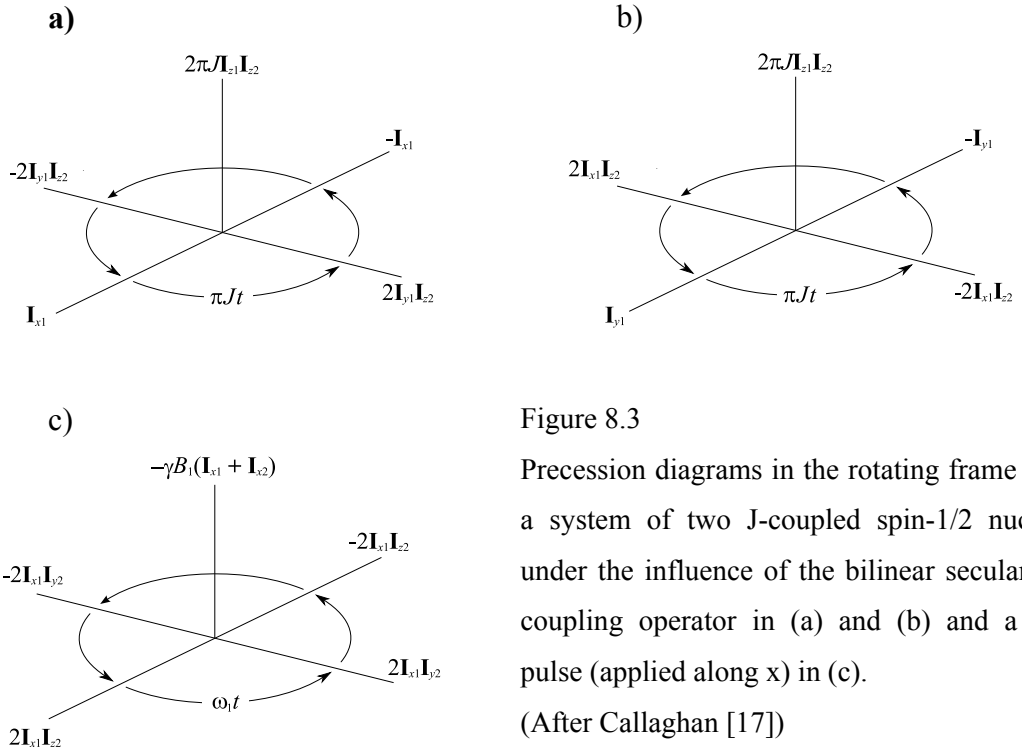

Figure 8.3
Precession diagrams in the rotating frame for a system of two J-coupled spin-1/2 nuclei under the influence of the bilinear secular J-coupling operator in (a) and (b) and a B_1 pulse (applied along x) in (c).
(After Callaghan [17])

Following our t_1 evolution, we apply a second broadband 90_x pulse using the operator: $-\pi/2(\mathbf{I}_{x1} + \mathbf{I}_{x2})$. The action of this pulse is described by the precession diagram in Figure 8.3(c). This second 90_x pulse is the mixing step in which magnetization is transferred between spins. For example, the final coherence in Eq.

8-4 evolves from $\mathbf{I}_{z1}\mathbf{I}_{y2}$ to $\mathbf{I}_{y1}\mathbf{I}_{z2}$ under the influence of the mixing pulse.

$$\xrightarrow{-\frac{\pi}{2}(\mathbf{I}_{x1}+\mathbf{I}_{x2})}\left[-\mathbf{I}_{z1}\cos(\omega_1 t_1)+\mathbf{I}_{x1}\sin(\omega_1 t_1)-\mathbf{I}_{z2}\cos(\omega_2 t_1)+\mathbf{I}_{x2}\sin(\omega_2 t_1)\right]\cos(\pi J t_1)$$

$$-\left[2(\mathbf{I}_{x1}\cos(\omega_1 t_1)+\mathbf{I}_{z1}\sin(\omega_1 t_1))\mathbf{I}_{y2}+2\mathbf{I}_{y1}(\mathbf{I}_{x2}\cos(\omega_2 t_1)+\mathbf{I}_{z2}\sin(\omega_2 t_1))\right]\sin(\pi J t_1)$$

8-5

In order to simplify the problem, we now discard all terms appearing in Eq. 8-5 which cannot produce observable (single-quantum) coherences during the final evolution period. This includes all double quantum coherences ($\mathbf{I}_{x1}\mathbf{I}_{y2}$ or $\mathbf{I}_{y1}\mathbf{I}_{x2}$) and pure longitudinal magnetization ($\mathbf{I}_{z1}$ and $\mathbf{I}_{z2}$). The remaining observable terms are listed in Eq. 8-6.

$$\longrightarrow\left[\mathbf{I}_{x1}\sin(\omega_1 t_1)+\mathbf{I}_{x2}\sin(\omega_2 t_1)\right]\cos(\pi J t_1)$$

$$-\left[2\mathbf{I}_{z1}\mathbf{I}_{y2}\sin(\omega_1 t_1)+2\mathbf{I}_{y1}\mathbf{I}_{z2}\sin(\omega_2 t_1)\right]\sin(\pi J t_1)$$

8-6

As with our first evolution step (Eq. 8-3 and Eq. 8-4) we apply the *J*-coupling and Zeeman terms sequentially during the detection period. First, we evolve under the influence of the *J*-coupling term for a time period t_2.

$$\xrightarrow{2\pi J\mathbf{I}_{z1}\mathbf{I}_{z2}}\left[\mathbf{I}_{x1}\sin(\omega_1 t_1)+\mathbf{I}_{x2}\sin(\omega_2 t_1)\right]\cos(\pi J t_1)\cos(\pi J t_2)$$

$$+\left[2\mathbf{I}_{y1}\mathbf{I}_{z2}\sin(\omega_1 t_1)+2\mathbf{I}_{z1}\mathbf{I}_{y2}\sin(\omega_2 t_1)\right]\cos(\pi J t_1)\sin(\pi J t_2)$$

$$-\left[2\mathbf{I}_{z1}\mathbf{I}_{y2}\sin(\omega_1 t_1)+2\mathbf{I}_{y1}\mathbf{I}_{z2}\sin(\omega_2 t_1)\right]\sin(\pi J t_1)\cos(\pi J t_2)$$

$$+\left[\mathbf{I}_{x2}\sin(\omega_1 t_1)+\mathbf{I}_{x1}\sin(\omega_2 t_1)\right]\sin(\pi J t_1)\sin(\pi J t_2)$$

8-7

Again we discard all but those terms which can give rise to signal-quantum

coherences under the influence of the Zeeman interaction. The remaining terms are listed in Eq. 8-8.

$$\rightarrow [\mathbf{I}_{x1}\sin(\omega_1 t_1)+\mathbf{I}_{x2}\sin(\omega_2 t_1)]\cos(\pi J t_1)\cos(\pi J t_2)$$

$$+[\mathbf{I}_{x2}\sin(\omega_1 t_1)+\mathbf{I}_{x1}\sin(\omega_2 t_1)]\sin(\pi J t_1)\sin(\pi J t_2) \qquad 8\text{-}8$$

Finally, we evolve under the influence of the Zeeman terms.

$$\rightarrow \begin{bmatrix} \mathbf{I}_{x1}\sin(\omega_1 t_1)\cos(\omega_1 t_2)-\mathbf{I}_{y1}\sin(\omega_1 t_1)\sin(\omega_1 t_2) \\ +\mathbf{I}_{x2}\sin(\omega_2 t_1)\cos(\omega_2 t_2)-\mathbf{I}_{y2}\sin(\omega_2 t_1)\sin(\omega_2 t_2) \end{bmatrix}\cos(\pi J t_1)\cos(\pi J t_2)$$

$$+\begin{bmatrix} \mathbf{I}_{x2}\sin(\omega_1 t_1)\cos(\omega_2 t_2)+\mathbf{I}_{y2}\sin(\omega_1 t_1)\sin(\omega_2 t_2) \\ -\mathbf{I}_{x1}\sin(\omega_2 t_1)\cos(\omega_1 t_2)-\mathbf{I}_{y1}\sin(\omega_2 t_1)\sin(\omega_1 t_2) \end{bmatrix}\sin(\pi J t_1)\sin(\pi J t_2) \qquad 8\text{-}9$$

The first four terms in Eq. 8-9 give rise to the diagonal peaks in the two-dimensional spectrum (Figure 8.2). These coherences are tagged with the same Larmor frequency in both the t_1 and t_2 time periods and so appear near the diagonal in the final spectrum. The small splitting between the peaks grouped on the diagonal is equal to the coupling constant, J and arises from the $\sin(\pi Jt)$ and $\cos(\pi Jt)$ factors in Eq. 8-9. The final four terms in Eq. 8-9 give rise to the off-diagonal peaks in the COSY spectrum. In this case, the magnetization originates on one spin during the evolution period (t_1) but is transferred to the other spin by the mixing pulse and so experiences a different Larmor frequency in the detection period (t_2). These off-diagonal peaks exhibit anti-phase behaviour because of the $\sin(\pi Jt)$ factors. In contrast, the diagonal peaks are in phase because these terms are modulated by $\cos(\pi Jt)$. This off-diagonal anti-phase behaviour can be a problem if the resolution of the spectrum is insufficient to resolve these peaks. In this case cancellation can occur. However, clever phase cycling pulse sequences can use this anti-phase behaviour to advantage to extract additional coupling information from COSY spectra.

It is evident from the calculation above that the transfer of magnetization will

not occur under the sole influence of the Zeeman interaction. It is the *J*-coupling which creates the two-spin coherences which are required for magnetization transfer via the mixing pulse. Therefore the presence of an off-diagonal peak at $\left(\frac{1}{2\pi}\omega_1, \frac{1}{2\pi}\omega_2\right)$ in the COSY spectrum indicates the presence of coupling between the two spins with Larmor frequencies of ω_1 and ω_2, respectively.

8.1.2. 2D Density Matrix Simulations

Analytical calculations of COSY spectra, like the one presented above, rapidly become intractable as more spins are added or, as is the case in many EFNMR COSY experiments, the weak coupling condition is violated. As we have seen in previous chapters, strong coupling greatly complicates 1D EFNMR spectra and this is equally the case for multi-dimensional spectra. In the case of strong coupling, the full $\mathbf{I}_1 \cdot \mathbf{I}_2$ coupling term must be applied to the system, not just the more manageable $\mathbf{I}_{z1} \cdot \mathbf{I}_{z2}$ secular term. In addition, the Zeeman and the indirect spin-spin coupling terms do not commute and so cannot be applied independently to the density matrix. Consequently, our theoretical investigation of multi-dimensional ENFMR COSY experiments will be carried out using an extended version of the density matrix simulation detailed in Chapter 6.

Adding an indirect evolution dimension to the density matrix simulation is relatively straightforward. Following the 90_x excitation pulse, a period of t_1 evolution is added in successive Δt_1 evolution steps: Δt_1, $2\Delta t_1$, $3\Delta t_1$, etc... Each evolution step is achieved by means of *m* applications of the evolution operator, where *m* is given by Eq. 8-10, Δt is the time step of the evolution operator and Δt_1 is the time step in the indirect dimension. Note that *m* must be an integer.

$$m = \frac{\Delta t_1}{\Delta t} \qquad 8\text{-}10$$

Following this evolution period, a second 90_x pulse is applied to the system by means of the same rotation operator used for the first excitation pulse. The evolution

of the system as a function of the sampling time, Δt_2, and the subsequent application of the observation operator are carried out in an identical manner to the 1D simulation. This entire process is then repeated for successively longer t_1 evolution periods so that we obtain a 2D time domain dataset, $S(t_2,t_1)$ which can be Fourier transformed to obtain the COSY spectrum, $s(f_{2,}f_1)$.

8.2. 2D COSY in the Earth's Field

8.2.1. Experimental Considerations

There are two main experimental considerations which need to be addressed before COSY can be successfully implemented on a Terranova-MRI Earth's field NMR system. The first is a hardware-specific issue regarding the actual phase and duration of the ULF excitation pulses. The second is a more general concern regarding aliasing in the indirectly detected dimension. Together these issues put strong constraints on the experimental parameters which must be used to successfully obtain a COSY spectrum in the Earth's field.

First we consider the problem of ULF pulse duration and phase. The difficulty arises from the question of what happens when an ULF pulse which, due to a combination of its initial phase, frequency and duration, terminates at a phase which is not a multiple of π radians and hence when the amplitude of the ULF pulse is finite. This pulse is driven by an oscillating output voltage from the spectrometer. The input signal to the B_1 coil will stop after the fixed pulse duration regardless of the phase of the pulse at that time. However, the response of the B_1 coil to the abrupt termination of the pulse at a voltage other than zero is not well understood. It is not unreasonable to assume that there will be some finite time during which the B_1 irradiation continues as the output goes to zero. This will introduce an uncertainty in the duration and therefore the flip angle of this pulse.

In high field NMR, where the Larmor frequencies are on the order of 100s of MHz and the pulse durations are on the order of μs, this is unlikely to be a problem. Under these conditions the Larmor period is orders of magnitude shorter than the

pulse duration and so any uncertainty in the duration of the pulse caused by the phase at which the pulse terminates is minimal compared to the overall pulse duration. Under the conditions of Earth's field NMR, the Larmor period is of the same order of magnitude as the pulse duration. Therefore, if there is uncertainty in the way in which the pulse terminates it will translate into a significant uncertainty in the duration of the pulse.

In order to ensure that the pulse duration and phase is consistent for each t_1 time step, we must chose the initial phase of the pulse such that the final phase is a multiple of π radians and we must require that the time step in the t_1 dimension, Δt_1, is an integer multiple of half the Larmor period so that this final pulse phase remains fixed throughout the COSY experiment. If these steps are not taken, the 2D COSY spectrum suffers from significant artifacts, often in the form of abnormal fold-back in the f_1 dimension.

The second issue to be considered, when setting up a COSY experiment in the Earth's field, is that of under-sampling t_1. In a COSY experiment, the bandwidth in the indirect dimension is determined by the inverse of the time step in the t_1 dimension, $(\Delta t_1)^{-1}$. In order to satisfy Nyquist in the indirect dimension, a Δt_1 of 200 μs would be required in a typical ^{1}H EFNMR COSY experiment. The resolution of the spectrum is given by $(N_1 \Delta t_1)^{-1}$, where N_1 is the number of steps in the t_1 dimension. 16384 t_1 steps are required to obtain a resolution of 0.3 Hz in the indirect dimension if Δt_1 = 200 μs. Each t_1 step requires a full t_2 transient to be acquired and therefore the time necessary to obtain 16384 t_1 steps is prohibitively long. In order to acquire ^{1}H EFNMR COSY data in a reasonable period of time we under-sample t_1. This under-sampling causes aliasing in the f_1 dimension. However, if Δt_1 is chosen carefully we can ensure that the aliasing does not result in a superposition of peaks in the final spectrum and therefore prevent information from being lost.

The first step to determining the necessary parameters to avoid fold-back artifacts is to choose an appropriate minimum bandwidth which is twice the bandwidth of the region of interest in the 1D EFNMR spectrum. For example, the minimum bandwidth of a ^{1}H – ^{19}F EFNMR spectrum of a sample such as trifluoroethanol in a field of 54 μT is twice the difference in Larmor frequency of ^{1}H and ^{19}F (2 * 136 Hz). In practice we increase the minimum bandwidth by 15 – 20%

to ensure that we have allowed for all peaks in the spectrum. This minimum bandwidth can be used to define a maximum time step, Δt_{1max} (3.1 ms in this case).

In order to ensure that there is no overlap of folded peaks in the indirect dimension, the frequencies at the upper and lower extremes of the spectral window must be reflected into the same region of the 2D spectrum, i.e. the entire region of interest must appear in the positive region or the negative region of f_1 in the final spectrum. Take, for example, a spectrum ranging from F_a to F_b which is folded into a final bandwidth, Δf, ranging from $-½\ \Delta f$ to $+½\Delta f$. Both F_a and F_b are much greater than Δf but $(F_b - F_a)$ is less than Δf. Peaks which occur at a frequency F in the true spectrum will appear at a frequency, F', in the "reduced" spectrum according to Eq. 8-11, where n is an integer given by Eq. 8-12 and *round*() indicates Swedish rounding.

$$F' = F - n\Delta f \tag{8-11}$$

$$n = round\left(\frac{F}{\Delta f}\right) \tag{8-12}$$

Using Eqs. 8-11 and 8-12, the folded frequencies can be calculated for the extremities of the true spectrum: F_a and F_b. If the sign of the folded frequencies, F_a' and F_b', are the same then the aliasing condition has been met and the minimum bandwidth can be used. If the signs are opposite, the aliasing condition is violated and this calculation needs to be repeated for a larger bandwidth. In this manner we iteratively increase the bandwidth until the aliasing condition is met. The minimum bandwidth at which the aliasing condition is met, Δf^*, is used to calculate the dwell time in the t_1 dimension: $\Delta t_1 = (\Delta f^*)^{-1}$.

Recall that the pulse phase problem discussed above requires that Δt_1 be a half-integer multiple of the period of the transmit frequency, $F_{transmit}$. Therefore the transmit frequency must be calculated from the chosen Δt_1 according to Eq. 8-13 where n is calculated from Eq. 8-12 with $F = F_a$ (or F_b) and $\Delta f = \Delta f^*$.

$$F_{transmit} = \frac{n}{2\Delta t_1}$$

8-13

Having set the bandwidth in the f_1 dimension, the spectral resolution in this dimension is determined by the number of t_1 steps, N_1.

Once the 2D COSY experiment is executed with these carefully chosen parameters the resultant 2D matrix of time domain data, $S(t_2,t_1)$, is Fourier transformed to obtain the 2D spectrum, $s(f_2,f_1)$. This spectrum will have four quadrants corresponding to positive and negative frequencies in f_1 and f_2. First we extract the desired bandwidth from the positive region of the f_2 dimension. Since this is the directly detected dimension it requires no further processing and the frequency axis is calculated in the same manner as for a 1D EFNMR spectrum.

The indirect dimension is slightly more complicated. First we must determine which frequency region, the positive or the negative, needs to be extracted. If F_a' and F_b' were both positive then the positive region in f_1 is extracted. If these folded frequencies were negative then the negative region in f_1 is extracted. If the negative portion of the spectrum is extracted, the data set needs to be reflected about the f_2 axis. However, if the positive portion of the spectrum is extracted no reflection is necessary.

$$f_1 = \begin{cases} F_{transmit} \rightarrow F_{transmit} + \dfrac{1}{2\Delta t_1}, F_a' > 0 \\ F_{transmit} - \dfrac{1}{2\Delta t_1} \rightarrow F_{transmit}, F_a' < 0 \end{cases}$$

8-14

Eq. 8-14 presents the maximum and minimum values of the f_1 frequency axis for both the case of positive folded frequencies and negative folded frequencies.

$F_{transmit}$ and F_a' (in Eq. 8-14) are calculated from Eq. 8-11, Eq. 8-12 and Eq. 8-13. The number of points in the f_1 dimension in the final spectrum is $\frac{1}{2}N_1$.

Ideally, we would phase the 2D complex COSY spectrum so as to observe the anti-phase nature of the off-diagonal peaks. However, in practice, imperfections of

the transceiver coil and long minimum t_1 times (> 20 ms due to the ring-down of the B_1 coil) result in a phase roll across the 2D spectrum which is difficult to remove. Therefore we observe the magnitude spectrum and any phase information is lost.

In the original Earth's field NMR COSY work presented by Robinson et al. [60], the sensitivity and resolution of the measurements were limited by (a) significant ULF noise interference, particularly at multiples of 50 Hz, the mains frequency harmonics, (b) local spatial inhomogeneities in the Earth's field and (c) temporal variations in the Earth's field over the 12+ hour measurements. The resolution and sensitivity of the Earth's field COSY experiments presented in this thesis are significantly improved with respect to these early experiments through the combined use of a Faraday screen, first-order shimming and field stabilization, as described in Chapter 4.

8.2.2. Monofluorobenzene

Consider the 1D ^{1}H EFNMR spectrum of monofluorobenzene (C_6H_5F), presented in Figure 8.4. This rather noisy spectrum appears to be a doublet with a single ^{19}F-^{1}H indirect spin-spin coupling constant of 5.8 Hz and a linewidth of around 1 Hz.

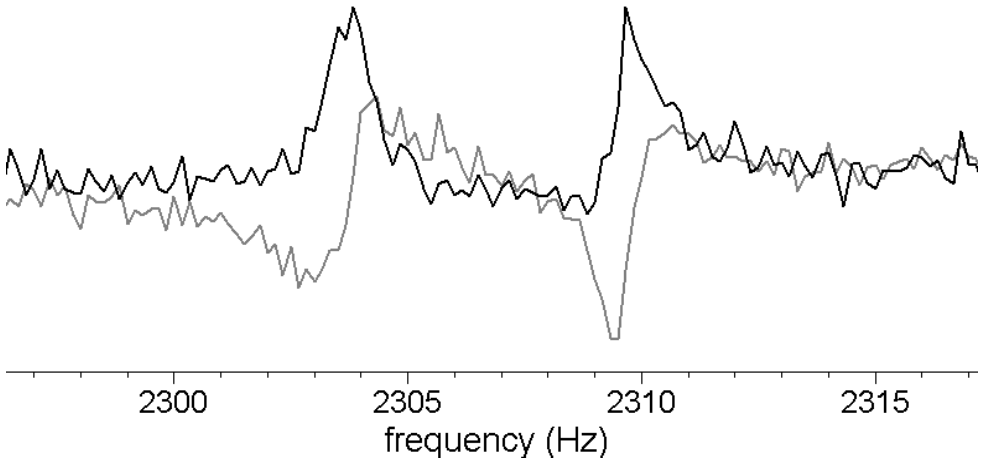

Figure 8.4 Complex ^{1}H EFNMR spectrum of monofluorobenzene. The real part is shown in black and the imaginary part is shown in gray. The average splitting is 5.8 Hz.

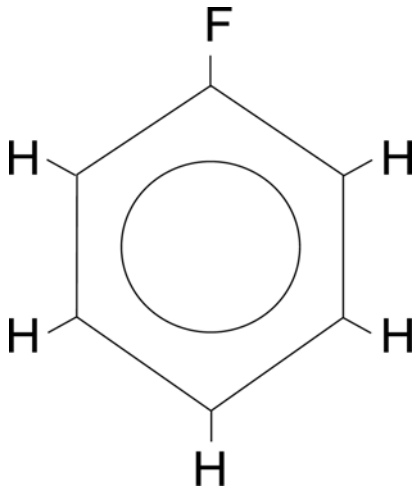

Figure 8.5 A schematic of the monofluorobenzene molecule.

The monofluorobenzene molecule is pictured in Figure 8.5. Inspection of this molecule suggests that there should be a range of both homonuclear and heteronuclear indirect spin-spin coupling constants associated with it. However, the spectrum in Figure 8.4 appears to contain only a single coupling constant.

The apparent simplicity of a ^{1}H NMR monofluorobenzene spectrum acquired in the Earth's field was first highlighted by Elliot and Schumaker in 1957, who put forward the suggestion that the observed spectrum was the result of an "average" of the ^{1}H-^{19}F couplings within the molecule [26]. Subsequent high-field observations of the ^{1}H NMR spectrum of monofluorobenzene by Bak, Schoolery and Williams [27] showed that there were in fact three unique ^{1}H-^{19}F spin-spin coupling constants present in this molecule. This finding suggested that either there was a strong dependence of J on field strength or the "average" coupling interpretation of Elliot and Schumaker was incorrect. In 1962, Thompson and Brown wrote a letter to the Journal of Chemical Physics [5] suggesting that a detailed study of the frequency components of a ^{1}H EFNMR FID acquired of monofluorobenzene did, in fact, yield a range of coupling constants in accordance with the findings, at high field, by Bak, Schoolery and Williams [27].

A high-resolution ^{1}H EFNMR COSY spectrum acquired from 300 mL of monofluorobenzene is presented in Figure 8.6. Only the ^{1}H spins are excited and detected in this measurement and so we observe only ^{1}H diagonal peaks with no off-diagonal components apparent in the spectrum. This corresponds to the top right-hand quadrant in the schematic in Figure 8.2.

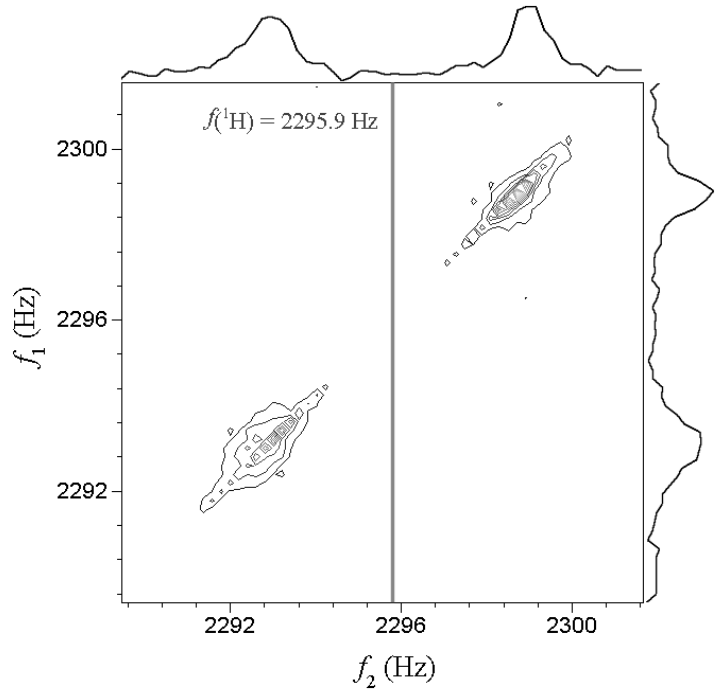

Figure 8.6 High-resolution EFNMR COSY acquired from 300 mL of pure monofluorobenzene. This spectrum contains only the $^{1}H - ^{1}H$ quadrant of the full COSY spectrum (top right peaks in the schematic in Figure 8.2).

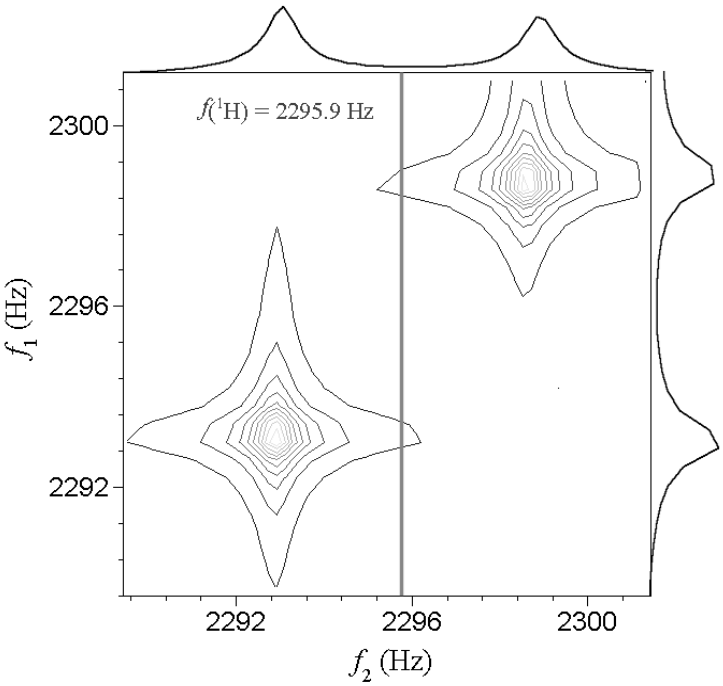

Figure 8.7 EFNMR COSY spectrum ($^{1}H - ^{1}H$ quadrant) calculated using a density matrix simulation of monofluorobenzene with a single "average" coupling constant of 5.8 Hz and a line-broadening of 0.7 Hz.

Figure 8.7 presents a simulated COSY spectrum of monofluorobenzene carried out with a single ^{1}H-^{19}F coupling constant of 5.8 Hz and a line-broadening of 0.7 Hz. While the 1D projections of the simulation in Figure 8.7 are similar to those of the experimental spectrum in Figure 8.6, the features of the 2D spectrum are significantly different. It is clear from a comparison of these spectra that the width of the peaks observed in the 1D ^{1}H EFNMR spectrum (Figure 8.4) is not due to line-broadening but rather the combined effect of a range of coupling constants.

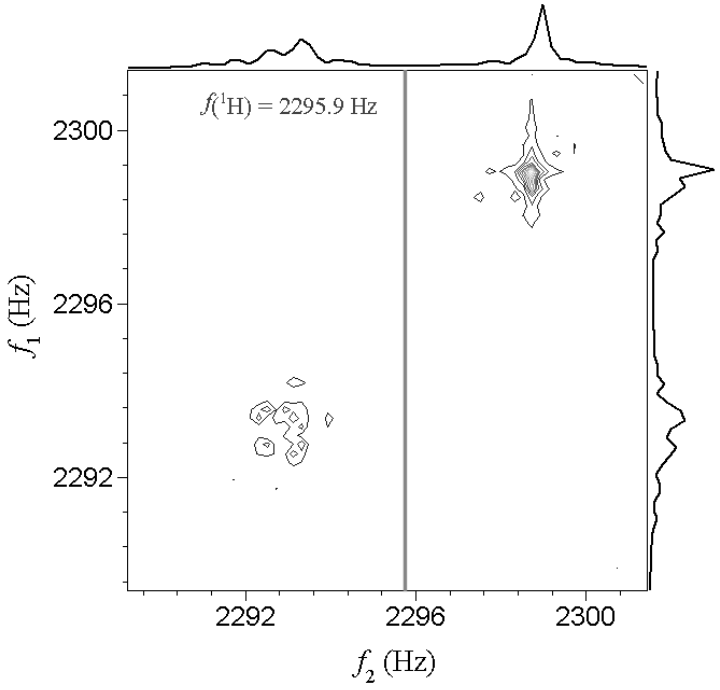

Figure 8.8 Density matrix simulation of a 2D EFNMR COSY (^{1}H – ^{1}H quadrant) of monofluorobenzene calculated using the full range of homonuclear and heteronuclear *J*-coupling constants reported in reference [95] (see Table 8.1).

Figure 8.8 presents a ^{1}H EFNMR COSY of monofluorobenzene calculated with a density matrix simulation using the full complement of indirect spin-spin coupling constants (both homonuclear and heteronuclear) measured at high-field by Castellano et al. [95] (see Table 8.1). Some of the high-resolution structure observed in the density matrix simulation is not fully resolved in the experiment (Figure 8.6) but we see that the overall structure of the simulated spectrum in Figure 8.8 is in much better agreement with experiment than the spectrum in Figure 8.7 which was simulated with a single "average" coupling constant.

Table 8.1 Indirect spin-spin coupling constants (in Hz) used for the simulated spectrum of monofluorobenzene in Figure 8.8 [95].

^{3}J(H,F)	^{4}J(H,F)	^{5}J(H,F)	^{3}J(H,H)	^{3}J(H,H)	^{4}J(H,H)	^{4}J(H,H)	^{5}J(H,H)
9.084	5.742	0.236	8.361	7.393	2.766	1.073	0.429

8.2.3. 1,4-difluorobenzene

The spectra presented in the previous section contain only a small portion of a full COSY spectrum, i.e. only the ^{1}H peaks occurring directly along the diagonal (top right corner in the schematic in Figure 8.2). The full 2D COSY spectrum of monofluorobenzene cannot be observed because the SNR of the ^{19}F signal is very low due to the number of peaks associated with it. In order to observe a full 2D COSY spectrum, we consider instead 1,4-difluorobenzene (Figure 8.9).

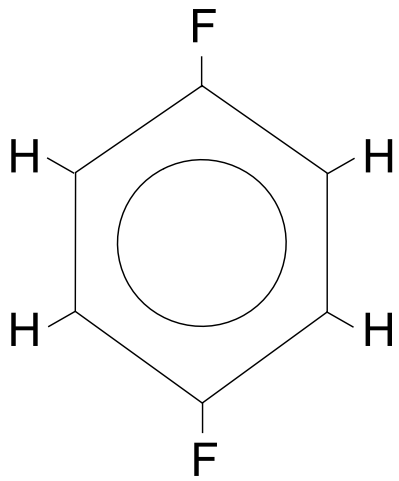

Figure 8.9 A schematic of the 1,4-difluorobenzene molecule.

The difluorobenzene molecule contains a range of hetero- and homonuclear *J*-coupling constants which have been measured at high field by Paterson and Wells [96]. The three bond heteronuclear indirect spin-spin coupling constant, $^3J(^1\text{H},^{19}\text{F})$ = 7.6 Hz, and the four bond heteronuclear indirect spin-spin coupling constant, $^4J(^1\text{H},^{19}\text{F})$ = 4.6 Hz, are significantly different. Therefore, although the protons, and similarly the fluorine nuclei, are chemically equivalent, they are not magnetically equivalent. This means that any calculations of spectra of this molecule must include the homonuclear proton-proton and fluorine-fluorine couplings.

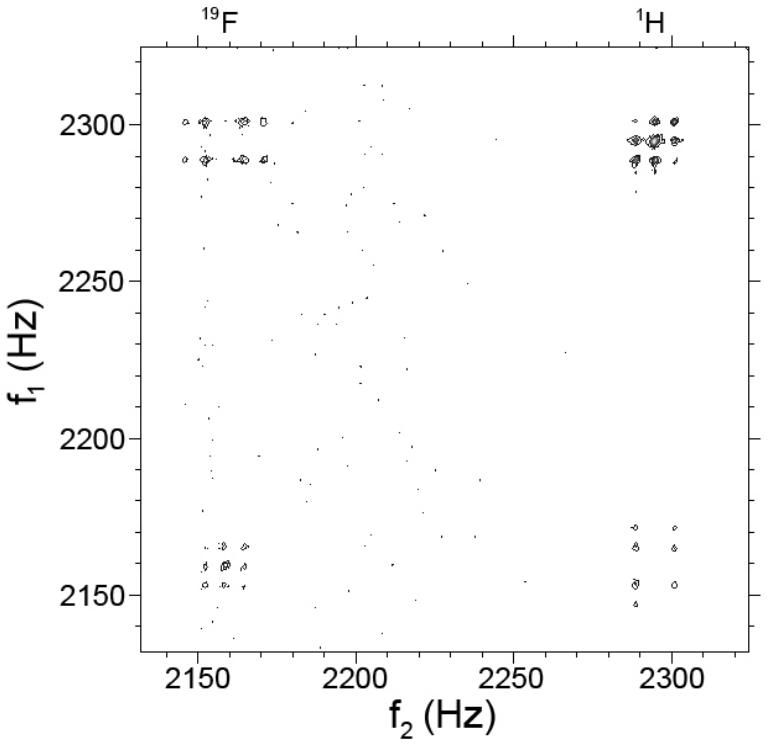

Figure 8.10 2D ^{1}H - ^{19}F COSY spectrum acquired from 500 mL 1,4-difluorobenzene in the Earth's magnetic field.

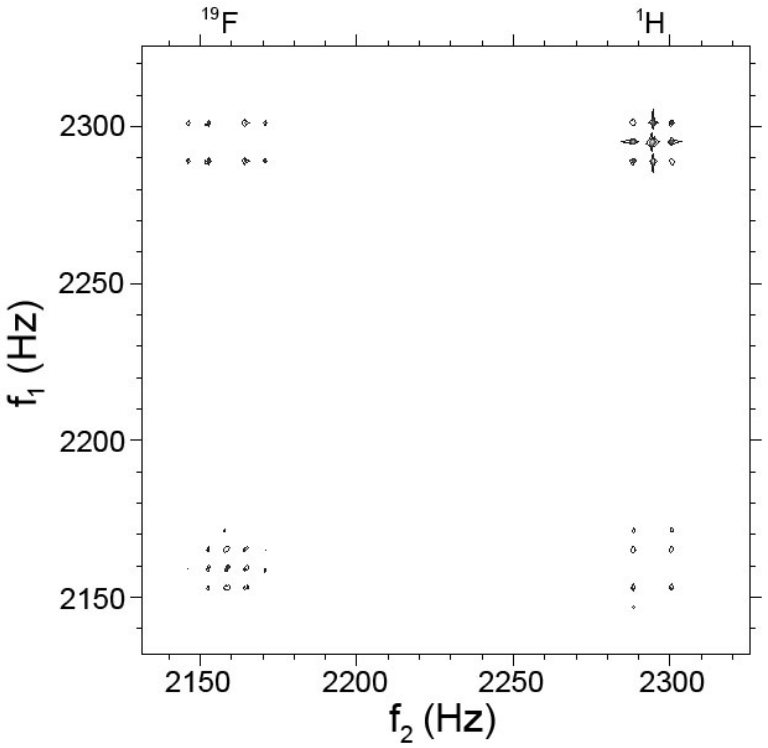

Figure 8.11 2D ^{1}H - ^{19}F COSY spectrum of 1,4-difluorobenzene calculated with a density matrix simulations and the coupling constants from reference [96].

Figure 8.10 presents a full 2D ^{1}H – ^{19}F EFNMR COSY measurement of 500 mL of 1,4-difluorobenzene. An analogous spectrum, calculated using a density matrix simulation and the coupling constants from reference [96] is presented in Figure 8.11 for comparison. Very good agreement between the experimental and calculated spectra is observed.

A 2D EFNMR COSY of this molecule was presented by Robinson et al. in 2006 [60]. The result in Figure 8.10 represents an improvement over this previously published result in terms of resolution and SNR due to the application of the apparatus and methodology developments (first order shimming, ULF noise screening and field stabilization) outlined in Chapter 4. However, we observe that the SNR of this measurement (which was acquired over a period of 15 hours) is not particularly high. In order to improve the performance of this experiment we must utilize the signal enhancement techniques explored in Chapter 5.

8.3. 2D COSY in the Earth's Field with DNP

In Chapter 5 we saw that dynamic nuclear polarization (DNP) can be used in EFNMR to achieve order of magnitude sensitivity enhancements, relative to prepolarization using the standard Terranova-MRI system, for samples on the order of 100 mL doped with about 1 mM of 4-oxo-TEMPO. As shown in the pulse sequence in Figure 8.1, DNP can be added to a COSY sequence in the preparation stage without changing any other aspects of the pulse sequence.

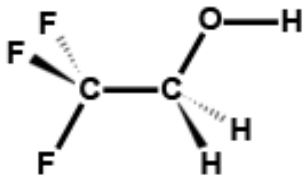

Figure 8.12 A schematic of the 2,2,2-trifluoroethanol molecule

Consider the 2,2,2-trifluoroethanol molecule pictured in Figure 8.12. The hydroxyl proton is in rapid chemical exchange and so experiences, on average, no indirect spin-spin couplings. NMR spectra of this molecule can be calculated using a

single heteronuclear indirect spin-spin coupling constant between the three magnetically equivalent ^{19}F nuclei and two magnetically equivalent ^{1}H nuclei.

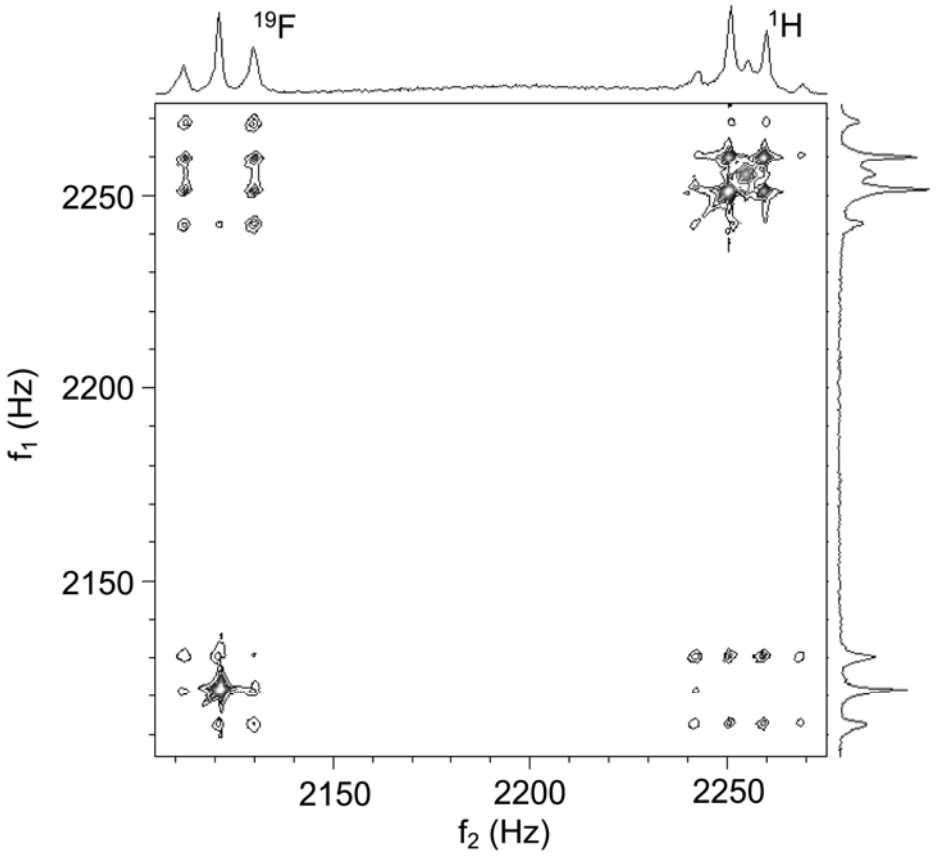

Figure 8.13 2D ^{1}H-^{19}F COSY of 100 mL 2,2,2-trifluoroethanol doped with 1.5 mM 4-oxo-TEMPO acquired in the Earth's magnetic field with DNP irradiation at 131.5 MHz in a prepolarization field of 2.7mT.

Figure 8.13 presents a 2D ^{1}H - ^{19}F EFNMR COSY spectrum of 100 mL of 2,2,2-trifluoroethanol doped with 1 mM of 4-oxo-TEMPO acquired with DNP irradiation at 131.5 MHz in a prepolarization field of 2.7 mT. A 2D COSY spectrum of 500 mL of 2,2,2-trifluoroethanol was presented by Robinson et al. [60]. The result presented in Figure 8.13 is of much higher quality than this previously reported result in terms of resolution and SNR. Furthermore, the DNP spectrum was acquired from only 100 mL of sample with an overall experiment time of 11 hours compared to a 15 hour measurement with 500 mL of sample.

For comparison with the experimental spectrum in Figure 8.13, a COSY spectrum calculated using a density matrix simulation and a coupling constant of 8.5

Hz is presented in Figure 8.16. The agreement between the experimental and simulated spectra is good but there are some noticeable differences, which can be attributed to a few unique features of spectra acquired using DNP.

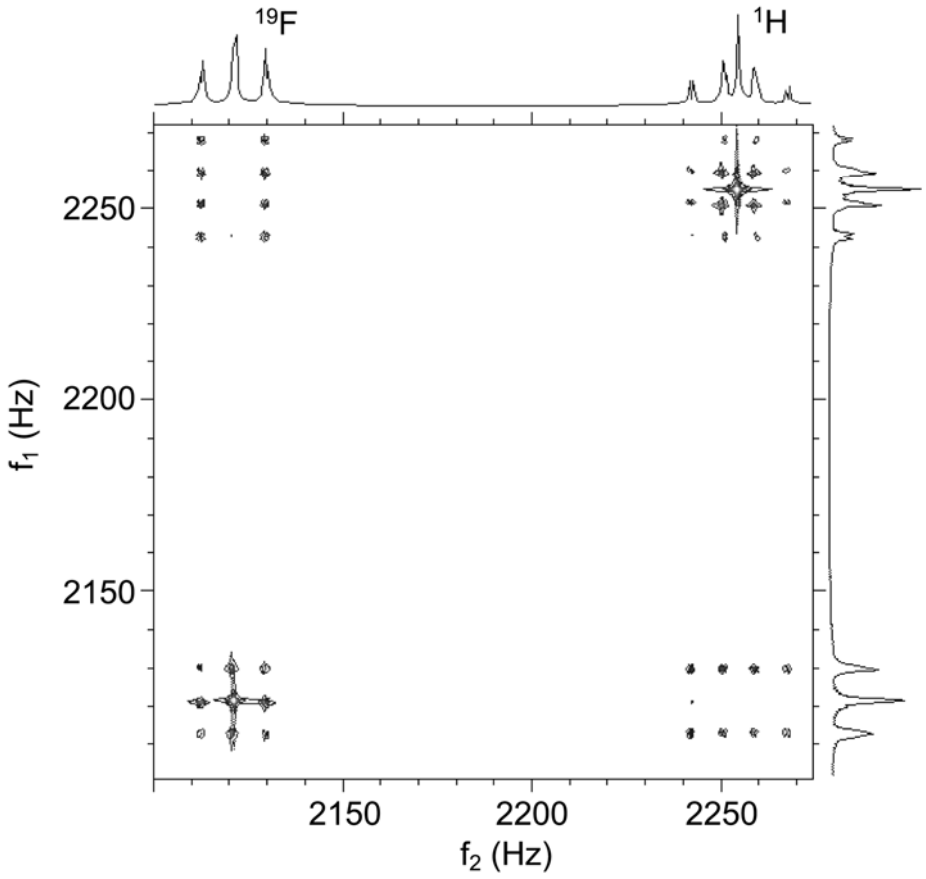

Figure 8.14 Density matrix simulation of a 2D ^{1}H-^{19}F COSY spectrum of 2,2,2-trifluoroethanol acquired in the Earth's magnetic field

To examine these differences in detail we compare a 1D projection of the experimental COSY spectrum (Figure 8.15) and a 1D spectrum calculated using a density matrix simulation (Figure 8.16). The relative peak integrals of the three magnetically equivalent ^{19}F nuclei, the two magnetically equivalent CH_2 ^{1}H nuclei and the hydroxyl ^{1}H nucleus in the experimental and calculated spectra are summarized in Table 8.2.

It is clear that the DNP enhancement of the ^{1}H nuclei in the CH_2 group is the most efficient, followed by the ^{19}F nuclei. The DNP enhancement of the ^{1}H on the hydroxyl group is the least efficient due to the rapid chemical exchange of this proton between molecules.

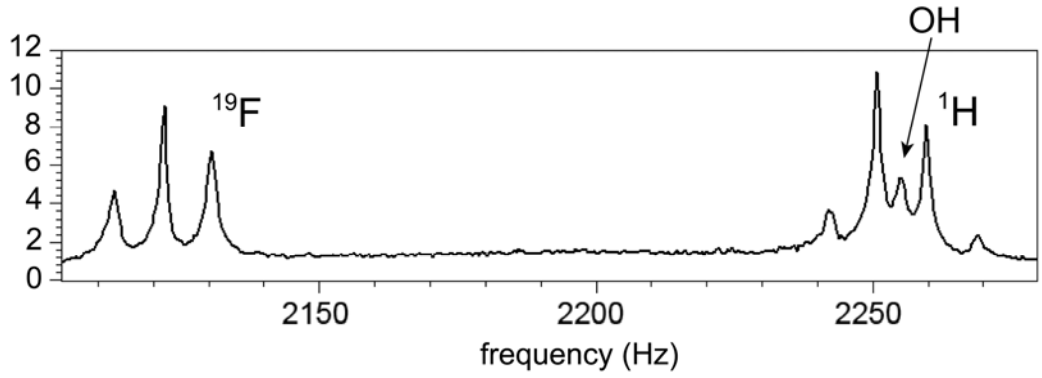

Figure 8.15 1D projection of the 2D COSY spectrum in Figure 8.13 summed over f_1.

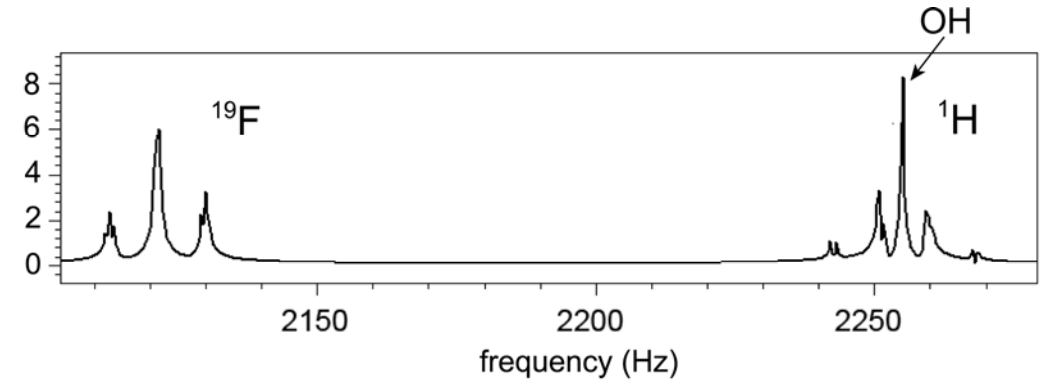

Figure 8.16 Density matrix simulation of a 1D ^{1}H-^{19}F EFNMR spectrum of 2,2,2-trifluoroethanol with $^{3}J(^{1}H,^{19}F)$ = 8.5 Hz.

Table 8.2 Relative peak integrals

	No. of Nuclei per Molecule	Calculated Spectrum	DNP Spectrum
^{19}F (CF_3)	3	50 %	44.1 %
^{1}H (CH_2)	2	33%	47.4 %
^{1}H (OH)	1	17%	8.5%

In addition to the difference in peak heights between the experimental and calculated spectra, we also observe in the calculated spectrum high-resolution structure which is not discernable in the experimental spectrum due to line-broadening. This high-resolution structure is a consequence of the relative strength of the ^{1}H – ^{19}F indirect spin-spin coupling. The coupling constant, $^{3}J(^{1}H,^{19}F)$ = 8.5 Hz, is 6.4% of the difference in Larmor frequency between ^{19}F and ^{1}H nuclei in a field of 53 mT (133.2 Hz). Therefore we can use third-order perturbation theory to model this

system. Such a calculation is presented in Figure 8.17. (Note that the uncoupled hydroxyl proton is omitted.) We find that the perturbation theory result is in good agreement with both the density matrix spectrum (Figure 8.16) and the experimental spectrum (Figure 8.15).

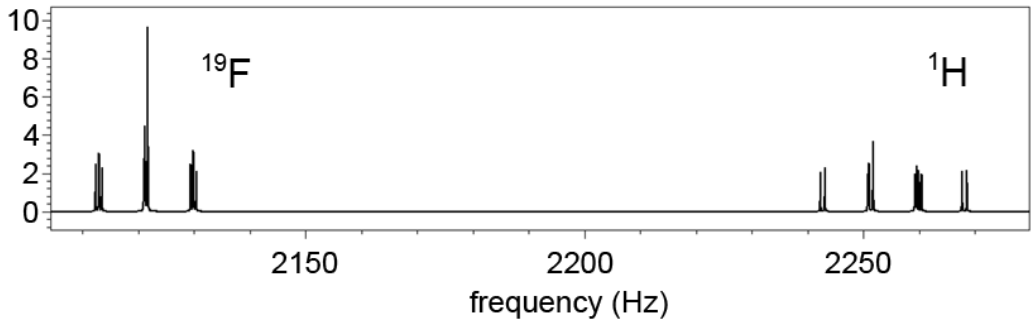

Figure 8.17 1D ^{1}H-^{19}F EFNMR spectrum of 2,2,2-trifluoroethanol calculated using third-order perturbation theory with $^{3}J(^{1}\mathrm{H},^{19}\mathrm{F})$ = 8.5 Hz. The uncoupled ^{1}H in the hydroxyl group was omitted in this calculation.

CHAPTER 9. Strong Coupling in Fields Below B_E

9.1. Introduction

Throughout this thesis, our discussion of the so-called strong coupling regime has focused on molecules for which the indirect spin-spin coupling constant, *J*, was a few percent of the difference in the Larmor frequency between the coupled nuclei. This is the situation commonly encountered when detecting NMR precession of coupled hetero-nuclei in the Earth's magnetic field (~ 50 μT). At fields below B_E, we encounter a different regime in which the indirect spin-spin coupling constant is equal to, or even larger than, the difference in Larmor frequency between the constituent nuclei. In this case, the observed spectral features are quite different from those typically observed in the Earth's field. It is important to note that this regime is fundamentally different from that which is often encountered at higher fields between homo-nuclei separated by only a very small chemical shift, where the difference in Larmor frequency of the coupled nuclei is much less than the J coupling constant, but the absolute Larmor frequency of the constituent nuclei is much larger than the indirect spin-spin coupling constant.

In a talk at the 10th International Conference on Magnetic Resonance Microscopy in 2009, Stephan Appelt postulated that the strong coupling regime which prevails in fields on the order of a few μT could be used for routine spectral analysis and identification in a manner analogous to high-field NMR [97]. In conventional high-field NMR, it is the chemical shift which separates chemical groups, allowing

for accurate chemical identification. At or below the Earth's magnetic field, chemical shifts of most nuclei are much smaller than the homogeneous spectral linewidth; therefore, it is only the indirect spin-spin coupling which provides chemical information. While the chemical shift separation is lost, the strong coupling regime in microtesla fields renders chemical groups like $^{13}CH_2$ and $^{13}CH_3$ distinguishable [58]. In his presentation at the ICMRM, Stephan Appelt determined the weakest field in which these distinguishing spectral features were observable by carrying out a perturbation theory calculation, similar to that in Chapter 7, but where the dominant interaction was the J coupling and the Zeeman term was the perturbation. He found that a field of 0.4 μT (4 mG) was sufficient to observe the characteristic strong coupling patterns which allow us to distinguish similar chemical groups such as $^{13}CH_3$ and $^{13}CH_2$.

In this chapter, we will use density matrix simulations and exact calculations to explore the strong coupling regime which is encountered when indirect spin-spin coupling dominates the interaction Hamiltonian. The goal of this investigation is to better understand this regime and to evaluate its potential for routine ultra-low field chemical analysis. In addition, we will explore the advantages of using a multi-dimensional EFNMR technique to simultaneously observe strongly coupled J spectra in both the Earth's field and a weaker field, thus allowing us to directly observe the evolution between these two very different strong coupling regimes.

9.2. Zero-field J coupled NMR

The observation of NMR precession in fields below the Earth's magnetic field, often called "zero"-field, or more correctly microtesla, NMR was first discussed by Weitekamp and co-workers [98-100] in the 1980s. The experiments presented by Weitekamp were essentially field-cycling pulse sequences in which the sample was polarized and detected at high field (4.2 T) but was allowed to evolve during an intermediate t_1 time period in "zero"-field. The "zero"-field condition was met by moving the sample to the fringe field of a superconducting magnet where an additional field, B_1, was applied such that it cancelled out the main fringe field. The residual field was less than 10 μT. The goal of these experiments was the acquisition

of high resolution spectra of poly-crystalline samples. This is difficult to achieve at high-field because of the significant line broadening which results from the combination of the Zeeman and dipolar interactions. In the "zero"-field case, the Hamiltonian is simplified because the Zeeman interaction is much smaller than the dipolar interaction and so the complexity of the resultant spectrum is dramatically reduced.

The direct detection of NMR precession in a field below B_E was first demonstrated by McDermott et al. [101] in 2002. Using a SQUID for NMR signal detection, the ^{1}H NMR spectrum of 3 mL of neat trimethyl phosphate was observed in a field of 4.8 μT. The observed spectrum was a doublet, centred about the ^{1}H Larmor frequency of 204 Hz, with a measured splitting of 10.4 Hz, corresponding to the hetero-nuclear indirect spin-spin coupling constant between the nine magnetically equivalent ^{1}H nuclei and the single ^{31}P nucleus. This coupling constant is 8.6% of the difference of Larmor frequency between the ^{1}H nuclei and the ^{31}P nucleus at 4.8 μT; however, the resolution of the measurement was such that no additional splitting due to the strong coupling was observed.

Recently, Ledbetter et al. [102] presented directly detected J coupled spectra in the true zero-field limit where no Zeeman interaction is present. This is achieved by first prepolarizing a small volume of the sample in a 1.8 T Halbach magnet. This prepolarized liquid flows into a shielded cavity where the prevailing magnetic field is on the order of 0.1 nT. The sample is exposed to a pulse of DC magnetic field perpendicular to the main field axis of the Halbach array. This pulse rotates each nucleus by an angle proportional to its gyromagnetic ratio. The longitudinal component of the magnetization is subsequently recorded by an atomic magnetometer. The magnetometer is built on the micrometer scale, thus allowing for the detection of NMR signal from very small (μL) volumes of sample.

The atomic magnetometer observes M_z directly; therefore the observation operator is given by Eq. 9-1, where the sum performed is over all observed nuclei.

$$\mathbf{I}_{obs} = \sum_i \gamma_i \mathbf{I}_{zi}$$

9-1

In the absence of a static magnetic field, the full interaction Hamiltonian is simply the sum of the indirect spin-spin coupling terms between the constituent nuclei (Eq. 9-2).

$$\mathcal{H} = 2\pi \sum_{i>j} J_{ij} \mathbf{I}_i \cdot \mathbf{I}_j \qquad 9\text{-}2$$

The eigenstates of this Hamiltonian are the total angular momentum states of the form: $\left|S, K; F, m_F\right\rangle$. In this formalism, S and K are the total angular momentum quantum numbers of two groups of magnetically equivalent spins coupled via the indirect spin-spin coupling interaction. F, the total angular momentum quantum number, is equal to the vector sum of S and K, and m_F is the corresponding azimuthal quantum number. Under the action of the observation operator in Eq. 9-1 the allowed transitions correspond to a change in F of ±1 and no change in m_F, i.e. $\Delta F = \pm 1$ and $m_F = 0$. These transitions are equivalent to the sigma transitions discussed in the DNP theory section of Chapter 5. The eigenvalues of Eq. 9-2 can be calculated from Eq. 9-3.

$$E = \frac{J_{SK}}{2}\left(F(F+1) - S(S+1) - K(K+1)\right) \qquad 9\text{-}3$$

Using these eigenvalues, eigenvectors and selection rules the expected spectra for a range of heteronuclear coupled systems can be easily computed. For example $^{13}C^{1}H_2$ has eigenstates: $\left|\tfrac{1}{2},1;\tfrac{3}{2},m_F\right\rangle$ and $\left|\tfrac{1}{2},1;\tfrac{1}{2},m_F\right\rangle$, where m_F takes values from $-F$ to F. The energy levels are: $J_{CH}/2$ and $-J_{CH}$ with a corresponding transition frequency of $3/2\ J_{CH}$. A similar calculation for $^{13}C^{1}H_3$ yields transitions at J_{CH} and $2J_{CH}$.

Ledbetter et al. [102] demonstrates both of the above cases using isotopically labeled methanol, ethanol 1 ($^{12}C^{1}H_3$-$^{13}C^{1}H_2$-O^{1}H) and ethanol 2 ($^{13}C^{1}H_3$-$^{12}C^{1}H_2$-O^{1}H). The latter two molecules have zero-field spectra which contain additional splittings caused by the presence of homonuclear coupling between the CH_2 and CH_3 protons, which are rendered magnetically non-equivalent by their different heteronuclear

coupling to the ^{13}C nucleus.

The ability to observe both homo- and hetero-nuclear spin-spin coupling at zero-field is a significant benefit when considering the possibility of using this technique to do a low-field analysis of small molecules. However, the patterns which result from this combination of homo- and hetero- nuclear coupling are not as simple and readily identifiable as their high-field counter-part.

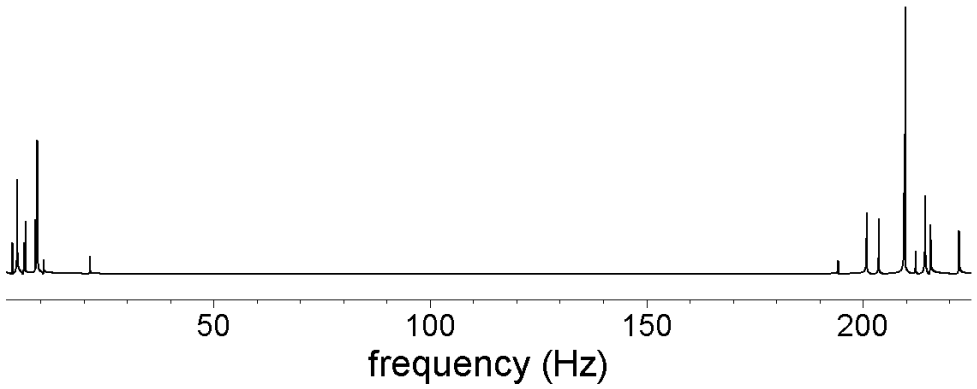

Figure 9.1 Density matrix simulation of the zero-field spectrum of ethanol 1 ($^{12}C^{1}H_3$-$^{13}C^{1}H_2$-O^{1}H) with $^{1}J(^{13}C,^{1}H)$ = 140 Hz, $^{2}J(^{13}C,^{1}H)$ = -4.6 Hz and $^{3}J(^{1}H,^{1}H)$ = 7 Hz. The uncoupled hydroxyl proton is not included in the calculation.

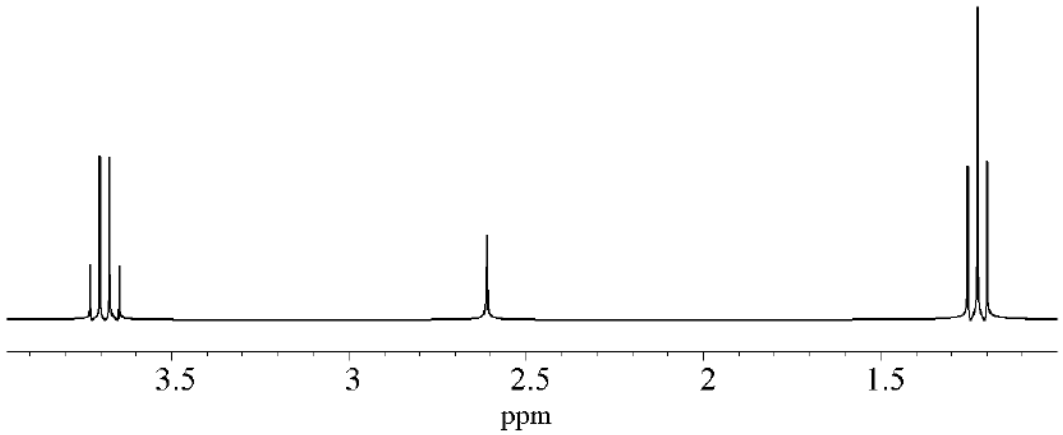

Figure 9.2 A simulated ^{1}H NMR spectrum of ethanol in the high-field limit.

Compare the simulated zero-field NMR spectrum of isotopically enriched ethanol 1 in Figure 9.1 with the simulated high-field 1H NMR spectrum of non-enriched ethanol in Figure 9.2. In the zero-field spectrum the methylene protons give rise to a peak at $3/2*^{1}J_{CH}$ (210 Hz) which is further split into a complicated

asymmetrical pattern by the homonuclear coupling to the methyl protons. The methyl protons give rise to peaks at $|^2J_{CH}|$ (4.6 Hz) and $2*|^2J_{CH}|$ (9.2 Hz) which are further split into a complicated pattern by the very strong homonuclear coupling to the methylene protons. In a more complicated molecule these assignments would be very challenging.

By comparison the high-field spectrum of ethanol is very easy to interpret. The contributions from the methyl, methylene and hydroxyl protons are unambiguously separated by their chemical shifts and are also identifiable by the simple peak multiplicity which arises from the weak homonuclear *J* coupling between the methyl and methylene groups. The hydroxyl proton experiences no net indirect spin-spin coupling and so is a singlet. The methylene protons are weakly coupled to the three methyl protons and so are split into a quartet with uniform splitting, $^3J_{HH}$, and with a characteristic 1:3:3:1 amplitude ratio pattern. The methyl proton peak is split into a triplet with characteristic peak amplitude ratios of 1:2:1 due to a homonuclear coupling to the two methylene protons.

Another limitation of zero-field NMR spectra is that the homonuclear couplings are only evident when heteronuclear couplings break the magnetic equivalence between homo-nuclei. This somewhat limits the technique to either isotopically labeled samples or those containing naturally abundant NMR active nuclei such as ^{19}F and ^{31}P. Thus, while zero-field NMR spectra may be useful for molecular identification in some cases, it can not, in its current form, rival the ability of high-field NMR for molecular identification or structure determination.

9.3. Microtesla (μT) NMR

Consider now the μT coupling regime where we observe the evolution of coupled nuclei in very weak fields, where the Larmor frequencies of the constituent nuclei are on the same order of magnitude as the indirect spin-spin coupling constant.

The complexity of the observed NMR spectrum of a given molecule rapidly increases as the field increases and the Zeeman interaction becomes more significant. Therefore we will consider first a rather simple example: $^{13}C^1H_3$. The protons in this methyl group are magnetically equivalent and so can be treated together. The angular

momenta of these nuclei can be combined to produce a total angular momentum of either 3/2 or 1/2. Therefore this problem can be divided into two parts: the coupling between total angular momenta: S = 1/2 and K = 1/2, for which the closed form analytical solution is well known, and the coupling of total angular momenta: S = 1/2 and K = 3/2, the energy levels for which we determined in Chapter 7.

$$
\begin{aligned}
E_1 &= \frac{3}{2}\nu_H + \frac{1}{2}\nu_C + \frac{3}{4}J \\
E_2 &= \nu_H - \frac{1}{4}J - \frac{1}{2}\sqrt{(\nu_C - \nu_H)^2 + 2J(\nu_C - \nu_H) + 4J^2} \\
E_3 &= -\frac{1}{4}J - \frac{1}{2}\sqrt{(\nu_C - \nu_H)^2 + 4J^2} \\
E_4 &= -\nu_H - \frac{1}{4}J - \frac{1}{2}\sqrt{(\nu_C - \nu_H)^2 - 2J(\nu_C - \nu_H) + 4J^2} \\
E_5 &= \nu_H - \frac{1}{4}J + \frac{1}{2}\sqrt{(\nu_C - \nu_H)^2 + 2J(\nu_C - \nu_H) + 4J^2} \\
E_6 &= -\frac{1}{4}J + \frac{1}{2}\sqrt{(\nu_C - \nu_H)^2 + 4J^2} \\
E_7 &= -\nu_H - \frac{1}{4}J + \frac{1}{2}\sqrt{(\nu_C - \nu_H)^2 - 2J(\nu_C - \nu_H) + 4J^2} \\
E_8 &= -\frac{3}{2}\nu_H - \frac{1}{2}\nu_C + \frac{3}{4}J \\
E_9 &= \frac{1}{2}\nu_H + \frac{1}{2}\nu_C + \frac{1}{4}J \\
E_{10} &= -\frac{1}{4}J - \frac{1}{2}\sqrt{(\nu_C - \nu_H)^2 + J^2} \\
E_{11} &= -\frac{1}{4}J + \frac{1}{2}\sqrt{(\nu_C - \nu_H)^2 + J^2} \\
E_{12} &= -\frac{1}{2}\nu_H - \frac{1}{2}\nu_C + \frac{1}{4}J
\end{aligned}
$$

9-4

The closed form expressions for the twelve energy levels are presented in Eq. 9-4. The first eight levels correspond to the S = 1/2, K = 3/2 coupled system, while the latter four levels belong to the S = 1/2, K = 1/2 coupled system.

Table 9.1 presents the eigenvectors for the limiting cases of $B_0 \rightarrow 0$ and $B_0 \rightarrow \infty$, written in the total angular momentum ($\left|F, m_F\right\rangle_F$) and product operator

($|m_S, m_k\rangle_{SK}$) formalisms, respectively. The total angular momentum kets in the "zero"-field case are expanded in terms of the product operator kets using the Clebsch-Gordan coefficients. This expansion will be useful when we relate the allowed transitions in the Earth's field (54 μT) with those in a much weaker field (1 μT). Note that the values of *S* and *K*, the total quantum numbers for the ^{13}C nucleus and the group of magnetically equivalent ^{1}H nuclei, respectively, are explicitly listed in the table in order to distinguish the eigenvectors (such as $|7\rangle$ and $|9\rangle$) which appear to be the same but in fact correspond to different values of *K*.

Table 9.1 Eigenvectors in the limiting cases of B → 0 and B → ∞, written in the total angular momentum and product operator formalisms, respectively. In the "zero"-field case, the total angular momentum kets are expanded in terms of the product operator kets using the Clebsch-Gordan coefficients.

$\|n\rangle$	*S*, *K*	Limit as $B \to 0$ $\|F, m_F\rangle_F \to \|m_S, m_k\rangle_{SK}$	Limit as $B \to \infty$ $\|m_S, m_k\rangle_{SK}$
$\|1\rangle$	$\frac{1}{2}, \frac{3}{2}$	$\|2,2\rangle_F = \left\|\frac{1}{2}, \frac{3}{2}\right\rangle_{SK}$	$\left\|\frac{1}{2}, \frac{3}{2}\right\rangle_{SK}$
$\|2\rangle$	$\frac{1}{2}, \frac{3}{2}$	$\|2,-1\rangle_F = \frac{\sqrt{3}}{2}\left\|-\frac{1}{2}, -\frac{1}{2}\right\rangle_{SK} + \frac{1}{2}\left\|\frac{1}{2}, -\frac{3}{2}\right\rangle_{SK}$	$\left\|-\frac{1}{2}, -\frac{1}{2}\right\rangle_{SK}$
$\|3\rangle$	$\frac{1}{2}, \frac{3}{2}$	$\|1,-1\rangle_F = \frac{1}{2}\left\|-\frac{1}{2}, -\frac{1}{2}\right\rangle_{SK} - \frac{\sqrt{3}}{2}\left\|\frac{1}{2}, -\frac{3}{2}\right\rangle_{SK}$	$\left\|\frac{1}{2}, -\frac{3}{2}\right\rangle_{SK}$
$\|4\rangle$	$\frac{1}{2}, \frac{3}{2}$	$\|2,0\rangle_F = \frac{1}{\sqrt{2}}\left\|-\frac{1}{2}, \frac{1}{2}\right\rangle_{SK} + \frac{1}{\sqrt{2}}\left\|\frac{1}{2}, -\frac{1}{2}\right\rangle_{SK}$	$\left\|-\frac{1}{2}, \frac{1}{2}\right\rangle_{SK}$
$\|5\rangle$	$\frac{1}{2}, \frac{3}{2}$	$\|1,0\rangle_F = \frac{1}{\sqrt{2}}\left\|-\frac{1}{2}, \frac{1}{2}\right\rangle_{SK} - \frac{1}{\sqrt{2}}\left\|\frac{1}{2}, -\frac{1}{2}\right\rangle_{SK}$	$\left\|\frac{1}{2}, -\frac{1}{2}\right\rangle_{SK}$
$\|6\rangle$	$\frac{1}{2}, \frac{3}{2}$	$\|2,1\rangle_F = \frac{1}{2}\left\|-\frac{1}{2}, \frac{3}{2}\right\rangle_{SK} + \frac{\sqrt{3}}{2}\left\|\frac{1}{2}, \frac{1}{2}\right\rangle_{SK}$	$\left\|-\frac{1}{2}, \frac{3}{2}\right\rangle_{SK}$
$\|7\rangle$	$\frac{1}{2}, \frac{3}{2}$	$\|1,1\rangle_F = \frac{\sqrt{3}}{2}\left\|-\frac{1}{2}, \frac{3}{2}\right\rangle_{SK} - \frac{1}{2}\left\|\frac{1}{2}, \frac{1}{2}\right\rangle_{SK}$	$\left\|\frac{1}{2}, \frac{1}{2}\right\rangle_{SK}$
$\|8\rangle$	$\frac{1}{2}, \frac{3}{2}$	$\|2,-2\rangle_F = \left\|-\frac{1}{2}, -\frac{3}{2}\right\rangle_{SK}$	$\left\|-\frac{1}{2}, -\frac{3}{2}\right\rangle_{SK}$

$\left\|9\right\rangle$	$\frac{1}{2},\frac{1}{2}$	$\left\|1,1\right\rangle_F = \left\|\frac{1}{2},\frac{1}{2}\right\rangle_{SK}$	$\left\|\frac{1}{2},\frac{1}{2}\right\rangle_{SK}$
$\left\|10\right\rangle$	$\frac{1}{2},\frac{1}{2}$	$\left\|0,0\right\rangle_F = \frac{1}{\sqrt{2}}\left\|\frac{1}{2},-\frac{1}{2}\right\rangle_{SK} - \frac{1}{\sqrt{2}}\left\|-\frac{1}{2},\frac{1}{2}\right\rangle_{SK}$	$\left\|\frac{1}{2},-\frac{1}{2}\right\rangle_{SK}$
$\left\|11\right\rangle$	$\frac{1}{2},\frac{1}{2}$	$\left\|1,0\right\rangle_F = \frac{1}{\sqrt{2}}\left\|\frac{1}{2},-\frac{1}{2}\right\rangle_{SK} + \frac{1}{\sqrt{2}}\left\|-\frac{1}{2},\frac{1}{2}\right\rangle_{SK}$	$\left\|-\frac{1}{2},\frac{1}{2}\right\rangle_{SK}$
$\left\|12\right\rangle$	$\frac{1}{2},\frac{1}{2}$	$\left\|1,-1\right\rangle_F = \left\|-\frac{1}{2},-\frac{1}{2}\right\rangle_{SK}$	$\left\|-\frac{1}{2},-\frac{1}{2}\right\rangle_{SK}$

In the limit as $B_0 \rightarrow 0$, where the indirect spin-spin coupling interaction dominates the interaction Hamiltonian, the conventional NMR formalism for signal detection does not apply. Without a dominant static field, B_0, the concept of excited magnetization precessing in a transverse plane no longer holds meaning. Therefore the traditional observation operator (Eq. 9-5) is no longer relevant.

$$\mathbf{I}_{obs} = \sum_n \mathbf{I}_{xn} + i\mathbf{I}_{yn} \qquad 9\text{-}5$$

Indeed the whole concept of detecting the NMR signal inductively is no longer a practical solution given the poor sensitivity of an induction coil at frequencies of only a few tens or hundreds of Hertz. For this reason, among others, the previously discussed sub-Earth's field NMR spectra were detected using either SQUIDs [101] or atomic magnetometers [102]. In these cases, the M_z magnetization is the quantity observed (not the rate of change of the flux through an induction coil) and so the observation operator is simply: $\gamma\mathbf{I}_z$.

For the purposes of our investigation of the evolution from the J coupling dominant regime at "zero"-field up to the Zeeman dominant regime which prevails in the Earth's magnetic field, it would be useful to have a way of observing the "zero"-field spectra with our conventional observation operator. Fortunately we can do this using a multi-dimensional NMR technique similar to that presented by Weitekamp et al. in 1983 [98].

9.3.1. Observation of μT NMR using Multi-dimensional EFNMR

Consider the two-dimensional pulse sequence presented in Figure 9.3. As with all of the previously presented multi-dimensional EFNMR pulse sequences in this thesis, the experiment starts with a pre-polarization period which includes a prepolarization pulse and/or a DNP irradiation pulse to increase the available polarization and so optimize the sensitivity of our measurement. This prepolarization period is followed by a broadband excitation pulse which rotates the magnetization of all spins into the transverse plane. During the subsequent t_1 evolution time period, an offset field, $\mathbf{B}_{off}$, is applied to the system. This field cancels out B_E such that the net field is our desired evolution field, $\mathbf{B}_{ev} = \mathbf{B}_E + \mathbf{B}_{off}$. At the end of the t_1 evolution period, B_{off} is switched off adiabatically and the NMR signal is sampled as a function of time, t_2, in the Earth's magnetic field. This sequence is repeated N_1 times, for an incrementally longer t_1 period each time, at which point we have acquired a full 2D data matrix, $S(t_1, t_2)$. The Fourier transform of this data set, $s(f_1, f_2)$, is a 2D spectrum with the evolution in B_E along f_2, the directly detected dimension, and the evolution in B_{ev} along f_1, the indirectly detected dimension. This 2D spectrum can be projected along f_1 and f_2 to recover the evolution field and Earth's field NMR spectra, but more interestingly the full 2D spectrum can be used to map the evolution from one regime to the other.

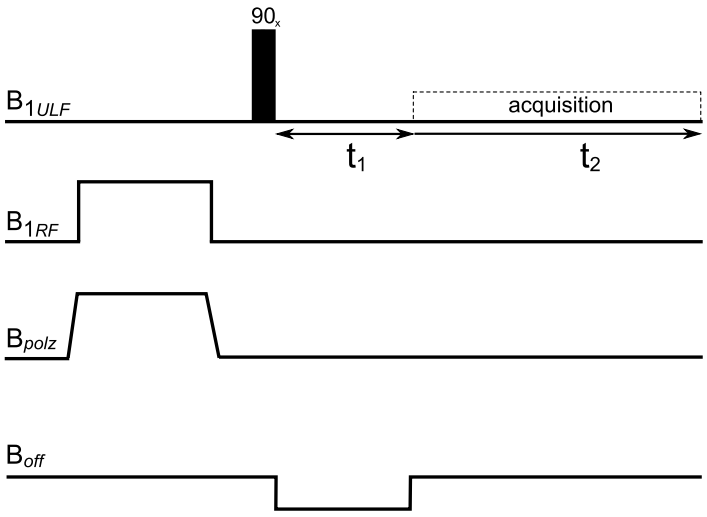

Figure 9.3 2D pulse sequence with evolution in the t_1 domain carried out in the evolution field ($\mathbf{B}_E + \mathbf{B}_{off}$) and the evolution in the t_2 domain carried out in $\mathbf{B}_E$.

In order to understand the output of this experiment we return to our example of $^{13}C^{1}H_3$. Consider first the case as B_0 approaches zero. The eigenstates collapse to the total angular momentum states, as shown in Table 9.1. Since we are eventually detecting our magnetization in the traditional inductively coupled fashion, in the presence of the Earth's magnetic field, we will consider only the effect of the standard NMR observation operator (Eq. 9-5) in this regime. The selection rules associated with this observation operator in the limit as $B_0 \rightarrow 0$ are a change in total angular momentum of ±1 or 0 and a change in azimuthal angular momentum of ±1. By inspection of the eigenstates in Table 9.1, we find that there are sixteen allowed transitions in this near zero-field regime (Eq. 9-6).

$$\Delta F = 0; \Delta m_F = \pm 1 \rightarrow T_{1-6}, T_{2-8}, T_{4-2}, T_{5-3}, T_{6-4}, T_{75}, T_{9-11}, T_{11-12}$$
$$\Delta F = \pm 1; \Delta m_F = \pm 1 \rightarrow T_{1-7}, T_{3-8}, T_{4-3}, T_{5-2}, T_{6-5}, T_{7-4}, T_{9-10}, T_{10-12}$$

9-6

Figure 9.4 presents a density matrix simulation of a 1D NMR spectrum of $^{13}C^{1}H_3$ in a field of 1 μT with J_{CH} = 140 Hz. The Larmor frequencies at 1 μT of ^{1}H and ^{13}C nuclei are 42.6 Hz and 10.7 Hz, respectively. Inset in Figure 9.4 are zoomed regions of the spectrum which reveal the multiplet structure of the peaks clustered around 40 Hz. Each peak in the spectrum is labeled according to the transitions in Eq. 9-6. Strictly speaking, a given line in an NMR spectrum does not directly result from a transition between two specific states. In NMR, we observe an evolution of spin magnetization with time and Fourier transform this time-dependent signal to obtain a spectrum. We do not directly observe energy emission or absorption. Therefore it is not entirely appropriate to refer to lines in an NMR spectrum as transitions. What these NMR lines really represent is the evolution of a phase coherence between two states. However, conceptually, it is much easier to think about "allowed transitions", "selection rules" and "transition frequencies" than phase coherences and these phenomena are closely related. Therefore, while acknowledging the slight irregularity of this terminology, we will continue to think about the frequency components of the NMR spectra in terms of the corresponding allowed transitions and selection rules of the coupled system for the sake of promoting an intuitive understanding of the coupling regime and the underlying quantum mechanics.

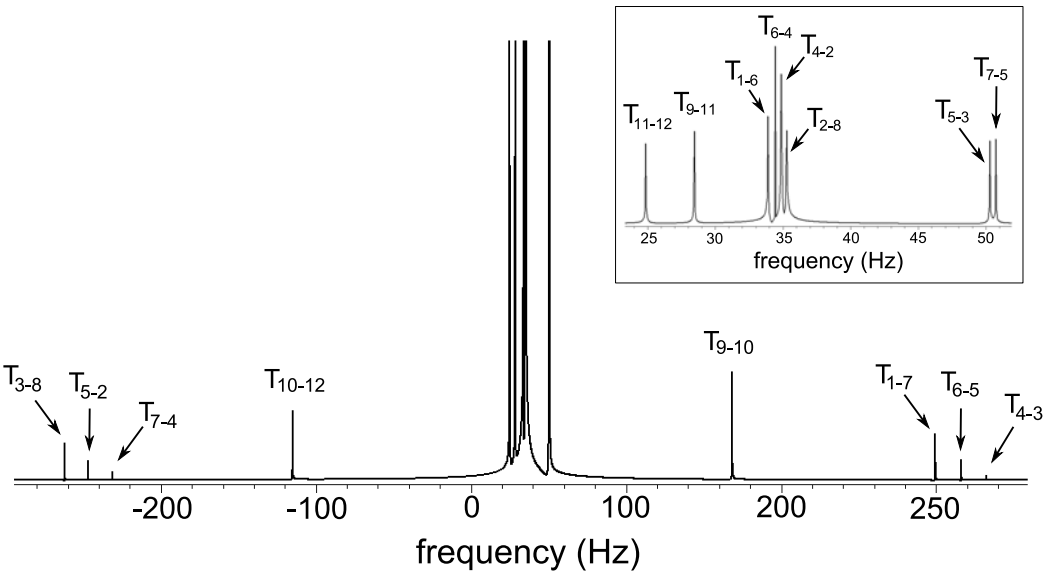

Figure 9.4 A 1D NMR spectrum of $^{13}C^{1}H_3$ in a field of 1 μT calculated using a density matrix simulation with the standard NMR observation operator. Inset is a zoomed region of the spectrum, around 40 Hz, which is included to show the multiplicity of the central groups of multiplets. All peaks are labeled according to the transitions listed in Eq. 9-6.

Returning to Figure 9.4, we can associate the triplets at either end of the spectrum with the $F = 2 \rightarrow F = 1$ transition for the $K = 3/2$, $S = 1/2$ coupled system. These peaks are shifted from the zero-field positions of $\pm 2J$ because of the introduction of a finite Zeeman interaction. Similarly, the singlet peaks corresponding to the $F = 1 \rightarrow F = 0$ transitions for the $K = 1/2$, $S = 1/2$ coupled system are shifted to higher frequency with respect to the zero-field peak positions of $\pm J$. The two peaks closest to zero correspond to the $\Delta F = 0$, $F = 1$, $\Delta m_F = 1$ transitions for the $K = 1/2$, $S = 1/2$ coupled system. The remaining quartet and doublet correspond to the $\Delta F = 0$, $\Delta m_F = 1$ transitions for the $K = 3/2$, $S = 1/2$ coupled system with $F = 2$ and $F = 1$, respectively.

Now consider the coupling situation in the Earth's magnetic field. While the indirect spin-spin coupling in the $^{13}C^{1}H_3$ group does not satisfy the weak coupling condition at 54 μT, this is still a Zeeman dominated regime and so the eigenstates are closely associated with the product operator states listed in Table 9.1. Under the influence of the observation operator in Eq. 9-5, the selection rules for this system are $\Delta m_S = \pm 1$ and $\Delta m_K = \pm 1$. Using these selection rules we can identify fourteen allowed

transitions (Eq. 9-7)

$$\Delta m_S = \pm 1, \Delta m_K = 0 \rightarrow T'_{1-6}, T'_{3-8}, T'_{5-2}, T'_{7-4}, T'_{9-11}, T'_{10-12}$$
$$\Delta m_S = 0, \Delta m_K = \pm 1 \rightarrow T'_{1-7}, T'_{2-8}, T'_{4-2}, T'_{5-3}, T'_{6-4}, T'_{7-5}, T'_{9-10}, T'_{11-12}$$

9-7

A comparison of Eq. 9-7 and Eq. 9-6 shows that the zero-field transitions $T_{4-3} = |2,0\rangle_F \rightarrow |1,-1\rangle_F$ and $T_{6-5} = |2,1\rangle_F \rightarrow |1,0\rangle_F$ are not allowed in the "high"-field case, i.e. their transition probabilities go to zero as the field increases.

Figure 9.5 presents a density matrix simulation of a 1D NMR spectrum of $^{13}C^{1}H_3$ in the Earth's field (54 μT) with J_{CH} = 140 Hz. The Larmor frequencies at 54 μT of ^{1}H and ^{13}C nuclei are 2299 Hz and 577.5 Hz, respectively. Inset in Figure 9.5 are zoomed regions of the spectrum which show the multiplet structure of the two quadruplets in the ^{1}H portion of the spectrum. The spectrum is labeled according to the associated transitions in Eq. 9-7.

The various components of this spectrum are much more easily identified than the 1 μT case for two reasons. First, the form of this spectrum is close to the weak field case which is familiar from conventional high-field NMR and second, the patterns which occur in this regime are easily divided into a contribution from the Zeeman interaction and the perturbation by the indirect spin-spin coupling interaction. The converse is not true in the "zero"-field regime. The six peaks centred about 577.5 Hz (the Larmor frequency of ^{13}C) can be associated with the four projections of the total angular momentum of the three ^{1}H nuclei (m_K = 3/2, 1/2, -1/2, and -3/2) with the additional splitting of the m_K = ±1/2 peaks resulting from the slightly different transition frequencies for the cases of K = 1/2 and K = 3/2. Similarly, the ^{1}H peaks centred about 2299 Hz can be divided into two quartets corresponding to the m_S = ±1/2 spin states of the ^{13}C nucleus. The quartet nature of these peaks corresponds to the three possible projections of the total angular momentum of two of the ^{1}H nuclei, assuming one of the ^{1}H nuclei is the observed nucleus, for the K = 3/2 case plus an addition peak resulting from the K = 1/2 case.

Having assigned the complete spectrum in both the 1 μT and 54 μT cases, we can simulate the full 2D experiment (depicted in Figure 9.3) and determine the

connection between the two regimes using the resultant 2D spectrum.

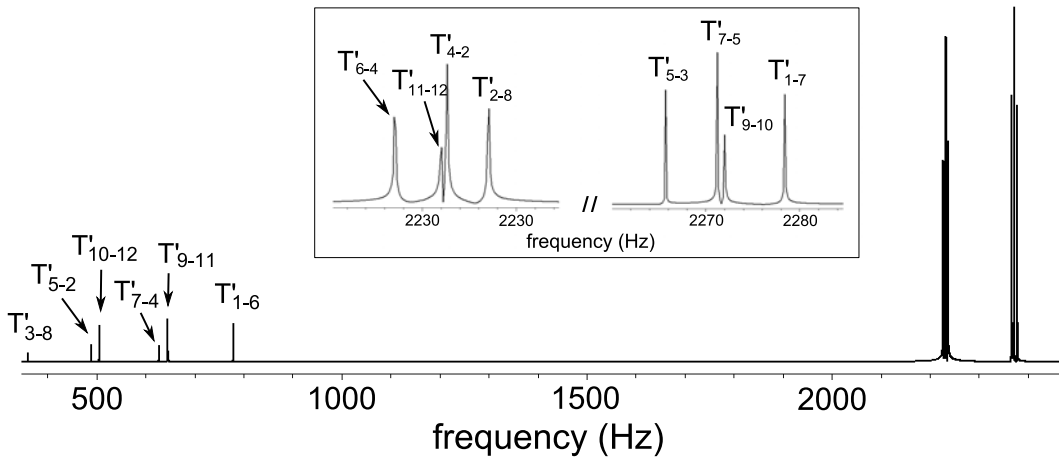

Figure 9.5 A 1D spectrum of $^{13}C^{1}H_3$ in a field of 54 μT calculated with a density matrix simulation. Inset is a zoomed view of the two ^{1}H multiplets. All peaks are labeled according to the transitions in Eq. 9-7.

Consider the 2D spectrum in Figure 9.6 which was calculated using a density matrix simulation with B_{ev} = 1 μT, B_E = 54 μT and J_{CH} = 140 Hz. The spectrum is divided, along f_2, into a ^{13}C region ($m_S = \pm 1$) and a ^{1}H region ($m_K = \pm 1$). With the exception of the central peaks of the ^{1}H quartets, all lines are well separated along f_2 and so, by taking vertical slices through the 2D spectrum at the frequency of each EFNMR transition, we can map the EFNMR peaks to the corresponding evolution field peaks.

A correspondence between a transition in the "zero"-field regime and the "high"-field regime means that the product operator states involved in the "high"-field transition evolve, as B → 0, into one or other of the total angular momentum states involved in the "zero"-field transition. Which states will evolve at "zero"-field into which states at "high"-field can be determined by considering the expansion of the total angular momentum "zero"-field states in terms of the product-operator "high"-field states.

For example, consider the transition between eigenstates $|3\rangle$ and $|8\rangle$. In the zero-field limit this transition occurs between the total angular momentum states: $|1,-1\rangle_F$ and $|2,-2\rangle_F$. The former is a superposition of the $|-\frac{1}{2},-\frac{1}{2}\rangle_{S,K}$ and $|\frac{1}{2},-\frac{3}{2}\rangle_{S,K}$

product operator states while the latter is exactly equal to the product operator state: $\left|-\frac{1}{2},-\frac{3}{2}\right\rangle_{S,K}$. In the high-field limit, eigenstate $|2\rangle$ collapses into the exact state: $\left|-\frac{1}{2},-\frac{1}{2}\right\rangle_{S,K}$ while eigenstate $|3\rangle$ becomes $\left|\frac{1}{2},-\frac{3}{2}\right\rangle_{S,K}$. Therefore the "zero"-field transition T_{38} is correlated with the "high"-field transition T'_{82} as well as T'_{38}.

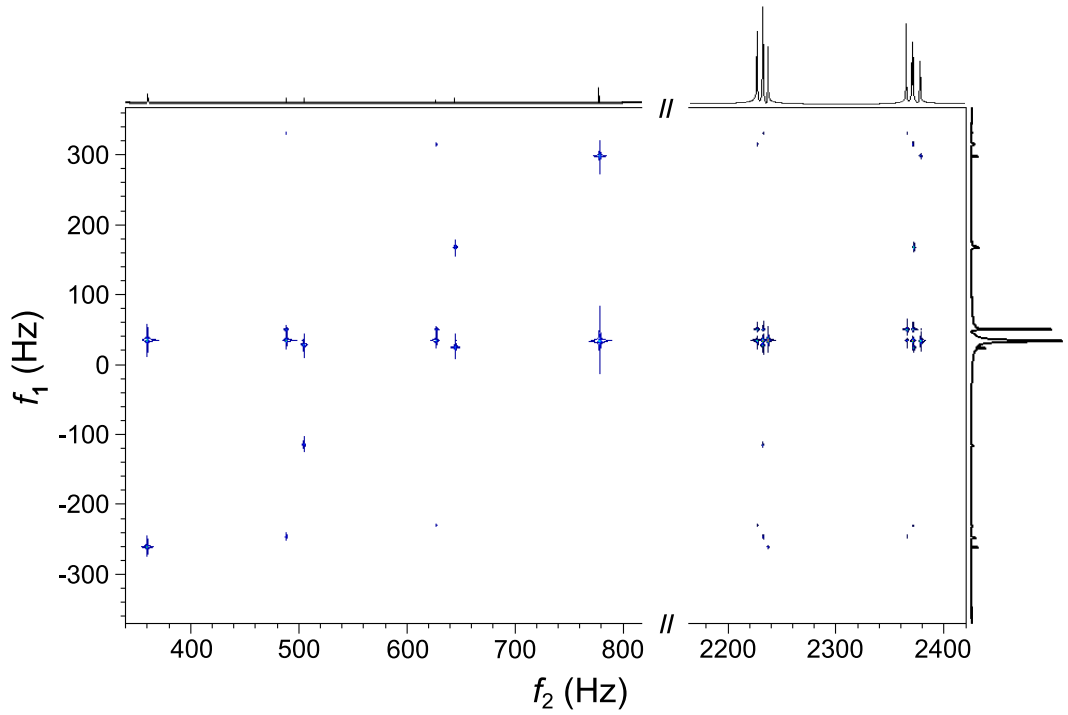

Figure 9.6 A contour map of the 2D spectrum of $^{13}C^{1}H_3$ calculated using a density matrix simulation of the pulse sequence in Figure 9.3 (with an evolution field of 1 μT and an Earth's field of 54 μT). The contour maps of the ^{13}C and ^{1}H portions of the spectrum (in f_2) are scaled separately in order to better indentify the much weaker peaks in the ^{13}C portion.

Table 9.2 presents a full map of the correlations between the "zero"-field transitions, T, and the "high"-field transitions, T'. The "high"-field transitions are listed along the top of each column while the "zero"-field transitions are listed at the start of each row. A gray cell connecting transitions T and T' indicates a correlation between these transitions. Note that the T_{43} and T_{65} transitions do not have direct correlations to T'_{43} and T'_{65} because these are forbidden transitions in the high-field limit.

In order to more easily compare the results in Table 9.2 directly to the calculated spectrum in Figure 9.6, the transitions which belong to the same multiplet in the 1 μT and 54 μT 1D spectra are grouped together by horizontal and vertical coloured boxes. By inspection we see that the mapping between *T* and *T'* in Table 9.2 is able to account for all of the peaks in the 2D spectrum.

Table 9.2 Summary of all of the possible correlations between allowed transitions in the Zeeman dominated regime (columns) and the "zero"-field regime (rows). Transitions are labeled according to the initial and final eigenstates and are ordered such that the table corresponds to the 2D spectrum in Figure 9.6. The coloured boxes group together transitions which are part of the same multiplet. A shaded box connecting two transitions indicates that the given "zero"-field transition correlates with the corresponding "high"-field transition.

"High"-field Transitions

"Zero"-field Transitions	3-8	5-2	12-10	7-4	9-11	1-6	6-4	11-12	4-2	8-2	5-3	7-5	9-10	1-7
4-3		■							■		■			
6-5				■			■					■		
1-7						■								■
9-10					■								■	
7-5				■			■					■		
5-3		■							■		■			
2-8	■									■				
4-2		■							■		■			
6-4				■			■					■		
1-6						■								■
9-11					■								■	
11-12			■					■						
12-10			■					■						
7-4				■			■					■		
5-2		■							■		■			
3-8	■									■				

9.3.2. *μT NMR of Small Molecules at Natural Abundance*

The isotopically enriched methyl group provides a good illustrative example for exploring the interplay between the two different strong coupling regimes present

in ultra-low fields. However, large quantities of isotopically enriched samples are rarely available. Since homonuclear J coupling can only be observed if there is heteronuclear J coupling present to remove magnetic equivalence between homonuclei, the study of non-isotopically enriched samples is limited to small molecules containing NMR active nuclei with high natural abundance such as ^{31}P and ^{19}F.

The opportunity for observing interesting effects in the "zero"-field indirect spin-spin coupling regime, even of small molecules at natural abundance containing either ^{31}P or ^{19}F, is limited for a number of reasons but there remain some interesting examples which are worth exploring.

In the case of fluorinated hydrocarbons, such as the trifluoroethanol and fluorobenzene molecules which were used for the COSY experiments in Chapter 8, the observed indirect spin-spin interactions tend to be at least three bond couplings which are on the order of 10 Hz. The difference in gyromagnetic ratio between ^{1}H and ^{19}F nuclei is only 6%. Therefore a regime does not exist in which both the difference in Larmor frequency between coupled ^{1}H and ^{19}F nuclei and their absolute Larmor frequencies are on the same order of magnitude as the scalar coupling. One or the other is typically either much larger or much smaller than J_{FH}.

In the case of ^{31}P, the difference in Larmor frequency between ^{31}P and ^{1}H is much more significant (60%) and there exist many examples of molecules quite large single bond, indirect spin-spin coupling constants. However in most of these ^{31}P containing molecules, and indeed most small molecules of interest, a further complication is introduced by either the sheer number of magnetically equivalent protons present or the existence of observable homonuclear couplings.

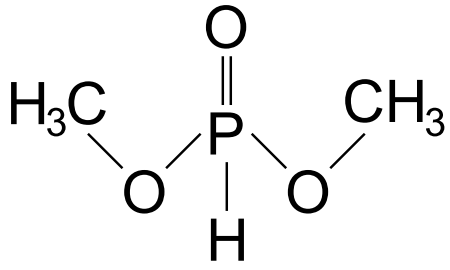

Figure 9.7 Dimethyl phosphite molecule

One interesting ^{31}P example to consider is dimethyl phosphite. This molecule

(pictured in Figure 9.7) contains a single ^{31}P nucleus which is very strongly coupled to a single ^{1}H, with a one-bond indirect spin-spin coupling constant of approximately 696 Hz. This ^{31}P nucleus is also coupled, less strongly, to six magnetically equivalent ^{1}H nuclei on two methyl groups. These methyl protons are magnetically non-equivalent with respect to the single proton and so experience a homonuclear coupling with respect to this proton which is, in theory, detectable.

In order to properly simulate our 2D experiment using the density matrix formalism, all six methyl protons need to be included. An 8-spin, 2D density matrix calculation is prohibitively long on a standard PC without first significantly optimizing the simulation code. However, a simulation of an imaginary molecule in which only one methyl group is present is feasible and will demonstrate the features to be expected from a true experiment using the entire molecule. Therefore the following results are simulated with five spins where one ^{1}H nucleus is coupled to the ^{31}P nucleus with a coupling constant of 696 Hz and three additional magnetically equivalent ^{1}H nuclei are coupled to the ^{31}P nucleus with a coupling constant of -12 Hz and to the other ^{1}H by a homo-nuclear coupling constant of 0.1 Hz.

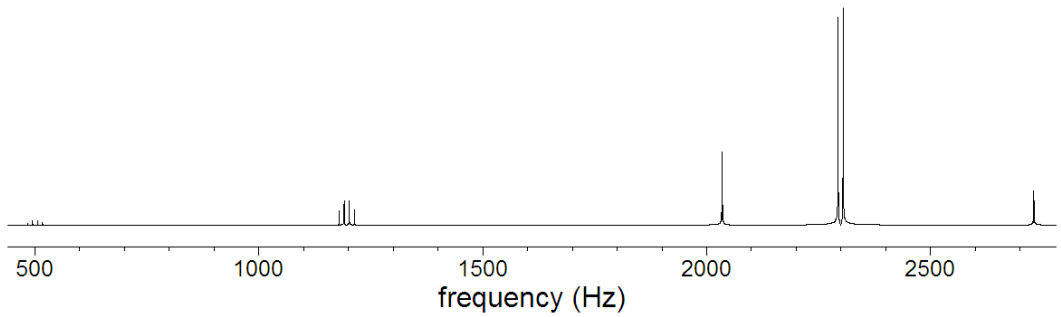

Figure 9.8 1D NMR spectrum of dimethyl phosphite in a field of 54 μT calculated using a density matrix simulation with only one methyl group and $^{1}J_{PH}$ = 696 Hz, $^{3}J_{PH}$ = -12 Hz and $^{4}J_{HH}$ = 0.1 Hz.

Figure 9.8 presents a 1D NMR spectrum of our imaginary methyl phosphite molecule acquired in the Earth's magnetic field (54 μT). The ^{31}P portion of the spectrum is split into two quartets, separated by approximately 700 Hz as a result of the coupling with the single ^{1}H. These peaks are quartets because of the coupling of the ^{31}P nucleus to the methyl protons. The ^{1}H portion of the spectrum is divided into a doublet which corresponds to the single, strongly coupled ^{1}H. The peaks which

make up this doublet have some high resolution multiplet structure due to homonuclear coupling with the methyl protons. The central pair of ^{1}H peaks corresponds to the methyl protons. This set of peaks are split by 0.5 Hz due to a combination of the homonuclear coupling and residual effects of the very strong one-bond coupling between the ^{31}P and the single ^{1}H, mediated by the coupling between the ^{31}P nucleus and the methyl protons.

Figure 9.9 presents a 1D NMR spectrum of our methyl phosphite molecule in a field of 6.8 μT, calculated using a density matrix simulation. The difference in Larmor frequency between ^{1}H and ^{31}P in this field is 25% of the strongest indirect spin-spin coupling constant in this molecule (171 Hz vs. 696 Hz) and the absolute Larmor frequency of the ^{1}H nuclei (289 Hz) is 40% of this strong coupling constant. Therefore this regime is comparable to that of $^{13}C^{1}H_3$ in a field of 1 μT.

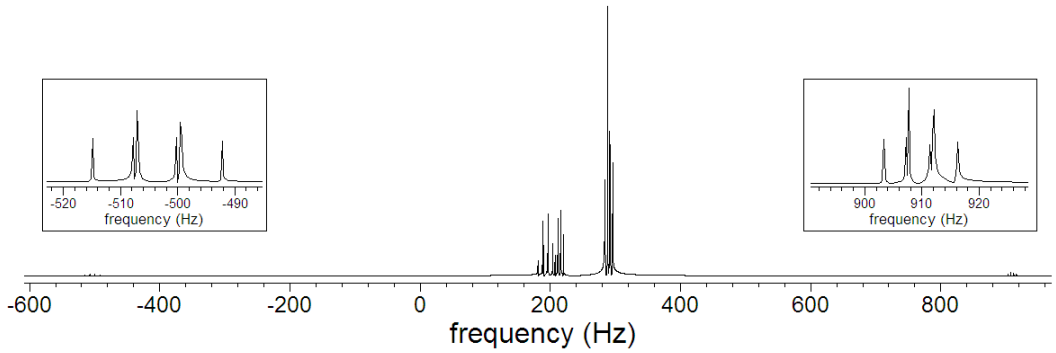

Figure 9.9 1D NMR spectrum of dimethyl phosphite in a field of 6.8 μT calculated using a density matrix simulation with only one methyl group and $^{1}J_{PH}$ = 696 Hz, $^{3}J_{PH}$ = -12 Hz and $^{4}J_{HH}$ = 0.1 Hz. The insets show the multiplet structure of the outermost peaks.

The spectrum in Figure 9.9 is not easily assigned because, unlike the previous example we considered, there are several couplings involved. However, we can identify some features of this spectrum. The outermost peaks, which are shown in the insets, consist of 6 peaks and likely correspond to $\Delta F = \pm 1$, $m_F = \pm 1$ transitions of the one-bond 696 Hz coupling between the ^{31}P nucleus and the single ^{1}H nucleus. The central multiplets around 289 Hz (the ^{1}H Larmor frequency) and 200 Hz (the average of the ^{1}H and ^{31}P Larmor frequencies) likely corresponds to transitions with $\Delta F = 0$ and $m_F = \pm 1$.

In order to obtain more insight into this "zero"-field spectrum, we can simulate the 2D spectrum and observe the correlation between the 6.8 μT peaks and those at 54 μT. The full calculated 2D spectrum is presented in Figure 9.10.

As we might expect, no correlations are present between the central ^{1}H peaks in f_2, which correspond to the methyl protons, and the outermost peaks in f_1. These methyl peaks in f_2 correlate exclusively with the multiplet at the ^{1}H Larmor frequency in f_1. The coupling constant between the ^{31}P nucleus and the methyl protons (-12 Hz) is much smaller than difference in Larmor frequency (171 Hz) and so no "zero"-field transitions at or near $\pm^3J_{PH}$ or $\pm2*^3J_{PH}$ are expected.

The non-methyl proton peaks in f_2 correlate only weakly with the peaks at the ^{1}H Larmor frequency in f_1. This correlation could be a consequence of the homo-nuclear coupling with the methyl protons. The non-methyl proton correlates most strongly with the multiplet at the average ^{1}H and ^{31}P Larmor frequency in f_1 with some correlation apparent with the outermost multiplets.

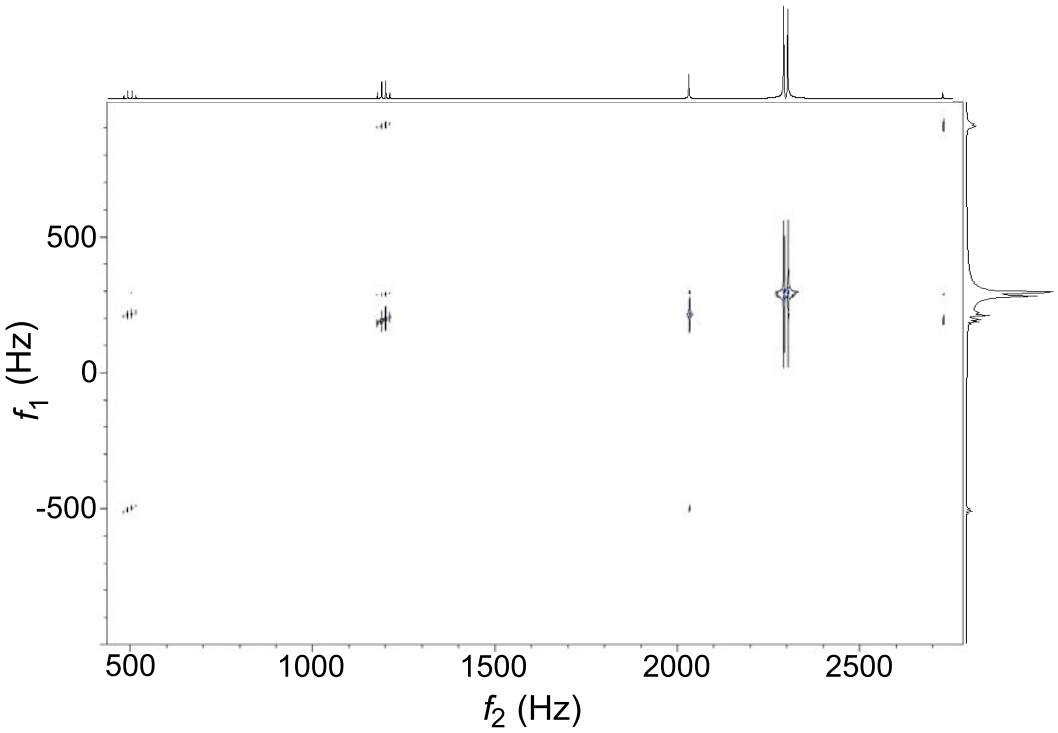

Figure 9.10 2D NMR spectrum of dimethyl phosphite calculated using a density matrix simulation with only one methyl group and $^1J_{PH}$ = 696 Hz, $^3J_{PH}$ = -12 Hz and $^4J_{HH}$ = 0.1 Hz. The evolution field (along f_1) was 6.8 μT and the Earth's field (evolution in f_2) was 54 μT.

The ^{31}P peaks in f_2 correlate most strongly with the multiplet at the average ^{1}H and ^{31}P Larmor frequency and the outermost $\Delta F = \pm 1$ multiplets in f_1; however, some correlation is also observed with the peaks at the ^{1}H Larmor frequency in f_1 due to the relatively weak coupling with the methyl protons.

Therefore we see that, while the unique strong coupling regime encountered in microtesla fields, where both the difference in Larmor frequency and the absolute Larmor frequencies of coupled nuclei is less than the indirect spin-spin coupling constant, exhibits some very interesting behaviour, the patterns which emerge are not easily identified and the underlying couplings are difficult to deduce without a complicated analysis. Therefore, at present, it seems unlikely that this method will prove to be useful for routine, ultra-low field chemical analysis. Nonetheless, the multidimensional technique could be used to provide insight into the interplay between the different strong coupling regimes present in ultra-low magnetic fields for some carefully chosen small molecules.

9.3.3. Experimental Considerations

The multidimensional experiment proposed in Figure 9.3 can be implemented in a number of ways. Like the COSY experiments discussed in Chapter 8, the prepolarization scheme can consist of simple electromagnet prepolarization, DNP polarization or some combination of the two.

The evolution phase can also be carried out in a number of ways. Conceptually, the simplest implementation is to build a coil for cancelling out the Earth's magnetic field and to switch this field on and off adiabatically at the start and end of the t_1 evolution time period. In practice, however, it may prove challenging to engineer a coil which is simultaneously strong enough, homogeneous enough and is also oriented in precisely the correct direction so as to cancel, almost completely, the Earth's magnetic field. If the orientation of this offset field is not quite right, the minimum absolute field which can be achieved will be limited. If the field is not sufficiently homogeneous, the spectrum in the indirect domain will suffer from significant T_2* broadening.

The problem of imperfect orientation of the offset coil can be avoided with a slightly different approach to the experiment. Instead of working in the Earth's field,

the experiment can be carried out in a shielded environment where the prevailing field is very small, similar to the experiments of Ledbetter et al. [102]. In this incarnation of our 2D experiment, the offset field is ramped up to a moderate value, in the Earth's field range, during the prepolarization stage and ramped down to the desired evolution field during t_1. At the end of the t_1 evolution period, the offset field is ramped back up to its initial value for the duration of the signal detection phase. This version of the experiment will also remove any difficulties associated with the temporal instability of the Earth's field and will dramatically decrease any pick-up noise originating from outside the shielded container. The success of the experiment, in this form, rests on the homogeneity and stability of the offset field.

The issue of an offset field which is not as homogeneous as the Earth's magnetic field can be countered through the introduction of a broadband refocusing pulse exactly in the centre of each t_1 evolution step. This can be achieved by dividing the pulse of offset field into two equal segments of $t_1/2$, with a 180 pulse applied in the presence of the Earth's magnetic field in the middle. If this is a true broadband 180 pulse which inverts both of the coupled nuclei exactly in the middle of t_1, the Zeeman evolution terms, including any T_2* decay, will be refocused at the end of t_1 but the evolution under the J coupling interaction will remain.

There are a couple of things to keep in mind regarding this version of the 2D experiment. First, the Zeeman interaction will be refocused by this experiment and so the spectrum in the indirect dimension, f_1, will be centred about 0 Hz. Therefore a projection along f_2 will result in a superposition of peaks. Any projections along f_2 will have to be taken locally, integrating over only a region of the directly detected EFNMR spectrum. Second, if the inhomogeneity of the evolution field is severe, the coupling regime experienced by spins in different portions of the sample will be demonstrably different. Therefore, even though the inhomogeneity is refocused, the full spectrum may contain residual inhomogeneity effects which might make it difficult to interpret.

CHAPTER 10. Dipolar Coupling in EFNMR

10.1. Introduction

One application of conventional NMR which has yet to be discussed in this thesis is the measurement of the anisotropy of complex fluids. The measurement of anisotropy in liquids via NMR is typically achieved through the observation of either the quadrupolar interaction or residual dipolar coupling. In this chapter we explore the possibility of detecting anisotropy using Earth's field NMR. This work was carried out with the invaluable assistance of Prof. Edward Samulski from the Department of Chemistry, University of North Carolina, Chapel Hill, North Carolina, USA.

Anisotropy in the electric field surrounding a quadrupolar nucleus, i.e. a nucleus which possesses a non-zero electric quadrupole moment, results in a splitting in the observed NMR spectrum. The size of this splitting is correlated with the degree of anisotropy and the relative orientation of the director of the anisotropic medium relative to the static magnetic field. While this is a powerful method for measuring anisotropy at high-field, it is not suitable for Earth's field NMR for two reasons. First, most quadrupolar nuclei are not observable via our EFNMR apparatus due to their characteristically short transverse relaxation times. This enhanced T_2 relaxation is due to the interaction of the non-zero nuclear quadrupole moment with local electric field fluctuations. One notable exception to this rule is deuterium. However, the gyromagnetic ratio of deuterium is very small, approximately one seventh that of

protons. The cubic relationship between the magnitude of the inductively detected NMR signal and the nuclear gyromagnetic ratio means that the NMR sensitivity of even 100s of mL of D_2O is far below the detection limit of our EFNMR device. Therefore any measurement of anisotropy carried out via EFNMR will depend on residual dipolar coupling of protons rather than the quadrupolar interaction.

Dipolar-coupled NMR spectra of liquid-crystal systems have previously been observed in the zero-field limit indirectly using a 2D pulse sequence in which the NMR signal was excited and detected in a high-field magnet [103-105]. In these experiments, evolution in the indirect dimension was carried out at "zero"-field through either field-cycling of the main B_0 field (in the case of an electromagnet) or shuttling of the sample to a region of "zero"-field outside the main magnet, as in the experiments of Weitekamp et al. discussed in Chapter 9 [98; 100].

10.2. Residual Dipolar Coupling in Anisotropic Liquids

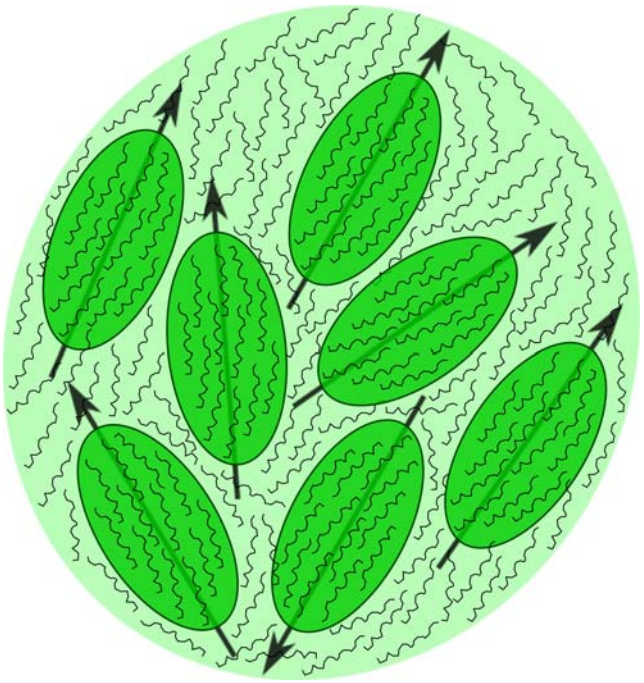

Figure 10.1 A cartoon representation of a nematic liquid crystal phase in which the liquid crystal molecules are aligned locally forming domains of uniform molecular orientation (depicted here as green ovals). The orientation of each domain is defined by a unit vector called a director.

Solutions of certain lyotropic liquid crystal molecules, within a specific range of concentration and temperature, form a nematic phase in which the rod-like long-chain molecules become aligned. This alignment is localized such that the system forms regions, or domains, in which the constituent liquid crystal molecules are aligned along a single director. In the absence of a magnetic field, the orientations of these directors are randomly distributed through out the sample (Figure 10.1).

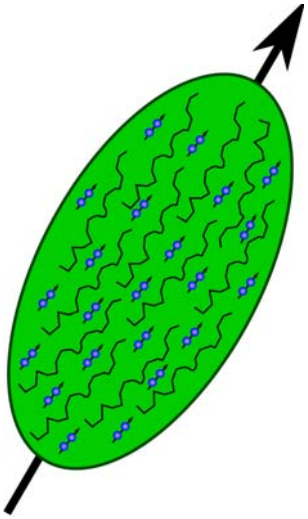

Figure 10.2 A cartoon depicting the preferential orientation experienced by the dipolar coupled protons on a solvent molecule (depicted here as blue spheres) as a result of the local anisotropy of the nematic phase of the liquid crystal molecules. If the size of a single domain is larger than the diffusion length of the solvent molecule, residual dipolar coupling will be observed in the NMR spectrum of the coupled nuclei.

Consider the effect of this local anisotropy on the dipolar coupling between two nuclei on a probe solvent molecule, such as the two protons in a single dichloromethane (CH_2Cl_2) molecule (Figure 10.2). If a single domain is larger than the diffusion length of the solvent molecule, its free tumbling will be restricted. There will be an orientation, or small distribution of orientations, which is slightly preferred. As we saw in section 2.3.4 of Chapter 2, this preferred orientation will result in an incomplete averaging of the dipolar coupling interaction between the coupled protons in the solvent molecule and so these nuclei will experience residual dipolar coupling. The strength of this residual coupling depends on the degree to which the free

tumbling of the molecule is restricted. This is quantified by the structure factor, *S*, defined in Chapter 2. The so-called residual dipolar coupling constant is the full dipolar coupling constant scaled by the structure factor.

The full interaction Hamiltonian for the intra-molecular, homonuclear dipolar interaction is given by Eq. 10-1, where the dipolar coupling constant is given by Eq. 10-2.

$$\mathcal{H}_{ij}^{DD,full} = b_{ij}\left(3\left(\mathbf{I}_i \cdot \mathbf{e}_{ij}\right)\left(\mathbf{I}_j \cdot \mathbf{e}_{ij}\right) - \mathbf{I}_i \cdot \mathbf{I}_j\right) \tag{10-1}$$

$$b_{ij} = -\frac{\mu_0}{4\pi}\frac{\gamma_i \gamma_j \hbar}{r_{ij}^3} \tag{10-2}$$

The Hamiltonian for residual dipolar coupling is similar to Eq. 10-1 but where the dipolar coupling constant, b_{ij}, is replaced by the residual dipolar coupling constant, d_{ij} (Eq. 10-3), where *S* is the structure factor.

$$d_{ij} = Sb_{ij} \tag{10-3}$$

In the weak coupling case, where the Zeeman interaction strongly dominates the Hamiltonian, the secular form of the dipolar Hamiltonian can be used. In the case of Earth's field NMR, this approximation is not necessarily appropriate. Therefore the full expansion (Eq. 10-4) should be used, where Θ is the polar angle and ϕ is the azimuthal angle associated with θ, the angle between the anisotropy director and the static magnetic field. However, if the system is axially symmetric, the net effect of the *C*, *D*, *E*, and *F* terms will be averaged to zero and so only the A and B terms will survive, even in the strong coupling case.

$$\mathcal{H}_{ij}^{RDC,full} = d_{ij}\left(A + B + C + D + E + F\right)$$

$$A = \mathbf{I}_{iz}\mathbf{I}_{jz}\left(3\cos^2\Theta - 1\right)$$

$$B = -\frac{1}{4}\left(\mathbf{I}_i^+\mathbf{I}_j^- + \mathbf{I}_j^+\mathbf{I}_i^-\right)\left(3\cos^2\Theta - 1\right)$$

$$C = \frac{3}{2}\left(\mathbf{I}_i^+\mathbf{I}_{jz} + \mathbf{I}_{iz}\mathbf{I}_j^+\right)\sin\Theta\cos\Theta e^{-i\phi}$$

$$D = \frac{3}{2}\left(\mathbf{I}_i^-\mathbf{I}_{jz} + \mathbf{I}_{iz}\mathbf{I}_j^-\right)\sin\Theta\cos\Theta e^{i\phi}$$

$$E = \frac{3}{4}\left(\mathbf{I}_i^+\mathbf{I}_j^+\right)\sin^2\Theta e^{-2i\phi}$$

$$F = \frac{3}{4}\left(\mathbf{I}_i^-\mathbf{I}_j^-\right)\sin^2\Theta e^{2i\phi}$$

10-4

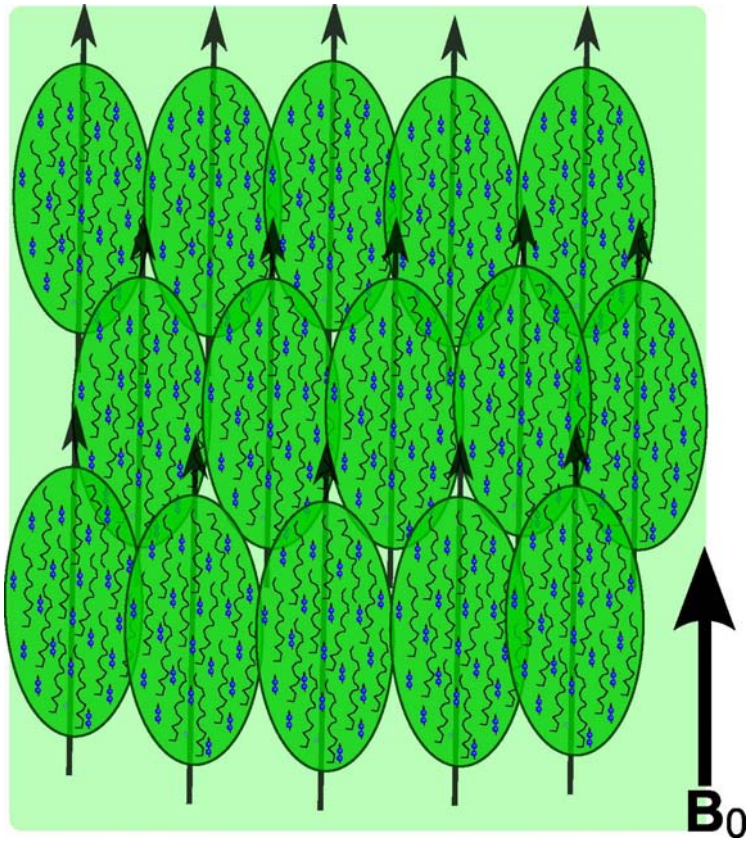

Figure 10.3 A cartoon representation of a lyotropic liquid crystal system in a nematic phase in the presence of a strong static magnetic field, B_0. The localised domains are reoriented by means of the interaction of the field with the positive magnetic field anisotropy of each individual domain. The residual dipolar coupling felt by the nuclei in the solvent molecules corresponds to a uniform angle $\Theta = 0$ with respect to the static field B_0. The resultant NMR spectrum is a doublet split by the residual dipolar coupling constant.

In the presence of a strong magnetic field, each domain experiences a torque as a result of the interaction of its net magnetic susceptibility anisotropy with the field. This torque reorients the domains such that, at equilibrium, all are aligned either along the field, in the case of positive magnetic field anisotropy (as shown in Figure 10.3), or perpendicular to the field, in the case of negative magnetic field anisotropy. An NMR spectrum acquired of the dipolar-coupled protons on the solvent molecules is a doublet split by the residual dipolar constant (Eq. 10-3) scaled by $\frac{1}{2}\left(3\cos^2\Theta - 1\right)$, where Θ is 0 for $\Delta\chi > 0$ or $\pi/2$ for $\Delta\chi < 0$.

The strength of the Earth's magnetic field is insufficient to align the liquid crystal domains and so a liquid crystal in a stable nematic phase will be ordered locally but will be globally unordered. In this case, there will be contributions to the NMR signal which arise from a random distribution of angles, θ. A random distribution of θ corresponds to a flat distribution of cos Θ between -1 and 1 and a flat distribution of ϕ between 0 and 2π. In the case of weak coupling, where only the A and B terms in Eq. 10-4 are retained, the resultant NMR spectrum contains the very distinctive powder pattern.

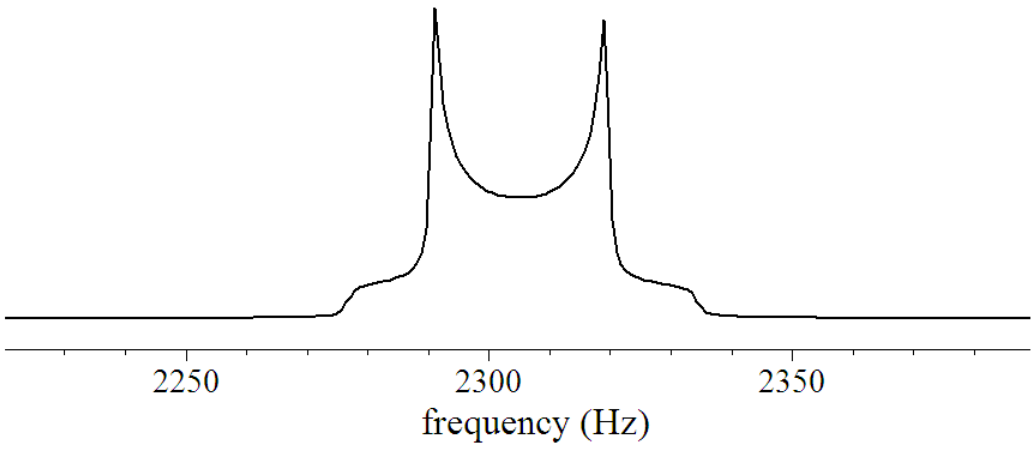

Figure 10.4 A density matrix simulation of a powder pattern calculated with a residual dipolar coupling constant of 57.4 Hz.

An example of a density matrix simulation of the NMR spectrum of a globally unordered nematic phase containing probe molecules with protons coupled with a residual dipolar coupling constant of 57.4 Hz is shown in Figure 10.4.

10.2.1. Poly-γ-benzyl-L-glutamate (PBLG)

In order to observe residual dipolar coupling using EFNMR we require a solvent molecule containing two coupled protons which we can use to probe ordering in the system. Water is ineligible, unfortunately, because any residual dipolar coupling effects are averaged out by the rapid chemical exchange of protons between molecules. Therefore we require a liquid crystal system which forms a nematic phase with a suitable organic solvent. One such lyotropic liquid crystal system, poly-γ-benzyl-L-glutamate (PBLG) in dichloromethane (CH_2Cl_2), was studied by E. Samulski in his PhD thesis in 1969 [106] and was found to display a residual dipolar coupling constant of 50 Hz in a stable nematic phase. PBLG is a readily commercially available, chemically inert homo-polypeptide which has good solubility in organic solvents. It was the first synthetic polymer to exhibit a liquid crystal phase in 1950 [107].

PBLG possesses a stable nematic phase over a range of concentrations. The width of this concentration range increases with the molecular weight of the PBLG due to the increase in length per unit diameter of the molecule [108]. Below this stable nematic region is a biphasic nematic/isotropic regime in which the nematic and isotropic phases coexist. The theory of lyotropic liquid crystal phase formation by Onsager [109] provides a means of roughly calculating the concentration at which the liquid crystal forms a nematic phase. First we define the aspect ratio of the molecule, $p = Ld^{-1}$, where L is the length of the rod-like liquid crystal molecule and d is it's diameter. The diameter is fixed for a particular system and is approximately 1.5 nm for a solvated PBLG molecule. PBLG forms an alpha helix structure in solution. Each peptide unit translates 0.15 nm along the helical axis; therefore, the length of a given PBLG molecule can be defined as the degree of polymerization, n, multiplied by 0.15 nm. Accordingly, $p = 0.1n$. The theory of Onsager states that the volume fraction of the liquid crystal molecule needs to be approximately $4.22p^{-1}$ for a nematic phase to form [109]. In the case of PBLG this is a volume fraction of $42.2n^{-1}$.

In recent work, Marx and Thiele [108] have investigated the critical concentration at interface between the biphasic and stable nematic phases as a function of PBLG molecular weight. The solvent used in these experiments was $CDCl_3$. They found that while the critical concentration decreases quite rapidly with

increasing molecular weight at low molecular weights, a plateau is reached at higher molecular weights. This behaviour is qualitatively in agreement with the Onsager model described above.

For the PBLG-$CDCl_3$ system, the plateau critical concentration value was 6% (see Table 10.1) which is higher than predicted by the Onsager model. In addition, Marx and Thiele found that the critical concentration of PBLG was solvent dependent. For example they found that the critical concentration of PBLG in CD_2Cl_2 was approximately 17% higher compared to that for PBLG in $CDCl_3$.

Table 10.1 Dependence of the critical concentration of PBLG in $CDCl_3$ as a function of molecular weight. Data taken from Marx and Thiele [108].

Molecular Weight (g/mol)	Critical Concentration (%w/w)
20 100	19.8
32 000	12.0
58 000	9.7
106 000	8.5
167 000	8.6
384 000	7.3
404 000	7.0
602 000	6.2

10.3. Experimental Results

10.3.1. Liquid Crystalline Sample

The sample used in the experiments reported in this chapter was originally prepared as 5 g of PBLG with an average MW of 162900 in 70 mL of CH_2Cl_2 with 350 μL of trifluoroacetic acid. This was found to be well below the critical concentration for the nematic phase and so additional PBLG was added. A summary of the quantities of PBLG in the final sample and the corresponding molecular weights and degree of polymerization (n) are listed in Table 10.2.

The relative sensitivity of dichloromethane with respect to water can be calculated as the ratio of the number of ^1H nuclei per unit volume for each molecule.

The density of dichloromethane is 1.3266 g/cm^3 and the molar mass is 84.93 g/mol. Therefore there are 3.12x10-2 moles of ^{1}H nuclei in every cm^3 of dichloromethane. There are 0.11 moles of ^{1}H nuclei in every cm^3 of water. Therefore the sensitivity of CH_2Cl_2 is about a third of that of water. If we combine this with the very small volume of solvent available (70 mL) and the broad nature of the anticipated powder spectrum (with an expected residual dipolar coupling constant of 50 Hz) we see that this is a very challenging experiment from the point of view of sensitivity. Therefore the experiments presented in this chapter are carried out using Halbach prepolarization at 0.3 T followed by rapid manual transport (~1.2 s) to the EFNMR probe for detection. This experiment was repeated several times and the results were signal averaged. The number of signal averages varied according to the SNR of the detected signal, i.e. the experiment was repeated until a reasonable SNR was achieved.

Table 10.2 Summary of PBLG sample parameters

Mass (g)	Molecular Weight (g/mol)	n
6.95	162 900	743
0.64	91 000	400
0.67	150 000	1132
0.27	248 000	416

10.3.2. Solid-Echo Pulse Sequence

The NMR pulse sequence used in these liquid crystal experiments was what is known as a solid echo (Figure 10.5). In the solid-echo pulse sequence, the sample is excited with a 90_x pulse and is subsequently allowed to evolve for a short period, τ, equal to the typical "dead"-time of the probe, i.e. the time required for the energy in the transceiver coil following an excitation pulse to dissipate. At a time τ following the first pulse, a second pulse, shifted in phase by $\pi/2$: 90_y, is applied to the system. At a time τ following this second pulse the bilinear dipolar interaction is fully refocused and the signal is acquired. This pulse sequence is called a solid-echo because it is widely used in the area of Solid-State NMR for measuring dipolar

couplings. Since the spectral lines associated with dipolar (or residual dipolar) coupling can be quite broad, the signal decays very rapidly in the time domain. The dead time of the detection coil is such that much important information is lost in the undetected region at the beginning of an FID. In the echo experiment, this information is refocused at a time following the second pulse, τ, which is longer than the dead time of the transceiver coil and so all of the critical information is contained in the observed echo signal.

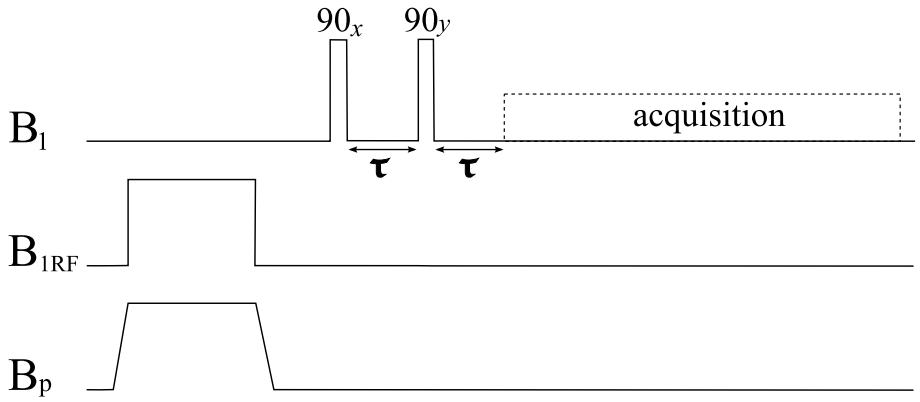

Figure 10.5 1D EFNMR solid-echo pulse sequence. In the experiments carried out for this chapter, prepolarization is achieved using a 0.3 T Halbach.

10.3.3. NMR Results

The first NMR spectrum of our PBLG sample was acquired on August 14, 2009, using a commercial 400 MHz Bruker spectrometer. The PBLG sample intended for Earth's field NMR was prepared in a 55 mm diameter glass jar with a Teflon screw top. In order to investigate the state of the sample in the high-field magnet, some of the bulk PBLG solution was poured into an 18 mm (outer diameter) tube and placed into a 25 mm diameter B_1 coil in the 400 MHz (9.4T) Bruker magnet. The spectral linewidth at 400 MHz for this sample size was on the order of a few 100 Hz, too broad to directly observe the anticipated residual dipolar splitting of 50 Hz. Therefore the dipolar splitting was observed indirectly using the 2D experiment in Figure 10.6.

In this 2D echo experiment, the 180_y pulse refocuses the Zeeman interaction but not the bilinear dipolar coupling. Therefore, by repeating the pulse sequence with

incrementally longer t_1 times, a 2D data matrix is built up as a function of both t_1 and t_2, the Fourier transform of which contains the dipolar spectrum in the indirect dimension with no contribution from the field inhomogeneity. In all experiments, the t_1 step size was 10 ms, resulting in a bandwidth in the indirect domain of 100 Hz. An integral over f_2, the direct frequency dimension, yields a dipolar coupled spectrum in f_1. An example 2D spectrum is shown in Figure 10.7 with the corresponding f_1 spectrum shown in Figure 10.8.

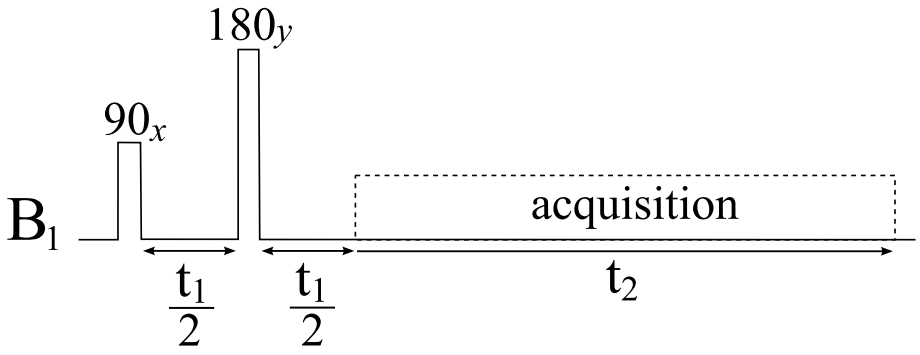

Figure 10.6 2D echo pulse sequence designed to observe high resolution dipolar coupled spectra in the indirect dimension by acquiring successive echo signals with incrementally longer t_1 and Fourier transforming the resultant 2D data matrix. The spectrum along the indirect (f_1) dimension of this 2D dataset is a high resolution spectrum containing only the effects of bilinear interactions such as dipolar coupling.

The 2D spectrum in Figure 10.7 (and corresponding 1D projection in Figure 10.8) was acquired of the PBLG solution on August 14, 2009. This spectrum contains a residual dipolar splitting of 28 Hz as well as an isotropic peak which accounts for approximately 25% of the total signal. This indicates that the sample is not in a stable nematic phase but rather is in the biphasic nematic/isotropic regime. Therefore, the concentration of PBLG needs to be increased in order to reach a stable nematic phase.

In order to increase the concentration of PBLG in our bulk sample, approximately 15% of the solvent was allowed to evaporate (leaving approximately 60 mL) and the full sample was left to equilibrate for a couple weeks. On October 14, 2009, the 2D spectroscopy experiment was repeated on the 400 MHz spectrometer. Once again only a portion of the bulk sample, poured into an 18 mm tube and placed

in a 25 mm B_1 coil inside the 9.4 T magnet, was used. Figure 10.9 presents the resultant indirectly detected ^{1}H NMR spectrum. A residual dipolar coupling of 57 Hz is observed with no significant isotropic peak present. There is a small amount of signal at 0 Hz; however a small artifact at 0 Hz is expected due to imperfections in the refocusing pulse. The result in Figure 10.9 was found to be stable over a range of temperatures from 15˚C to 25˚C.

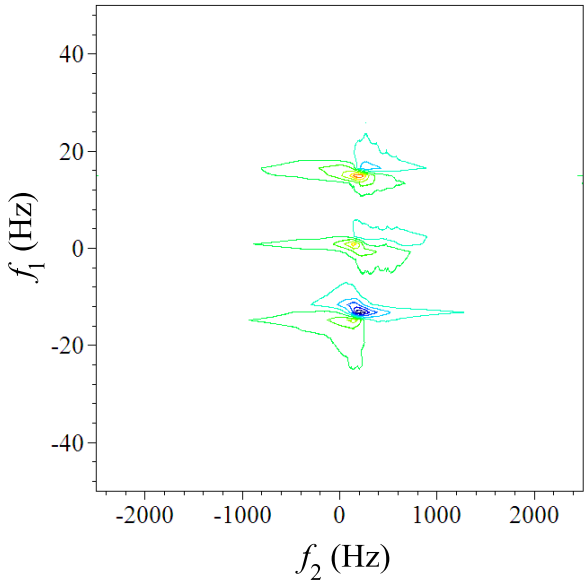

Figure 10.7 2D echo spectrum (using the pulse sequence in Figure 10.6) carried out on a 400 MHz Bruker spectrometer. This spectrum was acquired of the PBLG sample on August 14, 2009. The indirect f_1 dimension shows dipolar coupling with a splitting of 28 Hz along with a significant isotropic peak. The sample is in the biphasic nematic/isotropic phase.

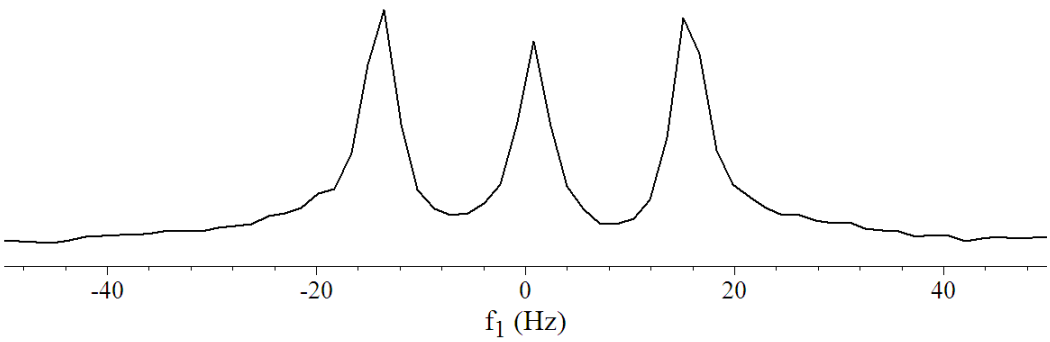

Figure 10.8 1D ^{1}H NMR magnitude spectrum of the PBLG sample, calculated from the complex 2D spectrum in Figure 10.7.

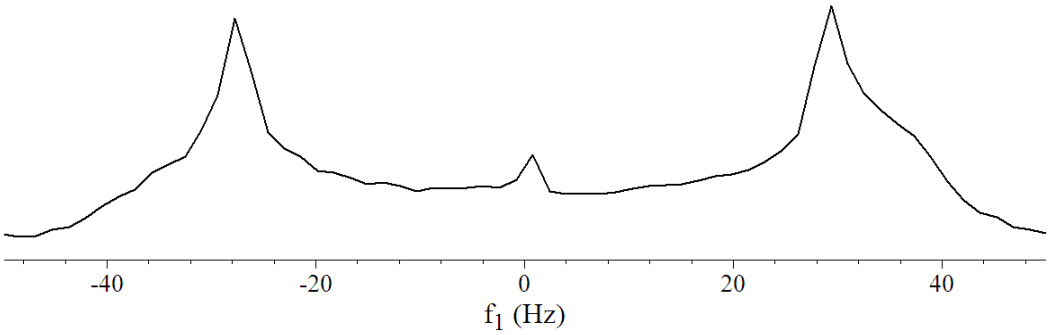

Figure 10.9 1D indirectly detected ^{1}H NMR spectrum of the more concentrated PBLG sample acquired on a 400 MHz Bruker spectrometer on October 14, 2009. The residual dipolar splitting is 57 Hz with no significant isotropic component. (Some signal at 0 Hz is expected due to imperfect refocusing pulses.)

Having achieved the stable nematic phase, the sample was once again recombined into the EFNMR sample vessel and left to equilibrate for a few days. On October 18, 2009 a series of solid-echo ^{1}H EFNMR spectra with Halbach prepolarization were acquired and signal averaged. The resultant spectrum is presented in Figure 10.10a. Despite the poor SNR, it is clear that there is residual dipolar coupling present in this system. Figure 10.11 presents the same experimental spectrum overlaid with a simulated ^{1}H EFNMR spectrum calculated with a powder averaged density matrix simulation using a residual dipolar coupling constant of 42.5 Hz.

The solid-echo experiment was repeated two days later on the same sample. With the exception of an increased number of signal averages in order to improve SNR, the measurement protocol was unchanged from the previous measurement on October 18th. The ^{1}H EFNMR spectrum (Figure 10.10b) was found to have narrowed. While the form of the spectrum continues to resemble a powder pattern, the apparent residual dipolar coupling constant, in this case, is only 27 Hz. A further narrowing of the spectrum was found on October 31, 2009. At this time, only a broad line with no apparent dipolar splitting was observed (Figure 10.10c). On November 23, 2009, the EFNMR solid-echo experiment produced a narrow line, with a linewidth comparable to that of tap water (Figure 10.10d). Only four signal averages (as compared to 37 averages employed for the spectrum in Figure 10.10b) were used because of the inherently high SNR of this narrow line. Repeated measurements at different temperatures, from 4°C to 20°C, gave the same result.

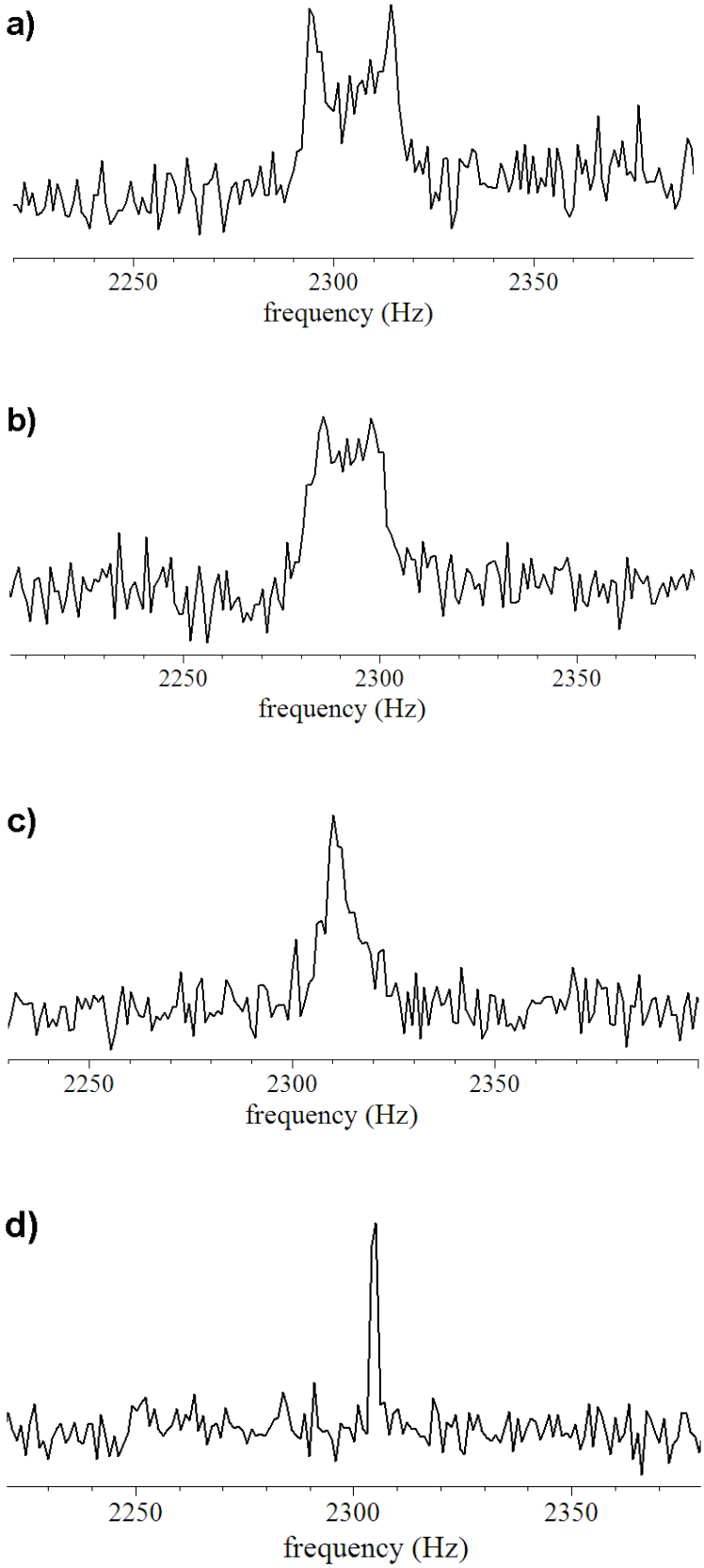

Figure 10.10 ^{1}H EFNMR solid-echo spectra of the PBLG solution acquired on (a) Oct. 18th, (b) Oct. 20th, (c) Oct. 31st, and (d) Nov. 23rd.

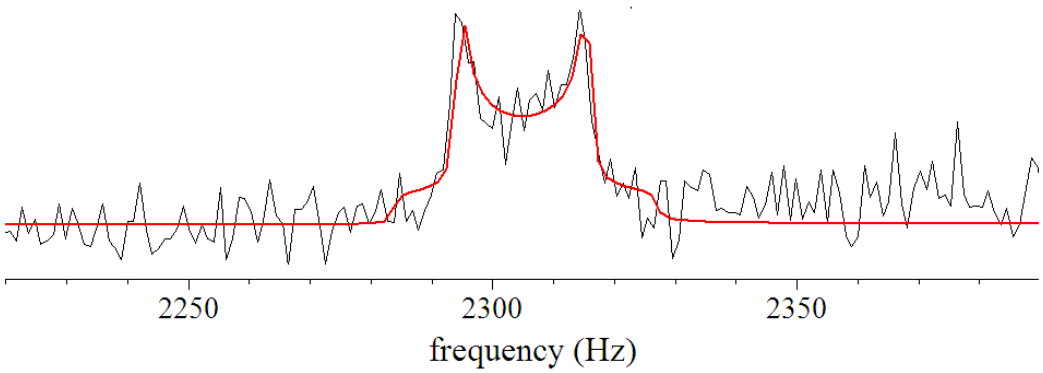

Figure 10.11 A comparison between the experimentally measured ^{1}H EFNMR solid-echo spectrum of the PBLG solution on October 18th (black) and a powder averaged density matrix simulation (red) using a residual dipolar coupling of 42.5 Hz. The full interaction Hamiltonian (Eq. 10-4) was used in the density matrix calculation.

10.4. Discussion and Future Work

Several features of the liquid crystal NMR spectra presented herein are puzzling and require further investigation.

The original PBLG solution measured at 9.4 T on August 14, 2009 contained a total of 8.53 g of PBLG (as summarized in Table 10.2) in 70 mL of dichloromethane. Using the model of Onsager [109] to predict the critical volume fraction of PBLG at the boundary of the nematic phase, we find that the nematic state transition should occur for this mass of PBLG at a volume of solvent (assuming no change of volume of PBLG in solution) of approximately 110 mL. This is inconsistent with our observations. However, if we consider the results of Marx and Thiele [108] summarized in Table 10.1 and include the apparent 17% increase in critical volume fraction for a PBLG solution in dichloromethane as opposed to chloroform, the volume of solvent required to reach the critical concentration is approximately 60 mL for the range of PBLG masses and molecular weights listed in Table 10.2. This is more in line with our findings at 9.4 T.

The observed ^{1}H NMR spectra in the Earth's magnetic field pose more difficult questions as to what is really happening in this liquid crystal system. The first recorded EFNMR spectrum (Figure 10.10a) exhibits a residual dipolar coupling of

42.5 Hz, rather than the 57 Hz splitting that was observed at high-field. It is possible that while the high-field sample was in the imperfectly sealed 18 mm sample tube some of the solvent evaporated, effectively increasing the PBLG concentration. Upon recombination of this sample with the bulk solution, the final PBLG solution would be fractionally less concentrated than the volume of sample observed at high-field. There is a strong dependence of residual dipolar coupling constant on the liquid crystal concentration because a more concentrated solution will posses a stronger degree of asymmetry and so a larger structure factor. Therefore, a reduction in concentration would be manifested in the spectrum as decrease in the observed residual dipolar coupling constant. In any future experiments a sample vessel needs to be designed which will fit into both the 400 MHz spectrometer and EFNMR probe so that the spectra can be compared directly without any ambiguity regarding the liquid crystal concentration. A 25 mm diameter, 150 mm long tube which is well sealed would fulfil this criterion.

Perhaps the most confusing aspect of the spectra presented in Figure 10.10 is the progressive decrease in apparent residual dipolar coupling as a function of the "age" of the sample. In this case, the sample was sealed between measurements and so a decrease in concentration is impossible. However, an increase in concentration, due to evaporation of the solvent, is possible. If the concentration is in fact increasing with time, the decrease in observed splitting is very puzzling as we would expect an increase in residual dipolar coupling constant with increasing concentration.

Concurrent with the changes observed in the EFNMR spectra with time, there were some observed macroscopic changes to the sample as well. Immediately prior to the EFNMR measurement on October 31, it was found that the viscosity of the sample had significantly increased such that it was not possible to flow a small volume of the sample into a 5 mm NMR tube. (When the sample was in the biphasic state in August, the viscosity was such that it could be transferred into a 5 mm NMR tube without much difficulty.) By November 23rd, the sample ceased flowing entirely, even when held upside-down for several minutes.

Based on the observed decrease in residual dipolar coupling with the age of our sample and the concurrent increase in viscosity, we postulate that the sample has undergone some sort of phase change into either: (a) a nematic state in which the ordered domains are much smaller than the diffusion length of the dichloromethane

molecules or (b) some kind of gel phase which does not possess any local anisotropy. In the future, we hope to recover the PBLG from our current highly viscous sample and make a fresh solution at a concentration in the stable nematic region. Comparable measurements of this fresh sample at both 9.4 T and in the Earth's magnetic field will hopefully resolve our questions regarding the apparent difference in measured residual dipolar coupling constant in these two regimes. In addition, we hope such experiments will confirm that we are in fact observing residual dipolar coupling via EFNMR and that such measurements are repeatable.

CHAPTER 11. Conclusions and Future Work

11.1. Conclusions

The detection of nuclear precession in the Earth's magnetic field is a very old idea, almost as old as NMR itself. Its high degree of spatial homogeneity, combined with the fact that it is readily available in all but a few places on the globe, render the Earth's magnetic field very attractive for use for detection in NMR. However there are many difficulties associated with obtaining and analyzing high-quality NMR spectra in such a weak field. In this thesis we investigated the resolution, sensitivity and information content of a simple, portable, low-cost Earth's field NMR apparatus with the ultimate goal of increasing the range of experiments and diversity of information which can be obtained using such a seemingly simple device.

The first challenge associated with EFNMR addressed in this thesis was the optimization of resolution and sensitivity. While the Earth's field itself is highly spatially homogeneous, this homogeneity is easily disrupted by ferrous or magnetic objects and suffers from small but significant temporal instabilities. In addition, the very low Larmor frequencies of nuclei in the Earth's field render EFNMR measurements highly susceptible to interference from external ULF noise sources. The sensitivity of EFNMR is also significantly limited by the dependence of signal on the square of the static field strength.

In Chapter 4 of this thesis we presented a range of apparatus improvements which were implemented to address the problems of field inhomogeneity, field instability and external noise interference. Through the use of first-order shimming,

field stabilization via a B_0 lock field and feedback loop and noise screening using a Faraday cage we demonstrated how high-resolution EFNMR spectra can be acquired in an indoor, urban environment.

Signal enhancement methods for EFNMR were considered in Chapter 5. First we compared the advantages and disadvantages of prepolarization by an electromagnet and by a permanent magnet array. The former method enjoys the benefit of ease of implementation and automation but is limited by resistive heating concerns to moderate field strengths (10s of mT) and so only modest signal enhancements are obtainable using this method. Permanent magnet arrays can be used to reach stronger fields (up to 2 T) and pose no problems with regards to sample or instrument heating, but it is difficult to implement this approach for multidimensional experiments and so its application is limited to predominantly one-dimensional, single-shot applications.

The next signal enhancement method to be considered was dynamic nuclear polarization, in which the polarization of unpaired electrons, excited by RF irradiation, is transferred to target nuclei via cross-relaxation. We showed that dynamic nuclear polarization can be used in the Earth's magnetic field to provide signal enhancements much greater than the ratio of the gyromagnetic ratios of the electrons and the target nuclei. This apparent violation of the high-field maximum DNP enhancement limit is due to the strength of the hyperfine coupling between the unpaired electron and neighboring ^{14}N nucleus in nitroxide free radicals. In ultra-low fields this hyperfine coupling dominates the interaction Hamiltonian and so the polarization of the electron is much greater than that predicted by the Zeeman interaction alone. Thus the amount of polarization which can be successfully transferred to the detected nuclei is not just a function of the field but of the hyperfine coupling constant as well.

In Chapter 5 we demonstrated a DNP enhancement of -2250 over thermal polarization in the Earth's field for ^{1}H nuclei in water doped with 1.5 mM of 4-oxo-TEMPO irradiated at 68 MHz. EFNMR signal enhancement using DNP was further improved through the application of the RF irradiation at a higher frequency in the prepolarization field, followed by detection in the Earth's magnetic field. This approach was used at 124 MHz, and in conjunction with a modified homogeneous prepolarization coil, to provide an SNR advantage of 14 over prepolarization at 18 mT

using the standard prepolarization coil. While this SNR advantage is a significant achievement this method has a few limitations. DNP requires the introduction of a free radical into the system, usually by doping the sample with a nitroxide radical such as 4-oxo-TEMPO. This free radical shortens the signal lifetimes of the target nuclei by providing additional pathways for relaxation. This cross-relaxation is the mechanism which drives the polarization transfer and so is to be desired. However it has the adverse effect of coarsening the spectral resolution through a reduction in T_2. Therefore the DNP signal enhancement method requires a compromise between resolution and sensitivity. In addition to this loss of resolution, the doping of the sample with a nitroxide free radical will not be desirable in all EFNMR applications.

The final signal enhancement method considered was hyperpolarization via optical pumping. A ^{129}Xe NMR spectrum of optically pumped xenon gas acquired in the Earth's magnetic field was presented and used to estimate the degree of polarization of the gas to be 9.2%. Despite the obvious SNR advantages of direct detection of hyperpolarized gases it was found that the use of hyperpolarized gas for the indirect polarization of target nuclei in a solvent via the SPINOE effect was inefficient in the case of the large sample volumes (100s of mL) which can be used in EFNMR without a significant loss in spectral resolution. Therefore prepolarization and dynamic nuclear polarization (DNP) methodologies were found to be the best signal enhancement methods for EFNMR. The choice between the prepolarization and DNP methods is strongly dependent on the sample and the application.

The second half of this thesis focused on the investigation of the information content of EFNMR. A number of one- and two-dimensional spectroscopy experiments were implemented and analyzed using numerical simulations, time-independent perturbation theory calculations and exact analysis.

A density matrix simulation tool was developed for the particular case of Earth's field NMR. This simulation does not use the secular approximation to evaluate the indirect spin-spin coupling term in the interaction Hamiltonian and therefore captures the features associated with strong coupling. The full indirect spin-spin coupling term is used in the interaction Hamiltonian. The evolution operator is consequently estimated from this Hamiltonian using a truncated Taylor series expansion. The order to which this series is calculated and the time step of the evolution operator are chosen such that the error associated with this truncation is

negligible. The simulation was written in Prospa v2.2 (Magritek, Ltd., Wellington, New Zealand). The full code is reproduced in Appendix A of this thesis

In Earth's field NMR, the difference in Larmor frequency between heteronuclei is such that strong indirect spin-spin coupling can be observed between nuclei of differing spin. While strong coupling between homonuclear spins, which necessarily have the same spin quantum number, has long been studied in high-field NMR, the situation of strong coupling between nuclei of differing spin has not previously been discussed in detail.

In Chapter 7, strong coupling between a plurality of ^{1}H nuclei and nuclei of differing spin (^{14}N, ^{11}B and ^{10}B) was investigated. Time-independent perturbation theory was evaluated as a tool for accurately modeling strongly coupled systems of nuclei of differing spin through comparisons with exact calculations of two-spin systems and density matrix simulations of systems of more than two strongly-coupled nuclei. It was found that second-order perturbation theory could be used to characterize the ^{1}H EFNMR spectrum of the ammonium ion, NH^{+}, in a field of approximately 54 μT. In this case the indirect spin-spin coupling between the ^{14}N nucleus and the ^{1}H nuclei is 2.5% of the difference in Larmor frequency. In the case of the tetrahydroborate ion, BH_4^{-}, it was found that third-order perturbation theory was required to accurately model the coupling between the ^{11}B nucleus and ^{1}H nuclei, where the indirect spin-spin coupling constant is 5.2% of the difference in Larmor frequency between nuclei at 54 μT. In this same system, the coupling between the ^{10}B nucleus and the ^{1}H nuclei is only 1.3% of the difference in Larmor frequency at 54 μT and so could be modeled by second-order perturbation theory.

In Chapter 8 we presented 2D EFNMR measurements using the correlation spectroscopy (COSY) experiment. A ^{1}H 2D COSY EFNMR spectrum of monofluorobenzene was presented and compared with density matrix simulations to show that the one-dimensional spectrum of this molecule, which appears to be a doublet suffering from significant line-broadening, is in fact the result of a range of heteronuclear and homonuclear coupling constants, as observed at high-field.

A full ^{1}H – ^{19}F 2D COSY spectrum of 1,4-difluorobenzene was also presented and compared to simulation. This spectrum was acquired using the various apparatus developments detailed in Chapter 4 (shimming, field stabilization and ULF screening)

and represented a significant improvement in SNR and resolution over the previously reported 2D EFNMR spectra results.

The sensitivity of these multi-dimensional EFNMR spectroscopy experiments was further improved through the use of dynamic nuclear polarization for signal enhancement. A high-quality, high-SNR 2D $^{1}H - ^{19}F$ COSY EFNMR spectrum acquired from 2,2,2-trifluoroethanol using DNP was presented and compared to simulation. Analysis of the observed spectrum showed that the signal enhancement associated with the CH_2 protons was the greatest, followed by the signal enhancement of the CF_3 ^{19}F nuclei. The hydroxyl proton, which is in rapid chemical exchange at room temperature, benefited the least from DNP signal enhancement.

In Chapter 9 we considered the indirect spin-spin coupling regime which prevails at fields significantly weaker than the Earth's magnetic field through simulations of 1D and 2D spectroscopy experiments. We found that for some molecules containing J coupled hetero-nuclei, there exists a coupling regime in which both the difference in Larmor frequency between the coupled nuclei as well as their absolute Larmor frequencies are on the same order of magnitude, but smaller than, the coupling constant. In this regime some very interesting spectral patterns emerge, although these patterns were found to be much more complicated than the analogous regime at high-field in which the Zeeman interaction strongly dominates over the indirect spin-spin coupling interaction.

We explored this unique coupling regime through a detailed analysis, combining density matrix simulations and exact calculations, of the coupling of the $^{13}C^{1}H_3$ chemical group in a field of 1 μT and in the Earth's magnetic field (54 μT).

The evolution from the "zero"-field coupling regime to that which prevails in the Earth's magnetic field was further investigated through the use of a novel 2D EFNMR pulse sequence in which the spins are allowed to evolve under the influence of an evolution field (much smaller than the Earth's field) during an evolution time period, t_1, prior to detection in the Earth's magnetic field. The resultant 2D spectrum correlates the peaks in the very weak t_1 evolution field with those in the Earth's magnetic field. This 2D pulse sequence was demonstrated through density matrix simulations of $^{13}C^{1}H_3$ and a modified version of the dimethyl phosphite molecule, in which only one methyl group was included. It was found that while, in some particular examples, these microtesla NMR spectroscopy experiments demonstrate

some very interesting quantum mechanics, the application of this technique to routine chemical analysis of a wide range of molecules is limited by the complexity of the spectral patterns and the necessity of having one or more NMR-active heteronuclei present to break the magnetic equivalence between homonuclei.

Anisotropy in ordered media is typically measured in NMR through the use of either the quadrupolar coupling of nuclei with spin > ½ or residual dipolar coupling. In Chapter 10 we considered the case of a liquid crystal (PBLG) in a nematic phase solution of dichloromethane. The residual intra-molecular dipolar coupling between the two ^{1}H nuclei on the dichloromethane molecule was measured at high-field to be 57 Hz in the mono-domain state induced in the sample by the strong magnetic field. In the Earth's magnetic field, a series of spectra were obtained, over time, which showed an evolution from a poly-domain state with a residual dipolar coupling of 42.5 Hz to a single narrow isotropic peak with no observed residual dipolar interaction. Concurrent macroscopic changes in the sample properties, such as a dramatic increase in viscosity, suggest that the sample transitioned into some kind of non-nematic state as a result of an increase in liquid crystal concentration due to solvent evaporation over time. More work is required on this liquid crystalline system to investigate the features of this system and fully explain our observed EFNMR results.

11.2. Future Work

There remain many avenues for future research in the area of Earth's field NMR spectroscopy. The following are a few ideas for interesting Earth's field NMR experiments which could be pursued in the future.

11.2.1. Non-^{1}H EFNMR spectroscopy with DNP

The most significant barrier to any Earth's field spectroscopic experiments in which the detected nucleus is not ^{1}H (or ^{19}F) is sensitivity. SNR is approximately equal to the cube of the gyromagnetic ratio. Two factors of γ arise from the expression for thermal polarization and one factor of γ is due to the faraday induction

at the γ-dependent Larmor frequency. For ^{19}F nuclei there is a loss in sensitivity of only 17% with respect to ^{1}H nuclei. The loss in sensitivity is much more catastrophic for other nuclei. ^{31}P nuclei, for example, suffer from a 93% loss in sensitivity compared to ^{1}H nuclei. Therefore detection of ^{31}P EFNMR spectra, even with prepolarization, is a significant challenge.

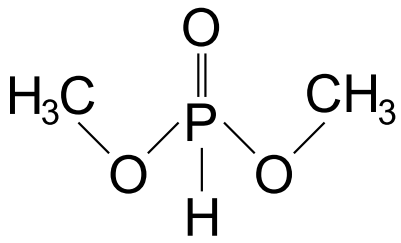

Figure 11.1 Dimethylphosphite

Consider the case of the dimethyl phosphite molecule, pictured in Figure 11.1. The single ^{31}P nucleus experiences a very strong one-bond, indirect spin-spin coupling with a ^{1}H nucleus ($^{1}J(^{31}P,^{1}H)$ = 696 Hz) and a weaker three-bond coupling with the remaining six methyl ^{1}H nuclei ($^{3}J(^{31}P,^{1}H)$ = -12 Hz). The former coupling constant is 49% of the difference in Larmor frequency between ^{1}H and ^{31}P and so this coupling is very strong indeed.

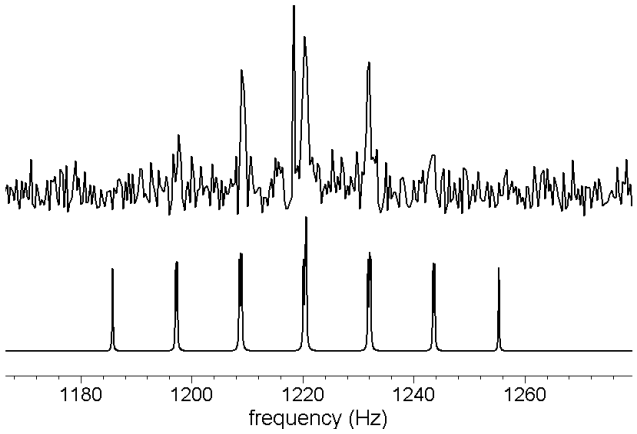

Figure 11.2 The higher-frequency portion of a ^{31}P EFNMR spectrum acquired from 500 mL of pure dimethylphosphite (300 averages, 2.5 hours). (The narrow peak occurring at a slightly lower frequency than the central peak is a noise peak.) A spectrum calculated using fourth-order perturbation theory is presented below the observed spectrum for comparison.

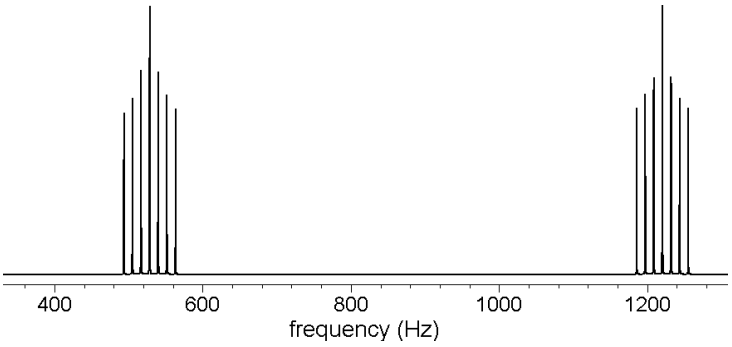

Figure 11.3 Full ^{31}P EFNMR spectrum of dimethylphosphite calculated from fourth-order perturbation theory.

The higher-frequency portion of a ^{31}P EFNMR spectrum of dimethyl phosphite is presented in Figure 11.2. Below the observed spectrum is a spectrum calculated using fourth-order perturbation theory. The full ^{31}P spectrum calculated from perturbation theory is presented in Figure 11.3. It is clear from Figure 11.2 that improved SNR is required to obtain high-quality ^{31}P spectra.

DNP is an attractive solution for ^{31}P EFNMR because its sensitivity does not depend on the thermal polarization of ^{31}P and so the only explicit dependence of SNR on gyromagnetic ratio is via the Larmor frequency and Faraday induction. The coupling factor between the unpaired electrons in the free radical and the ^{31}P nuclei is dependent on γ and so we may find a decreased efficiency of polarization transfer from the unpaired electrons to the ^{31}P nuclei compared to ^{1}H nuclei. However, the overall SNR benefits of DNP should be significant.

11.2.2. Modified 2D COSY EFNMR experiments

During the evolution (t_1) period in a 2D COSY experiment, it is possible to refocus the heteronuclear indirect spin-spin coupling by selectively rotating one of the constituent nuclei by 180˚. If this modification to the COSY sequence is applied in the middle of the t_1 time period, as pictured in the pulse sequence in Figure 11.4, there will be no net effect of the heteronuclear coupling during the evolution portion of the experiment.

The effects of heteronuclear coupling will only be observed in the directly detected dimension, t_2. Any homonuclear coupling will not be affected by the

selective 180˚ pulse and so some off-diagonal structure in the modified COSY spectra would be expected in situations where homonuclear indirect spin-spin coupling is present between magnetically non-equivalent nuclei.

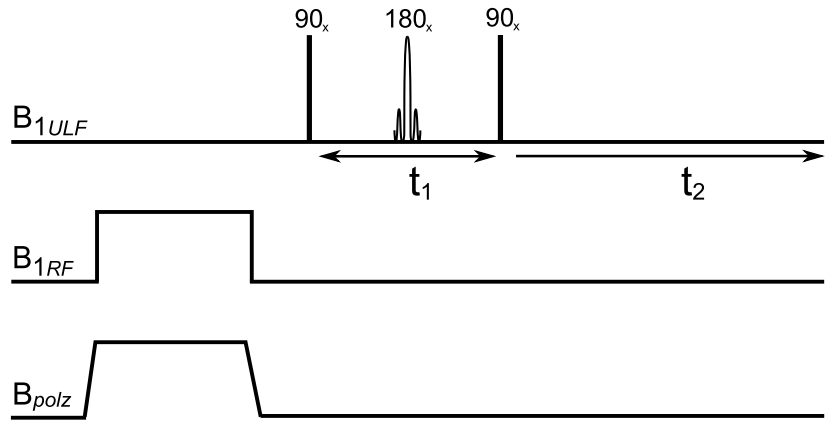

Figure 11.4 2D COSY pulse sequence with a selective 180˚ pulse introduced in the middle of the t_1 evolution time period.

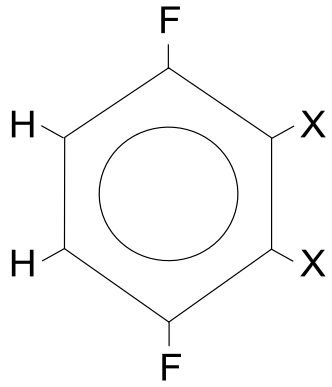

Figure 11.5 The four spin system used for the modified COSY simulations.

Consider the molecule pictured in Figure 11.5. This molecule contains a range of heteronuclear $^{1}H - ^{19}F$ indirect spin-spin couplings as well as homonuclear $^{1}H - ^{1}H$ and $^{19}F - ^{19}F$ couplings. These are summarized in Table 11.1.

Table 11.1 Coupling constants used for COSY simulations

$^{3}J(^{1}H,^{19}F)$ (Hz)	$^{4}J(^{1}H,^{19}F)$ (Hz)	$^{3}J(^{1}H,^{1}H)$ (Hz)	$^{5}J(^{19}F,^{19}F)$ (Hz)
7.6	4.6	8	12

A COSY spectrum and modified COSY spectra, simulated from this spin system, are presented in Figure 11.6, Figure 11.7 and Figure 11.8, respectively. The first thing we notice in the modified spectra is that peaks only appear along a narrow range of frequencies in the f_1 dimension. This range of frequencies corresponds to the Larmor frequency of the spin which is not refocused by the 180˚ pulse. In Figure 11.7 the ^{19}F nuclei are refocused and so in f_1 we observe signal near 2300 Hz only. The opposite is the case in Figure 11.8 and so in f_1 we observe signal around 2265 Hz only.

If we compare the off-diagonal peaks in the modified COSY spectra with the traditional COSY spectrum we see some curious features appear in the former which are quite different from the features observed in the latter. The form of these features will be dependent on the homonuclear coupling constants. Therefore analysis of this type of spectrum may provide information on the homonuclear coupling constants which is not readily apparent in the traditional COSY spectrum containing the full influence of heteronuclear as well as homonuclear coupling in the indirect dimension. More simulation and experiment would be required to fully understand the relationship between these modified spectra and the underlying coupling constants.

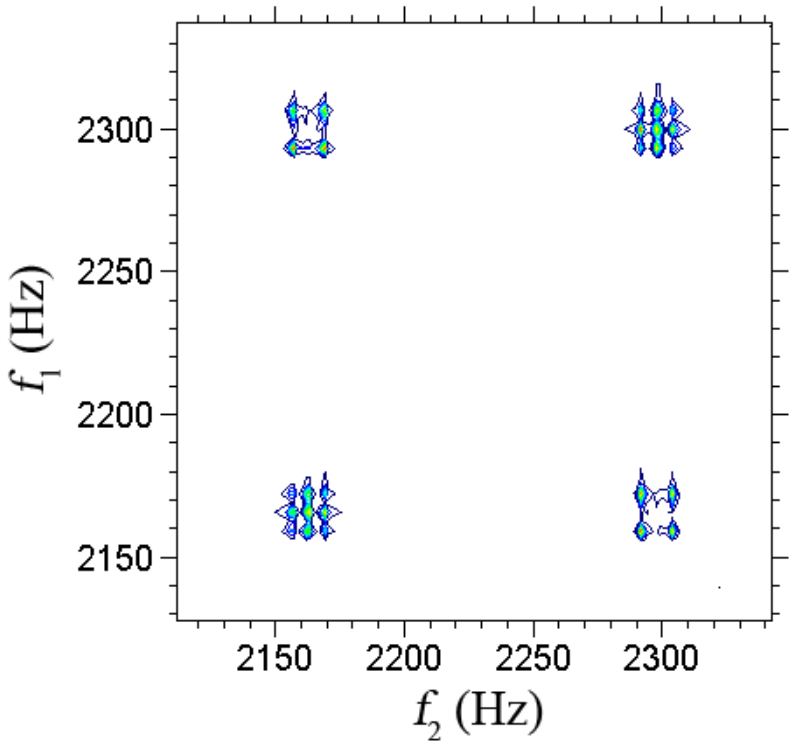

Figure 11.6 COSY spectrum simulation of an H_2F_2 system

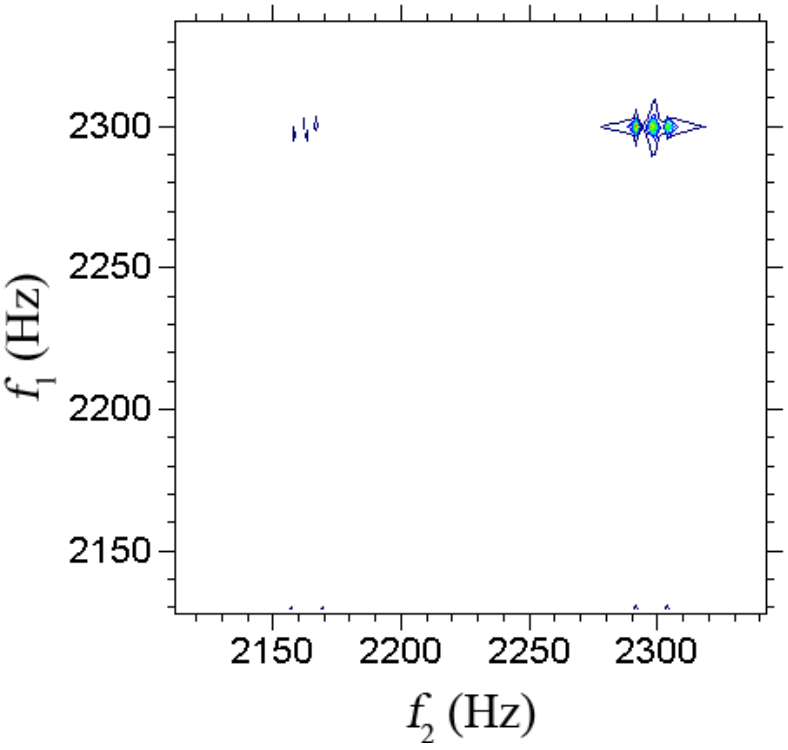

Figure 11.7 Modified COSY spectrum simulation of a H_2F_2 system (^{19}F refocused)

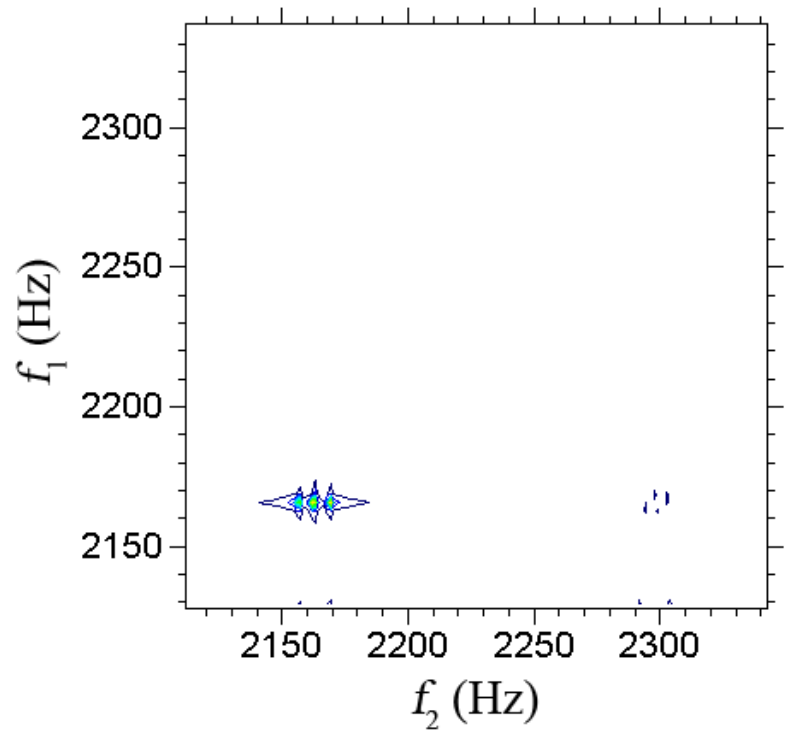

Figure 11.8 Modified COSY spectrum simulated of a H_2F_2 system (^{1}H refocused)

Appendix A. Prospa Density Matrix Simulation

```
procedure(simulate_COSY)

# Initialise the clock
   time(0)

# Some constants
   gammaC13 = 6.728e7        # Additional gamma value 13C
   gammaF19 = 2.517e8        # Additional gamma value 19F
   gammaSi29 = -5.319e7      # Additional gamma value 29Si
   gammaElec = -1.761e11     # Additional gamma value for electrons
   gammaN14 = 1.9338e7       # Additional gamma value for 14N
   gammaB11 = 8.5847e7       # Additional gamma value for 11B
   gammaB10 = 2.874e7        # Additional gamma value for 10B
   gammaP31 = 10.8394e7      # Additional gamma value for 31P

# Experimental conditions
   BE = 2295.9*2*pi/gamma     # Earth's magnetic field (T)
   T2 = 5                     # Long T2 to permit good res. (s)

# Spin system
   # Relative gammas of spins in system
   gammaVect = [gammaF19,gamma,gamma,gamma,gamma,gamma]/gamma
   numSpins = [1,1,1,1,1,1]
   observe = [0,1,1,1,1,1]
   spin = [0.5,0.5,0.5,0.5,0.5,0.5]
   num_spins = size(gammaVect)       # Number of spins

# Only measure about the centre frequency
   centreFreq = 0

# Define J coupling constants
   JFF = 12*2*pi
   JFH3 = 8.5*2*pi
   JFH4 = 5*2*pi
   JFH5 = 2*2*pi
   JHH3 = 8*2*pi
   JHH4 = 2*2*pi
   JHH5 = 0*2*pi
```

```
# J coupling matrix
   Jmat = matrix(num_spins,num_spins)
   Jmat[1,0] = JFH3
   Jmat[2,0] = JFH4
   Jmat[3,0] = JFH5
   Jmat[4,0] = JFH4
   Jmat[5,0] = JFH3
   Jmat[2,1] = JHH3
   Jmat[3,1] = JHH4
   Jmat[4,1] = JHH5
   Jmat[5,1] = JHH4
   Jmat[3,2] = JHH3
   Jmat[4,2] = JHH4
   Jmat[5,2] = JHH5
   Jmat[4,3] = JHH3
   Jmat[5,3] = JHH4
   Jmat[5,4] = JHH3

# Angles in degrees. phi --> x  alpha --> y  theta --> z
   phi = [0,90,90,90,90,90]      # Rotation angle for each nucleus
   alpha = [0,0,0,0,0,0]
   theta = matrix(num_spins)

# Acquisition parameters (t2 domain)
   O = 28
   bandwidth = 6666.67
   numPts = 32768*2
   numSmpls =16384*2
   freqRes = bandwidth/numSmpls
   acqTime = 1/freqRes
   dwell = acqTime/numPts
   dwellt2 = acqTime/numSmpls
   ratio = dwellt2/dwell
   t2 = [0:1:numSmpls-1]*dwellt2
   f2 = ([0:1:numSmpls-1]-numSmpls/2)/acqTime

# Acquisition parameters (t1 domain)
   numt1 = 256                # number of t1 steps
   dwellt1 = 18.9e-3          # dwell time in the t1 domain (s)
   maxt1 = dwellt1*numt1      # maximum t1 time
   ratio2 = dwellt1/dwell     # Number of evolution steps for each
                                dwellt1
   if (ratio2 - trunc(ratio2)) != 0
      message("Warning","dwellt1 was changed from $dwellt1*1000$
               ms to $round(ratio2)*dwell*1000$ ms")
      ratio2 = round(ratio2)
      dwellt1 = ratio2*dwell
   endif
   Error = 2*pi*numSmpls*(bandwidth*dwell)^(O-1)/factorial(O)

# Define output matrix
   output = cmatrix(numSmpls,numt1)

# Make unique output file name and define output matrix
   if numt1 > 1
      expDim = "2D"
      extension = ".2d"
   else
      expDim = "1D"
      extension = ".1d"
```

```
    endif
    root = getmacropath()
    specName = "\\COSYC6H5Fsim"
    filename = root+specName+extension
    index = 0
    while isfile(filename)
       index=index+1
       filename = root+specName+"$index$"+extension
    endwhile

# Output parameters to CLI
    pr "\nEvolution Parameters"
    pr "\n   Number of Points:   $numPts$"
    pr "\n   dwell time:         $dwell$"
    if expDim = "2D"
       pr "\n\nt1 Parameters"
       pr "\n   Number of t1 steps: $numt1$"
       pr "\n   dwell time:         $dwellt1$ s"
       pr "\n   Resolution:         $1/dwellt1/numt1$ Hz"
    endif
    pr "\n\nAcquisition Parameters"
    pr "\n   Number of Points:   $numSmpls$"
    pr "\n   dwell time:         $dwellt2$ s"
    pr "\n   Resolution:         $1/acqTime$ Hz"
    pr "\n\nError"
    pr "\n   Error:              $Error$"
    pr "\n   Centre Frequency:   $centreFreq/2/pi$ Hz"

# Pauli spin matrices for I = 1/2
    Ixs0.5 = [0, 1/2; 1/2, 0]
    Iys0.5 = [0,-1/2; 1/2, 0]*i
    Izs0.5 = [1/2, 0; 0, -1/2]

# Pauli spin matrices for I = 1
    Ixs1 = [0,1,0;1,0,1;0,1,0]/sqrt(2)
    Iys1 = [0,-1,0;1,0,-1;0,1,0]*i/sqrt(2)
    Izs1 = [1,0,0;0,0,0;0,0,-1]

# Pauli spin matrices for I = 1.5
    Ixs1.5 =
    [0,sqrt(3),0,0;sqrt(3),0,2,0;0,2,0,sqrt(3);0,0,sqrt(3),0]/2

    Iys1.5 = [0,-sqrt(3),0,0;sqrt(3),0,-2,0;0,2,0,-
    sqrt(3);0,0,sqrt(3),0]*i/2

    Izs1.5 = [3,0,0,0;0,1,0,0;0,0,-1,0;0,0,0,-3]/2

# Pauli spin matrices for I = 3
    Ixs3 =
    1/sqrt(2)*[0,sqrt(3),0,0,0,0,0;sqrt(3),0,sqrt(5),0,0,0,0;0,sqrt(5)
    ,0,sqrt(6),0,0,0;0,0,sqrt(6),0,sqrt(6),0,0;0,0,0,sqrt(6),0,sqrt(5)
    ,0;0,0,0,0,sqrt(5),0,sqrt(3);0,0,0,0,0,sqrt(3),0]

    Iys3 = i/sqrt(2)*[0,-sqrt(3),0,0,0,0,0;sqrt(3),0,-
    sqrt(5),0,0,0,0;0,sqrt(5),0,-sqrt(6),0,0,0;0,0,sqrt(6),0,-
    sqrt(6),0,0;0,0,0,sqrt(6),0,-sqrt(5),0;0,0,0,0,sqrt(5),0,-
    sqrt(3);0,0,0,0,0,sqrt(3),0]
    Izs3 =
    [3,0,0,0,0,0,0;0,2,0,0,0,0,0;0,0,1,0,0,0,0;0,0,0,0,0,0,0;0,0,0,0,-
    1,0,0;0,0,0,0,0,-2,0;0,0,0,0,0,0,-3]
```

```
# Create identity matrices for each spin

   for n = 0 to num_spins-1
      dimension = spin[n]*2+1
      Id = identity(dimension,dimension)
      assign("Id$n+1$",Id,"local")
   next(n)

   for d = 0 to 2

      if d = 0
         dim = "x"
         angle = eval("phi")*pi/180
      elseif d = 1
         dim = "y"
         angle = eval("alpha")*pi/180
      elseif d = 2
         dim = "z"
         angle = eval("theta")*pi/180
      endif


      for m = 1 to num_spins

         if spin[m-1] != 0.5
            R = eval("Id$m$")
         else
            R = cmatrix(2,2)
            if dim = "x"
               R[0,0] = cos(angle[m-1]/2)
               R[0,1] = -i*sin(angle[m-1]/2)
               R[1,0] = -i*sin(angle[m-1]/2)
               R[1,1] = cos(angle[m-1]/2)
            elseif dim = "y"
               R[0,0] = cos(angle[m-1]/2)
               R[0,1] = sin(angle[m-1]/2)
               R[1,0] = -sin(angle[m-1]/2)
               R[1,1] = cos(angle[m-1]/2)
            else
               R[0,0] = exp(-i*angle[m-1]/2)
               R[1,1] = exp(i*angle[m-1]/2)
            endif
         endif
         Rn = trans(conj(R))
         if m = 1
            A = eval("I$dim$s$spin[0]$")
            B = R
            C = Rn
         else
            A = Id1
            B = outer(B,R)
            C = outer(C,Rn)
         endif
         for n = 2 to num_spins
            if n=m
               A = outer(A,eval("I$dim$s$spin[n-1]$"))
            else
               A = outer(A,eval("Id$n$"))
            endif
         next(n)
```

```
            assign("I$dim$$m$",A,"local")
         next(m)
         assign("R$dim$",B,"local")
         assign("R$dim$n",C,"local")
      next(d)

# Construct the Hamiltonian (in ang. freq. units) and density
  matrix

      # First the Zeeman terms
      H = (-gammaVect[0]*gamma*BE+centreFreq)*Iz1
      rho = numSpins[0]*gammaVect[0]*gamma*BE*Iz1
      for n = 1 to num_spins-1
         H = H + (- gammaVect[n]*gamma*BE+centreFreq)*eval("Iz$n+1$")
         rho = rho +
               numSpins[n]*gammaVect[n]*gamma*BE*eval("Iz$n+1$")
      next(n)

      # J coupling terms
      for n = 0 to num_spins-2
         for m = n+1 to num_spins-1
            Jterm = Jmat[m,n]*(eval("Ix$n+1$")*eval("Ix$m+1$")
                              +eval("Iy$n+1$")*eval("Iy$m+1$")
                              +eval("Iz$n+1$")*eval("Iz$m+1$"))
            H = H + Jterm
            rho = rho - Jterm
         next(m)
      next(n)

# Calculate the evolution matrix to Oth order
      dimensionality = spin[0]*2+1
      for n = 1 to num_spins-1
         dimensionality = dimensionality*(2*spin[n]+1)
      next(n)
      Id = identity(dimensionality,dimensionality)
      E = Id
      for n = 1 to O
         for m = 1 to n
            if m = 1
               Hprime = i*dwell*H
            else
               Hprime = Hprime*i*dwell*H
            endif
         next(m)
         E = E + Hprime/factorial(n)
      next(n)
      En = trans(conj(E))

# Create a matrix for the evolution of one step in t2
      Ent2 = En
      Et2 = E
      for n = 1 to ratio-1
         Ent2 = Ent2*En
         Et2 = Et2*E
      next(n)

# Create a matrix for the evolution matrix for on step in t1
      if expDim = "2D"
         Ent1 = "En"
         Et1 = "E"
```

```
      for n = 1 to ratio2-1
         Ent1 = Ent1*En
         Et1 = Et1*E
      next(n)
   endif

# Generate observation operator
   first = 1
   for n = 1 to num_spins
      if observe[n-1] = 1
         if first = 1
            Iobs = eval("Ix$n$")+ i*eval("Iy$n$")
            first = 0
         else
            Iobs = Iobs + eval("Ix$n$")+ i*eval("Iy$n$")
         endif
      endif
   next(n)


####### BEGIN EXPERIMENT ##########


# Apply first x rotation pulse
   rho_plus = Rxn*rho*Rx

# Loop over t1 steps

   for tt = 0 to numt1-1

      if expDim = "2D"

         # Evolve during the t1 time period (include T2 decay)
         rho_plus = exp(-dwellt1/T2)*Ent1*rho_plus*Et1

         # Apply second x rotation pulse
         rho_t2 = Rxn*rho_plus*Rx

      else

         rho_t2 = rho_plus

      endif

   # Observe as a function of time by applying time evolution with
     Hamiltonian (and relaxation) and then

      for n = 0 to numSmpls-1
         rho_t2 = exp(-dwellt2/T2)*Ent2*rho_t2*Et2
         output[n,tt] = trac(rho_t2*Iobs)
      next(n)

      if tt%10 = 0
         pr "\nt1 step number $tt$  time = $time()/60,4.2f$ min"
      endif

   next(tt)

   save(filename,output)
   time2 = time()
```

```
    hrs  = trunc(time2/3600)
    mins = trunc((time2-hrs*3600)/60)
    secs = time2-hrs*3600-mins*60

    pr "\n\nTotal Simulation Time:
       $hrs,2.0f$:$mins,2.0f$:$secs,2.0f$"
    pr "\nSaved to: $filename$"

    if expDim = "1D"
       output1D = submatrix(output,0,numSmpls-1,0,0)
       multiplot("1d",2,1)
       curplot("1d",1,1)
       drawplot("false")
       plot(t2,output1D)
       xlabel("time (s)")
       title("Time Domain Data")
       ylabel("")
       curplot("1d",2,1)
       plot(f2+centreFreq/2/pi,mag(ft(output1D)))
       xlabel("frequency (Hz)")
       title("Frequency Spectrum")
       ylabel("")
       drawplot("true")
    else
       image(output,[0,acqTime],[0,maxt1])
       title("Time Domain COSY Data")
       xlabel("t2 (s)")
       ylabel("t1 (s)")
    endif

    assign("output",output,"global")
    assign("t2",t2,"global")
    assign("f2",f2,"global")

endproc()
```

Appendix B. Publications from this Thesis

[1] Meghan E. Halse, Paul T. Callaghan, Brett Feland and Roderick E. Wasylishen, Quantitative analysis of Earth's field NMR spectra of strongly-coupled heteronuclear systems, J. Magn. Reson. 200 (2009) 88-94.

[2] Meghan E. Halse and Paul T. Callaghan, Terrestrial Magnetic Field NMR: Recent Advances in "Encyclopedia of Nuclear Magnetic Resonance", Eds. D.M. Grant, and R.K. Harris, John Wiley & Sons, Chichester, 2009.

[3] Meghan E. Halse, Andrew Coy, Robin Dykstra, Craig D. Eccles, Mark W. Hunter and Paul T. Callaghan, Multi-dimensional Earth's field NMR in "Magnetic Resonance Microscopy", Eds. Sarah Codd and Joseph Seymour, Wiley-VCH, Germany, 2009.

[4] Meghan E. Halse and Paul T. Callaghan, A dynamic nuclear polarization strategy for multidimensional Earth's field NMR spectroscopy, J. Magn. Reson. 195 (2008) 162-168.

[5] M. Halse, A. Coy, R. Dykstra, C. Eccles, M. Hunter, R. Ward, P.T. Callaghan, A practical and flexible approach to MRI in the Earth's magnetic field, J. Magn. Reson. 182 (2006) 75 – 83.

[6] Meghan E. Halse and Paul T. Callaghan, Imaged deconvolution: a method for extracting high-resolution NMR spectra from inhomogeneous fields, J. Magn. Reson. 185 (2007) 130-137. (*Results not discussed in this thesis*.)

References

[1] M. Packard, and R. Varian, Free Nuclear Induction in the Earth's Magnetic Field. Physical Review 93 (1954) 941.

[2] R.J.S. Brown, and B.W. Gamson, Nuclear magnetism logging. Transactions of the American Institute of Mining and Metallurgical and Petroleum Engineers 219 (1960) 201-209.

[3] R.J.S. Brown, and D.D. Thompson, Second-Order Effects in Low-Field NMR for Ammonium Ion Solutions. Journal of Chemical Physics 34 (1961) 1580-3.

[4] D.D. Thompson, and R.J.S. Brown, Nuclear Free Precession in Very Low Magnetic Fields. Journal of Chemical Physics 40 (1964) 3076-9.

[5] D.D. Thompson, and R.J.S. Brown, The Earth's Field Proton Free-Precession Signal of Fluorobenzene. Journal of Chemical Physics (1962) 2812.

[6] D.D. Thompson, R.J.S. Brown, and R.J. Runge, Dynamic nuclear polarization of liquids in very weak fields. Physical Review A - General Physics 136 (1964) 1286-1290.

[7] G.J. Bene, High resolution NMR spectroscopy in the terrestrial magnetic field range. Colloque Ampere XIV 21 (1967) 903-916.

[8] M. Merck, R. Sechehaye, A. Erbeia, and G.J. Béné, Free precession experiments in terrestrial magnetic field. in: R. Blinc, (Ed.), Magnetic Resonance and Relaxation, North-Holland Publishing Company, Amsterdam, 1967, pp. 952-956.

[9] P.T. Callaghan, C.D. Eccles, and J.D. Seymour, An earth's field nuclear magnetic resonance apparatus suitable for pulsed gradient spin echo measurements of self-diffusion under Antarctic conditions. Review of Scientific Instruments 68 (1997) 4263-4270.

[10] P.T. Callaghan, C.D. Eccles, T.G. Haskell, P.J. Langhorne, and J.D. Seymour, Earth's field NMR in Antarctica: A pulsed gradient spin echo NMR study of restricted diffusion in sea ice. Journal of Magnetic Resonance 133 (1998) 148-154.

[11] P.T. Callaghan, R. Dykstra, C.D. Eccles, T.G. Haskell, and J.D. Seymour, A nuclear magnetic resonance study of Antarctic sea ice brine diffusivity. Cold Regions Science and Technology 29 (1999) 153-171.

[12] O.R. Mercier, M.W. Hunter, and P.T. Callaghan, Brine diffusion in first-year sea ice measured by Earth's field PGSE-NMR. Cold Regions Science and Technology 42 (2005) 96-105.

[13] M.W. Hunter, R. Dykstra, M.H. Lim, T.G. Haskell, and P.T. Callaghan, Using Earth’s Field NMR to Study Brine Content in Antarctic Sea Ice: Comparison with Salinity and Temperature Estimates. Applied Magnetic Resonance 36 (2009) 1-8.

[14] C.P. Slichter, Principles of magnetic Resonance, Springer Heidelberg, 1990.

[15] M.H. Levitt, Spin Dynamics: Basics of Nuclear Magnetic Resonance, John Wiley and Sons, Ltd, Chichester, UK, 2008.

[16] A. Abragam, Principles of Nuclear Magnetism, Oxford University Press, Oxford, 1961.

[17] P.T. Callaghan, Principles of Nuclear Magnetic Resonance Microscopy, Oxford University Press, 1991.

[18] R.E. Wasylishen, Indirect nuclear spin-spin coupling tensors. in: D.M. Grant, and R.K. Harris, (Eds.), Encyclopedia of Nuclear Magnetic Resonance, John Wiley & Sons, Inc., 2002, pp. 274-282.

[19] S. Appelt, F.W. Häsing, H. Kühn, J. Perlo, and B. Blümich, Mobile high resolution xenon nuclear magnetic resonance spectroscopy in the earth's magnetic field. Physical Review Letters 94 (2005).

[20] G.J. Béné, Nuclear Magnetism of Liquid Systems in the Earth Field Range. Physics Reports (Review Section of Physics Letters) 58 (1980) 213-267.

[21] A. Mohorič, and J. Stepišnik, NMR in the Earth's magnetic field. Progress in Nuclear Magnetic Resonance Spectroscopy 54 (2009) 166-182.

[22] J. Stepišnik, V. Erzen, and M. Kos, NMR imaging in the Earth's magnetic field. Magnetic Resonance in Medicine 15 (1990) 386-391.

[23] J. Stepišnik, M. Kos, G. Planinsic, and V. Erzen, Strong nonuniform magnetic-field for self-diffusion measurement by NMR in the Earth's magnetic-field. Journal of Magnetic Resonance Series A 107 (1994) 167-172.

[24] A. Mohorič, J. Stepišnik, M. Kos, and G. Planinsic, Self-diffusion imaging by spin echo in Earth's magnetic field. Journal of Magnetic Resonance 136 (1999) 22-26.

[25] A. Mohorič, G. Planinsic, M. Kos, A. Duh, and J. Stepišnik, Magnetic resonance imaging system based on Earth's magnetic field. Instrumentation Science & Technology 32 (2004) 655-667.

[26] D.F. Elliott, and R.T. Schumacher, Proton resonance of fluorobenzene in the Earth's magnetic field. Journal of Chemical Physics 26 (1957) 1350-1350.

[27] B. Bak, J.N. Shoolery, and G.A. Williams, Nuclear spin-spin coupling between fluorine and hydrogen in fluorobenzene. Journal of Molecular Spectroscopy 2 (1958) 525-538.

[28] N. Kernevez, and H. Glenat, Description of a high-sensitivity cw scalar DNP-NMR magnetometer. IEEE Transactions on Magnetics 27 (1991) 5402-5404.

[29] K. Lang, M. Moussavi, and E. Belorizky, New, high-performance, hydrogenated paramagnetic solution for use in earth field DNP-NMR magnetometers. Journal of Physical Chemistry A 101 (1997) 1662-1671.

[30] R.J.S. Brown, R. Chandler, J.A. Jackson, R.L. Kleinberg, M.N. Miller, Z. Paltiel, and M.G. Prammer, History of NMR well logging. Concepts in Magnetic Resonance 13 (2001) 335-413.

[31] P.T. Callaghan, and M. Legros, Nuclear spins the Earth's magnetic field. American Journal of Physics 50 (1982) 709-713.

[32] A.G. Semenov, M.D. Schirov, A.V. Legchenko, A.I. Burshtein, and A.Y. Pusep, A device for measuring the parameters of an underground mineral deposit, Great Britain, 1989.

[33] O.A. Shushakov, Groundwater NMR in conductive water. Geophysics 61 (1996) 998-1006.

[34] O.A. Shushakov, and V.M. Fomenko, Surface-NMR relaxation and echo of aquifers in geomagnetic field. Applied Magnetic Resonance 25 (2004) 599-610.

[35] D.V. Trushkin, O.A. Shushakov, and A.V. Legchenko, The potential of a noise-reducing antenna for surface NMR groundwater surveys in the Earth's magnetic field. Geophysical Prospecting 42 (1994) 855-862.

[36] D.V. Trushkin, O.A. Shushakov, and A.V. Legchenko, Modulation effects in non-drilling NMR in the Earth's field. Applied Magnetic Resonance 5 (1993) 399-406.

[37] D.V. Trushkin, O.A. Shushakov, and A.V. Legchenko, Surface NMR applied to an electroconductive medium. Geophysical Prospecting 43 (1995) 623-633.

[38] P.T. Callaghan, A. Coy, R. Dykstra, C.A. Eccles, M.E. Halse, M.W. Hunter, O.R. Mercier, and J.N. Robinson, New Zealand developments in earth's field NMR. Applied Magnetic Resonance 32 (2007) 63-74.

[39] G. Planinsic, J. Stepišnik, and M. Kos, Relaxation-time measurement and imaging in the Earths magnetic-field. Journal of Magnetic Resonance Series A 110 (1994) 170-174.

[40] G. Planinsic, J. Stepišnik, and M. Kos, Relaxation-time measurement and imaging in the Earths magnetic-field. Journal of Magnetic Resonance Series A 111 (1994) 233-233.

[41] M.E. Halse, A. Coy, R. Dykstra, C. Eccles, M. Hunter, R. Ward, and P.T. Callaghan, A practical and flexible implementation of 3D MRI in the Earth's magnetic field. Journal of Magnetic Resonance 182 (2006) 75-83.

[42] W. Myers, D. Slichter, M. Hatridge, S. Busch, M. Mossle, R. McDermott, A. Trabesinger, and J. Clarke, Calculated signal-to-noise ratio of MRI detected with SQUIDs and Faraday detectors in fields from 10 mu T to 1.5 T. Journal of Magnetic Resonance 186 (2007) 182-192.

[43] M. Mossle, S.I. Han, W.R. Myers, S.K. Lee, N. Kelso, M. Hatridge, A. Pines, and J. Clarke, SQUID-detected microtesla MRI in the presence of metal. Journal of Magnetic Resonance 179 (2006) 146-151.

[44] R. McDermott, N. Kelso, S.K. Lee, M. Mossle, M. Mück, W. Myers, B. ten Haken, H.C. Seton, A.H. Trabesinger, A. Pines, and J. Clarke, SQUID-

detected magnetic resonance imaging in microtesla magnetic fields. Journal of Low Temperature Physics 135 (2004) 793-821.

[45] R. McDermott, S.K. Lee, B. ten Haken, A.H. Trabesinger, A. Pines, and J. Clarke, Microtesla MRI with a superconducting quantum interference device. Proceedings of the National Academy of Sciences of the United States of America 101 (2004) 7857-7861.

[46] M.A. Espy, A.N. Matlachov, P.L. Volegov, J.C. Mosher, and R.H. Kraus, SQUID-based simultaneous detection of NMR and biomagnetic signals at ultra-low magnetic fields. IEEE Transactions on Applied Superconductivity 15 (2005) 635-639.

[47] J. Clarke, M. Hatridge, and M. Mossle, SQUID-detected magnetic resonance imaging in microtesla fields. Annual Review of Biomedical Engineering 9 (2007) 389-413.

[48] M. Espy, M. Flynn, J. Gomez, C. Hanson, R. Kraus, P. Magnelind, K. Maskaly, A. Matlashov, S. Newman, M. Peters, H. Sandin, I. Savukov, L. Schultz, A. Urbaitis, P. Volegov, and V. Zotev, Applications of Ultra-Low Field Magnetic Resonance for Imaging and Materials Studies. IEEE Transactions on Applied Superconductivity 19 (2009) 835-838.

[49] V.S. Zotev, A.N. Matlashov, P.L. Volegov, A.V. Urbaitis, M.A. Espy, and R.H. Kraus, SQUID-based instrumentation for ultralow-field MRI. Superconductor Science & Technology 20 (2007) S367-S373.

[50] V.S. Zotev, P.L. Volegov, A.N. Matlashov, M.A. Espy, J.C. Mosher, and R.H. Kraus, Parallel MRI at microtesla fields. Journal of Magnetic Resonance 192 (2008) 197-208.

[51] S. Xu, C.W. Crawford, S. Rochester, V. Yashchuk, D. Budker, and A. Pines, Submillimeter-resolution magnetic resonance imaging at the Earth's magnetic field with an atomic magnetometer. Physical Review A 78 (2008) 013404.

[52] I.M. Savukov, V.S. Zotev, P.L. Volegov, M.A. Espy, A.N. Matlashov, J.J. Gomez, and R.H. Kraus, MRI with an atomic magnetometer suitable for practical imaging applications. Journal of Magnetic Resonance 199 (2009) 188-191.

[53] V.S. Zotev, A.N. Matlashov, P.L. Volegov, I.M. Savukov, M.A. Espy, J.C. Mosher, J.J. Gomez, and R.H. Kraus, Microtesla MRI of the human brain combined with MEG. Journal of Magnetic Resonance 194 (2008) 115-120.

[54] R.H. Kraus, M.A. Espy, P.L. Volegov, A.N. Matlachov, J.C. Mosher, A.V. Urbaitis, and V.S. Zotev, Toward SQUID-based direct measurement of neural currents by nuclear magnetic resonance. IEEE Transactions on Applied Superconductivity 17 (2007) 854-857.

[55] A.N. Matlachov, P.L. Volegov, M.A. Espy, R. Stolz, L. Fritzsch, V. Zakosarenko, H.G. Meyer, and R.H. Kraus, Instrumentation for simultaneous detection of low field NMR and biomagnetic signals. IEEE Transactions on Applied Superconductivity 15 (2005) 676-679.

[56] S. Appelt, F.W. Häsing, H. Kühn, J. Perlo, and B. Blümich, Mobile high resolution xenon nuclear magnetic resonance spectroscopy in the Earth's magnetic field. Physical Review Letters 94 (2005) 197602.

[57] S. Appelt, H. Kühn, F.W. Häsing, and B. Blümich, Chemical analysis by ultrahigh-resolution nuclear magnetic resonance in the Earth's magnetic field. Nature Physics 2 (2006) 105-109.

[58] S. Appelt, F.W. Häsing, H. Kühn, U. Sieling, and B. Blümich, Analysis of molecular structures by homo- and hetero-nuclear J-coupled NMR in ultra-low field. Chemical Physics Letters 440 (2007) 308-312.

[59] S. Appelt, F.W. Häsing, H. Kühn, and B. Blümich, Phenomena in J-coupled nuclear magnetic resonance spectroscopy in low magnetic fields. Physical Review A 76 (2007) 023420.

[60] J.N. Robinson, A. Coy, R. Dykstra, C.D. Eccles, M.W. Hunter, and P.T. Callaghan, Two-dimensional NMR spectroscopy in Earth's magnetic field. Journal of Magnetic Resonance 182 (2006) 343-347.

[61] G. Planinsic, Shielding of low-frequency magnetic interference in weak-field MRI by a single-layer cylindrical coil. Journal of Magnetic Resonance 126 (1997) 30-38.

[62] M.W.M. Ronald T. Merrill, Phillip L. McFadden, The Magnetic Field of the Earth: Paleomagnetism, the Core and the Deep Mantle, Academic Press, San Diego, NM, USA, 1998.

[63] A.W. Overhauser, Polarization of nuclei in metals. Physical Review 92 (1953) 411-415.

[64] B.D. Armstrong, and S. Han, A new model for Overhauser enhanced nuclear magnetic resonance using nitroxide radicals. Journal of Chemical Physics 127 (2007) 10.

[65] I. Solomon, Relaxation processes in a system of 2 spins. Physical Review 99 (1955) 559-565.

[66] T. Guiberteau, and D. Grucker, EPR spectroscopy by dynamic nuclear polarization in low magnetic field. Journal of Magnetic Resonance Series B 110 (1996) 47-54.

[67] G. Planinsic, D. Grucker, and J. Stepišnik, New method for contrast manipulation in DNP-Enhanced MRI. Magnetic Resonance in Medicine 35 (1996) 379-383.

[68] G. Planinsic, T. Guiberteau, and D. Grucker, Dynamic nuclear polarization imaging in very low magnetic fields. Journal of Magnetic Resonance Series B 110 (1996) 205-209.

[69] D. Grucker, T. Guiberteau, and G. Planinsic, Proton-electron double resonance: Spectroscopy and imaging in very low magnetic fields. Research on Chemical Intermediates 22 (1996) 567-579.

[70] T. Guiberteau, and D. Grucker, Dynamic nuclear-polarization of water protons by saturation of sigma and pi EPR transitions of nitroxides. Journal of Magnetic Resonance Series A 105 (1993) 98-103.

[71] D.J. Lurie, I. Nicholson, and J.R. Mallard, Low-field EPR measurements by field-cycled dynamic nuclear-polarization. Journal of Magnetic Resonance 95 (1991) 405-409.

[72] C. Polyon, D.J. Lurie, W. Youngdee, C. Thomas, and I. Thomas, Field-cycled dynamic nuclear polarization (FC-DNP) of N-14 and N-15 nitroxide radicals at low magnetic field. Journal of Physics D-Applied Physics 40 (2007) 5527-5532.

[73] W. Happer, Optical-pumping. Reviews of Modern Physics 44 (1972) 169.

[74] T.G. Walker, and W. Happer, Spin-exchange optical pumping of noble-gas nuclei. Reviews of Modern Physics 69 (1997) 629-642.

[75] M.S. Albert, G.D. Cates, B. Driehuys, W. Happer, B. Saam, C.S. Springer, and A. Wishnia, Biological magnetic-resonance-imaging using laser polarized Xe-129. Nature 370 (1994) 199-201.

[76] H. Middleton, R.D. Black, B. Saam, G.D. Cates, G.P. Cofer, R. Guenther, W. Happer, L.W. Hedlund, G.A. Johnson, K. Juvan, and J. Swartz, MR-imaging with hyperpolarized He-3 gas. Magnetic Resonance in Medicine 33 (1995) 271-275.

[77] Z.I. Cleveland, G.E. Pavlovskaya, N.D. Elkins, K.F. Stupic, J.E. Repine, and T. Meersmann, Hyperpolarized Kr-83 MRI of lungs. Journal of Magnetic Resonance 195 (2008) 232-237.

[78] G. Navon, Y.Q. Song, T. Room, S. Appelt, R.E. Taylor, and A. Pines, Enhancement of solution NMR and MRI with laser-polarized xenon. Science 271 (1996) 1848-1851.

[79] S. Appelt, F.W. Häsing, S. Baer-Lang, N.J. Shah, and B. Blümich, Proton magnetization enhancement of solvents with hyperpolarized xenon in very low-magnetic fields. Chemical Physics Letters 348 (2001) 263-269.

[80] O.W. Sørensen, G.W. Eich, M.H. Levitt, G. Bodenhausen, and R.R. Ernst, Progress in Nuclear Magnetic Resonance Spectroscopy 16 (1983) 163-192.

[81] P.K. Wang, and C.P. Slichter, A Pictorial Operator Formalism for NMR. Coherence Phenomena. Bull. Magnetic Resonance 8 (1986) 3-16.

[82] R.R. Ernst, G. Bodenhausen, and A. Wokaun, Principles of Nuclear Magnetic Resonance in One and Two Dimensions, Oxford University Press, Oxford, 1987.

[83] W.A. Anderson, Nuclear magnetic resonance spectra of some hydrocarbons. Physical Review 102 (1956) 151-167.

[84] H.G. Hecht, Analysis of NMR spectra of magnetically inequivalent nuclei using perturbation theory. Theoretica Chimica Acta 3 (1965) 202-210.

[85] G.J. Béné, High resolution NMR spectroscopy in the terrestrial magnetic field range. in: R. Blinc, (Ed.), Magnetic Resonance and Relaxation, North-Holland Publishing Company, Amsterdam, 1967, pp. 903-916.

[86] P.L. Corio, Structure of High-Resolution NMR Spectra, Academic Press Inc., New York, 1967.

[87] R.A. Bernheim, and B.J. Lavery, Absolute signs of indirect nuclear spin-spin coupling constants. Journal of the American Chemical Society 89 (1967) 1279-1280.

[88] R.E. Wasylishen, and J.O. Friedrich, Deuterium-isotope effects on the nitrogen chemical-shift and $^{1}J(N,H)$ of the ammonium ion. Journal of Chemical Physics 80 (1984) 585-587.

[89] B.E. Smith, B.D. James, and R.M. Peachey, Hydrogen-deuterium exchange between MBH_4 and MBD_4 (M = Li, Na) - Isotope effects on H-1 and B-11 NMR-spectra of BH_ND_{4-N} anions and a discussion of exchange-reactions in some covalent tetrahydroborate systems. Inorganic Chemistry 16 (1977) 2057-2062.

[90] J. Jeener, Ampere International Summer School, Basko Polje, Yugoslavia, 1971.

[91] W.P. Aue, E. Bartholdi, and R.R. Ernst, 2-Dimensional spectroscopy - application to nuclear magnetic-resonance. Journal of Chemical Physics 64 (1976) 2229-2246.

[92] A. Bax, Two-Dimensional Nuclear Magnetic Resonance in Liquids, Delft University Press, Dordrecht, Holland, 1984.

[93] A. Bax, and R. Freeman, Investigation of complex networks of spin-spin coupling by two-dimensional NMR. Journal of Magnetic Resonance 44 (1981) 542-561.

[94] P.T. Callaghan, Translational Dynamics and Magnetic Resonance: Principles of Pulsed Gradient Spin Echo NMR, Oxford University Press, Oxford, (forthcoming publication).

[95] S. Castellano, R. Kostelnik, and C. Sun, NMR spectral parameters of monosubstituted benzenes - halobenzenes. Tetrahedron Letters (1967) 4635-4639.

[96] W.G. Paterson, and E.J. Wells, NMR spectrum of para-difluorobenzene. Journal of Molecular Spectroscopy 14 (1964) 101.

[97] B. Blumich, F. Casanova, and S. Appelt, NMR at low magnetic fields. Chemical Physics Letters 477 (2009) 231-240.

[98] D.P. Weitekamp, A. Bielecki, D. Zax, K. Zilm, and A. Pines, Zero-Field Nuclear Magnetic Resonance. Physical Review Letters 50 (1983) 1807.

[99] D.B. Zax, A. Bielecki, K.W. Zilm, and A. Pines, Heteronuclear zero-field NMR. Chemical Physics Letters 106 (1984) 550-553.

[100] D.B. Zax, A. Bielecki, K.W. Zilm, A. Pines, and D.P. Weitekamp, Zero-field NMR and NQR. Journal of Chemical Physics 83 (1985) 4877-4905.

[101] R. McDermott, A.H. Trabesinger, M. Mück, E.L. Hahn, A. Pines, and J. Clarke, Liquid-state NMR and scalar couplings in microtesla magnetic fields. Science 295 (2002) 2247-2249.

[102] M.P. Ledbetter, C.W. Crawford, A. Pines, D.E. Wemmer, S. Knappe, J. Kitching, and D. Budker, Optical detection of NMR J-spectra at zero magnetic field. Journal of Magnetic Resonance 199 (2009) 25-29.

[103] M. Luzar, A.M. Thayer, and A. Pines, Zero-field NMR of uniaxial and biaxial smectic liquid-crystals. Molecular Physics 62 (1987) 573-583.

[104] A.M. Thayer, M. Luzar, and A. Pines, Heteronuclear zero-field NMR of liquid-crystals. Journal of Magnetic Resonance 72 (1987) 567-573.

[105] A.M. Thayer, M. Luzar, and A. Pines, Zero-field NMR of nematic liquid-crystals with positive and negative magnetic susceptibility anisotropies. Journal of Physical Chemistry 91 (1987) 2194-2197.

[106] E.T. Samulski, Princeton University, Princeton, New Jersey, USA, 1969.

[107] A. Elliott, and E.J. Ambrose, Evidence of chain folding in polypeptides and proteins. Discussions of the Faraday Society (1950) 246-&.

[108] A. Marx, and C. Thiele, Orientational Properties of Poly-gamma-benzyl-L-glutamate: Influence of Molecular Weight and Solvent on Order Parameters of the Solute. Chemistry-a European Journal 15 (2009) 254-260.

[109] L. Onsager, The effects of shape on the interaction of colloidal particles. Annals of the New York Academy of Sciences 51 (1949) 627-659.